HYSTERESIS EFFECTS DURING MARTENSITIC PHASE TRANSFORMATIONS IN Cu-Zn-Al SHAPE MEMORY ALLOYS

THESE N° 1115 (1993)

PRESENTEE AU DEPARTEMENT DE PHYSIQUE

ECOLE POLYTECHNIQUE FEDERALE DE LAUSANNE

POUR L'OBTENTION DU GRADE DE DOCTEUR ES SCIENCES

PAR

JOHANNES STOIBER

Ingénieur diplômé Friedrich-Alexander Universität Erlangen-Nürnberg
de nationalité allemande

acceptée sur proposition du jury:

Dr R. Gotthardt, rapporteur
Dr J.-E. Bidaux, corapporteur
Prof. E. Cesari, corapporteur
Prof. B. Ilschner, corapporteur
Dr J. Van Humbeeck, corapporteur

Lausanne, EPFL
1993

ABSTRACT

This dissertation has been addressed to the investigation of microstructural mechanisms which contribute to the hysteresis effect that is observed during martensitic phase transformations in Cu-Zn-Al alloys. Three different experimental methods have been used. The macroscopic hysteresis curves have been derived from electrical resistance measurements which allow for the determination of the transformed volume fraction. The microstructural evolution of a transforming material has been studied during *in situ* transformations by transmission electron microscopy (TEM). The method of internal friction (IF) has been used to measure the energy that is dissipated during the motion of transforming interfaces in order to get a quantitative measure of the associated microscopic hysteresis effect. The combination of these experimental techniques has allowed to establish a relationship between the microscopic hysteresis effect (IF behaviour) that is involved in the microstructural evolution (observed by TEM), and the macroscopic hysteresis effect (electrical resistance measurements). Two different transformation systems have been investigated.

In *single variant transformations*, the microscopic hysteresis effect (IF) is due to a small stress hysteresis ($\Delta\sigma = 0.2$ MPa) which is equal to the macroscopic stress hysteresis that is involved in the motion of a single martensite-austenite interface. The IF values could be explained with the results that the interface motion is a partially reversible process and that the main part of energy dissipation occurs by the anelastic shear deformation in the habit plane system.

During *polyvariant transformations*, the microscopic hysteresis effect (IF) increases in the course of the martensitic transformation. It was shown that the transient IF peak is not only dependent on the volume fraction that is transformed during oscillation, but also on the density of mobile martensite-martensite interfaces. The motion of martensite-martensite interfaces was directly observed by TEM during *in situ* experiments. The displacement of these interfaces, together with the motion of partial dislocations, was related to both the application of an external stress and the creation of a local elastic (internal) stress. Based on the mathematical description of the thermoelastic balance equation, it was demonstrated that the microstructural evolution which allows for the relaxation of the elastically stored energy, is responsible for typical macroscopic hysteresis effects such as: the asymmetric hysteresis shape, the internal transformation trajectories and the shift of transformation sub-loops.

RESUME

Le but de ce travail était d'étudier les mécanismes microscopiques qui contribuent à l'effet d'hystérèse observé au cours de la transformation martensitique dans les alliages de Cu-Zn-Al. Pour cela, trois techniques expérimentales complémentaires ont été utilisées. Des mesures de résistivité électrique, qui permettent de déterminer la fraction volumique de martensite ont permis de mettre en évidence le phénomène d'hystérèse macroscopique. L'évolution de la microstructure au cours de la transformation a été étudiée *in situ* par microscopie électronique (MET). Finalement, le frottement intérieur (FI) a été utilisé pour mesurer l'énergie dissipée par le mouvement des interfaces au cours de la transformation afin d'obtenir une mesure quantitative de l'effet d'hystérèse microscopique associé. La combinaison de ces techniques expérimentales a permis d'établir une relation entre l'effet d'hystérèse microscopique (comportement en FI), qui provient de l'évolution de la microstructure (observée en MET), et l'effet d'hystérèse macroscopique (mesures de résistivité électrique). Deux différents systèmes de transformation ont été étudiés.

Dans le cas d'une *transformation à une seule variante*, l'effet d'hystérèse microscopique est dû à une faible hystérèse de la contrainte ($\Delta\sigma = 0.2$ MPa) égale à celle de l'hystérèse macroscopique qui provient du mouvement d'une seule interface martensite-austenite. Les valeurs obtenues par FI ont pu être expliquées par le fait que le mouvement des interfaces est un processus partiellement réversible et que la principale contribution à la dissipation a lieu par déformation anélastique dans le plan d'habitat.

Au cours de *transformations à plusieurs variantes*, l'effet d'hystérèse microscopique (FI) s'accroît au cours de la transformation martensitique. Il a été démontré que le pic de FI transitoire ne dépend pas uniquement de la fraction volumique transformée au cours d'une oscillation mais également de la densité des interfaces martensite-martensite mobiles. Le mouvement des interfaces martensite-martensite a été directement mis en évidence par les observations MET *in situ*. Le déplacement de ces interfaces ainsi que le mouvement des dislocations partielles apparaissent soit lorsque l'on applique une contrainte externe, soit lorsque l'on crée un champ de contrainte élastique interne. Sur la base d'une modélisation mathématique des équations d'équilibre thermoélastique, il a été établi que l'évolution de la microstructure, qui permet la relaxation de l'énergie élastique emmagasinée, est à l'origine des effets typiques d'hystérèse macroscopique tels que: la forme asymétrique de l'hystérèse, les chemins de transformation internes et l 'évolution des sous-cycles de transformation.

TABLE OF CONTENTS

CHAPTER 2 Experimental Techniques

CHAPTER 3 The Hysteresis Effect during Martensitic Phase Transformations in Cu-Zn-Al Polycrystals : Results and Interpretations

INTRODUCTION

Cu-base alloys, which undergo a martensitic phase transformation, have received a lot of technological interest because of their unusual mechanical properties such as pseudoelasticity and the shape memory effect. The general knowledge of martensite and martensitic transformations in Cu-Zn, Cu-Zn-Al and Cu-Al-Ni alloys has developed considerably, and it is now generally accepted that the thermoelastic character of martensite in these alloys is responsible for their capability of reversible shape changes during transformation.

The hysteresis effect that is associated with martensitic phase transformations results from the irreversible dissipation of energy during one transformation cycle. Energy can be dissipated by nucleation processes, relaxation of elastic energy, ageing or stabilization of the parent and martensite phase, as well as by the work necessary to move the interfaces of the transformation front. The energy dissipative processes, and hence the hysteresis effect, depend strongly on the microstructure of the transforming material. The hysteresis properties (transformation temperatures, hysteresis width and slope) are influenced by the alloy composition and by the concentration of vacancies, dislocations and precipitates. The formation of crystal defects can be controlled by an initial thermomechanical treatment, but it is also dependent on the experimental conditions at which subsequent transformation cycles are performed.

For practical applications, the hysteresis effect and its dependency on microstructural properties can be both beneficial and detrimental. On the positive side, different shape memory applications can be realized with a given material. On the negative side, shape memory alloys are subject to time-dependent phenomena such as creep, fatigue, plastic deformation and ageing effects. These effects originate from changes of the microstructural properties and lead to degradation of the shape memory properties.

The theoretical understanding of the hysteresis effect is still restricted to special cases, where the experimental conditions are well defined and the microstructural properties of the material can be simplified. For more complicated situations, e.g. when small stress and temperature fluctuations occur in the transformation regime, the prediction of the hysteresis behaviour is much more difficult. Hence, more work is needed in order to explain the hysteresis effect of shape memory alloys and its dependence on microstructural properties.

The present study was undertaken in an attempt to increase the understanding of microstructural mechanisms, which are involved in the hysteresis effect. The movement of transforming interfaces and their contribution to the amount of energy that is dissipated during martensitic transformations, has been emphasized. The migration of martensite-austenite as well as martensite-martensite interfaces has been studied under different experimental conditions and microstructural properties.

The two main experimental techniques that were employed in this study are transmission electron microscopy (TEM) *in situ* observations and internal friction (IF) measurements. In the TEM experiments, the motion of transforming interfaces was directly observed and the crystallographic nature of participating crystal defects was analyzed. The internal friction (IF) measurements were conducted in order to get quantitative results about the microscopic hysteresis effects that occur during the transformations. The microscopic hysteresis effects have been correlated with microstructural mechanisms which are believed to have an important influence on the macroscopic hysteresis effect.

The manuscript is organized as follows:

Chapter 1 is a general review about the present knowledge of martensitic transformations in Cu-base shape memory alloys. Special emphasis has been placed on the explanation of the transformation hysteresis effect.

Chapter 2 is addressed to the description of the experimental techniques which have been used. The inverted torsion pendulum that was employed for the internal friction (IF) measurements and the TEM straining stage, which has been developed for observations of low temperature *in situ* transformations, are presented.

Chapter 3 characterizes the hysteresis phenomena that have been observed during martensitic transformations in different Cu-Zn-Al alloys. The hysteresis behaviour during complete, as well as during partial transformation cycles, has been investigated by means of IF measurements. The obtained IF behaviour is quantitatively analyzed, and the transitory part of the IF peak is related to the evolution of microstructural parameters.

Chapter 4 includes an investigation of the relationship between macroscopic and microscopic hysteresis effects in Cu-Zn-Al single crystalline specimens. The internal friction (microscopic hysteresis effect) has been studied during single variant transformations where the crystallographic nature of anelastic deformation can be identified from the knowledge of the orientation relations, and the hysteretic character of the interface motion can be established quantitatively.

Chapter 5 presents results of TEM observations, which have been conducted during *in situ* transformation and deformation of Cu-Zn-Al single crystals. Special emphasis has been placed on the microstructural evolution that occurs when a previously formed polyvariant martensitic structure is modified by small stress and temperature changes.

Chapter 6 is the general discussion of the results that have been obtained in this work. The goal of this discussion is to relate the observed microscopic hysteresis effects (IF) and microstructural mechanisms (TEM) to the macroscopic hysteresis that occur in different transformation systems. The damping mechanism of Cu-Zn-Al alloys is revised with respect to existing IF models and the experimental results of this work. The macroscopic hysteresis effect and the hysteresis instabilities obtained during incomplete transformation cycling are explained in terms of the thermoelastic balance equation, which includes a microscopical interpretation of the respective energy contributions.

CHAPTER 1

Bibliography:
The Martensitic Phase Transformation in Cu-Zn-Al Alloys

This chapter presents the most important aspects of the current understanding about martensite and martensitic transformations that has been developed in Cu-base shape memory alloys. Microstructural properties are illustrated by the crystallographic analysis and by models of transformation mechanisms. The actual understanding of the transformation hysteresis and the description of energy dissipative processes are outlined. The comparison of the phenomenological hysteresis models and experimentally observed hysteresis instabilities has been used to select the subject of the present investigation.

More complete information about martensitic transformations can be found in several books (e.g. Christian, 1965, and Nishiyama, 1978) and in a recent publication of Delaey (1991).

1.1 General Introduction to Martensitic Transformations, Hysteresis Effect and Shape Memory Effect

1.1.1 The Definition of Martensitic Transformations

The martensitic transformation is generally considered as the classical example of a displacive/diffusionless phase transformation in the solid state. A solid state structural change is termed "displacive/diffusionless" if it occurs by coordinated shifts of atoms and if long range diffusion during the phase change is not needed. The structural changes usually consist of small atomic movements over less than the interatomic distances. Within the overall class of displacive/diffusionless phase transformations, martensitic transformations have been defined by Cohen et al. (1979) as follows:

"A martensitic transformation is a lattice-distortive, virtually diffusionless structural change having a dominant deviatoric component and associated shape change such that the strain energy dominates the kinetics and morphology during the transformation."

Cohen et al. (1979) describe a displacive phase transformation as the combination of a lattice distortive deformation and shuffles. The lattice distortive deformation causes a homogeneous lattice deformation and a shuffle is a coordinated shift of atoms within a unit cell (figure 1.1). In martensitic transformations lattice distortive displacements rather than shuffles play the major role as it is indicated by the characteristic morphologies of martensite. The existence of an undistorted line puts the martensitic transformations into the sub-category, where the deviatoric rather than the dilatation component of the lattice deformation is dominant. The lattice distortive displacements are large enough that the kinetics and morphology during martensitic transformations are dominated by the strain energy. As a consequence, martensitic transformations are accomplished by nucleation and growth of the new phase; martensitic phase transformations are first-order reactions.

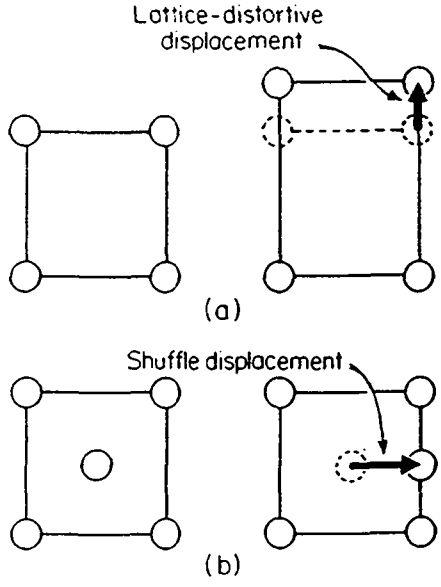

Figure 1.1: Schematic illustration of simple lattice-distortive and shuffle displacements.

Another characteristic commonly observed in martensitic transformations is the occurrence of lattice invariant or inhomogeneous deformations which do not alter the crystal structure. They are necessary in order to relieve the elastic strain energy that is generated by the lattice distortive displacements. Lattice invariant displacements are accomplished by means of slips, twinning or the formation of stacking faults.

1.1.2 Thermodynamics of Martensitic Transformations

Because of its diffusionless character, changes in chemical composition are not associated with the martensitic phase transformation. The parent and product phase have the same chemical composition and can therefore be treated as a single-component system. The evolution of the chemical Gibbs free energy of both the parent and martensite phase (G^P and G^M, respectively) is shown schematically in figure 1.2.

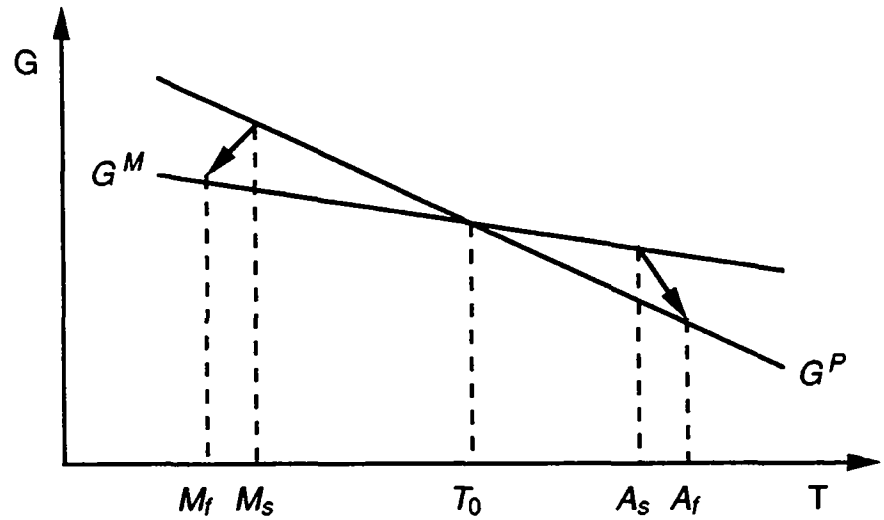

Figure 1.2: Schematic representation of the Gibbs free energy of the parent and martensite phases (G^P and G^M) as a function of temperature (T).

The difference between G^P and G^M is the chemical driving force (ΔG), which is the basis of the classical thermodynamic theory of first-order phase transitions (Kaufmann and Cohen, 1958). In general, the martensitic transformation does not start at T_0, the true first-order equilibrium temperature where $\Delta G = 0$, but at M_s ("martensite start") which is lower than T_0. Non-chemical energy contributions oppose the forward transformation and an increase in the chemical driving force is needed in order to complete the transformation at M_f ("martensite finish"). The reverse transformation starts at the A_s temperature ("austenite start") which is higher than T_0 and is finished at A_f ("austenite finish"). The temperature spans between M_s and M_f or A_s and A_f are associated with the effect of *thermoelasticity* while the differences between the forward and reverse transformation temperatures represents the *transformation hysteresis*.

1.1.3 The Hysteresis Effect of Martensitic Transformations

Martensitic phase transformations show a hysteresis effect. Hysteresis means that the evolution of the transformed volume fraction (n) is not a unique function of the external field parameters (temperature, T, or stress, σ) and that different paths are followed during forward and reverse transformations (figure 1.3a).

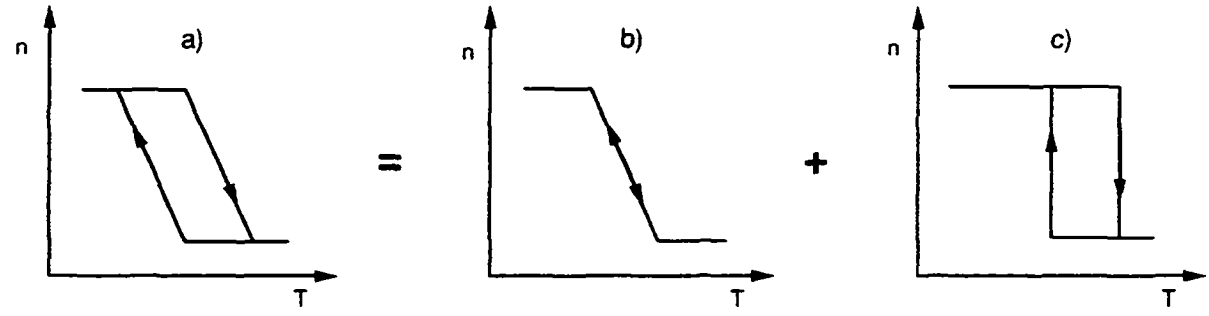

Figure 1.3: Schematic representation of the transformation hysteresis (transformed volume fraction (n) as a function of temperature (T)) : a) General case: elastic and energy dissipative contributions, b) only elastic contribution and c) only energy dissipative contribution.

The shape of the transformation hysteresis is dominated by elastic and energy dissipative contributions. The increasing stored elastic strain energy modifies the equilibrium temperature between the martensite and austenite phase and a finite slope of the $n(T)$ curve results, called *thermoelastic* hysteresis slope. Figure 1.3b shows the ideal case of a complete thermoelastic transformation, where any finite variation in the (thermal) driving force produces a corresponding increase or decrease in the volume of martensite. The amount of dissipated energy during transformation is characterized by the width of the hysteresis. Figure 1.3c shows the case where only energy dissipative contributions appear during the transformation.

1.1.4 Mechanical Properties:
Shape Memory Effect, Pseudoelasticity and High Damping Capacity

The Shape Memory Effect

When a fully martensitic shape memory material is apparently plastically deformed at any temperature below M_f and subsequently heated to temperatures above A_f, one observes that the

shape, which the specimen had prior to deformation starts to recover as soon as the A_S temperature is reached. The restoration is completed at A_f. This behaviour illustrated in figure 1.4, is called the "*shape memory effect*". If the specimen is subsequently cooled below M_S and its shape remains unchanged, this is termed the "*one-way shape memory effect*". On the other hand, if the specimen deforms spontaneously on cooling below M_S into a shape which approaches the shape that it had after the initial plastic deformation, the effect is called the "*two-way shape memory effect*".

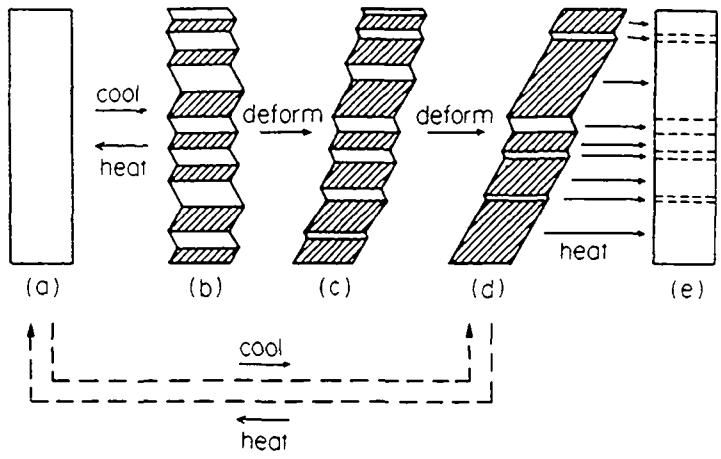

Figure 1.4: Schematic illustration of the shape memory effect after Otsuka and Shimizu (1986): a<->b: spontaneous transformation, b->c->d->e: One-way effect, a<->d: Two-way effect.

The appearance of a two-way memory effect requires special training procedures. In general, two different methods can be distinguished. A specimen can be cycled several times by applying an external stress in the direction of the desired deformation, or, the specimen can be subjected to stress-induced transformation cycles above A_f. During the training procedure the transforming variants leave dislocations inside the austenite phase which are, due to symmetry reasons, energetically less favorable for other variant orientations. Therefore, if a significant dislocation density is formed during training, the following spontaneous transformation will be carried by those variants which were formed during training and a macroscopical deformation will result without applying external loads. Details of the shape memory mechanism revised in connection with new aspects of this effect have been recently published by Stalmans et al. (1992).

Pseudoelasticity

The effect of pseudoelasticity is observed in shape memory alloys during stress-induced transformation at temperatures above A_f (figure 1.5). When the material is subjected to an increasing load, the transformation starts at a critical stress level (σ_c). After the transformation is finished the elastic deformation of the martensitic phase begins. If the stress is released before the martensite deforms plastically, the deformation is reversed completely in the course of the retransformation (martensite -> austenite). The large amounts of reversible strain describe the *effect of pseudoelasticity* ($5\% < \varepsilon_{psel} < 8\%$). The enclosed area of the σ-ε curve is a direct measure for the dissipated energy during one transformation cycle.

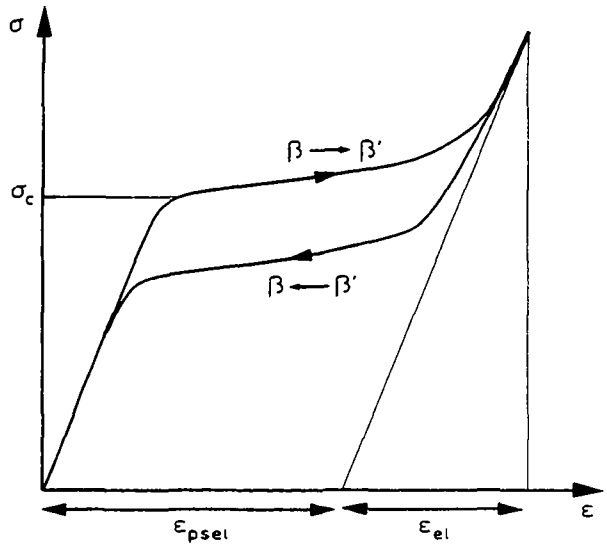

Figure 1.5: Pseudoelastic deformation behaviour observed during stress-induced transformation in shape memory alloys (σ_C is the critical stress, ε_{psel} and ε_{el} are the pseudoelastic and elastic strains).

High Damping Capacity

The hysteresis behaviour that is observed during one pseudoelastic cycle is also manifested in the high damping capacity which characterizes shape memory alloys. High damping arises either in the transformation region, when the applied alternating stress exceeds the critical stress that is necessary to induce the transformation, or in the martensitic state, where the movement of intervariant boundaries starts under the action of the oscillating stress. In both cases, the hysteretic forward and backward motion of the boundaries leads to damping. The damping capacity of martensitic shape memory alloys is one of the highest that has been observed in metals and alloys. Shape memory alloys are said to belong to the high damping materials (HIDAMETS), which have been reviewed by Schaller and Van Humbeeck (1992).

1.2 Crystallography of Martensitic Transformations

Due to the diffusionless character of the martensitic transformation, the martensitic phase shows a close crystallographic relationship to the parent phase. The knowledge of the transformation crystallography is essential for the understanding of the resulting martensitic microstructure and possible transformation mechanisms. The first step of the crystallographic analysis is the determination of the parent and martensitic phase structures.

1.2.1 The Parent Phase

For a wide range of compositions the equilibrium phase of Cu-Zn-Al alloys at high temperature is the β phase, a typical "electron Hume-Rothery phase" with a valency electron concentration (e/a) around 1.5 and the body centered (A2) structure. Its stability range decreases with decreasing temperature (figure 1.6) and centers around an e/a value of 1.48. At lower temperatures ordering reactions take place, forming a B2 or $L2_1$ superlattice. On cooling, the ordering reaction A2 to B2 takes place first and the B2 to $L2_1$ transition occurs at lower temperatures (figure 1.7). While the B2 ordering reaction can not be surpressed or affected by quenching the disordered β phase, fast quench from intermediate temperatures changes the degree of $L2_1$ ordering very drastically (Planes et al., 1990).

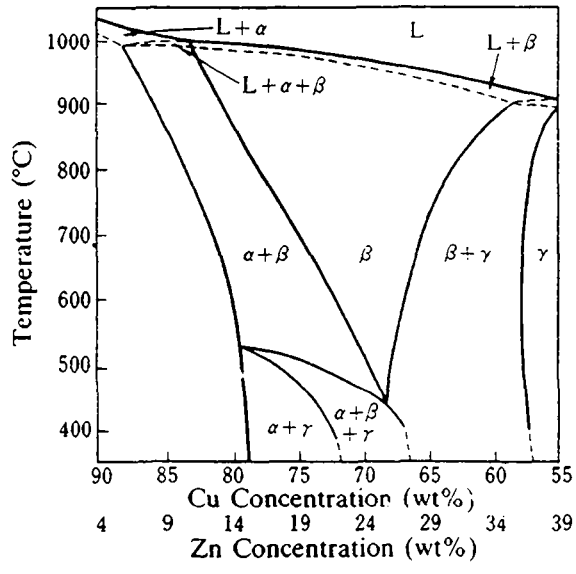

Figure 1.6:
Ternary equilibrium phase diagram of the Cu-Zn-Al system sectioned at 6 wt% Al (Delaey et al., 1978).

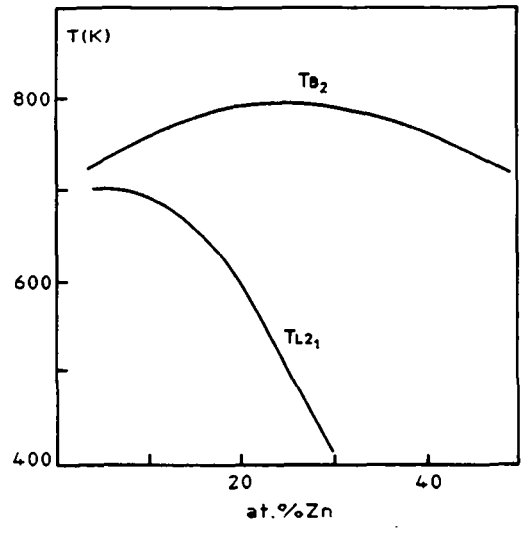

Figure 1.7:
Critical ordering temperatures for Cu-Zn-Al alloys with a constant electron/atom ratio e/a = 1.48 (Rapacioli and Ahlers, 1977).

The B2 and $L2_1$ superlattices can be described in terms of four *fcc* sublattices denoted as I-IV (figure 1.8). In the B2 structure sublattices I and II are occupied by Cu atoms, while sublattices III and IV are occupied with equal probabilities by the remaining atoms. In the $L2_1$ structure, sublattices I and II are also occupied by Cu atoms, but sublattice III is now occupied by Cu and Zn atoms, and sublattice IV by Al and Zn atoms.

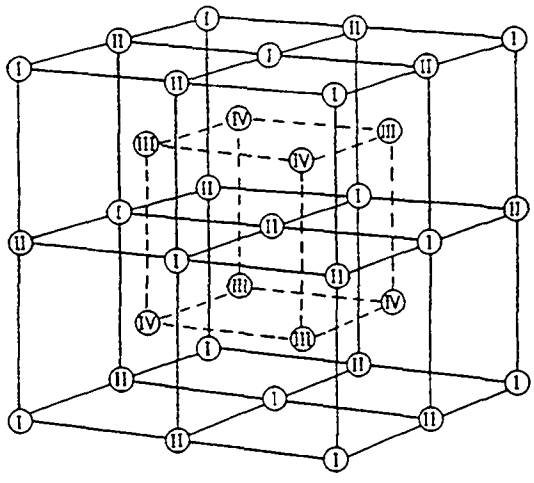

Figure 1.8: Primitive cell that represents the B_2 and $L2_1$ structure, depending on the occupancies of the four sublattice sites denoted by I, II, III and IV (see text).

1.2.2 The Martensite Phase

The martensite phase is obtained when the β phase is cooled to the M_s temperature. The ordered β phase transforms martensitically into close-packed structures with close packed planes, commonly called *basal planes*, which are derived from the {110} planes of the parent phase. Three different types of martensitic structures are commonly observed in Cu-base alloys, namely α', β', and γ' martensite. α' martensite has a face centered cubic stacking sequence, *ABC*, while γ' has a *AB* or hexagonal structure. The stacking sequence of β' is *ABCBCACAB*, that is a face centered cubic structure with one intrinsic stacking fault on each third plane. Alternative descriptions use the rhombohedral (R) or hexagonal (H) symmetry in the stacking sequence, and add the number of stacking planes in the unit cell. α', β', and γ' martensites are then called 3R, 9R and 2H.

The number of close-packed layers in the unit cell of the martensitic structure depends on the type of long range order prior to transformation. Eighteen layers are necessary to describe the structure of the β_1' and β_3' (DO_3 and $L2_1$ ordered) structures illustrated in figure 1.9:

AB'CB'CA'CA'BA'BC'BC'AC'AB'.

Because of the different atomic radii of Cu, Zn, and Al, their ordered distribution in the lattice leads to systematical lattice distortions. In particular, the regular hexagon configuration in the basal planes modifies the shift between the adjacent basal plane layers and the *c*-axis is no longer perpendicular the *a*-axis. Therefore, the unit cell of a 18R structure is not orthorhombic but monoclinic and the structure is called M18R. An exception to this modification is the 2H martensite that remains orthorhombic in spite of the distortions (Ahlers, 1986).

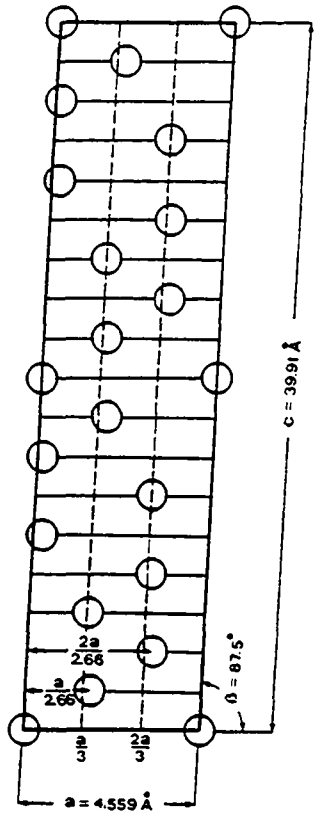

Figure 1.9: The modified M18R structure of martensite as observed in $Cu_{30}Au_{15}Zn_{45}$ alloys according to Shimizu (1977).

1.2.3 The Classical Phenomenological Theory

The crystallography of martensitic transformation has been explained by a general theory, which was developed independently by Wechsler et al. (1953) and Bowles and Mackenzie (1954). This *classical phenomenological theory* has been extended and successfully applied to many alloy systems including Cu-base alloys.

The theory is a matrix formulation of the distortions applied to the parent phase in order to obtain the martensite phase. With the knowledge of the structure and lattice parameters of the two phases, the theory predicts the orientation relationship between the two structures, the orientation of the habit plane and the macroscopic shape deformation. The basic assumption in this theory is that the interface between parent phase and the martensite phases (the "*habit plane*") is undistorted on a macroscopic scale (figure 1.10a). This requires an invariant plane strain (IPS) and the most general case of an IPS is the combination of a simple shear parallel to the invariant plane and a strain normal to the invariant plane, which leads to a change in volume (figure 1.10b).

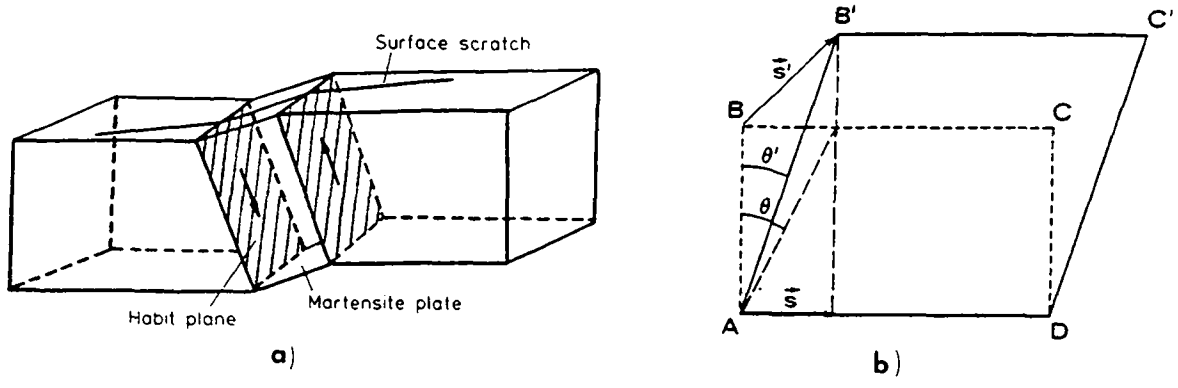

Figure 1.10: a) Schematic representation of a single martensite plate embedded in a single crystal of the matrix phase. b) General case of an invariant plane strain (IPS): simple extension + simple shear.

The phenomenological theory shows that the macroscopic shape change matrix S of an invariant plane transformation can be described by a combination of a pure lattice deformation B, a rigid lattice rotation R and an inhomogeneous lattice-invariant deformation P, as is illustrated in figure 1.11. The pure deformation matrix B gives the lattice correspondence between parent and product phase. The lattice invariant matrix P accounts for the measured shape deformation and the observed invariant plane and is an additional deformation. The pure rotation matrix R gives the final orientation relationships by matching the parent and product phase together, along the habit plane. The matrix S is commonly expressed by:

$$\mathbf{S = R P B} \qquad (1.1)$$

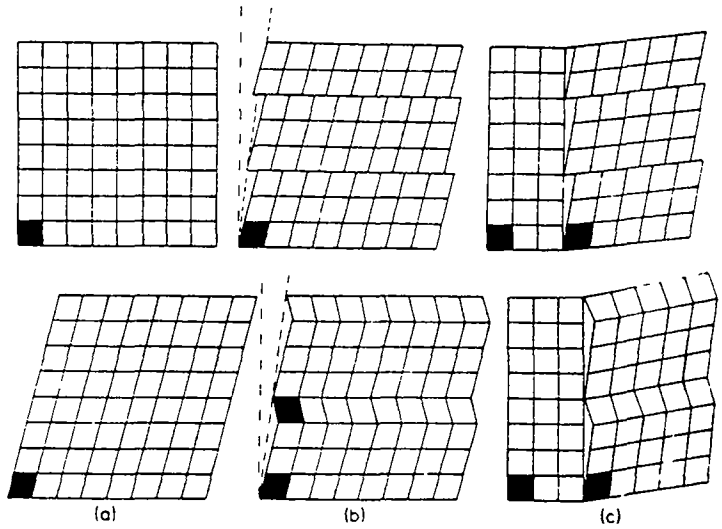

Figure 1.11: Schematic of the homogeneous lattice deformation (a), the inhomogeneous lattice invariant deformation through slip and twinning (b), and the lattice rotation (c).

The crystallography of the β_1 -> β_1' transformation was described by De Vos et al. (1978), when they developed a generalized mathematic model based on the phenomenological theory. The results of this model will be used in order to determine the crystallographic relationships of the single variant transformation system that is investigated in chapter 4.

The pure deformation matrix $\boldsymbol{B}$ is obtained by a homogeneous "Bain"-distortion, where the *bcc* lattice is transformed into a close-packed 9R structure that derives from a hypothetical face centered (*fcc*) structure (figure 1.12). The Bain distortion consists of an expansion parallel to the $[011]_{\beta_1}$-axis and a compression parallel to the $[100]_{\beta_1}$-axis. In a long-range ordered structure (B2 or $L2_1$) the effect of different sizes of the constituent atoms causes that the $(c/a)_{fcc}$ ratio is not 1. A hypothetical face centered tetragonal (*fct*) structure, which is characterized by its *tetragonal distortion* ψ ($\psi = c_{fct} / a_{fct}$), is introduced and a zero volume change is assumed (i.e. $a_{fct}^2 \cdot c_{fct} = a_{fcc}^3$). The invariant deformation matrix $\boldsymbol{P}$ consists of shears on the basal planes, which are the $(111)_{fcc}$ planes. With reference to an orthogonal system as defined in figure 1.12, the product between $\boldsymbol{B}$ and $\boldsymbol{P}$ is expressed by the matrix $\boldsymbol{F}$:

$$\mathbf{F} = \mathbf{P}\mathbf{B} = \begin{bmatrix} \eta_1 & 0 & 0 \\ 0 & \eta_2 & g\,\eta_3 \\ 0 & 0 & \eta_3 \end{bmatrix} \tag{1.2}$$

with

$$g = g_1 + \frac{1+2\psi^2}{18\sqrt{2}\psi} \tag{1.3}$$

The dilatation parameters η_1, η_2 and η_3 are listed in figure 1.12c. It can be seen that η_1, η_2 and η_3 only depend on the values of the tetragonal distortion (ψ) and the volume change parameter ($r = a_{fcc} / a_{bcc}$), both of which depend on the alloy composition.

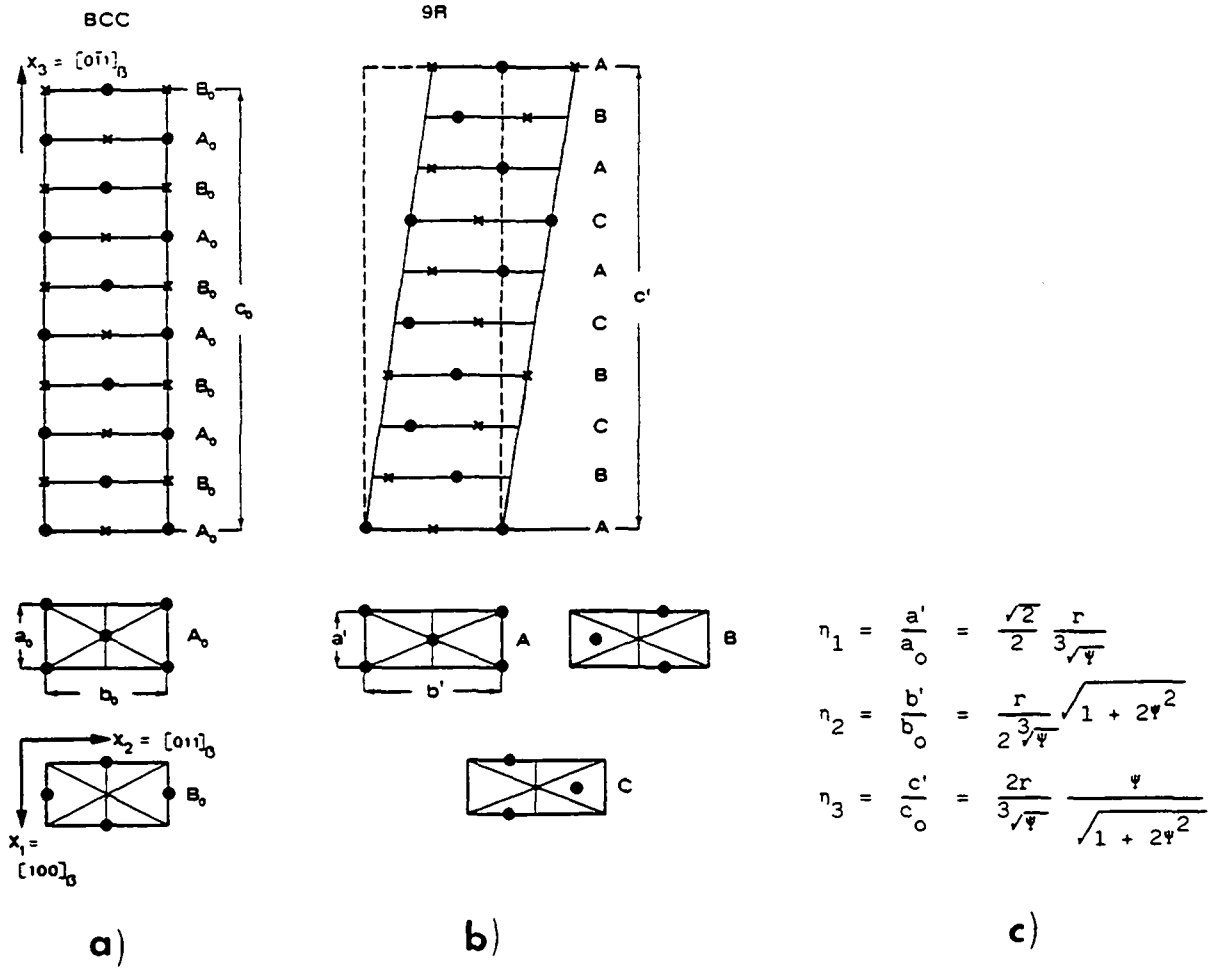

$$\eta_1 = \frac{a'}{a_o} = \frac{\sqrt{2}}{2}\,\frac{r}{\sqrt[3]{\psi}}$$

$$\eta_2 = \frac{b'}{b_o} = \frac{r}{2\sqrt[3]{\psi}}\,\sqrt{1 + 2\psi^2}$$

$$\eta_3 = \frac{c'}{c_o} = \frac{2r}{\sqrt[3]{\psi}}\,\frac{\psi}{\sqrt{1 + 2\psi^2}}$$

Figure 1.12: Orthorhombic presentation of the *bcc* lattice (a), the considered 9R structure as derived from a hypothetical *fcc* structure (b), and a list of the dilatation parameters (c).

The condition for an invariant plane transformation is given by

$$\mathrm{Det}\,(\mathbf{F}^t\,\mathbf{F}) = 0, \qquad (1.4)$$

which gives two values for g_1. Further diagonalization of **F** gives two values of g and thus four possible habit planes, which are listed in table 1.1. Since six differently oriented *bcc* lattices can be defined, a total of 24 variants can be formed from a single crystal of the parent phase.

From the knowledge of the matrix $\boldsymbol{F}$ the pure rotation matrix $\boldsymbol{R}$ can be determined. This is the matrix, which rotates the vectors resulting from the application of $\boldsymbol{F}$ into vectors lying in the habit plane.

Table 1.1: Direction cosines of the habit plane normals for the four variants that result from the lattice correspondence in figure 1.12.

H_1	H_2	H_3	H_4
$\sqrt{1-\eta_1^2}/\eta$	$\sqrt{1-\eta_1^2}/\eta$	$\sqrt{1-\eta_1^2}/\eta$	$\sqrt{1-\eta_1^2}/\eta$
$\sqrt{\eta_2^2-1}/\eta$	$-\sqrt{\eta_2^2-1}/\eta$	$-\sqrt{\eta_2^2-1}/\eta$	$\sqrt{\eta_2^2-1}/\eta$
$-\eta_2\sqrt{\eta_3^2-1}/\eta$	$\eta_2\sqrt{\eta_3^2-1}/\eta$	$-\eta_2\sqrt{\eta_3^2-1}/\eta$	$\eta_2\sqrt{\eta_3^2-1}/\eta$

The macroscopic shear deformations S and S' defined in figure 1.10b are given by

$$S = \sqrt{\eta_2^2\eta_3^2 + \eta_1^2 - 1 - \eta_1^2\eta_2^2\eta_3^2} \qquad (1.5)$$

$$S' = \eta_2\eta_3 - \eta_1 \qquad (1.6)$$

The total volume change due to the transformation is: $\Delta V = \eta_1\eta_2\eta_3 - 1$.

The results show that the only independent parameters that have to be considered for the calculation of the habit plane directions, the macroscopic deformation and the volume change are η_1, η_2 and η_3. Since these parameters can be calculated from ψ and r, the crystallographic relationships between parent and martensite phases can be completely determined, if the dependence of ψ and r on the alloy composition is known. For Cu-Zn-Al alloys, experimental values have been published by Ahlers (1974).

1.2.4 Habit Planes, Shape Deformation and Self-Accommodating Groups

The positions of the habit planes in M18R martensites are generally found to be clustered around the $\{110\}_\beta$ planes as shown in figure 1.13. While the magnitude of macroscopic shear strain is the same for all 24 variants ($\approx$ 19 %), the shear direction is different for each variant.

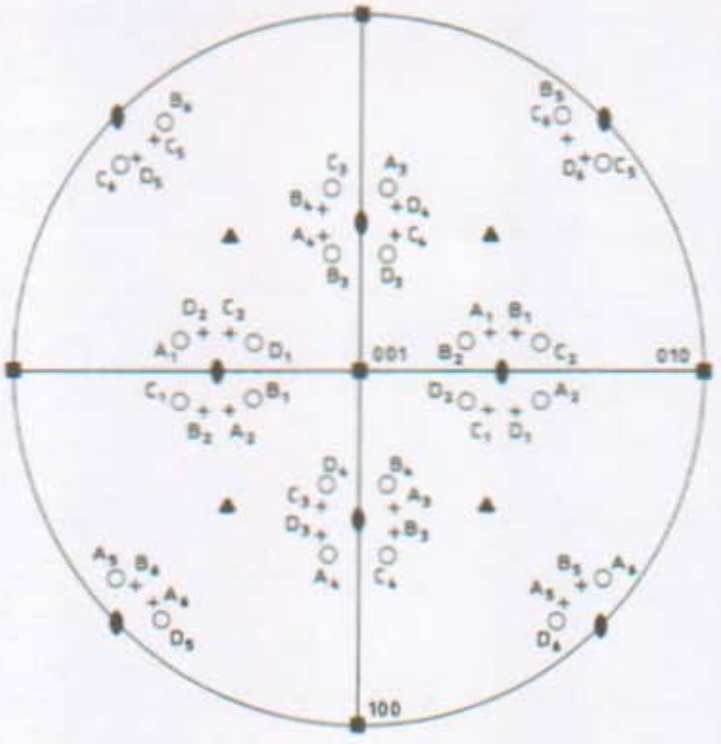

Figure 1.13: Position of the habit plane normals (o) and macroscopic shear directions (+) of the 24 variants formed from a single crystal of the parent β phase.

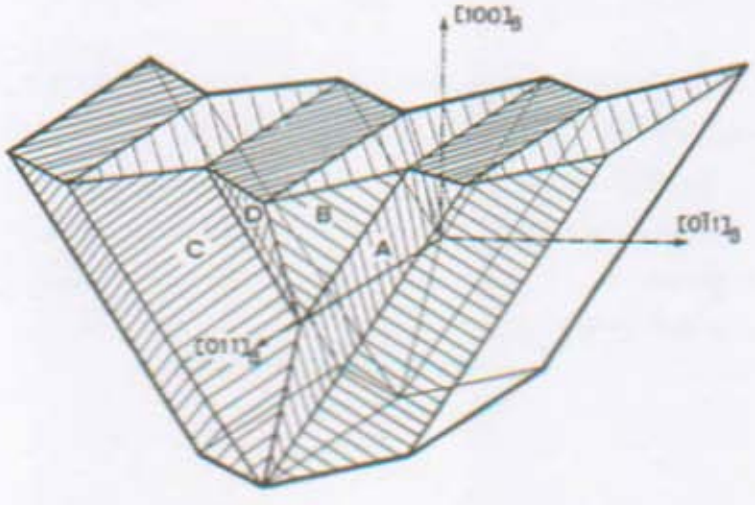

Figure 1.14: Three dimensional representation of the four variants in a self-accomodating group as proposed by Tas et al. (1973).

For a self-accomodating group, the habit plane normals and the shear directions of the variants are clustered around the same $\{110\}_\beta$ pole and <110> direction, respectively. The numerical results of the phenomenological theory show that the formation of equal volumes of the four

variants of a self-accomodating group gives an almost zero net shape deformation. That means that the shape deformations associated with each of the four variants is compensated by the others. It has been experimentally observed that the variants A and B (or C and D) as well as A and C (or B and D) produce opposite surface reliefs. On the other hand, for variants A and D (or B and C) the shape deformations are additive. Figure 1.14 illustrates a three dimensional model of the self-accomodating group developed by Tas et al. (1973), which accounts for the direction and sense of the macroscopic shears.

1.2.5 Orientation Relationships

The orientation relationship between the β_1 and β_1' phases can be obtained from the relative position of prominent planes and directions before and after transformation. The standard stereographic projection of figure 1.15 shows that there are two martensite poles, $(\bar{1}\,\bar{2}\,8)_{\beta_1'}$ and $(\bar{3}\,2\,0)_{\beta_1'}$, which coincide exactly with the parent phase poles $(0\,1\,1)_{\beta_1}$ and $(1\,\bar{1}\,1)_{\beta_1}$. The direction perpendicular to the $(\bar{3}\,2\,0)_{\beta_1'}$ plane is the $[\bar{2}\,1\,0]_{\beta_1'}$ direction. Note that the pole of a plane in the monoclinic M18R lattice does not necessarily have the same indices as the direction perpendicular to this plane.

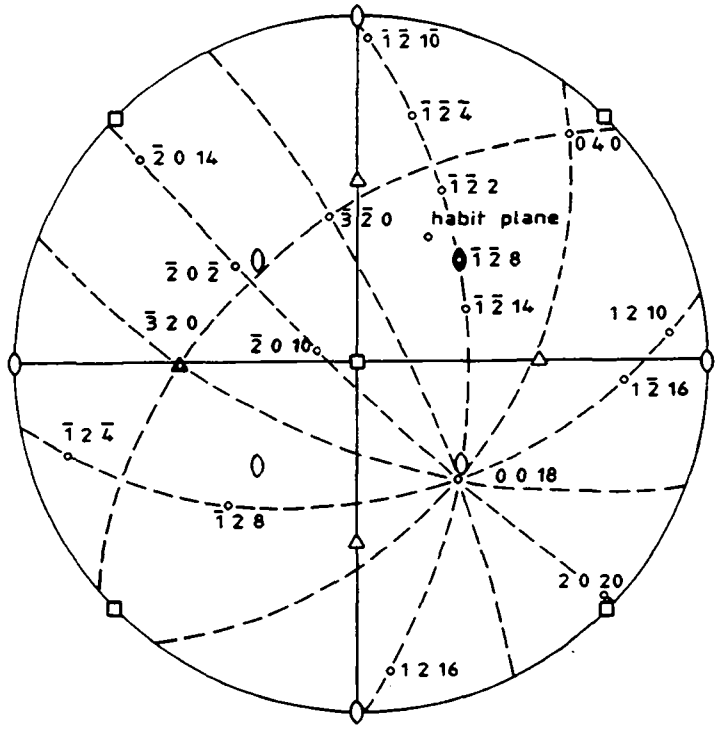

Figure 1.15: Orientation relations between the β_1 and β_1' structures. The indices in the stereo graphic projection refer to the 18R structure according to Tas et al. (1973).

As proposed by Tas et al. (1973) the orientation relationship between the β_I and β_I' phases can be expressed by:

$$(0\,1\,1)_{\beta_1} // (\bar{1}\,\bar{2}\,8)_{\beta_1'}$$

$$[1\,\bar{1}\,1]_{\beta_1} // [\bar{2}\,1\,0]_{\beta_1'}$$

The relation between the $\{110\}_{\beta_1}$ planes with respect to the $(\bar{1}\,\bar{2}\,8)_{\beta_1'}$, $(\bar{1}\,2\,8)_{\beta_1'}$ and $(0\,0\,18)_{\beta_1'}$ planes are shown in figure 1.16 by the geometrical model originally proposed by Delaey (1976). It can be seen that, by forming a self-accomodating group from a β crystal, four of the six $\{110\}_{\beta_1}$ planes are transformed into the $(0\,0\,18)_{\beta_1'}$ basal planes of the four variants, a fifth $\{110\}_{\beta_1}$ plane is transformed into the common unrotated $(\bar{1}\,\bar{2}\,8)_{\beta_1'}$ plane and the last produces the $(\bar{1}\,2\,8)_{\beta_1'}$ planes. The $(\bar{1}\,2\,8)_{\beta_1'}$ planes are crystallographically equivalent planes to the $(\bar{1}\,\bar{2}\,8)_{\beta_1'}$ planes and are of particular interest because of the presence of faults in this plane, which limit the basal plane stacking faults (Andrade (1983) and Lovey et al., 1984).

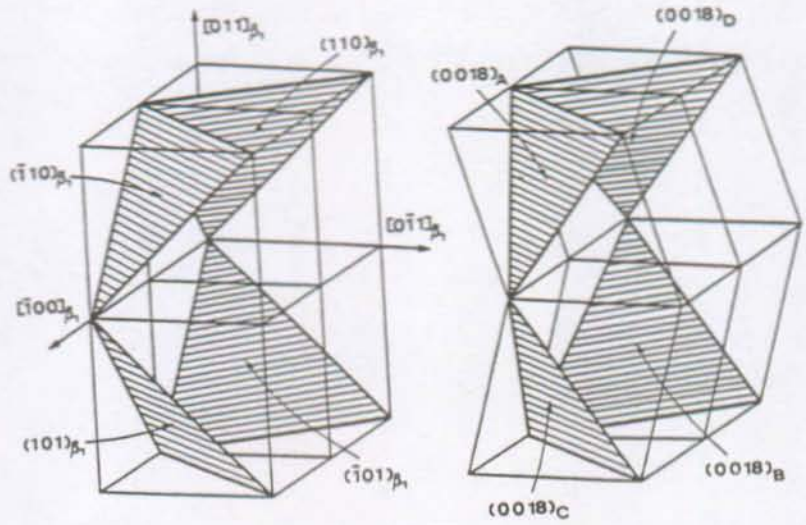

Figure 1.16:
Geometrical representation of the relations between the $\{110\}_{\beta 1}$ planes and the (0 0 18), $(\bar{1}\,\bar{2}\,8)$ and $(\bar{1}\,2\,8)$ planes of the four variants A, B, C and D in a self-accomodating group (Delaey, 1976); $(011)_{\beta_1} \rightarrow (\bar{1}\,\bar{2}\,8)$, $(0\bar{1}1)_{\beta_1} \rightarrow (\bar{1}\,2\,8)$.

1.2.6 The Martensitic Intervariant Boundaries

The orientation relationships between the four variants of a self-accomodating group are characterized by the fact that any two variants of the group are twin related. Typical couplings between these variants are represented in figure 1.17 and are referred to using the nomenclature,

which has been originally proposed by Schroeder and Wayman (1977). The three different types of interfaces which join the variants can be distinguished as the A/B , A/C and A/D type interfaces.

The twinning plane between variants (A and C) and (B and D) is the $(\bar{1}\,\bar{2}\,8)_{\beta_1'}$ plane, which is also the interface plane between variants (A and C) and (B and D). Variants A and B are twin related about the $(0\,\bar{1}\,1)_{\beta_1}$ plane, which is approximately 12° from the $(\bar{1}\,2\,8)_{\beta_1'}$ plane. The interface of these variants, however, is not the twinning plane but close to the habit planes of both variants, which are very close to each other. Therefore, these variants (A and B) are usually referred to as habit plane variants. The twinning plane between variants A and D is parallel to the $(1\,0\,0)_{\beta_1}$ plane, which is approximately parallel to the $(2\,0\,20)_{\beta_1'}$ plane. The interface of these variants is not usually planar, but it is close to the $(2\,0\,20)_{\beta_1'}$ or $(2\,0\,\overline{16})_{\beta_1'}$ planes.

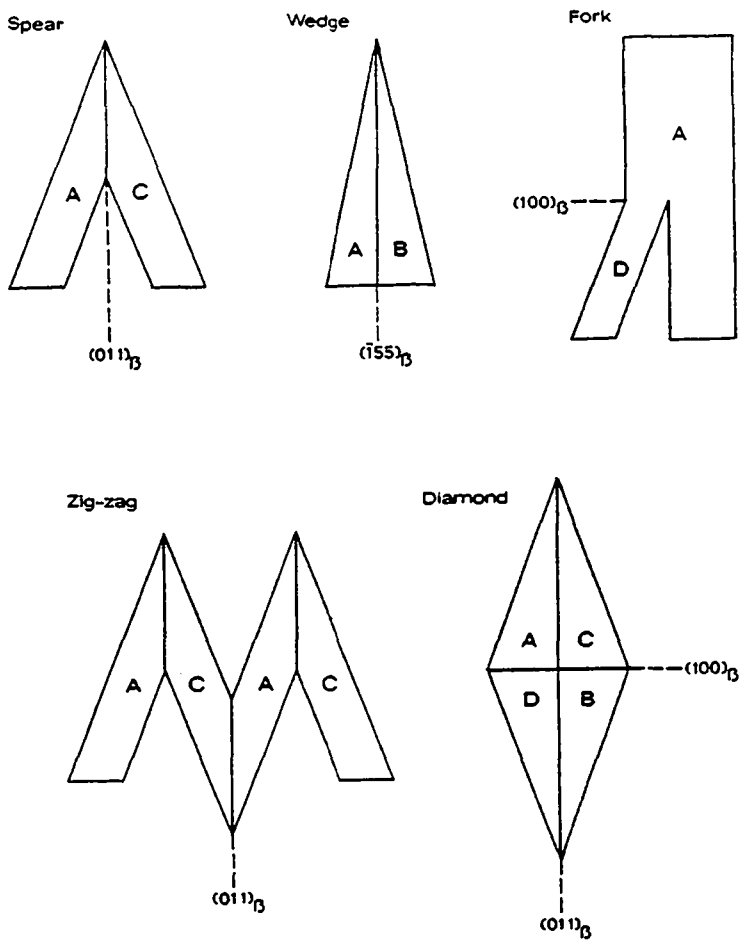

Figure 1.17:
Schematic representation of the spear, wedge, fork or kink, zig-zag and diamond configurations (Schroeder and Wayman, 1977).

All of the above mentioned interfaces are mobile under relatively low stresses as compared to those stresses which are required for the motion of dislocations in ordered Cu-base alloys. The mobility of intervariant boundaries is the basis for the existence of recoverable deformation in shape memory alloys. During memory deformation, coalescence and rearrangement of martensite plate variants favors the variant that gives the maximum strain in the direction of the applied stress. The conversion mode or the displacement of martensitic interfaces has been explained by the mechanism of deformation twinning, and will be discussed in chapter 5.

1.3 Transformation Mechanisms

It has to be emphasized that the pure lattice distortions, as considered in the phenomenological theory, do not necessarily describe the actual path, that the atoms will follow during a martensitic phase transformation. Based on experimental observations, different transformation mechanisms have been proposed. For the *bcc* to 9R transformation, Ahlers (1974) has developed a geometrical model that presents a two-shear mechanism (figure 1.18).

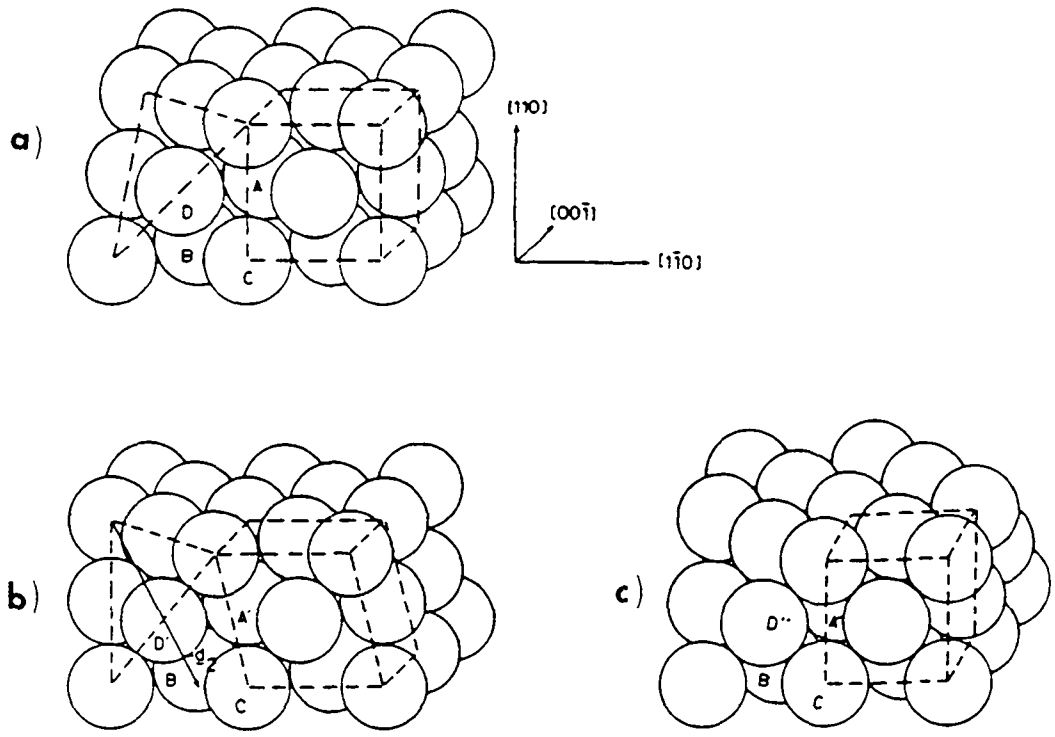

Figure 1.18: a) The *bcc* structure represented as the stacking of $(110)_{bcc}$ planes.
b) The intermediate structure after the first shear. The arrow denoted by $-d_2$ gives the direction of the second shear. c) The final fcc structure.

In this model, the first shear on the $(110)_{bcc}$ plane in the $(\bar{1}10)_{bcc}$ direction transforms the $(011)_{bcc}$ plane into a close-packed plane. The close-packed planes, however, are not in the proper stacking order. Therefore, a second shear in the close-packed planes is considered in order to obtain the close-packed *fcc* stacking (figure 1.18c). When successive planes are sheared in such a way that after two consecutive planes the sense of the shear is inversed, the 9R structure results.

Since martensitic transformations are first-order phase transitions, they occur by nucleation and growth. The growth stage takes place by the motion of interfaces which convert the parent phase to the product phase. Two types of paths have been proposed for the stage of nucleation, the *classical* nucleation path proposed by Olson et al. (1982) and the *non-classical* path as proposed by Guénin et al. (1982). Both theories take into account the heterogeneous character of martensitic nucleation, but while the classical approach involves the formation of a nucleus of the final martensitic structure, the non-classical approach involves a continuous change in structure near a mechanically unstable zone.

1.3.1 Nucleation

The Classical Theory

In the classical theory, the martensitic nucleus forms with a constant composition and structure. Because shear strains are involved in the martensitic transformation, the shape of the nucleus is determined by both the strain energy and the surface energy. Assuming an oblate spheroidal shape, the aspect ratio (c/r) of the critical nucleus will be such that for any change of the shape, the decrease in free strain energy (ΔG_{el}) is balanced by an increase in interfacial energy (ΔG_s). If the nucleation occurs at a lattice defect, the defect energy (G_d) as well as the nucleus-defect interaction energy (G_i) has to be considered.

According to Olson and Cohen (1982), the total free energy, $G(r,c)$, describing the formation of a martensite nucleus becomes:

$$G(r,c) = G_d + G_i + \Delta G_{ch} + \Delta G_{el} + \Delta G_s \qquad (1.7)$$

where ΔG_{ch} is the chemical free energy change per plate.

The calculations of the critical free energy for nucleation have shown that in the case of homogeneous nucleation (G_d and G_i are zero) the necessary energy barrier is too high by several orders of magnitude. Therefore, inhomogeneous nucleation at lattice defects has been emphasized over the possibility of homogeneous nucleation.

The Non-Classical Theory

In many β phase alloys anomalies in the elastic behaviour have been observed when the M_S temperature is reached upon cooling (Nakanishi, 1975). The elastic shear constant C', $C' = 0.5\ (C_{11} - C_{12})$, has a relatively low value at M_S. C' represents the resistance against shear deformation on the $\{110\}\langle 110\rangle_\beta$ system, which is close to the habit plane deformation system. Therefore, many attempts have been made to correlate the low value of C' at M_S ("*softening*") with the formation of martensite.

Since the homogeneous soft-mode concept is not adequate to describe the nucleation of martensite (C' does not become zero at M_S), a "*localized soft mode theory*" has been proposed by Guénin and Clapp (1986). This model is based on the assumption that stresses and strains around lattice defects can induce a mechanical instability, where the nucleus can develop without generating any strain energy and the only resisting force is the surface energy. These conditions lead to a reduced critical size of the nucleus, which is further decreased as the temperature is lowered.

1.3.2 Thermoelastic Growth

In the noble metal shape memory alloys, the martensitic transformation is athermic and a thermoelastic type of growth occurs. Thermoelasticity in the course of martensitic transformation was first observed by Kurdjumov and Khandros (1949). They found that γ' martensitic plates of a Cu-Al alloy grew continuously when the temperature was lowered and shrunk continuously when the temperature was increased. The thermoelastic behaviour has been defined as an equilibrium condition between chemical and non-chemical forces, which is achieved during the growth (or shrinkage) of an individual plate, if the matrix is able to accommodate the shape deformation of the martensite plate elastically. The mechanical analog to thermoelasticity is the pseudoelastic behaviour, where the increase or decrease in stress controls the growth or shrinkage of individual martensitic plates.

The conditions which have been found to be helpful in establishing thermoelastic behaviour are: a relatively low chemical driving force at M_S, a parent phase with a high flow stress and an anomalous positive temperature dependence of elastic constants near M_S (Olson and Cohen, 1975). A low chemical driving force at M_S assures that the initially transformed martensite will not grow so fast that the deformation strains can not be accommodated elastically ("burst" type of growth). Also, a parent phase with a high flow stress and low elastic constants promotes the elastic accomodation.

Single interface transformations, where the martensite plate reaches the free specimen surface, have been considered to proceed without storage of elastic energy and thermoelasticity has been assumed to be absent (Olson and Cohen, 1975). Salzbrenner and Cohen (1979) showed experimentally that a β_1 -> γ_1' single interface transformation starts and finishes within a 0.5 K temperature interval. However, an intrinsic thermoelasticity was recently found for the movement of a β_1 -> β_1' single interface in Cu-Zn-Al (Lovey et al., 1990). The thermoelastic slope of the interface position versus temperature curve ($x(T)$) depends on the thermal treatment to which the specimen is subjected, see figure 1.19. Samples cooled slowly in air after betatizing showed a thermoelastic slope $x(T)$ that is 10 - 20 times higher than for water quenched specimens. The additionally required undercooling in water quenched specimens has been attributed to the interaction of martensite and pre-existing matrix dislocations. Dislocations, whose Burgers vector lies out of the basal plane, loose their translation symmetry when embedded in martensite and stacking faults must be created in the martensite. Hence more and more fault will be dragged as the martensite absorbs the dislocations, and further undercooling is required for the transformation. In polyvariant martensitic transformations, this intrinsic thermoelasticity is masked by other contributions, such as intervariant interactions, which are stronger than martensite-dislocation interactions.

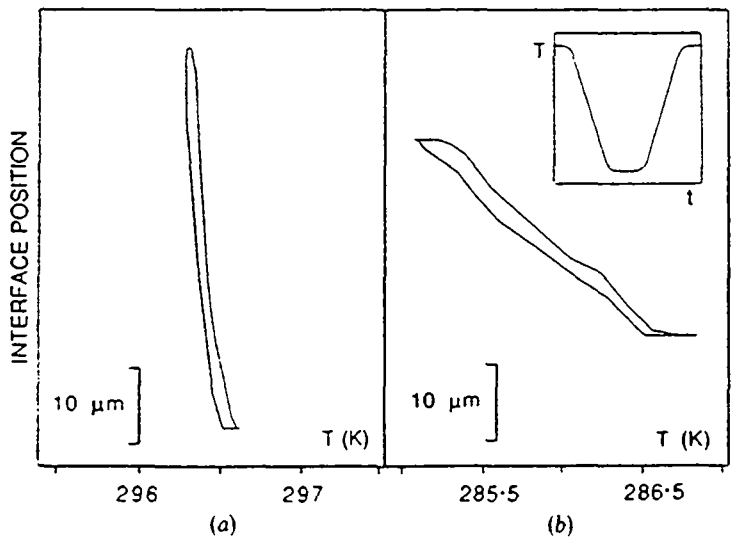

Figure 1.19: Hysteresis cycles of interface position x versus temperature T (Lovey et al., 1990): a) after air cooling, b) after quenching in water.

1.4 Transformation Hysteresis in Shape Memory Alloys

1.4.1 Energy Dissipative Processes

The closed hysteresis loop is contoured in a sense such that it encloses a positive area, which represents the energy lost in the cycling process (figure 1.3). Therefore, the hysteresis behaviour is always related to energy-dissipative processes. Delaey et al. (1987) have shown that energy dissipative effects originate from :

i) Intrinsically non-equilibrium processes, such as nucleation,

ii) non-equilibrium processes induced by the external field (temperature or stress) which drives the transformation (e.g. local relaxation of elastically stored strain energy),

iii) irreversible contributions to the thermoelastic equilibrium (frictional work to move the interfaces which accomplish a transformational shear strain),

iv) ageing and stabilization.

Nucleation

Olson and Cohen (1977) have shown that an intrinsic hysteresis is present, even for a thermo-elastically growing martensitic plate, because the initial nucleation and growth at the M_S temperature and the reversion at the A_f temperature do not occur in thermoelastic equilibrium. At M_S, the first nucleus forms with a critical volume fraction through an intrinsically out-of-equilibrium process. During reversion the shrinking plate becomes unstable radially and the martensitic particle disappears at A_f, out of equilibrium.

Nucleation is an important hysteresis contribution, if the formation of the first nucleus of the new phase becomes very difficult, as it is the case for the β_1 -> γ_1' transformation in Cu-Zn-Al and Cu-Al-Ni alloys (Pelegrina and Ahlers, 1992).

Friction Forces

Frictional work is dissipated during the motion of transforming interfaces. Suzuki (1986) proposed that the multiplication and motion of dislocations which form the interfaces, is the most important factor for the amount of dissipated energy during interface motion. Considering

the motion of atoms during *bcc->hcp* and *fcc->hcp* transformations, Suzuki derived the free energy dissipation for different types of martensite with respect to the deformation mode, i.e. if twinning, faulting or regular dislocation motion is involved in the transformation process. For shape memory martensite the results show a very low energy dissipation, which is confirmed by the small hysteresis width (0.2 - 0.5 K) that has been experimentally observed during single interface transformations (figure 1.19). However, the description of Suzuki does not seem to explain the larger hysteresis that is observed during martensitic polyvariant transformations.

Relaxation of Elastically Stored Energy

The relaxation of elastic strain energy is considered to be a very important hysteresis contribution during polyvariant or multiple interface transformations. In this case, elastic strain energy, which is built up during the growth of an individual variant, can be relaxed by the formation of another variant that produces the opposite macroscopic deformation. The results of this investigation will show that the relaxation of elastic energy, in the course of the successive formation of self-accomodating groups of martensitic variants, is an important contribution to the hysteresis effect and influences the partial transformation behaviour (chapter 6).

Ageing and Stabilization

Diffusion controlled processes, like changes in the atomic order in the parent and martensite phase, take place during ageing. As a result, the relative thermodynamic stability of one phase with respect to the other changes and the transformation temperatures and therefore the hysteresis are modified (Rapacioli and Ahlers, 1977). These processes are thermally activated and are one of the factors, which limit the temperature range for shape memory applications to a maximum temperature of 200°C. In this study, the influence of thermally activated vacancy diffusion could be avoided by an appropriate heat treatment, where the excess vacancies were annealed at temperatures above M_S (step-quenching).

1.4.2 Hysteresis Effects during Partial Transformation Cycling

Apart from the overall hysteresis curve, hysteresis sub-loops can be produced by partial temperature (stress) cycling, where either an incomplete forward transformation with subsequent heating (unloading) or an incomplete reverse transformation with subsequent cooling (loading)

is performed. During partial transformation cycling, the thermodynamical transformation paths inside the two-phase region are rather distinct. The typical properties, which are illustrated in figure 1.20, were first defined by Cory and McNichols (1985) and recently summarized by Ortin and Planes (1991):

i) All the transformation trajectories are located within the two phase region of the n-σ-T space and are bounded by the trajectories of a complete transformation cycle.

ii) Each transformation path depends only on the set of extreme values (return points) reached by the external driving force (T or σ) on the trajectory. The system keeps "memory" of this set of values.

iii) Each time that a transformation trajectory returns to an earlier extreme value of T or σ the influence of this value on the trajectory is lost (wiping out property). Due to that property partial transformation cycles exhibit self-similar behaviour.

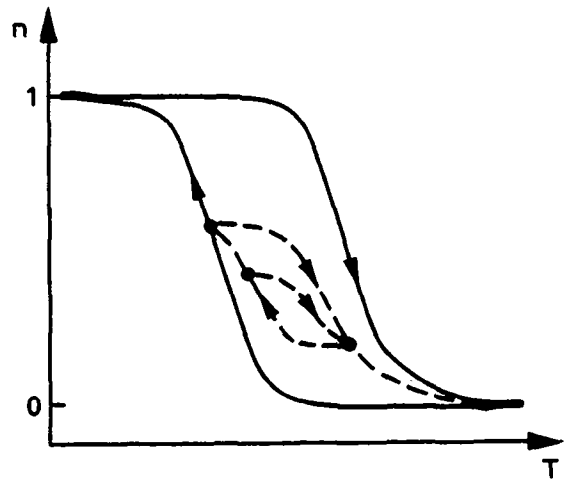

Figure 1.20:
Main characteristics of partial transformation cycles. The reversion points are marked with full circles.

The above mentioned characteristics have been experimentally observed during partial cycles of both thermally and stress-induced transformations in different shape memory alloys such as: Cu-Zn (Cornelis and Wayman, 1976), Cu-Zn-Al (Lü Li et al., 1990, Zhougguo and Dazhi, 1988) and NiTi (Paskal and Monasevich, 1981).

1.4.3 Hysteresis Instabilities

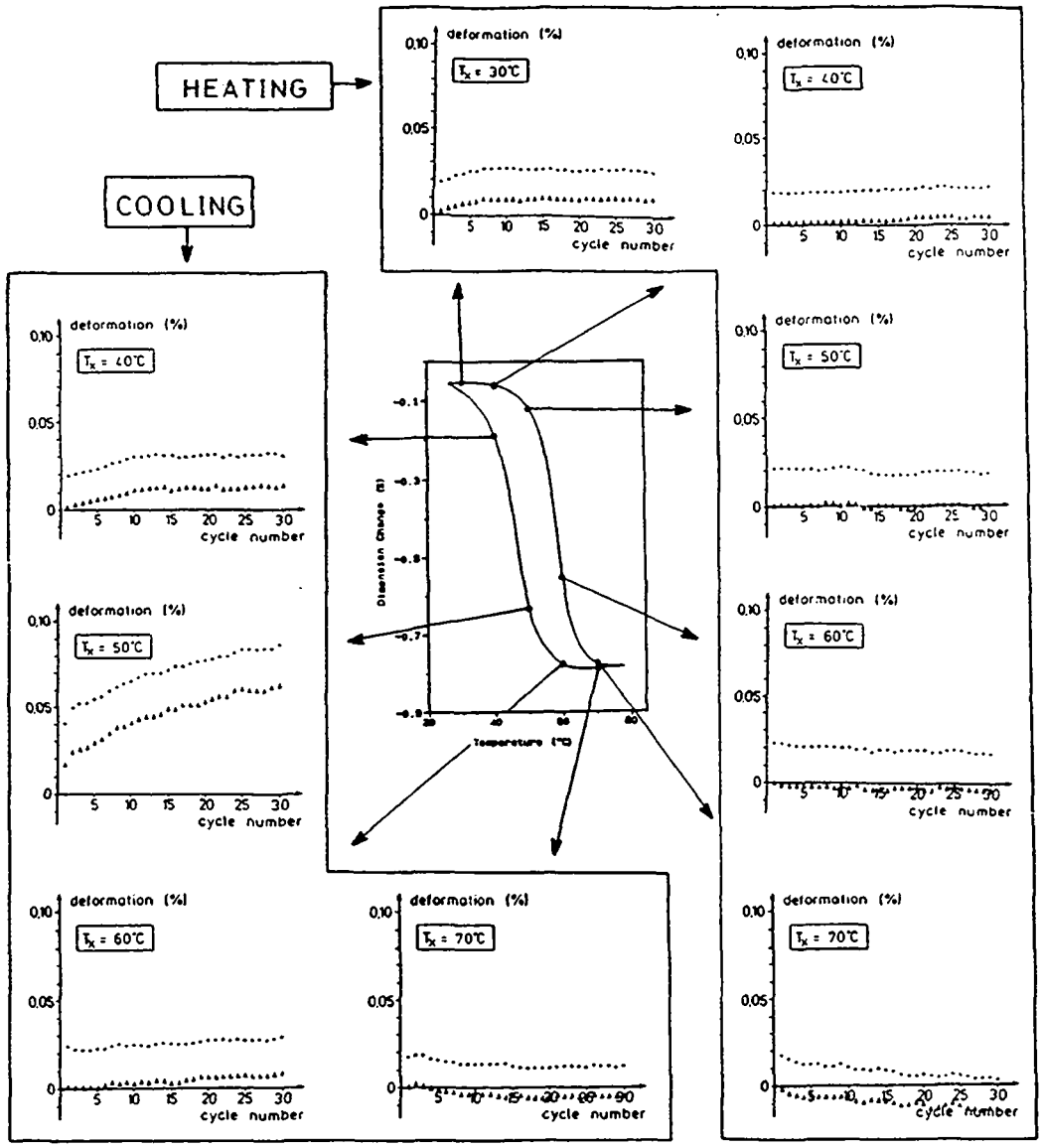

Figure 1.21: Overview of partial stress cycling experiments performed with a small stress amplitude (between 0 and 7 MPa) in a trained Cu-Zn-Al alloy:
Note the positive and negative creep behaviour (Van Humbeeck et al., 1990).

Hysteresis instabilities have been observed when incomplete transformation cycles or transformation sub-loops were performed repetitively. Van Humbeeck and Stalmans (1990) have investigated the shape response of educated Cu-Zn-Al specimens during small temperature and stress cycles in the transformation regime. They found that after cooling from the austenitic state repetitive cycling resulted in a positive creep of the specimen, while after heating from the

martensitic state a significant amount of negative creep was observed during cycling (figure 1.21). Electrical resistivity measurements conducted by Steiner (1986) during spontaneous transformation in Cu-Zn-Al polycrystals showed a significant shift of the hysteresis sub-loops (figure 1.22).

The microscopical origins of these hysteresis instabilities are not yet well understood. The hysteresis models that will be presented in the following paragraph, are of phenomenological nature and microscopical aspects are in general not considered.

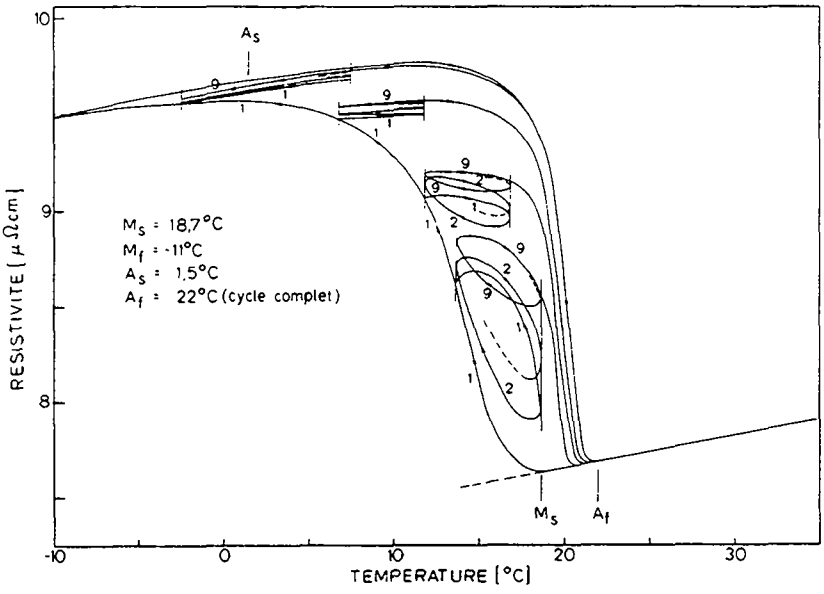

Figure 1.22: Electrical resistivity as a function of temperature showing the shift of transformation sub-loops (Steiner, 1986).

1.4.4 Hysteresis Models

The Landau-Devonshire Theory

Müller et al. (1991) have developed a model of pseudoelastic hysteresis that is based on the Landau-Devonshire theory, which was firstly applied to shape memory alloys by Falk (1980). In this theory, the hysteresis effect is due to the appearance of non-monotone load-deformation equilibrium curves. The width of the hysteresis is determined by the interfacial energy of the boundaries between martensite and austenite. Internal hysteresis loops contain metastable states

that loose their metastability on the line, which defines phase equilibrium (figure 1.23). The model of Müller accounts for the existence of internal trajectories, but does not reproduce the memory properties that have been shown in figure 1.20.

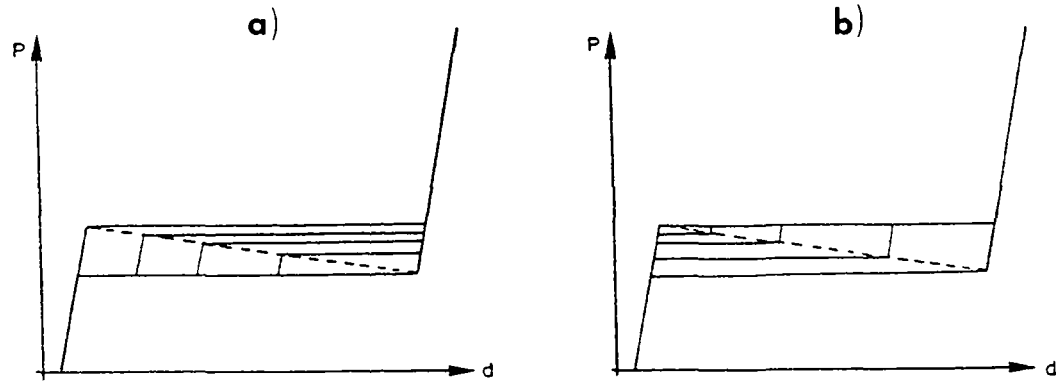

Figure 1.23: Theoretical transformation trajectories according to Müller et al. (1991): a) Partial loading curves, b) partial unloading curves.

The Preisach Model

Another approach to modeling pseudoelastic hysteresis cycles has been recently formulated by Ortin (1992), namely the Preisach model. The Preisach model was firstly developed to describe ferromagnetic hysteresis phenomena and recently, a mathematical basis of this model has been established by Mayergoyz (1985). A superposition of elementary operators $\gamma_{\alpha\beta}$ (defined in figure 1.24a) with different α, β values provides the strain $\varepsilon(t)$ that corresponds to a value $\sigma(t)$ of the applied stress and gives the transformation path ($\varepsilon(t)$) of any sub-cycle by the following integral:

$$\varepsilon(t) = \iint_{S^+(t)} \mu(\alpha,\beta)\, d\alpha\, d\beta \qquad (1.8)$$

where the function $\mu(\alpha,\beta)$ represents the population of operators, determined from a set of experimental first-order trajectories and $S^+(t)$ is a region, which contains all the (α,β) points of elementary operators in the +1 state at the time t.

Figure 1.24b shows an example of a first-order trajectory. Memory of the return points is retained by the particular shape of $S^+(t)$. Preliminary applications to pseudoelastic cycles in Cu-Zn-Al single crystals have shown a fine sensitivity of the trajectories for the precise values

of experimental return points and a good reproducibility of the internal transformation paths. The advantages of this model are that there is a direct connection with experimental data and that the quantitative prediction of any trajectory inside the two-phase region is possible. However, this model does not take into account any physical properties of thermoelastic martensites and must therefore be seen as a pure mathematical description.

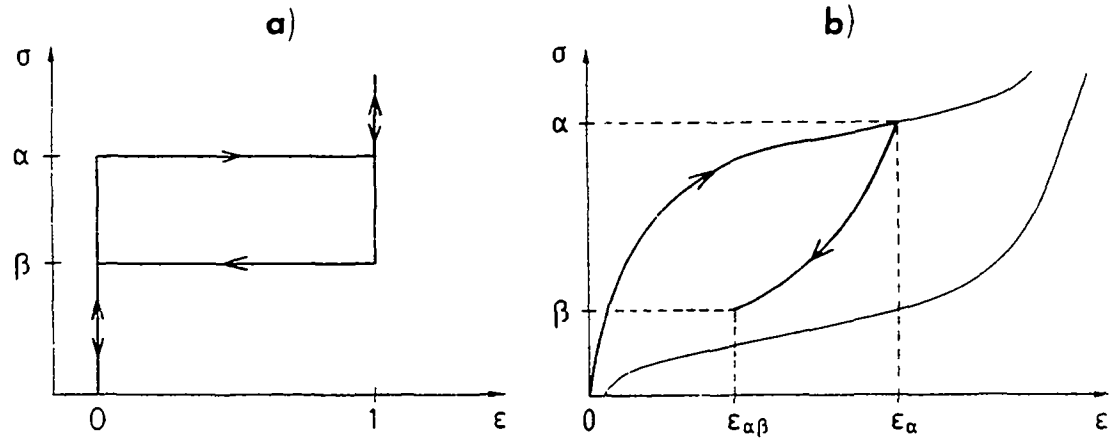

Figure 1.24: a) Definition of the elementary hysteresis operator $\gamma_{\alpha\beta}$ and b) schematic of a first-order reversal trajectory, according to Ortin (1992).

The Thermoelastic Balance Equation

The thermoelastic balance equation is based on the idea that during forward transformations the chemical driving force is balanced by the increasing elastic strain energy and the resistive forces against interface motion, while during reverse transformation both the chemical driving force and the stored elastic energy promote the reversion into the parent phase and must be balanced by the resistive forces (Olson and Cohen, 1975 and 1977). The thermoelastic balance equation can be written for the Gibbs free energy change of the moving plates:

$$\Delta G_{ch} + \Delta G_{el} + W_{ir} = 0 \qquad (1.9)$$

ΔG_{ch} gives the difference in chemical Gibbs free energy (kJ/mole) between the parent and the martensite phase. ΔG_{el} is the elastic energy contribution due to the interfacial energy and elastic volume strains. If no other contribution than ΔG_{el} had to be considered for the non-chemical energy, a complete reversible transformation behaviour would result. W_{irr} stands for the irreversible contributions to the non-chemical free energy change.

Equation (1.9) has been employed to evaluate the different energy contributions to the thermoelastic balance. Ortin and Planes (1988, 1989) have measured the heat exchanged between the

sample and the surroundings during calorimetric experiments and evaluated ΔG_{ch}, ΔG_{el} and W_{irr} separately. The condition for this analysis, as presented in figure 1.25, is that the specimen must recover its original thermodynamic state after one transformation cycle. The transformation must take place without any irreversible dissipation of heat and the friction work of transforming interfaces is supposed to be dissipated in form of acoustic (mechanical) waves. Since this condition is equivalent with a null entropy production it has been termed the "*entropy argument*". The validity of this assumption has been critically discussed in the work of Torra and Tachoire (1992).

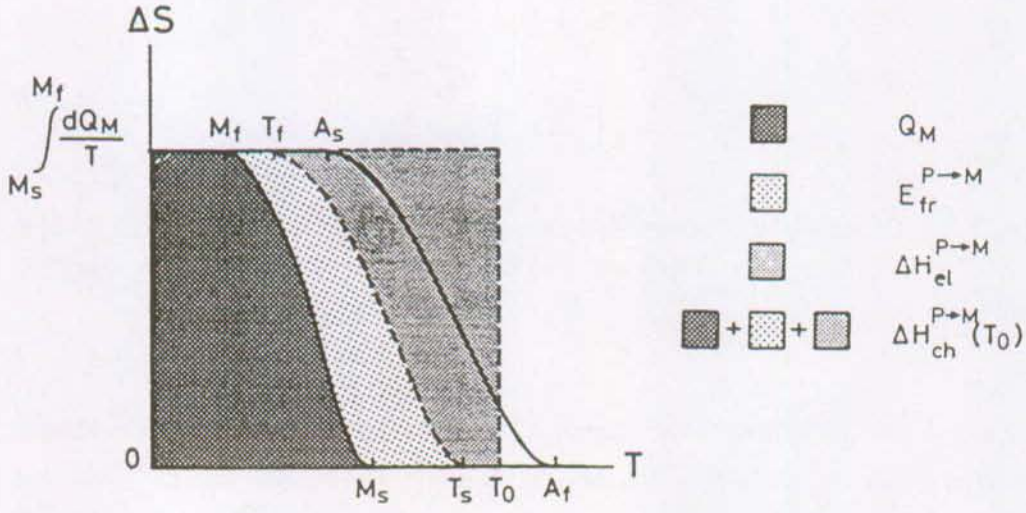

Figure 1.25: Schematic representation of the hysteresis contributions (E_{fr} = frictional work, ΔE_{el} = elastic strain enthalpy, ΔH_{CH} = latent heat, Q_M = total measured heat) as can be determined during a calorimetric run (Ortin and Planes, 1988).

Equation (1.9) can be used for the prediction of hysteresis loops, when the functional terms of all energy contributions are established. In the phenomenological model of Lü Li et al. (1990) the shape memory specimen is represented as a network of shape memory operators (figure 1.26). The balance equation of thermoelasticity is verified in each operator, but the chemical driving force (T_0 temperature) differs by a constant value from operator to operator. The dissipative term in each operator is explicitly defined to keep memory of the last return point. Coupling a number of these operators in parallel transforms individual straight line trajectories into global trajectories with smooth curvature. The model accurately reproduces the essential features of hysteresis loops in the stress-strain plane at constant temperature and in the temperature-strain plane at constant stress. The main drawback of this approach is that there is no experimental evidence which proves the validity of the assumed distribution of the T_0 temperatures. As an alternative, the explanation of the partial temperature behaviour, as presented in chapter 6, concentrates on the variation of the elastic strain energy and the local

character of relaxation processes both of which change continuously the thermoelastic equilibrium inside the material.

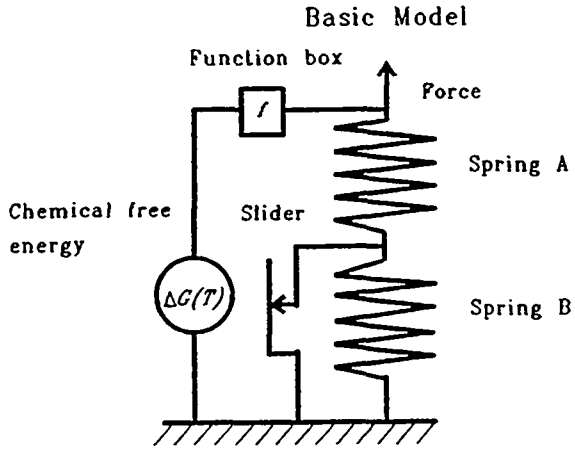

Figure 1.26: Shape-memory operator as used in the model of Lü Li et al. (1990), is composed of two springs, one slider and a function box.

A more simplified hysteresis model, which is based on the concept of thermoelasticity, has been proposed by Cesari et al. (1991). This model is built on the simplest choice for the chemical and non-chemical free energies. Apart from the global hysteresis the model is able to describe the sub-loop behaviour. This model is explicitly formulated in the discussion of chapter 6 and extended with microstructural interpretations of the non-chemical energy contributions.

1.5 Motivation and Concept of the Present Investigation

The review of the actual knowledge of martensitic transformations in Cu-base alloys has shown that a variety of analysis and interpretations exist for the understanding of transformation mechanisms, the martensitic microstructure and the transformation hysteresis. However, the direct relationship between microstructural descriptions of the transformation mechanisms and the macroscopically observed hysteresis effect is very difficult. Only a few attempts have been made to correlate the microstructural evolution during the transformation with the amount of dissipated energy.

The present investigation was undertaken as an attempt to supply more information about the interaction between the microstructural properties of a transforming material and the resulting hysteresis effect. It will be demonstrated that the technique of internal friction (IF) measurements can be used to relate the macroscopical hysteresis to the microstructural mechanisms which govern the transformation process (figure 1.27). The measured IF gives quantitative information about the energy dissipation that is associated with the hysteretic motion of crystal defects which are involved in the martensitic transformation. The information about the nature of these defects (interfaces, partial dislocations) will be obtained from *in situ* experiments by transmission electron microscopy (TEM).

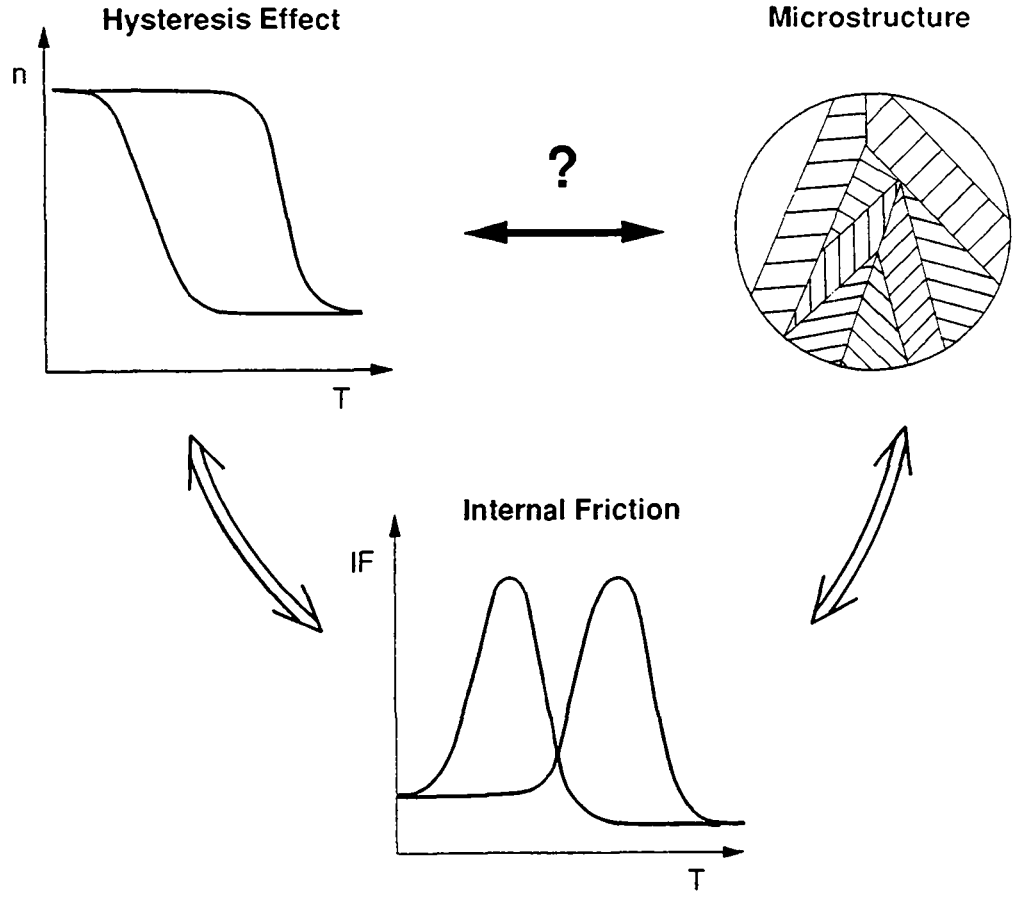

Figure 1.27: The relations between internal friction, microstructure and the macroscopic hysteresis effect. For explanations see text.

The concept of the investigation includes two main aspects:

First, the relationship between the martensitic microstructure that is formed during transformation and the IF behavior as well as between the macroscopic hysteresis effect and the internal friction have to be established. The results of this study will allow for a more detailed description of the damping mechanism, which governs the anelastic deformation during the transformation of shape memory alloys.

Second, the information obtained from the first aspect will be used to explain the relationship between the macroscopic hysteresis and the microstructural evolutions that are observed during complete and incomplete transformation cycles in different Cu-Zn-Al shape memory alloys.

CHAPTER 2

Experimental Techniques

This chapter explains the experimental techniques which have been used for the study of hysteresis effects during martensitic phase transformations. The method of internal friction (IF) is described as well as the employed inverted torsion pendulum which has been modified in order to allow for the study of both temperature- and stress-induced transformations. The straining stage that has been developed for the TEM *in situ* observations at low temperatures is also presented. These techniques are complementary methods for the study of hysteresis effects. Energy dissipative mechanisms are detected quantitatively by means of the IF measurements and can be related to microstructural evolutions, which are observed under similar conditions in the TEM during *in situ* experiments.

2.1 Internal Friction Measurements

2.1.1 Method

The *internal friction* is a physical quantity describing the effect of anelasticity, which is observed in many different materials. A detailed treatment of anelasticity in crystalline solids can be found in the book of Nowick and Berry (1972). The internal friction (IF) is generally measured in dynamic deformation experiments. In these experiments an alternating stress (or strain) is imposed on the system and the phase lag of the strain behind the stress (or the stress behind the strain), usually called δ, is determined. In the linear case, where the strain is a linear function of stress, $tan\delta$ gives a measure of the fractional energy loss per cycle due to anelastic behaviour of the specimen. The quantity $tan\delta$ is commonly known as the IF of the material. Expressing the IF by the inverted quality factor (Q^{-1}) the definition of IF becomes equal to:

$$IF = Q^{-1} = \frac{1}{2\pi}\frac{\Delta W}{W} = \tan\delta \qquad (2.1)$$

where W is the stored elastic energy and ΔW is the dissipated energy during one oscillation cycle.

In an inverted torsion pendulum, as it is described in the following paragraph, the IF is measured by the decay or damping of free vibrations. A specimen is excited in torsion until a fixed vibration amplitude is attained. After excitation the system is isolated from external forces and the decay of the oscillation amplitude is measured (figure 2.1). Then, the IF can be calculated from the logarithmic decrement Δ, which represents the natural logarithm of the ratio of amplitudes *(A)* of the *i*th and *(n+i)*th oscillation:

$$Q^{-1} = \frac{\Delta}{\pi} = \frac{1}{n\pi}\ln\left(\frac{A_i}{A_{n+i}}\right) \qquad (2.2)$$

Both measures of IF, $tan\delta$ and Δ, are directly related by the factor π:

$$\Delta = \pi \tan\delta \qquad (2.3)$$

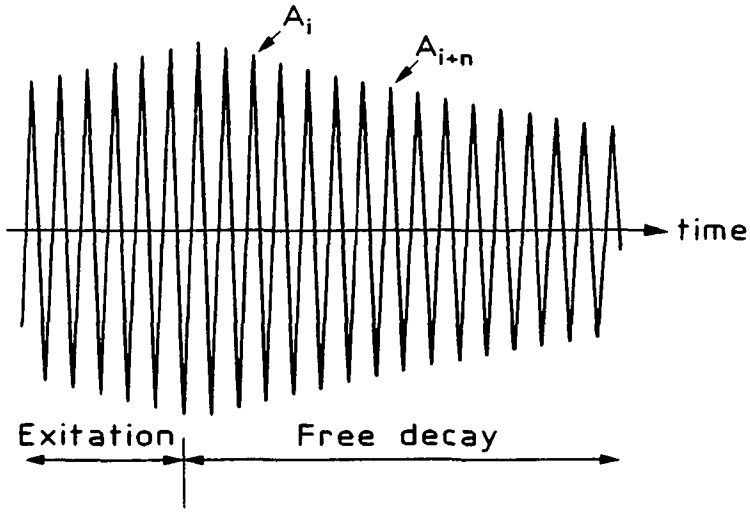

Figure 2.1: Excitation and free decay of oscillations during IF measurement in a torsion pendulum.

In the present study, a more accurate method for the determination of Q^{-1} than the traditional analysis of the wave height (logarithmic decrement) has been chosen. The wave form analysis, as described by Yoshida et al. (1981), calculates the IF via the Fourier transform of the oscillations. The basis of the calculations is the enlarged peak of the frequency spectrum observed for damped oscillations. The shape of the peak which is situated at the resonance

frequency of the pendulum, determines the IF. The main advantage of this technique is that the oscillation signal is filtered and perturbations due to parasitic frequencies of the system can be eliminated (Baur and Kulik, 1983).

In a pendulum that works at free vibrations the oscillation frequency f gives information about the shear modulus G of the specimen. f depends on the inertial moment I of the system and on the resistance moment of the specimen, if the pendulum is constructed such that all other resistance moments are negligible (Secrétan et al., 1962). For this case, f becomes equal to:

$$f = \frac{1}{2\pi}\sqrt{\frac{C}{I}} \qquad (2.4)$$

C is the constant of the resistance moment. For a specimen with rectangular cross section, C can be calculated with the following equation (Timoshenko, 1963):

$$C = \frac{\beta\, b\, c^3\, G}{L} \qquad (2.5)$$

where L is the length of the specimen, b and c are the thickness and the width of the rectangular section, and β is a numerical factor that depends on the L/c ratio.

2.1.2 Apparatus: The Inverted Torsion Pendulum

General Characteristics

A classical inverted torsion pendulum has been employed for the measurement of the IF. The installation is mounted onto an antivibrational structure and the pendulum is enclosed by a vacuum chamber so that an excellent mechanical stability is guaranteed during the measurements. The experiments are usually performed in 5 Torr He-atmosphere in which the thermal conductivity is sufficient to control the temperature of the specimen. Under these conditions, the influence of air friction on the oscillations as well as ice formation at low temperatures and surface oxidation at higher temperatures, are eliminated.

Apart from the determination of the IF (Q^{-1}), the apparatus allows for the simultaneous measurement of the resonance frequency *(f)*, the electrical resistance *(R)*, the actual temperature *(T)*, the applied tensile force *(F)*, the elongation *(dL)* and the torsion angle or zero drift *(Z)* of a specimen. Controlled temperature and tensile force changes are possible covering the ranges between 80 K and 700 K and between 0 and 50 N, respectively. The oscillation frequency can be varied between 0.5 Hz and 1.5 Hz and the applied deformation amplitudes during oscillation vary between 10^{-7} and 10^{-3}.

Description of the Pendulum

The schematic of figure 2.2 shows the principle mechanical, electronic and data acquisition units of the inverted torsion pendulum.

The specimen (10) is fixed at its lower part and its upper part is connected to the inertial mass of the excitation system (6). The counter weight (13) provides for the mechanical equilibrium of the pendulum. The inertial mass is excited by two magnetic coils (7) until a fixed deformation amplitude of the specimen is attained. The movement of the specimen is transmitted by a laser beam (2), which is reflected to the photoelectric cell (5) via an arrangement of different mirrors. The first mirror (3) is connected to the specimen and the second mirror can be rotated by an electromotor (4) in order to correct deviations of the laser beam from the zero position, called zero shift Z. The photoelectric cell divides the electronic signal into a DC signal accounting for the Z-measurement and an AC signal giving the oscillation amplitude spectrum as a function of time. The latter signal is used for the determination of the oscillation frequency and the IF.

For the electrical resistance measurement, a current of 1 A is applied to the specimen and the voltage drop across the specimen is detected at both specimen grips. The resolution of the detected electrical resistance is 1 $\mu\Omega$.

Temperature and Tensile Force Control

The experiments can be performed during controlled temperature and tensile force programs. For measurements below room temperature, the lower part of the pendulum which is enclosed by a tube of stainless steel, is submerged in a liquid nitrogen bath. Heating of the specimen is performed with a resistance furnace (8). The temperature is measured by two Pt 100 sondes (9), which are fixed at the furnace directly across from the specimen. A PID regulation program controls the power supply of the furnace. The temperature stability is about $\pm$ 0.05 K at the furnace, but a temperature gradient of 0.02 K/mm exists along the length of the specimen.

The stress application device has been developed in the frame of this study. It consists of an electromagnet (14), which is connected to the counter weight and applies a tensile force to the specimen proportional to the electrical current. The force is measured by a load cell (12), which is fixed on the upper part of the counter weight and is controlled by the D.C. supply of a commercial PID regulator. The maximum force of this system is about 50 N and the stability is at least $\pm$ 0.02 N. The regulator can be programmed to perform ramps with constant force rates in the range between 0.1 N/min and 2 N/min. A LVDT (linear voltage differential transducer, (11)) detects, indirectly, the changes in the length of the specimen by the displacement of the counter weight.

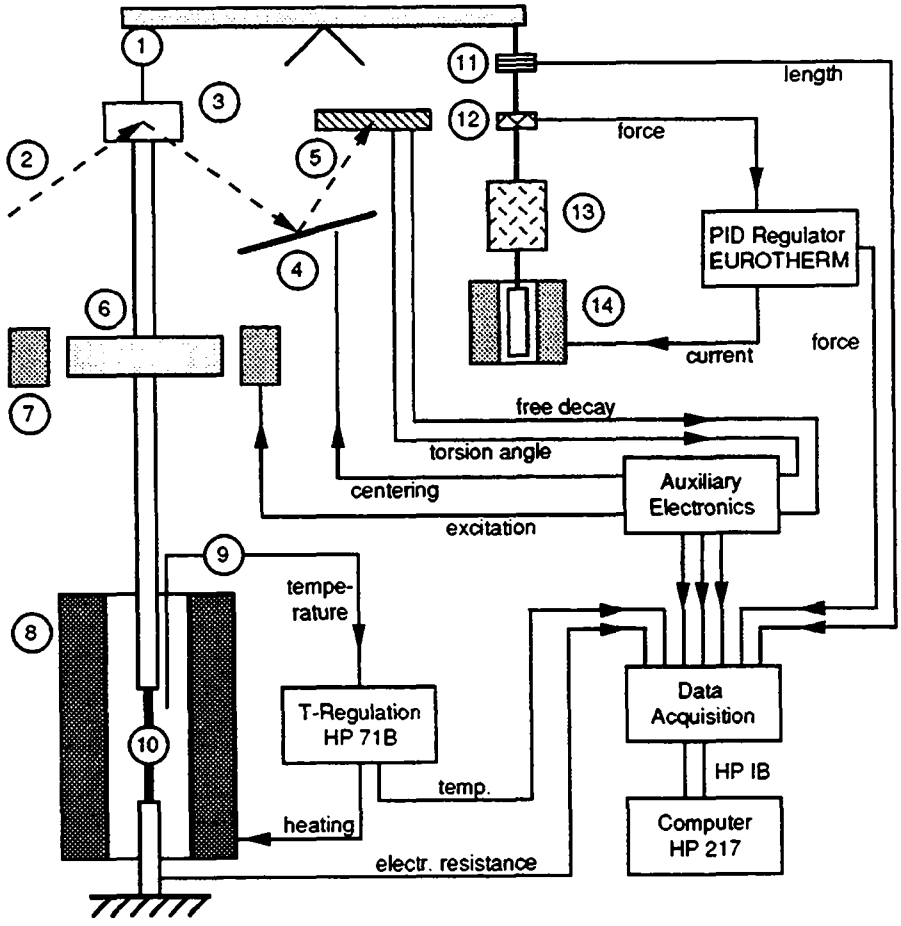

Figure 2.2: Schematic of the inverted torsion pendulum.
1: Suspension (3 wires), 2: Laser beam, 3: Mirror, 4: Centering device, 5: Photoelectric Cell, 6: Inertial mass, 7: Excitation coils, 8: Furnace, 9: Pt 100 sonde, 10: Specimen, 11: LVDT transducer, 12: Load cell, 13: Counter weight, 14: Electro magnet.

Data Acquisition and Control System

The installation described above has a complete automatic control system that consists of a HP 217 computer and a HP 3497A data acquisition unit, see also figure 2.2.

The main component in the data acquisition unit (HP 3497A) is a rapid DC voltmeter which samples the free decay signal with a sufficiently high frequency. Furthermore, it provides the reading of the actual values of the measuring parameters. Additional relays control the excitation pulses, the resistance measurement, the correction of zero position, and the level of the liquid nitrogen bath. A counter determines the oscillation frequency on the base of the number of zero crossing pulses within a fixed time period.

The experimental data are transmitted from the voltmeter to the HP computer, where a program controls all of the different tasks during the measurement. For the realization of one measurement point, the following task sequence, which takes about 40 seconds is conducted:

1. Measure the zero drift Z and correct the laser beam position.

2. Measure the frequency f in order to guarantee that the excitation pulses are sent at the correct moment.

3. Excite the specimen with a fixed deformation amplitude ε. ε is a function of the specimen geometry and the torsion angle θ:

$$\varepsilon = \frac{\beta}{\alpha} \frac{c\,\theta}{L} \tag{2.6}$$

   where c is the width of the rectangular section and L is the length of the specimen. β and α are numerical factors depending on the ratio of L/c, see Timoshenko (1963).

4. Register the alternative signal of the photoelectric cell. In the mean time perform the Fast Fourier Transform (FFT) of the preceding free decay and determine Q^{-1}.

5. Measure the temperature (T), the applied force (F), the electrical resistance (R), and the change of the specimen length (dL).

6. Store all the experimental results on a magnetic medium and display them on the graphic screen.

2.1.3 Internal Friction Measurement during Martensitic Transformations

The experimental technique of IF measurements that has been described in the previous paragraphs allows for the characterization of different aspects of martensitic phase transformations. As an example, figure 2.3 shows results obtained with a Cu-Zn-Al alloy, which was subjected to a shape memory training procedure. The evolution of the physical parameters which are measured in the torsion pendulum during martensitic transformation, give the following information:

i) The internal friction or the dissipated energy (Q^{-1}) is a measure of the *microscopic hysteresis effect* during transformation. The analysis of the IF peak in the transformation regime allows for the identification of possible mechanisms, which contribute to the macroscopic hysteresis effect.

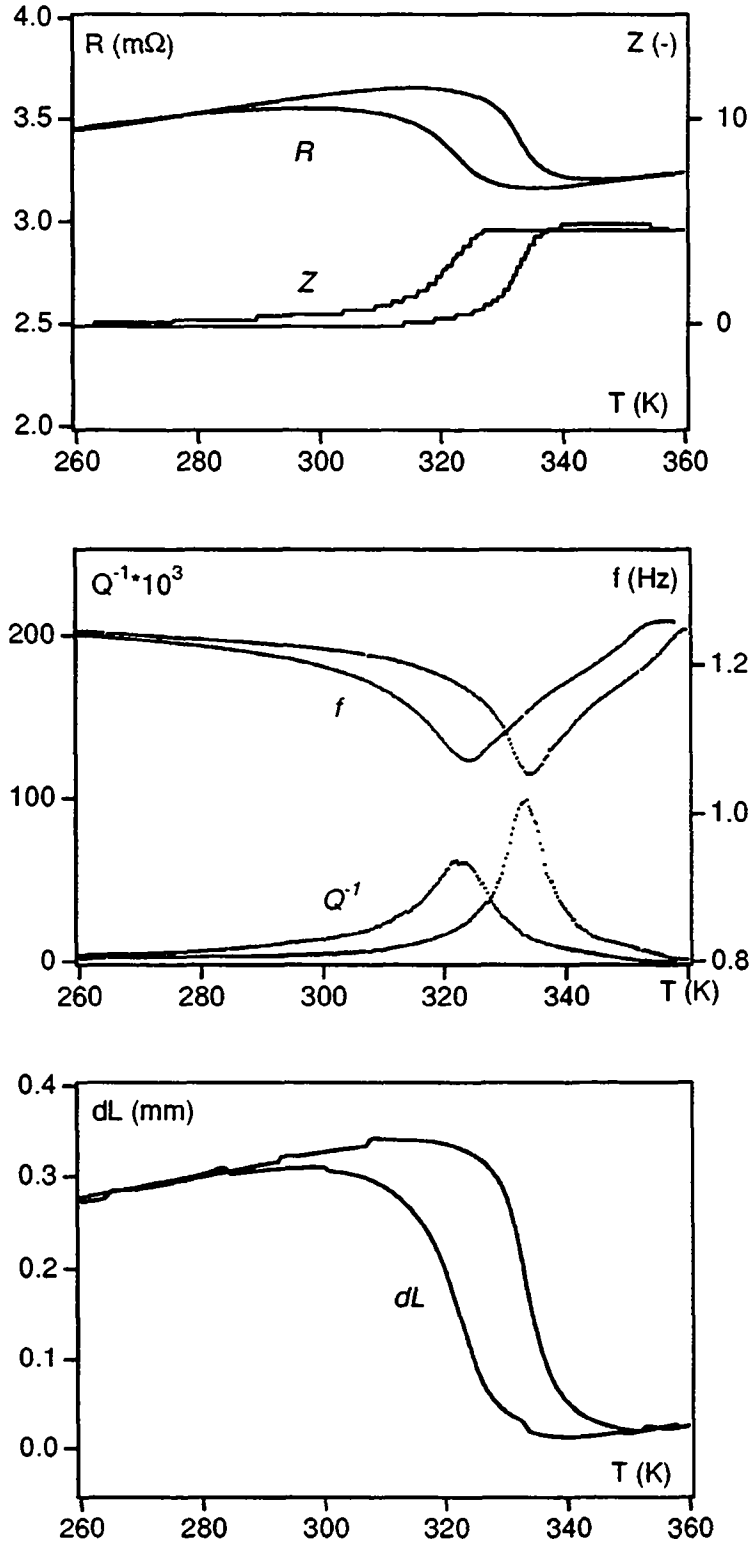

Figure 2.3: Evolution of the measured parameters during thermally-induced martensitic transformation in an educated Cu-Zn-Al shape memory alloy: *R*, *Z*, *f*, Q^{-1} and *dL* as a function of *T*.

ii) The evolution of the oscillation frequency f is related to changes in the *elastic shear modulus (G)* of the specimen, derived from: $f \alpha \sqrt{G}$.

iii) The electrical resistance R as a function of T during temperature-induced transformation or as a function of force during stress-induced transformation represents the macroscopic hysteresis effect and allows for the calculation of the *transformed volume fraction (n)* as a function of temperature.

iv) Shape changes of the specimen, derived from Z and dL, give information about transformation reversibility or about the recoverable deformation during heating *(shape memory effect)*. In the example of figure 2.3, a shape memory effect of 1% can be derived from the initial length of the specimen (L_0 =30 mm) and the reversible length change (dL = 0.3 mm).

v) F as a function of dL during stress-induced transformations can be directly transformed into a stress-strain curve (σ-ε) that allows for the calculation of the *irreversible energy* contribution of the transformation process.

REMARK:

By using the electrical resistance (R) and not the electrical resistivity (ρ) for the determination of the transformed volume fraction (n), the macroscopic shape changes that occur during transformation are not considered. However, R measurements that have been performed during stress-induced transformations showed that the shape change effect compared to the transformation effect is negligible. The dependency of R on the length change of the specimen was found to be 0.01 mΩ/mm in the elastic part and 0.5 mΩ/mm in the pseudoelastic part (transformation regime) of the stress-strain curve. This result reveals that changes in the electrical resistance which are due to changes of the transformed volume, are 50 times bigger than R changes due to shape changes of the specimen. Therefore, the difference between the electrical resistivity that accounts for shape changes and the electrical resistance should be very small and the determination of n from the R curves should give representative results.

2.1.4 *In situ* Observations during IF Measurements

The IF installation has been provided with "optical windows" for the observation of the specimen surface during the experiments. A window was machined into the furnace, and the vacuum chamber of the lower part of the pendulum as well as the liquid nitrogen reservoir were fabricated of a quartz tube. With this construction, the surface relief that develops during a martensitic transformation can be observed and filmed with a video camera.

As will be presented in chapter 4, the relation of the martensitic morphology and the measured parameters is essential in order to verify that a single variant transformation is occurring. Figure 2.4 shows an example of the growth of a single martensitic variant in a Cu-Zn-Al single crystal. The photographs have been copied from the video tapes.

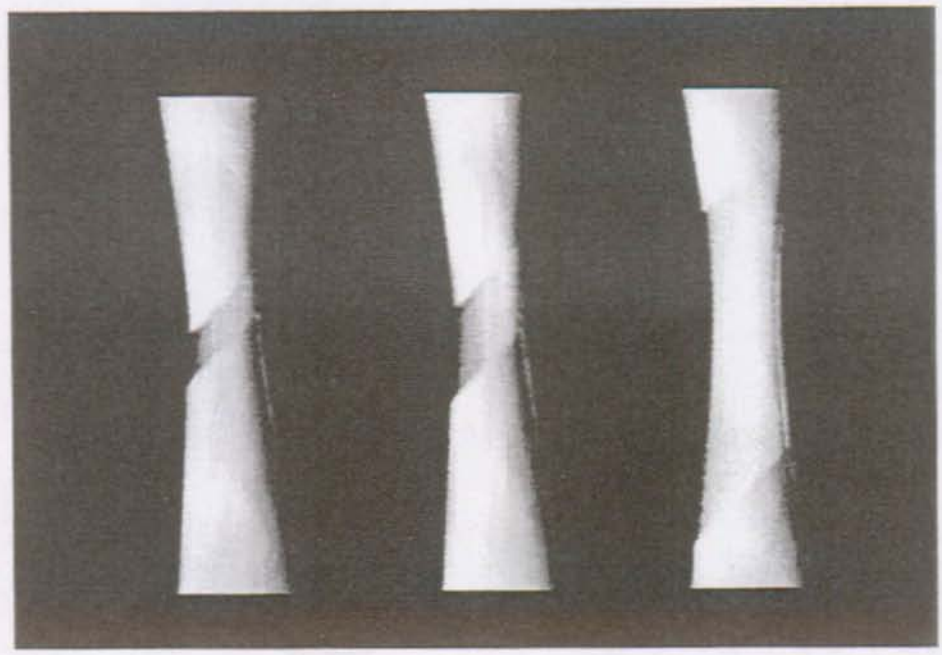

Figure 2.4: Micrographs showing the growth of a martensitic single variant during loading.

2.1.5 Specimens

The IF measurements have been performed with different Cu-Zn-Al alloys. The chemical compositions and M_s temperatures are described in connection with the obtained IF results in chapter 3. Specimens have been cut to the final dimensions by electro erosion. For the study of temperature-induced transformations in polycrystalline materials, a 30 mm x 2.5 mm x 0.6 mm plate shaped geometry was used. Specimens for stress-induced transformations had smaller

dimensions (20 mm x 1.5 mm x 0.35 mm) in order to reduce the necessary applied tensile forces. The specimen surfaces have been polished with fine grinding paper and diamond paste finishing with a particle size of 1 μm. A special specimen geometry developed for the study of single interface transformations is described in chapter 4.

Just before the final polish the specimens were subjected to a heat treatment according to the step-quench method. First, the specimens were betatized at high temperatures ($750°C < T < 850°C$) for 30 minutes and fast quenched into water of 90°C. Annealing 90 minutes at this temperature (90°C), which was higher than M_S, allowed for the annihilation of excess vacancies, which always remain in the specimen after quenching.

2.2 Transmission Electron Microscopy (TEM) *in situ* Observations

2.2.1 The Straining Stage for Low Temperatures

General Characteristics

The TEM *in situ* observations of microstructural evolution during martensitic transformations have been performed using a 200kV Hitachi (H700H) microscope. In the course of this study, a straining stage has been built which can operate at low temperatures. It provides the possibilities of cooling to 110 K, of heating to 370 K and of stressing a specimen with a maximum tensile force of 50 N (maximum elongation of 1.2 mm). The maximum tilt angle is about ± 25°.

Low temperatures are required for the study of martensitic phase transformations in Cu-base alloys, if one is interested in excluding the influence of thermal vacancy diffusion on the transformation process. Vacancies are mobile in β brass alloys, even below room temperature, and the transformation behaviour is affected by these vacancies, especially if specimens are kept for long times in the martensitic state (Abu Arab et al., 1988, and Segers et al., 1988). Changes in the atomic order of martensite and pinning of martensitic interfaces due to vacancy migration are the mechanisms responsible for the effect of martensite stabilization. In addition, reorientation between different martensitic variants is very limited when their interfaces become immobile. Therefore, the present specimen stage has been designed for the study of martensitic transformations at temperatures lower than 250 K, where vacancy diffusion can be neglected.

For the employed 200kV Hitachi microscope, a high temperature straining stage (300 - 1000 K) had been built in 1983 by Carrard et al. As pointed out in the earlier work, this microscope has a

very small outside diameter for the stage tip (7.5 mm) and therefore imposes specific geometrical problems that had to be solved in the present work. Some of the basic concepts could be used from the low temperature straining stage for a 200kV JEOL microscope, although the geometrical conditions are less restrictive in that microscope (Gotthardt et al., 1979).

Straining Device

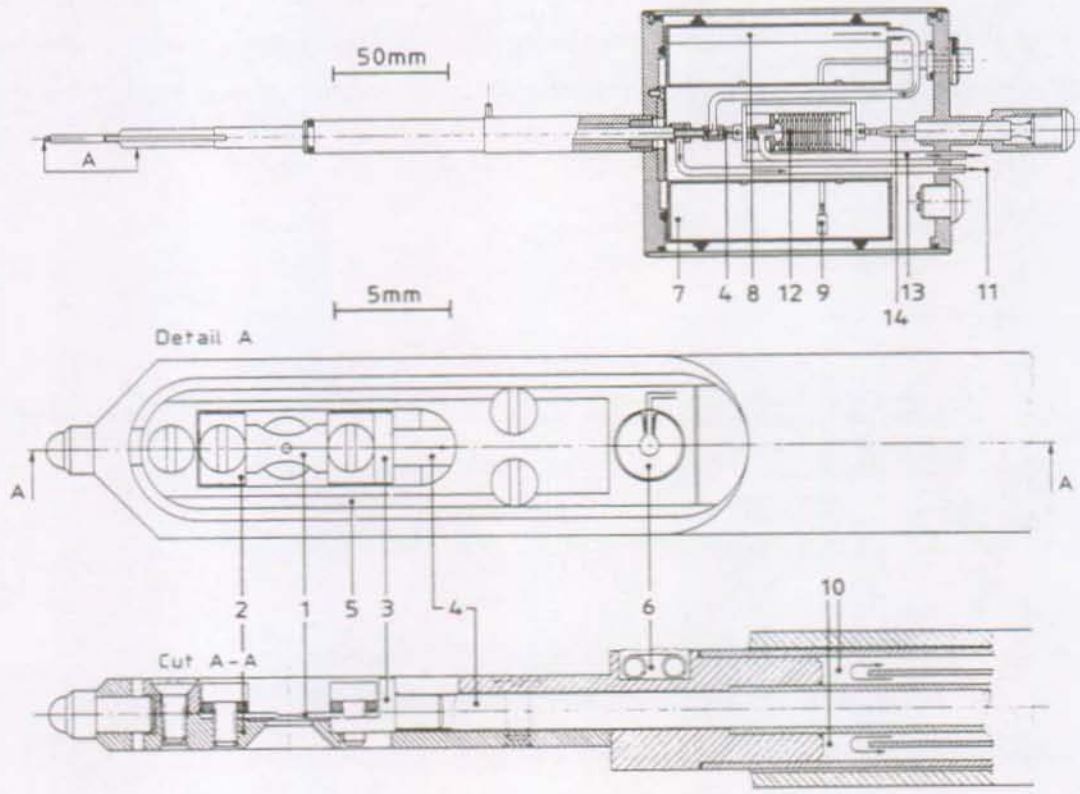

Figure 2.5: The low temperature TEM straining stage with :
1: Thin foil specimen, 2: Fixed jaw, 3: Mobile jaw, 4: Pull rod, 5: Position of the thermocouple, 6: Furnace, 7: Liquid nitrogen, 8: Nitrogen gas, 9: Pt 100 resistance heater, 10: Concentric tubes for N_2-circuit, 11: Nitrogen exit, 12: Metallic bellow, 13: Microtube for helium, 14: Displacement transducer.

As in former stages, a pneumatic system is used to pull the specimen (figure 2.5). It consists of a metallic bellows (12) which is connected to a kind of "fork" ending in the pull rod (4). The bellows is mounted under a fixed mechanical compression, which exceeds the expansion pressure that is caused in the bellow when the specimen stage is introduced into the vacuum of the microscope. Therefore, no pre-deformation is produced in the specimen by entering the stage in the microscope. The specimen (1) can either be glued on a copper frame, which is then

mounted to both the fixed and the mobile jaws (2,3), or a specimen prepared with two holes can be screwed directly into the jaws. Figure 2.6 illustrates the stage tip with a mounted specimen.

To deform a specimen by traction, Helium gas is pressed through a microtube (13) into the bellows. The pressure in the bellows is measured by a pressure transducer and is controlled by adjusting the Helium flow or the vacuum pump rate with a fine metering valve (flow rates can be controlled at than $0.2dm^3/h$). This valve is connected to the helium bottle and to the vacuum pump, see also figure 2.7. The system allows for the application of constant loading/unloading rates to the specimen ($0.5\ N/min < dF/dt < 5\ N/min$), which is of particular interest when studying thermoelastic martensitic transformations. The maximum force is about 50 N. A displacement transducer (14), which is connected to the bellows, measures the corresponding elongation of the specimen.

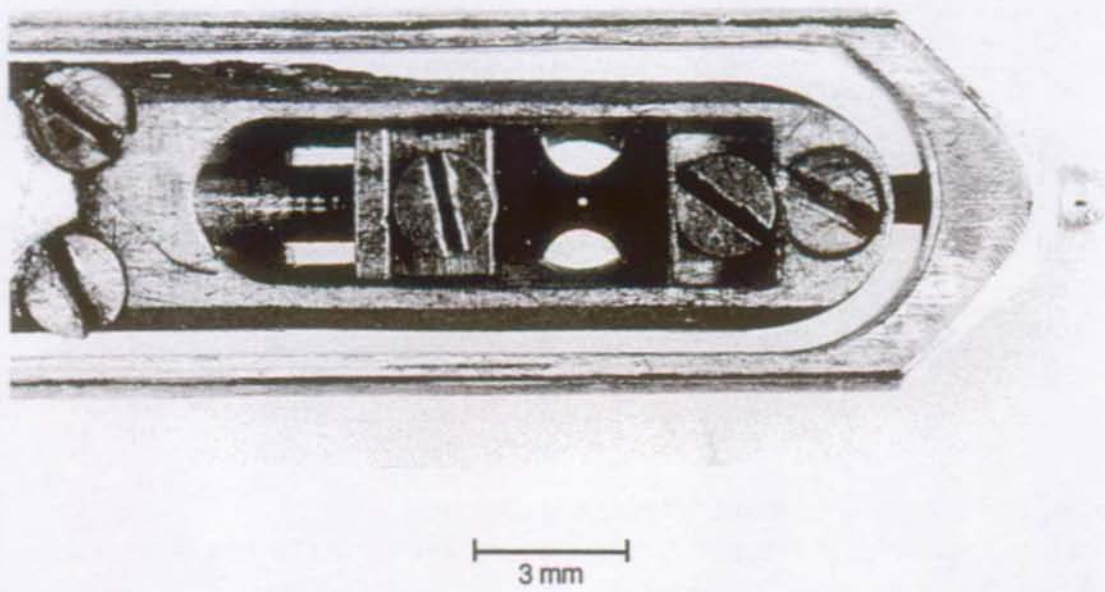

Figure 2.6: Stage tip with a mounted thin foil specimen. The small hole in the center of the specimen is obtained by a two-step electrolytical polishing procedure.

Cooling/Heating System

The cooling system consists of a cylindrical liquid nitrogen reservoir (7), a Pt 100 resistance heater for nitrogen evaporation (9), and two concentric tubes for a nitrogen gas circuit (10) where the incoming nitrogen flows through the inner tube. This concept of concentric tubes had already been applied for a specimen stage with a helium cooling system (Gotthardt et al., 1979), and its great efficiency has also been demonstrated in the present case, where it easily attains a minimum temperature of 110 K. Thanks to special construction measures concerning thermal isolation, it is possible to maintain low temperatures (around 150 K) for several hours. The temperature is measured by a thermocouple (Chromel-Alumel) fixed near the specimen (5). In order to improve the facility for changing the temperature, a small furnace (made of tungsten) has been installed above the pull rod between the specimen and the point of heat exchange of the cooling system (6). Final temperature control is performed by a commercial PID controller (EUROTHERM), which changes either the current for the furnace or for the Pt100 resistance heater, depending on the requirement. The temperature stability is about 0.1 K and ramps can be performed with constant temperature rates in the range between 0.1 K/min and 5 K/min.

Data Acquisition and Image Recording

The microscopic observations are filmed using a video camera that is mounted below the observation screen of the microscope, and recorded by a SVHS video recorder, see figure 2.7. The actual values of the measured parameters (pressure P, temperature T, length change dL) are indicated on the TV screen, so that microscopic observations can be related to the macroscopic properties of the specimen. In addition, the evolution of P, T and dL can be collected by a chart recorder or, via data acquisition unit, by a HP computer. This allows the data points to be plotted in real time.

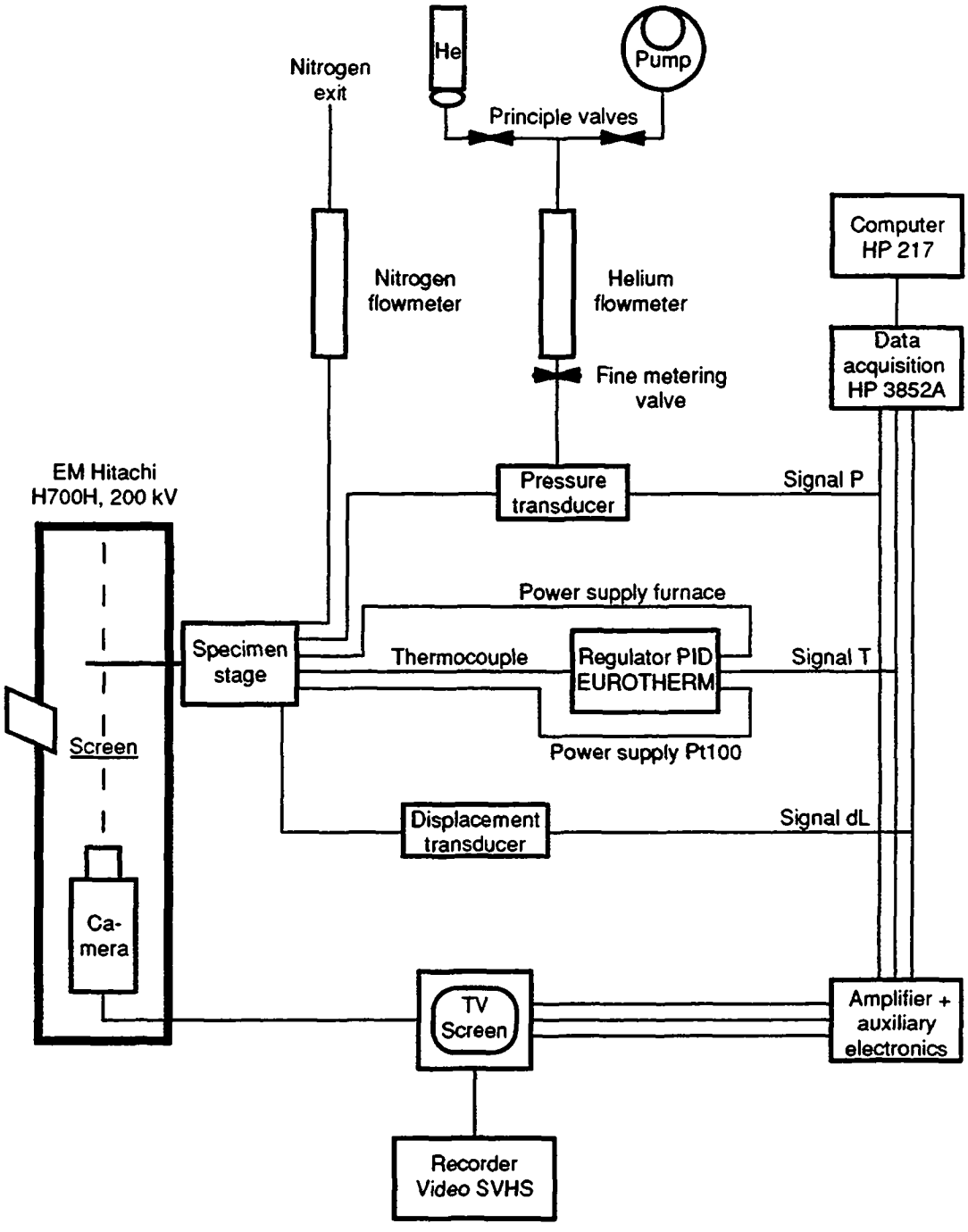

Figure 2.7: Schematic drawing of the installation for *in situ* observations, including straining-, heating- and cooling devices as well as data acquisition and image recording systems.

2.2.2 Specimens

Specimens have been prepared from a Cu-Zn-Al single crystal (nominal composition 66.3 at.% Cu, 19.3 at.% Zn and 14.4 at.% Al), which was grown by the Bridgman technique. This composition was chosen in order to have a low transformation temperature (M_S = 160 K) so that the transformation takes place without thermal diffusion of vacancies. Rectangular plates (7.5 mm × 2.5 mm × 0.1 mm) were cut by electro erosion. Holes for the fixation, as well as the round shaped notches in the middle of the specimen, were obtained by punching. The photograph of figure 2.8 shows a thin foil specimen used for *in situ* observations. After grinding the surfaces, a hole for TEM observations was prepared in the center of the specimen by a two-step polishing procedure. Pre-polishing was performed either by a dimple grinder or by an initial jet polishing in a 25% H_2SO_4/methanol solution (T = 0°C, U = 15 V). The final electropolishing procedure was done in a saturated solution of chromium trioxide in phosphoric acid (T = 20°C, U = 3 V).

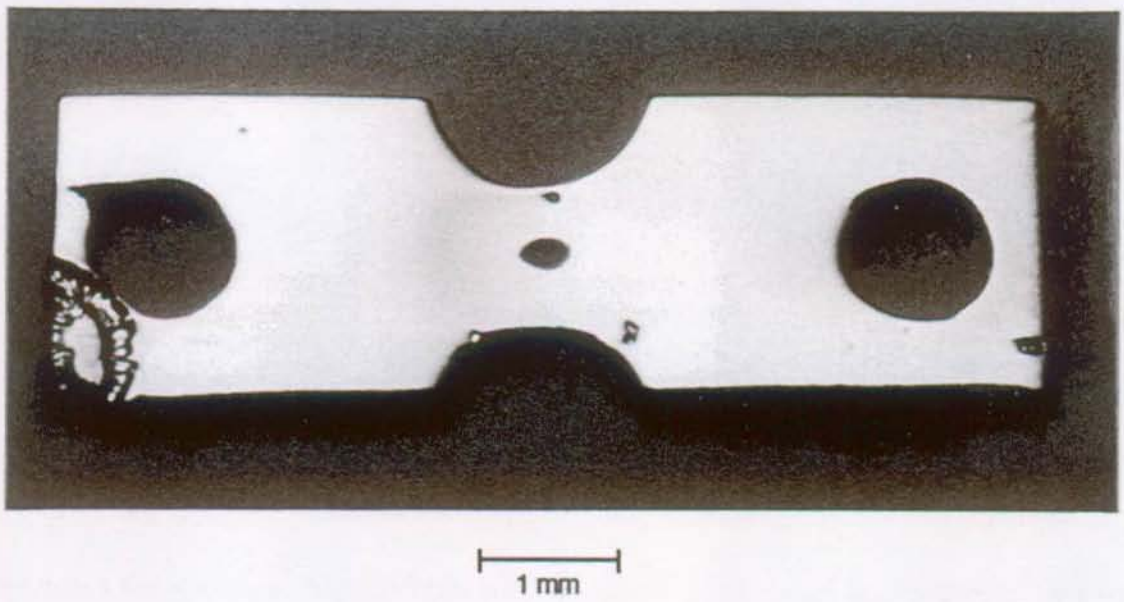

Figure 2.8: Specimen geometry for the present specimen stage.

2.2.3 Stress Conditions during *in situ* Deformation

When a thin foil specimen is deformed by an uniaxial tensile stress, a particular stress distribution around the prepared hole has to be considered. The theory of elasticity gives the plane stress components for an infinite plane under uniaxial tension (figure 2.9a). With respect to polar coordinates, $\sigma_{\theta\theta}$ attains its maximum value for $\theta = \pi/2$ and $\theta = 3\pi/2$ (θ is measured at

the center of the hole, between the vertical intersection and the line that contains a particular point of the plate). The value of $\sigma_{\theta\theta(max)}$ is three times the uniformly distributed stress (σ), giving a stress concentration factor of three. For $\theta = 0$ and $\theta = \pi$, $\sigma_{\theta\theta}$ attains a compressive value ($-\sigma$).

In the case of a thin foil specimen with a polished zone, the thickness of the plate is no more homogeneous. A finite element calculation published by Coujou et al. (1990) which was conducted with a specimen geometry similar to that of figure 2.8, showed that a stress concentration factor of four has to be considered at the edges of the hole which are parallel to the tensile axis (figure 2.9b). But, the stresses in these regions are homogeneously distributed and the observations during *in situ* deformation when they are conducted in those parts of the specimen, should give representative information about the deformation behaviour of the studied material.

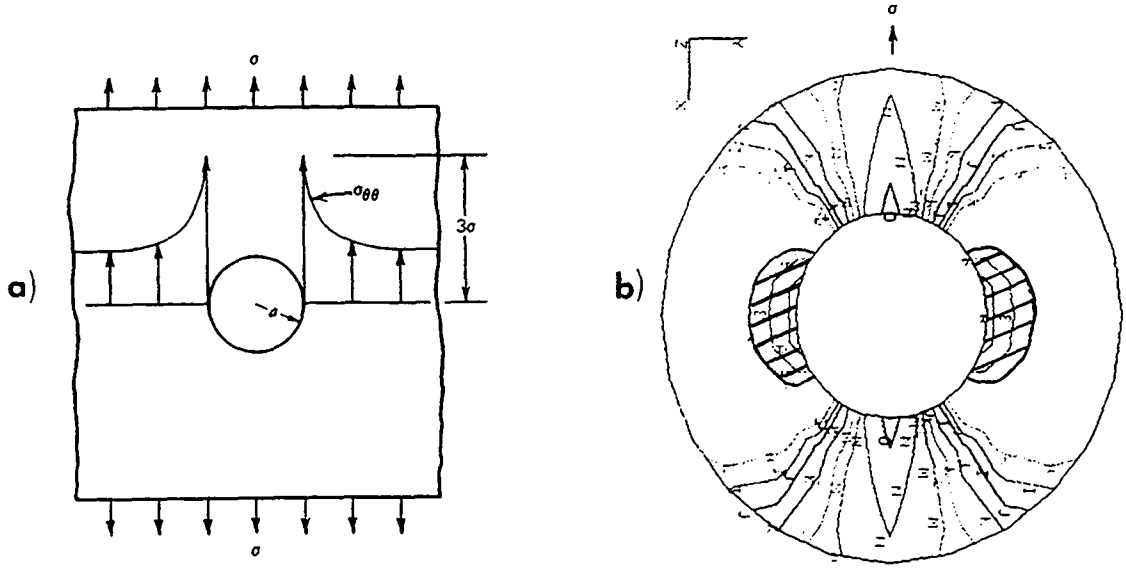

Figure 2.9: a) Infinite plate with a small circular hole and distribution of $\sigma_{\theta\theta}$ for $\theta = \pi/2$ (taken from Boresi et al., 1985). b) Contour plot of the major principle stress level for the entire polishing zone, the hatched zones indicates the regions with a homogeneous tensile stress (stress concentration is four), taken from Coujou et al. (1990).

For the present specimen stage and specimen geometry this stress concentration factor results in a maximum tensile stress of 1000 MPa at the edges of the hole parallel to the applied stress. For the study of martensitic phase transformations this implies that small deformations around the hole are possible with relatively high stresses. For larger deformations, which occur when transforming interfaces (martensite-austenite or martensite-martensite interfaces) traverse the entire specimen, only the value of the applied stress (σ) can be considered.

Cooling/Heating System

The cooling system consists of a cylindrical liquid nitrogen reservoir (7), a Pt 100 resistance heater for nitrogen evaporation (9), and two concentric tubes for a nitrogen gas circuit (10) where the incoming nitrogen flows through the inner tube. This concept of concentric tubes had already been applied for a specimen stage with a helium cooling system (Gotthardt et al., 1979), and its great efficiency has also been demonstrated in the present case, where it easily attains a minimum temperature of 110 K. Thanks to special construction measures concerning thermal isolation, it is possible to maintain low temperatures (around 150 K) for several hours. The temperature is measured by a thermocouple (Chromel-Alumel) fixed near the specimen (5). In order to improve the facility for changing the temperature, a small furnace (made of tungsten) has been installed above the pull rod between the specimen and the point of heat exchange of the cooling system (6). Final temperature control is performed by a commercial PID controller (EUROTHERM), which changes either the current for the furnace or for the Pt100 resistance heater, depending on the requirement. The temperature stability is about 0.1 K and ramps can be performed with constant temperature rates in the range between 0.1 K/min and 5 K/min.

Data Acquisition and Image Recording

The microscopic observations are filmed using a video camera that is mounted below the observation screen of the microscope, and recorded by a SVHS video recorder, see figure 2.7. The actual values of the measured parameters (pressure P, temperature T, length change dL) are indicated on the TV screen, so that microscopic observations can be related to the macroscopic properties of the specimen. In addition, the evolution of P, T and dL can be collected by a chart recorder or, via data acquisition unit, by a HP computer. This allows the data points to be plotted in real time.

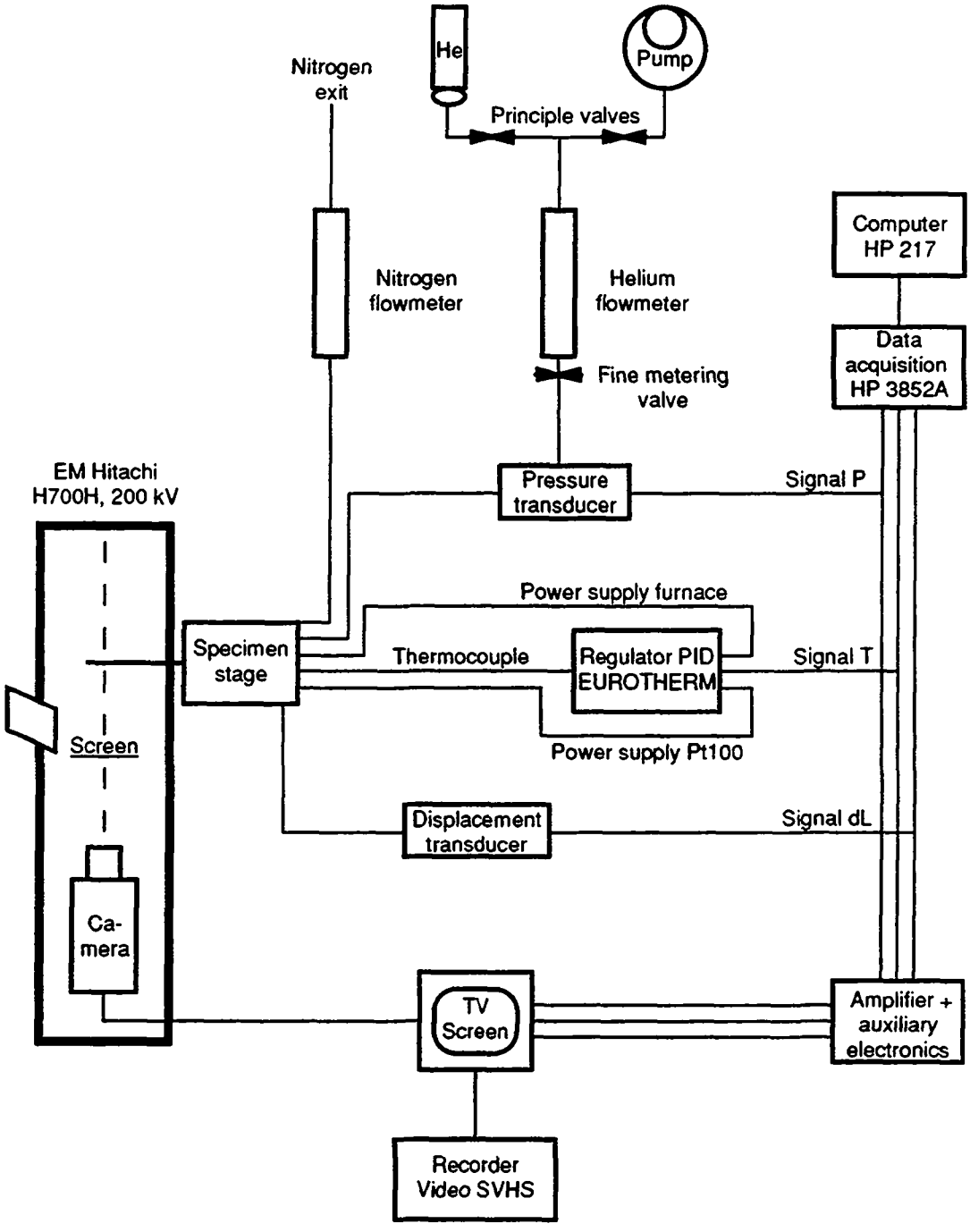

Figure 2.7: Schematic drawing of the installation for *in situ* observations, including straining-, heating- and cooling devices as well as data acquisition and image recording systems.

CHAPTER 3

The Hysteresis Effect during Martensitic Phase Transformations in Cu-Zn-Al Polycrystals : Results and Interpretations

This chapter presents the transformation behaviour of different Cu-Zn-Al polycrystals, which have been characterized by the macroscopic hysteresis, the martensitic microstructure and the evolution of internal friction (IF) that was measured in the course of temperature- and stress-induced transformations. Along with complete transformation cycles, incomplete hysteresis loops have been investigated during partial forward and reverse transformations as well as during repetitive transformation cycles in small temperature and stress intervals.

The theoretical basis for the analysis of the IF behaviour is given by a review of existing IF models, which attempt to explain the anelastic effects that occur during martensitic phase transformations. The transient part of the IF peak is analyzed in dependence of external parameters and of the microstructural parameter that is generally considered for this IF term. The IF behaviour of partial transformation cycles is analyzed in order to get information about the origins of the observed macroscopic hysteresis effects which include the characteristic transformation paths and the evolution of small transformation sub-loops with increasing number of cycles.

3.1 Alloy Composition and Thermomechanical Treatment

The Cu-Zn-Al alloys, which have been chosen for the following experiments are listed in table 3.1. Alloys 1 and 2 are industrial shape memory alloys and have been supplied by PROTEUS (Belgium) in the frame of an European research program (EURAM). Alloy 1 is a ternary Cu-Zn-Al alloy that has a relatively coarse grain size. In alloy 2 the grain size is significantly smaller because of the addition of Boron which prevents grain growth during solidification. The industrial interest of grain refined alloys is that they exhibit better cold working properties than those alloys which have a coarse grain size.

The transformation behaviour of alloy 2 has been investigated in specimens that have received the standard heat treatment (2A) and in specimens which were subjected to a thermomechanical treatment (2B). Specimens 2B showed a 1% two-way memory effect. Alloy 3 has been added to the investigation as a low-temperature alloy (M_S = -70°C), where thermal diffusion of vacancies does not take place during transformation.

Table 3.1: Characterization of the studied alloys.

alloy	composition (wt%)	grain size	treatment	M_S (°C)
1	Cu-26Zn-4Al	1 - 2 mm	15' at 750°C ⇒ 90' at 90°C	20
2A	Cu-20Zn-6Al-0.04B	0.2 - 0.5 mm	15' at 750°C ⇒ 90' at 90°C	60
2B	Cu-20Zn-6Al-0.04B	0.2 - 0.5 mm	as 2A + 1% Two-way memory effect	65
3	Cu-19Zn-7Al	2 - 2.5 mm	slowly cooled after casting	-70

3.2 Martensitic Microstructures

Figure 3.1 shows optical micrographs which illustrate the microstructure of the martensitic phase in alloys 1 and 2 that developed during transformation. Significant differences in their martensite morphology can be observed. The martensite structure of alloys 1 and 2A consists of different groups of self-accomodating variants, which allow for the minimization of the elastic strain energy. In alloy 1 (coarse grains) these groups are found in several different sizes, e.g. close to a grain boundary (figure 3.1a). The martensitic microstructure of this alloys can be described by the successive fragmentation of martensitic variants (see also chapter 6). In comparison to the coarse grain alloy 1, this *"fragmentation" effect* is less pronounced in the grain-refined alloy 2A (figure 3.1b). In the trained specimens (figure 3.1c) no self-accommodating groups are found, but packages of mostly two variants per grain, which produce the educated macroscopic strain during transformation, can be observed.

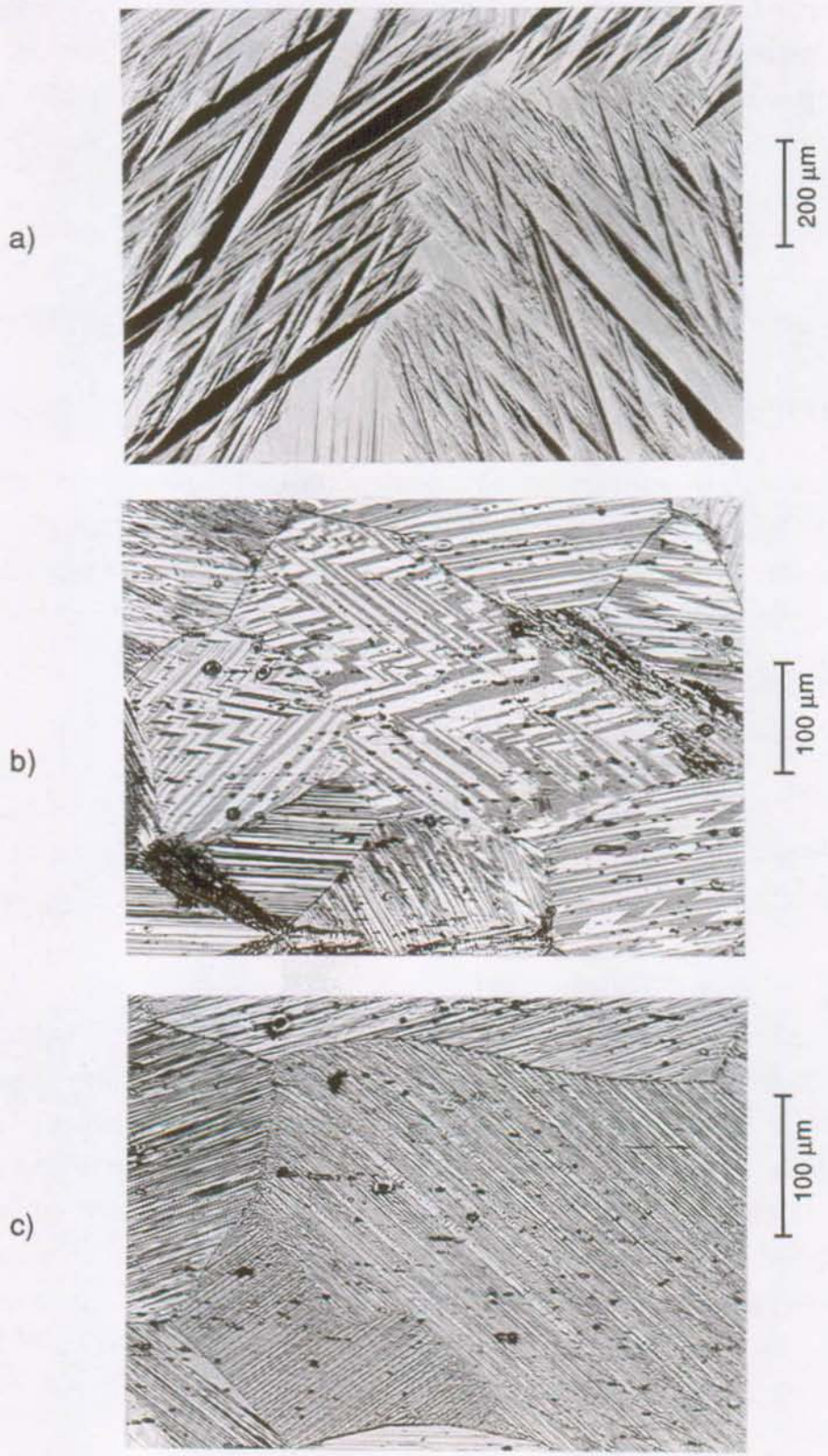

Figure 3.1: Optical micrographs showing the martensitic microstructure of the studied alloys: a) alloy 1, b) alloy 2A, c) alloy 2B.

The presence of a second phase can be detected in the microstructure of alloy 2. It is the formation of Boron-precipitates inside of the grains. As can be seen in figures 3.1b and 3.1c, these homogeneously distributed particles have no influence on the morphology of the transforming variants. The particles are incorporated in the martensitic variants and self-accomodating groups. This behaviour is different to the influence that γ precipitates have on the transformation behaviour of Cu-Zn-Al alloys, as will be shown in chapter 4.

3.3 Macroscopic Hysteresis Behaviour during Complete Transformation Cycles

3.3.1 Temperature-Induced Transformations

In figure 3.2, the *thermal transformation hysteresis* of the studied alloys are presented by the evolution of the transformed volume fraction *(n)* as a function of temperature *(T)*. *n* has been estimated from electrical resistance *(R)* measurements. Assuming that changes in the electrical resistance during transformation are proportional to changes in the transformed volume of the specimen (chapter 2), *R* can be expressed by:

$$R = n\, R_{\beta'} + (1-n)\, R_{\beta}\,, \qquad (3.1)$$

where $R_{\beta'}$ and R_{β} are the temperature-dependent parts of the electrical resistance in the martensitic and austenitic phase, respectively. $R_{\beta'}$ and R_{β} can be determined from the *R(T)* curve and it follows that:

$$n = \frac{R - R_{\beta}}{R_{\beta'} - R_{\beta}} \qquad (3.2)$$

Figure 3.2 shows that the macroscopic hysteresis differs only slightly in alloys 1 and 2A. The hysteresis width is between 10 K and 15 K, and the average thermoelastic slope ($\partial n/\partial T$) of the hysteresis is lower during cooling (forward transformation) than it is during heating (reverse transformation). The difference of the hysteresis slopes will be described by an *"asymmetric hysteresis shape"*. The effect of a two-way shape memory training on the transformation hysteresis is expressed by alloy 2B, which has a much smaller average slope. But, the difference in the thermoelastic slopes of the forward and reverse transformations is very small so that this type of hysteresis can be termed a *"symmetric hysteresis shape"*.

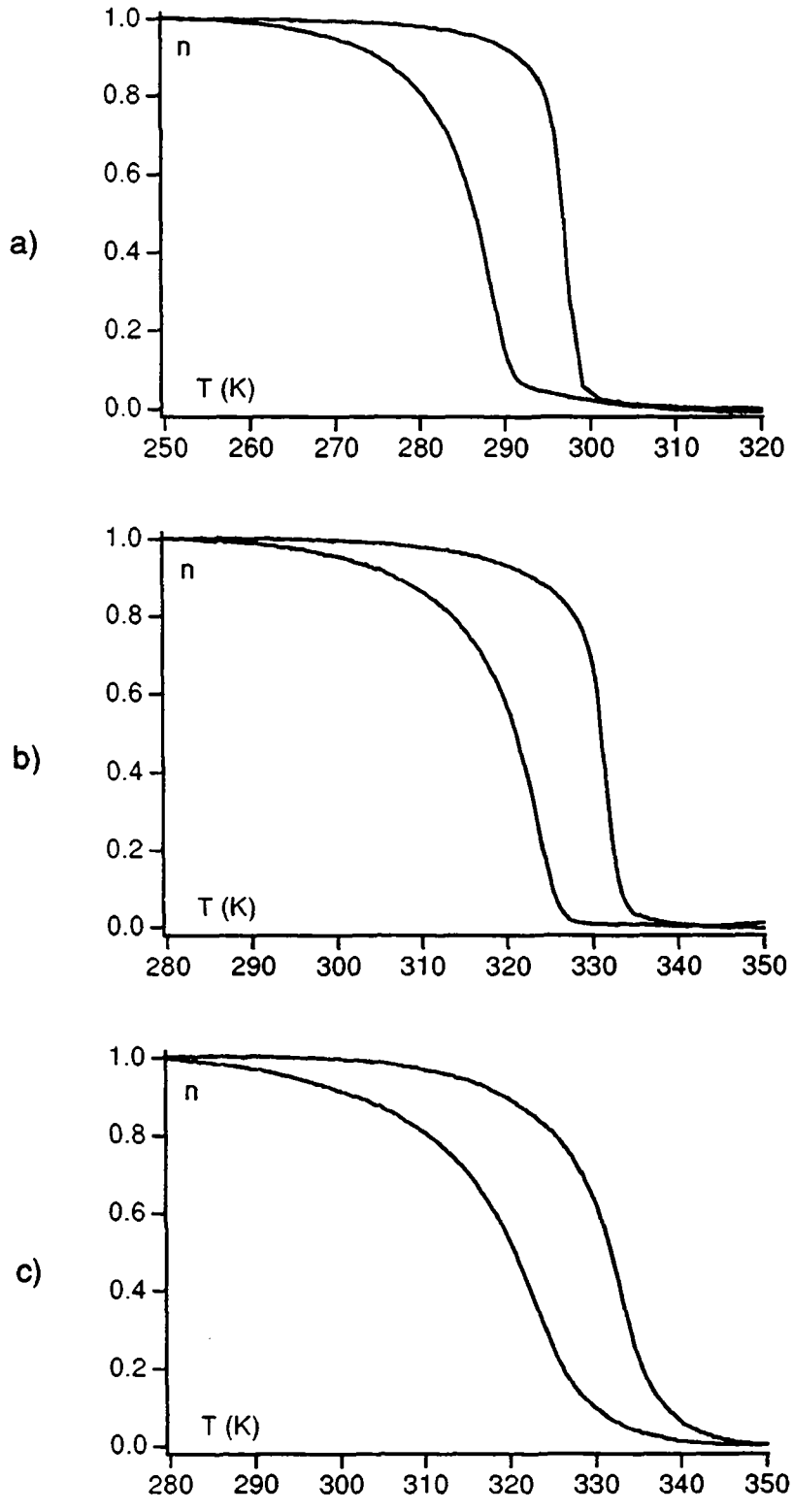

Figure 3.2: Transformation hysteresis of the Cu-Zn-Al alloys as presented by the *n(T)* curves: a) alloy 1, b) alloy 2A, c) alloy 2B.

3.3.2 Stress-Induced Transformations

The study of *stress-induced martensitic transformations* has been undertaken in order to get further information about the relationships between the microscopic properties of martensite, the transformation hysteresis and the IF behaviour. The morphology of stress-induced martensite is almost completely governed by the externally applied stress. Only those variants are formed, which give the maximum macroscopic deformation in the direction of the external stress. Therefore, the microstructures of stress-induced and educated martensites are comparable and the relationship between the macroscopic hysteresis and the IF behaviour should be similar in both cases.

Figure 3.3 presents the transformation hysteresis during a stress-induced transformation in alloy 2. The enclosed surface of the observed $(\sigma\text{-}\varepsilon)$ curve gives a direct measure of the dissipated energy during transformation (figure 3.3a). The $(\sigma\text{-}\varepsilon)$ curve can be transformed into a $n(\sigma)$ diagram from the measurement of R by relating the absolute change of R that was found during a temperature-induced transformation to the state of complete transformation (n=1). Figure 3.3b shows the obtained $n(\sigma)$ curve that can be compared to the $n(T)$ curves presented in figure 3.2. The hysteresis width varies between 15 MPa and 35 MPa, which corresponds to a width of 5 K to 10 K when the mutual relation between stress and temperature is considered (see paragraph 3.4.2). It is interesting to note that the hysteresis width is smallest at the end of the transformation. This indicates that the reverse transformation is governed by the elastic energy which is stored during the forward transformation.

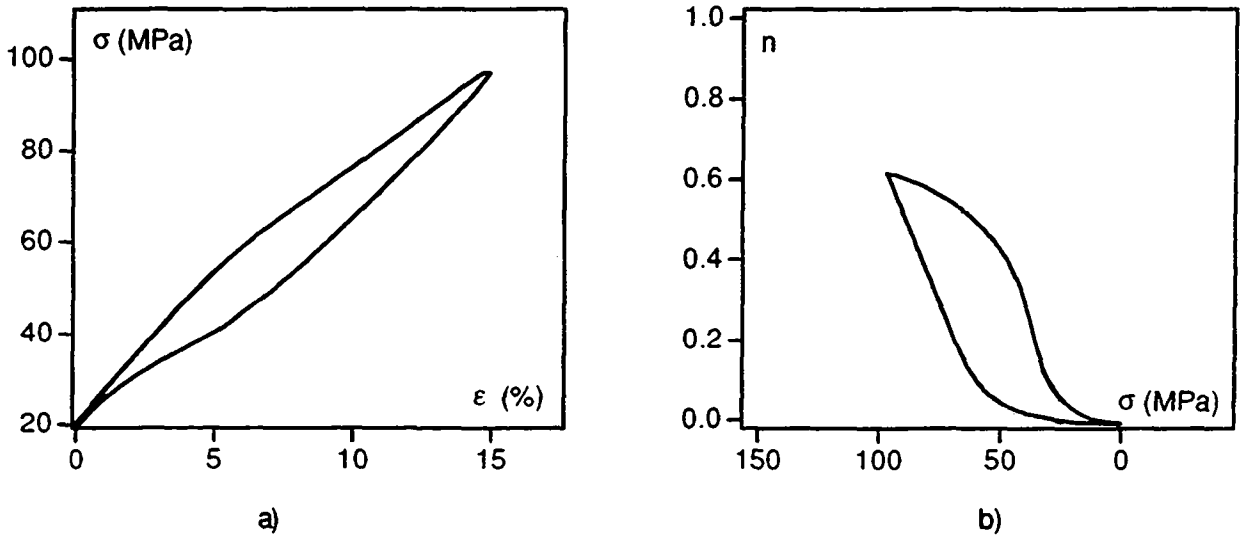

Figure 3.3: Transformation hysteresis during stress-induced transformation in alloy 2A at T=335K: a) σ - ε curve, b) n as a function of σ.

3.4 Internal Friction (IF) Behaviour during Complete Transformation Cycles

3.4.1 IF during Temperature-Induced Transformations

The IF behaviour has been studied in the present alloys during complete temperature cycles, where the temperature has been varied with a constant temperature rate covering the whole transformation region, i.e.: $T_{min} < M_f$ and $T_{max} > A_f$.

Figure 3.4 shows the typical behaviour of internal friction (Q^{-1}) and resonance frequency (f) for alloys 1 and 2. The temperature rate $(\dot{T})$ and the oscillation amplitude (ε_0) during IF measurement have been kept constant for all specimens. The transformation region is characterized by a high damping (Q^{-1}) peak and a corresponding f minimum, which appear during both the forward and reverse transformations (cooling and heating, respectively). Furthermore, the internal friction values of the martensitic phase are significantly higher than in the austenitic state.

By comparing the observed IF behaviour of the different alloys one finds that the Q^{-1}-peak in alloy 1 (coarse grain size) is higher and larger than in alloy 2A (grain refined). This corresponds to a higher elastic modulus defect as can be derived from the f-minimum. The effect of a two-way shape memory training is presented by the Q^{-1}- and f-curves of alloy 2B. As compared with an untrained specimen (alloy 2A), the Q^{-1}-maximum is significantly lower in alloy 2B. Another interesting difference is that the Q^{-1}-values of the high temperature phase are higher in the trained specimen, suggesting that stabilized martensitic variants are present even at temperatures above A_f (A_f = 350 K). This has been derived from the $n(T)$ curve (figure 3.2c).

3.4.2 IF during Stress-Induced Transformations

The IF measurements during stress-induced transformations have only been conducted with alloy 2A. As it will be shown in chapter 4, the distribution of the resulting shear stresses in the specimen during torsion requires that the grain size is small with respect to the geometrical dimensions of the specimen. During stress-induced transformation in coarse grains the transforming variants become very large and the effect of opposing shear stresses, which act on single interfaces, prevents their global displacement during the IF measurements. Quantitative analysis of the measured IF behaviour gets then very difficult. For the present investigation, the study of stress-induced transformations has been restricted to the grain refined alloy 2A.

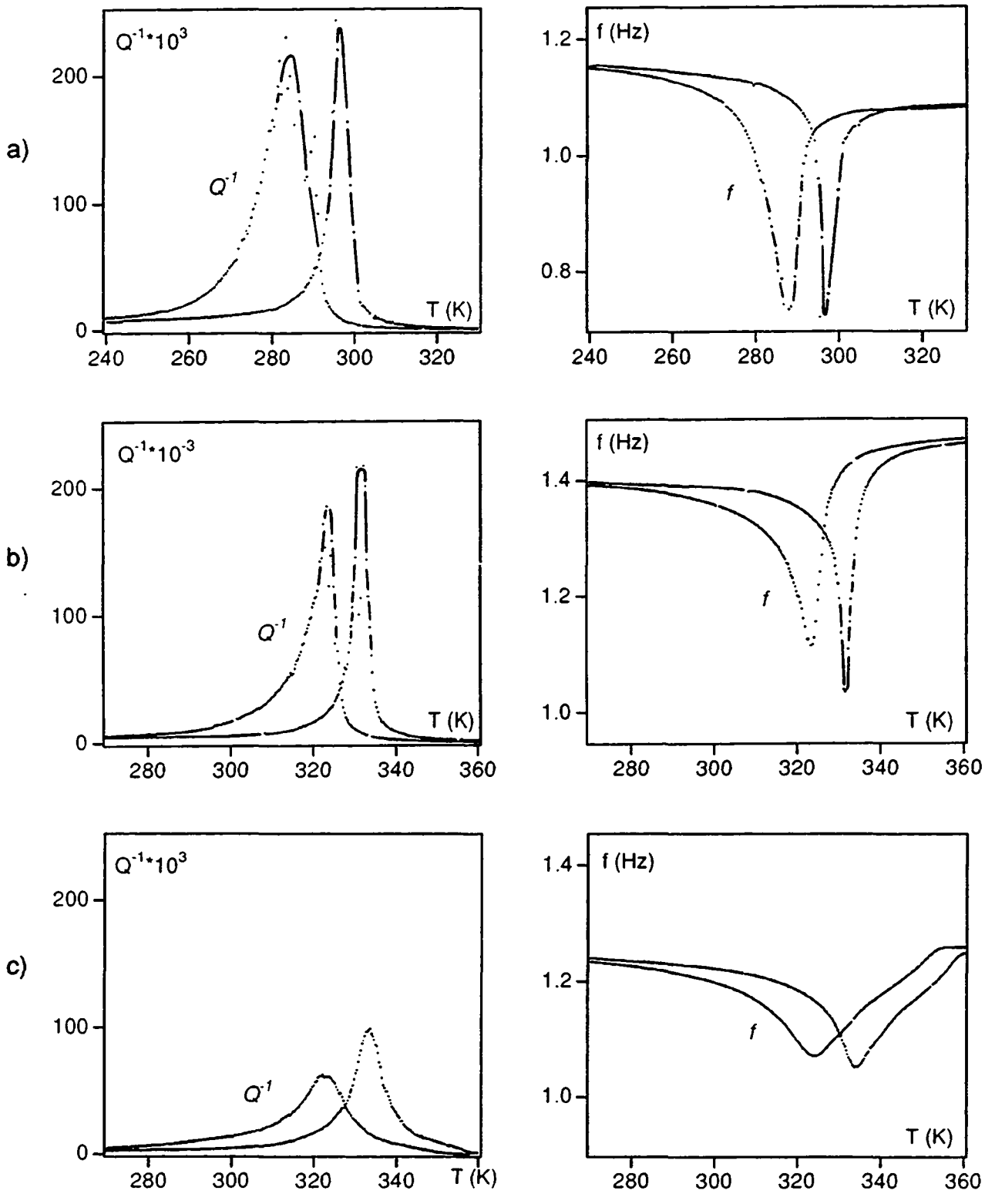

Figure 3.4: Q^{-1} and f during complete thermal cycles ($\dot{T}$= 0.5 K/min, ε_0 = 2.5·10^{-5}):
a) Alloy 1 (coarse grains), b) alloy 2A (grain refined) and c) alloy 2B (trained specimen).

In analogy to the study of temperature-induced transformations with constant $\dot{T}$, stress-induced transformations have been performed by changing the applied tensile stress (σ) with a constant stress rate ($\dot{\sigma}$). In order to get comparable conditions of the transformation rate in both experiments, the mutual influence of the external field parameters (T and σ) on the transformation had to be established for alloy 2A. Their physical relationship is given by the modified Clausius-Clapeyron equation (Ahlers, 1986) that predicts a linear relationship between the transformation temperature (T_t) and the critical stress necessary to induce the transformation (σ_c). The slope of the $\sigma_c(T_t)$ curve is related to the entropy difference between the two phases (ΔS) and the transformation strain (ε^t):

$$\frac{d\sigma_c}{dT_t} = \frac{\Delta S}{V \varepsilon^t}, \qquad (3.3)$$

where V is the molar volume.

When σ_c for alloy 2A is plotted as a function of T_t, a linear dependence is obtained (figure 3.5). The slope can be calculated to be:

$$d\sigma_c / dT_t = 3.4 \text{ MPa/K}.$$

$\dot{\sigma}$ has been set to 1.7 MPa/min during the IF measurements, corresponding to the value of $\dot{T}$ ($\dot{T}$= 0.5 K/min) that was used during temperature-induced transformations.

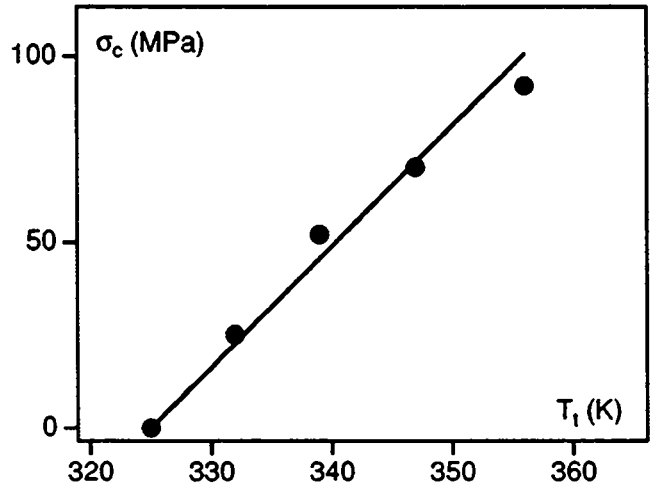

Figure 3.5: Critical stress (σ_c) as a function of transformation temperature (T_t) in alloy 2A.

Figure 3.6 shows the Q^{-1}- and f-spectra as a function of σ, for measurements performed at constant temperature above M_S (T = 335 K). This type of presentation has been chosen in order to give an adequate comparison with the usual $Q^{-1}(T)$ plot that is associated with thermally induced transformations (figure 3.4).

Qualitatively, $Q^{-1}(\sigma)$ shows the same characteristics as $Q^{-1}(T)$, namely a Q^{-1}-maximum during forward and reverse transformation corresponding to a f-minimum. However, the IF peak is very "flat", especially during loading, and this indicates that the forward transformation has not been completed. The estimated $n(T)$ curve of figure 3.3 confirms that the transformation was stopped at n = 0.65. The completion of the stress-transformation in grain-refined alloys is in general very difficult, since the necessary stresses are very high so that plastic deformation of the initially formed martensite may occur simultaneously. Therefore, stress-induced transformations were always stopped before completion ($n < 1$).

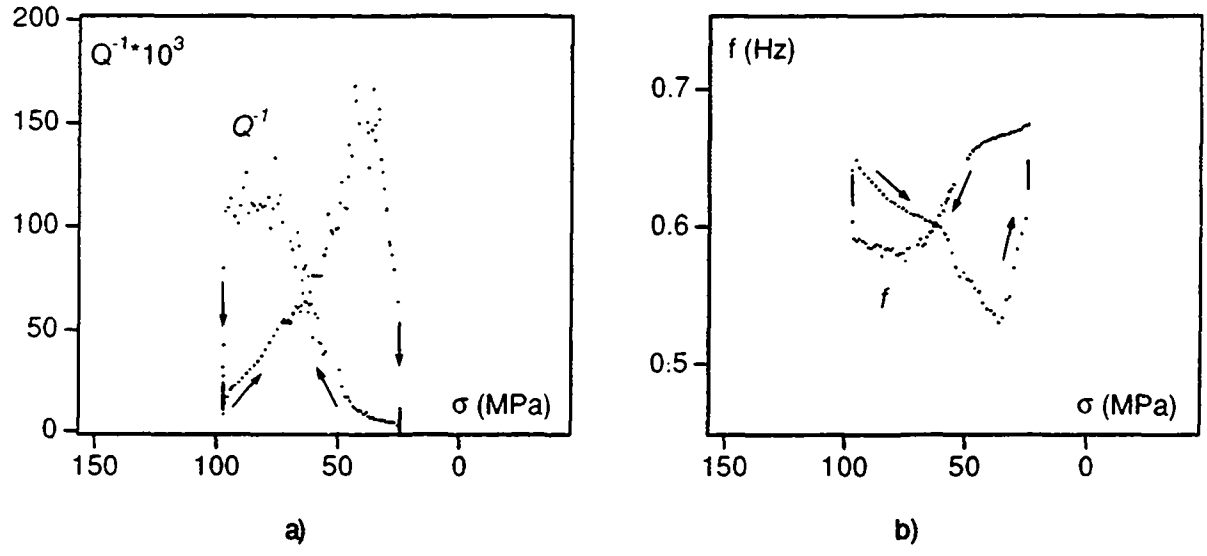

Figure 3.6: IF measurement during a stress-induced transformation in alloy 2A, T = 335 K, $\varepsilon_0 = 2.5 \cdot 10^{-5}$, $\dot{\sigma}$=1.7 MPa/min : a) Q^{-1} as a function of σ, b) f as a function of σ.

3.4.3 The Transient Character of the IF Peak: $\dot{T}$- and $\dot{\sigma}$ - Effects

The transient character of the Q^{-1}-peak during temperature-induced transformation is called the $\dot{T}$- effect, which characterizes the temporal decrease of Q^{-1} when the cooling (heating) rate is stopped inside the transformation regime. In the following, an analogous transient effect of the Q^{-1}-peak has been observed during stress-induced transformations, where Q^{-1} decreases with

time when the loading (unloading) rate is stopped during the transformation ($\dot{\sigma}$ - effect). While the $\dot{T}$- effect has been studied in all the present alloys (1, 2A, 2B and 3), the investigation of the $\dot{\sigma}$ - effect only concerns alloy 2A.

$\dot{T}$- and $\dot{\sigma}$-Effect in Alloy 2A

Figure 3.7 illustrates the transient character of the IF peak as has been observed in alloy 2A during both temperature- and stress-induced transformations. A dramatic decrease of the IF occurs when the cooling (stress) rate is stopped at different temperatures (stresses). The temperature (stress) was kept constant for 60 minutes (30 minutes) before cooling (stressing) was continued. In analogy to the $\dot{T}$-effect, see figure 3.7a, the observation of figure 3.7b is defined as the $\dot{\sigma}$-effect. As can be further seen from figure 3.7, the high damping peak almost vanishes in isothermal and constant stress conditions. Therefore, the main contribution to the IF peak of the studied alloys stems from its transient part, called $Q^{-1}{}_{Tr}$.

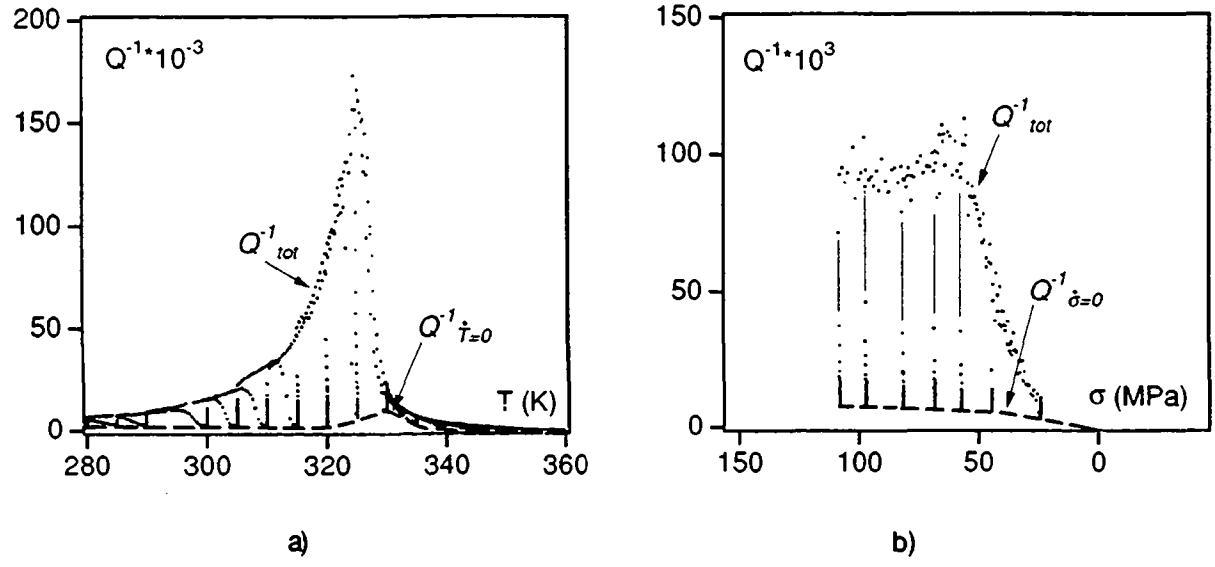

Figure 3.7: Q^{-1} during $\dot{T}$- and $\dot{\sigma}$-experiments in alloy 2A:
a) Isothermal holds during cooling, b) Constant stress holds during loading.

$Q^{-1}{}_{Tr}$ is represented by the difference between the total amount of IF during transformation ($Q^{-1}{}_{tot}$) and the "static" IF contribution ($Q^{-1}(\dot{T}=0)$ or $Q^{-1}(\dot{\sigma}=0)$) :

$$\dot{T}\text{-effect:} \qquad Q_{Tr}^{-1} = Q_{tot}^{-1} - Q^{-1}(\dot{T}=0) \qquad (3.4a)$$

$$\dot{\sigma}\text{-effect:} \qquad Q_{Tr}^{-1} = Q_{tot}^{-1} - Q^{-1}(\dot{\sigma}=0) \qquad (3.4b)$$

Apart from the determination of Q^{-1}_{Tr}, the $\dot{T}$- and $\dot{\sigma}$ - experiments give information about the time-dependent "relaxation" behaviour of the actual martensitic microstructure when the transformation is stopped. The temporal decrease of Q^{-1} has been followed after stopping the transformation at about 50% transformed volume during cooling (figure 3.8a) and loading (figure 3.8b). As can be seen from both graphs, the Q^{-1}-values decrease slowly to a constant level in both cases.

During the $\dot{T}$-experiment the slow decrease of Q^{-1} must be related to the thermal inertia of the system (specimen and grips) so that the transformation rate does not go immediately to zero after cooling is stopped. This can be concluded from the small increase of R after $t = 0$, (figure 3.8a). Calibration tests, where the temperature has been measured directly at the specimen, showed that $\dot{T}=0$ is only reached after 30 minutes. On the other hand, since the transformation rate is stopped abruptly during $\dot{\sigma}$ - experiments, see the R-curve in figure 3.8b, the slow decrease of Q^{-1} as a function of time has to be associated with mechanisms other than the transformation. Relaxation processes which reduce the elastically stored energy such as the motion of martensitic interfaces can contribute to the internal friction, as it will be discussed in chapter 6.

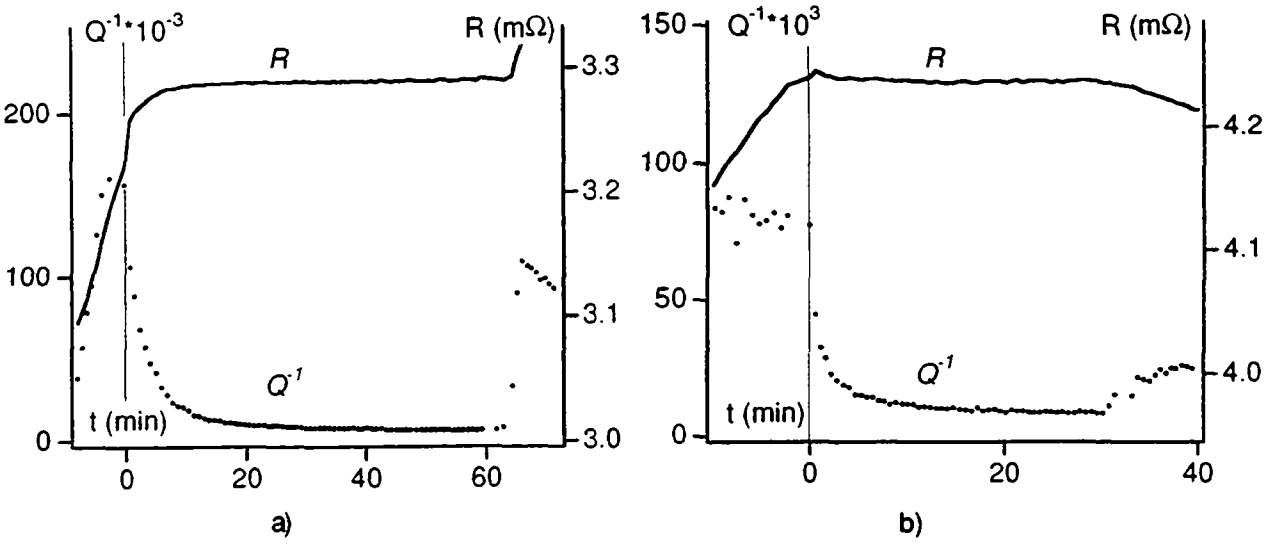

Figure 3.8: Temporal decrease of Q^{-1} as a function of time (t) in alloy 2A :
a) After stopping the temperature rate at T = 325 K and
b) after stopping the stress rate at σ = 78.5 MPa.

$\dot{T}$ - Effect at Low Temperatures (Alloy 3)

The transient character of the IF peak as well as the temporal decrease of Q^{-1} that occurs after the transformation is stopped, have been investigated in alloy 3. In this alloy, the transformation takes place at sufficiently low temperatures (M_S = 200 K) so that the influence of thermally activated mechanisms on the $\dot{T}$- effect can be excluded. Figure 3.9 shows the evolution of $Q^{-1}(T)$ and $Q^{-1}(t)$ during $\dot{T}$- experiments, which are the equivalent curves of those obtained for alloy 2A in figures 3.7a and 3.8a. From these results, it can be concluded that the IF behaviour during $\dot{T}$-experiments is not affected by the transformation temperature.

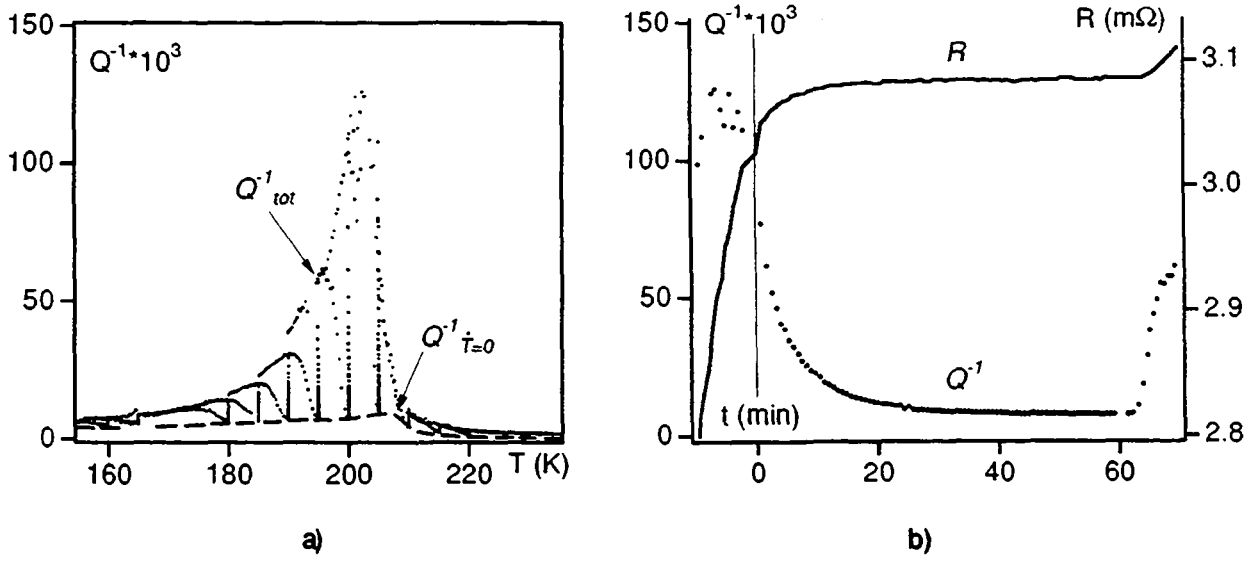

Figure 3.9: a) Q^{-1} during $\dot{T}$- experiment in alloy 3.
b) Temporal decrease of Q^{-1} after stopping the cooling rate at T = 200 K in alloy 3.

3.4.4 Amplitude Dependence of the IF Peak

The amplitude dependence of the IF peak gives important information about possible damping mechanisms which are involved in the martensitic phase transformation. This will be discussed in connection with the presentation of different IF models (section 3.5). The influence of the oscillation amplitude (ε_0) on the IF curve over a complete cooling cycle has been investigated in alloy 1.

Figure 3.10 shows three superimposed Q^{-1}-curves, which have been measured with different ε_0. Q^{-1}_{tot} has been separated into Q^{-1}_{Tr} and $Q^{-1}(\dot{T}=0)$ and it can be seen that Q^{-1}_{Tr} decreases with increasing ε_0, while $Q^{-1}(\dot{T}=0)$ increases. This ε_0-dependency of the IF peak was

qualitatively similar in all of the Cu-Zn-Al alloys and has also been reported by Morin et al. (1980).

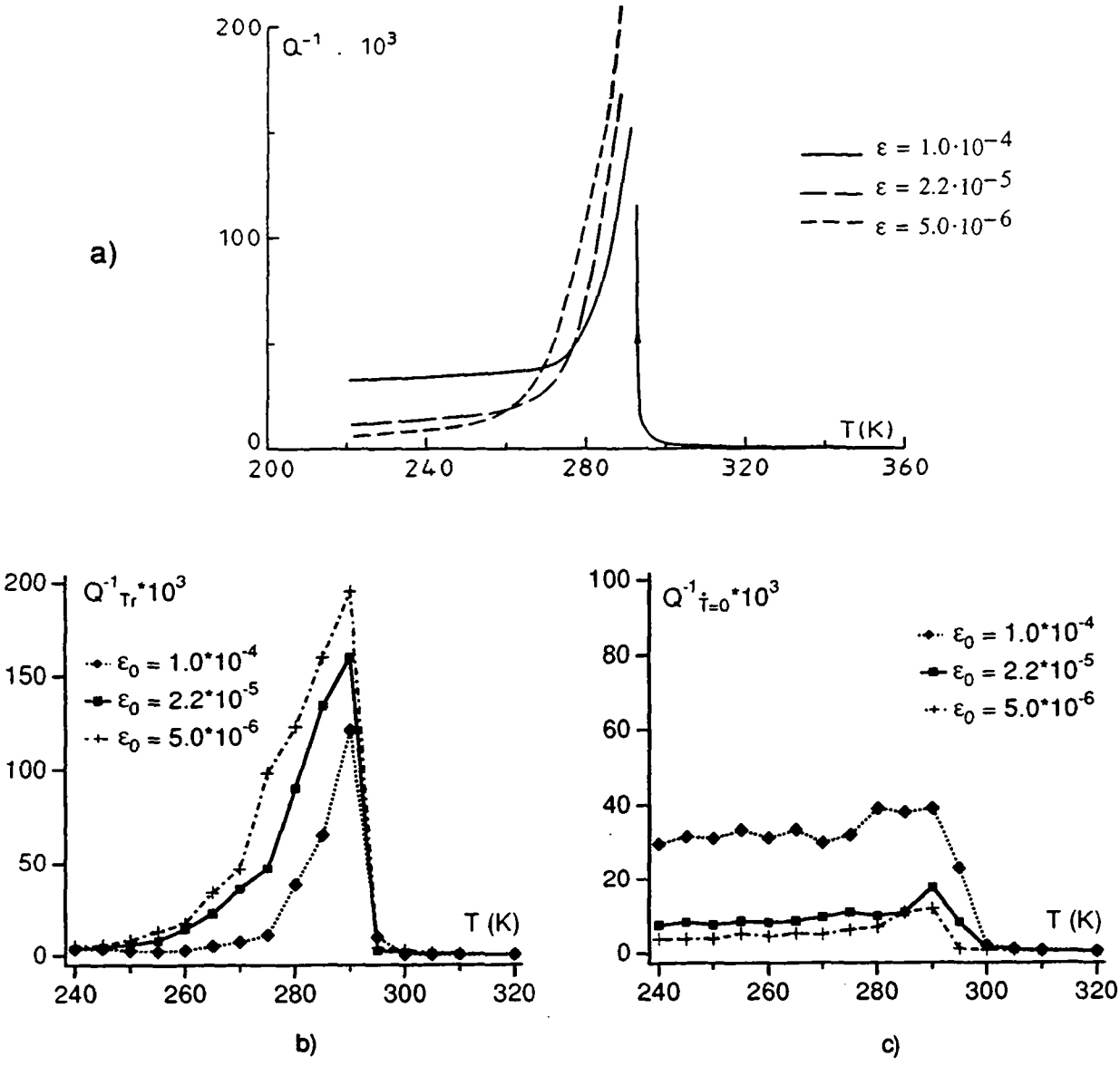

Figure 3.10: IF measured at different oscillation amplitudes (ε_0) in alloy 1: a) Q^{-1}_{tot}, b) Q^{-1}_{Tr}, and c) $Q^{-1}(\dot{T}=0)$.

The continued aim of this investigation is to find out whether by means of a detailed analysis of the IF behaviour, the damping mechanisms of the different Cu-Zn-Al alloys can be characterized and a relationship to the microstructural aspect and macroscopic hysteresis behavior can be established. The IF analysis will be conducted in terms of existing models, which are presented and discussed in the next section.

3.5 Models of the Internal Friction (IF) Peak during Martensitic Transformation

3.5.1 General Aspects of the IF Peak

The internal friction peak, which is observed during martensitic phase transitions in many alloy systems has received a lot of interest and several models have been developed in order to explain its physical origins. Formally, the total amount of the observed IF peak (Q^{-1}_{tot}) can be decomposed into three contributions, see figure 3.11:

$$Q^{-1}_{tot} = Q^{-1}_{Tr} + Q^{-1}_{PT} + Q^{-1}_{int} \qquad (3.5)$$

Q^{-1}_{Tr} is the transient part of Q^{-1}_{tot}, and it exists only during cooling or heating ($\dot{T} \neq 0$) and depends on external parameters like temperature rate ($\dot{T}$), resonance frequency (f) and oscillation amplitude (σ_0). Q^{-1}_{Tr} depends on the transformation kinetics and is therefore proportional to the volume fraction which is transformed per unit of time. Q^{-1}_{PT} is related to mechanisms of the phase transformation (PT), which are independent of the transformation rate ($\dot{T} = 0$), such as the movement of parent-martensite and martensite-martensite interfaces. Q^{-1}_{PT} exhibits a small peak when the interface mobility is highest. Q^{-1}_{int} is composed of the IF contributions of each phase and is strongly dependent on microstructural properties (interface density, vacancies), especially in the martensitic phase.

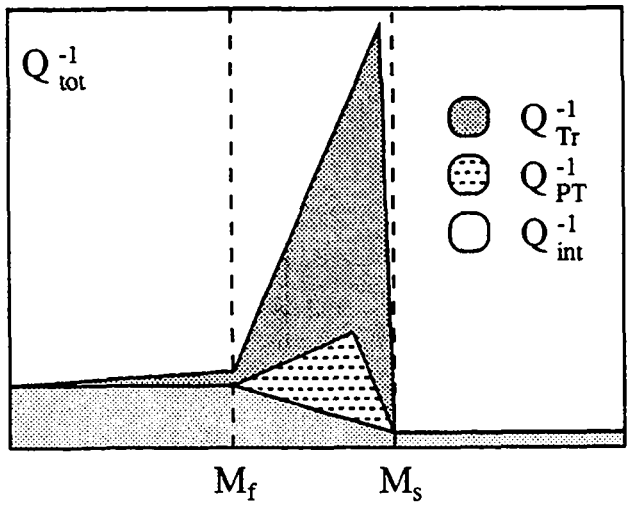

Figure 3.11: Schematic of Q^{-1} and its contributions during martensitic phase transformations.

In the next paragraph the most important models and interpretations for the IF contributions that actually exist in the literature, will be presented. The "static" IF contributions (Q^{-1}_{PT} and Q^{-1}_{int})

will be shortly reviewed and the transient IF contribution (Q^{-1}_{Tr}) will be described in detail with respect to further analysis and discussion of the observed IF behaviour.

3.5.2 The IF in the Martensite Phase, Q^{-1}_{int}

The IF of the martensite phase depends strongly on the microstructural properties, which are present in a given martensitic structure (Van Humbeeck, 1984). Two factors influence the damping capacity of the martensitic phase, the density of mobile defects and their mobility. In thermoelastic polyvariant martensite, a high density of mobile intervariant boundaries can be displaced by the applied oscillation stress and the IF is relatively high. In non-thermoelastic martensites like in Fe-Mn-Si alloys, the martensitic interfaces can not be displaced by external stresses and the measured damping spectrum exhibits very low IF values (Van Humbeeck et al., 1989). In a martensitic monovariant of Cu-Zn-Al, which contains no martensitic interfaces, Morin et al. (1982) have also measured a relatively low IF.

The mobility of intervariant boundaries in thermoelastic martensites is affected by the vacancy concentration, which is dependent on the thermal treatment. Specimens which are quenched into the martensitic phase from high temperatures show small IF values. The so-called "Peaking" effect has been attributed to a progressive pinning of interfaces by vacancies during the oscillations and the increase of damping after interruption of the oscillations has been explained by the redistribution of vacancies in the matrix (Van Humbeeck and Delaey, 1984).

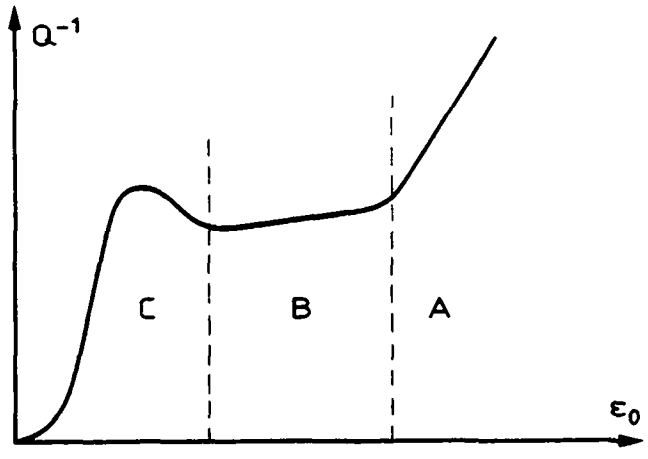

Figure 3.12: The dependence of the IF on the oscillation amplitude (ε_0) measured in Cu-Zn-Al martensite according to Koshimizu (1981).

In the martensitic phase the dependence of IF on the oscillation amplitude (ε_0) can be divided into three amplitude domains (figure 3.12). For lower amplitudes ($10^{-7} < \varepsilon_0 < 10^{-6}$) in region C, the IF was dedicated to the mechanism proposed by Granato and Lücke (1956), namely an amplitude dependent dislocation damping due to unpinning from weak pinning points. In region B ($10^{-6} < \varepsilon_0 < 10^{-5}$) the IF has no amplitude-dependence and should be due to the interaction between dislocations and weak pinning defects (Koshimizu, 1981). The critical amplitude, where an amplitude dependent IF returns, has been attributed to the breakaway stress for the movement of intervariant boundaries (Dejonghe et al., 1977).

3.5.3 The Non-Transient IF Peak, Q^{-1}_{PT}

For an explanation of the Q^{-1}_{PT} peak one can find different approaches in the literature. The model of Dejonghe et al. (1976) considers a maximum of the interface mobility in the transformation region that is expressed by a maximum amount of transformed volume fraction per stress unit ($\partial n/\partial\sigma\,(T)$). When the temperature rate is zero or if the oscillation frequency is very high ($f > 50$ Hz), the transient IF goes to zero and only the amplitude dependent part remains:

$$Q^{-1}_{PT} = \frac{2k}{3\pi J}\sigma_0 \frac{\partial n}{\partial \sigma}\left[1 - \left(\frac{\sigma_c}{\sigma_0}\right)^3\right] \tag{3.6}$$

where k is a constant, J is the elastic compliance, σ_0 is the stress amplitude and σ_c is the critical stress to move the intervariant boundaries.

Mercier et al. (1976) proposed a dislocation mechanism, which takes into account the effect of anisotropy on the elastic energy of dislocations. They showed that the dislocation damping in a crystal is inversely proportional to the crystallographic anisotropy factor (A) and Q^{-1}_{PT} has been expressed by:

$$Q^{-1}_{PT} \sim \frac{\lambda l^4 B\omega}{\left[F\left(\sqrt{A^{-1}}\right)\right]^2} \tag{3.7}$$

where λ is the dislocation density, l the average dislocation length, B the damping constant, ω the angular frequency and the function F depends on the crystallographic directions of the dislocations. By assuming that the anisotropy factor A is maximum at the M_S temperature, equation (3.7) predicts that Q^{-1}_{PT} goes through a maximum at this temperature.

Koshimizu (1981) calculated the IF by using a Landau approximation of a first-order phase transition (Nowick and Berry, 1972). In a thermodynamical treatment, the Gibbs free energy is developed as a function of stress (σ), temperature (T) and an internal variable (ξ), called the

order parameter. Considering a relaxation type of damping, the calculations show discontinuities of Q^{-1}_{PT} and the relaxed modulus at the transition temperatures. In order to describe the σ_0 dependence of Q^{-1}_{PT}, Koshimizu extended his model by considering a hysteretic friction and a depinning mechanism for dislocation damping, which influences the order parameter ξ.

3.5.4 Models of the Transient Part of IF, Q^{-1}_{Tr}

In the frequency range ($f \approx 1$ Hz) where the IF measurements of the present investigation have been conducted, the transient part (Q^{-1}_{Tr}) is the most important contribution to the IF peak. Therefore, a more detailed description of damping mechanisms and equations for Q^{-1}_{Tr} will be given in this section. The starting point for any IF modeling is the basic equation for Q^{-1},

$$Q^{-1} = \frac{1}{\pi J \sigma_0^2} \oint \sigma \, d\varepsilon_{an}, \quad \sigma = \sigma_0 \sin\omega t \tag{3.8}$$

where J is the elastic compliance, σ_0 is the oscillation amplitude, ω is the angular frequency ($\omega = 2\pi f$) and $d\varepsilon_{an}$ is the anelastic or irreversible part of deformation during one oscillation cycle.

The first attempt to explain the transient character of the IF peak during martensitic transformation dates from 1956, when Scheil et al. related Q^{-1}_{Tr} to the transformation rate $(\partial n/\partial t)$. The anelastic deformation $(d\varepsilon_{an})$ in equation (3.8) arises from the lattice deformation that occurs when material is transformed during the IF measurement.

$$d\varepsilon_{an} = k \cdot \frac{\partial n}{\partial t} dt \tag{3.9}$$

This basic idea which is expressed by a proportionality between $d\varepsilon_{an}$ and $\partial n/\partial t$, has been maintained in all the following models. The crucial point for the further development of an expression for Q^{-1}_{Tr} has been defining the influence of temperature (T) and oscillation amplitude (σ_0) on the anelastic deformation $(d\varepsilon_{an})$ as well as on the transformation rate $(\partial n/\partial t)$.

A thermally activated type of anelastic behaviour is based on the model of Belko et al. (1969). $d\varepsilon_{an}$ is due to the thermally activated formation and growth of nuclei of the new phase. The associated activation energy necessary to pass from the state of nucleation to the state of growth, is modified by the oscillation stress. The resulting anelastic deformation has been calculated using the classical formalism of relaxation processes. However, the proposed T^{-1}- and $\Delta G/G$-dependencies of Q^{-1}_{Tr} have never been observed during martensitic phase transformations in shape memory alloys. Therefore, this model which is based on a thermally activated type of

anelasticity, does not seem to be appropriate for describing the IF peak found in alloys, where the transformation is strictly athermic.

The IF models that are presented in the following are based on an athermic or hysteretic type of anelastic deformation and can be applied for martensitic transformations in shape memory alloys. They are classified in table 3.2 with respect to their suppositions for the oscillation amplitude dependence of $d\varepsilon_{an}$ and $\partial n/\partial t$.

Model of Transformation "Plasticity": $d\varepsilon_{an}(\sigma, \partial n/\partial t)$

Delorme and Gobin (1973) have proposed an expression for $d\varepsilon_{an}$, which is based on the analysis of static "*transformation plasticity*" experiments. They found that the transformation deformation $(d\varepsilon_p)$ increases linearly with the transformed volume fraction and the applied stress,

$$d\varepsilon_p = k\,\sigma\,dn\,, \tag{3.10}$$

and assumed that $d\varepsilon_{an}$ obeys the same law during dynamic measurements (table 3.2). The transformation rate $(\partial n/\partial t)$ has been assumed to be proportional to both the transformed volume fraction per temperature unit $(\partial n/\partial T)$ and the temperature rate $(\dot{T})$, following one of the basic assumption for $\partial n/\partial t$ (table 3.2):

$$\frac{\partial n}{\partial t} = \frac{\partial n}{\partial T}\dot{T} \tag{3.11}$$

Assuming further that $\partial n/\partial T$ is constant during one oscillation cycle, equation (3.8) can be combined with equations (3.10) and (3.11) and integrated. By doing this the following equations for $Q^{-1}{}_{Tr}$ and the modulus defect $(\Delta G/G)$ have been derived:

$$Q_{Tr}^{-1} = \frac{k}{J}\frac{dn}{dT}\frac{\dot{T}}{\omega} \qquad \frac{\Delta G}{G} = Q_{Tr}^{-1} \tag{3.12}$$

Two possible physical interpretation of equation (3.10) have been proposed in order to describe the anelastic deformation that occurs during an IF measurement. First, Delorme included an accomodation effect that accounts for the plastic deformation during transformation. Plastic deformation was considered to occur in order to remove the internal stresses, which are created by the formation of the new phase due to its volume difference with respect to the parent phase, and the oscillation stress was assumed to orient the dislocation motion. However, during thermoelastic transformations the volume change and therefore the plastic deformation are very small and this effect should not contribute significantly to the IF in Cu-Zn-Al shape memory alloys (see also discussion in chapter 6).

Table 3.2: Existing models of the high damping peak during martensitic transformations

$$Q^{-1} = \frac{1}{\pi J \sigma_0^2} \oint \sigma \, d\varepsilon_{an}, \qquad \sigma = \sigma_0 \sin\omega t \qquad \text{(equ. 3.8)}$$

$d\varepsilon_{an} = k \sigma \frac{\partial n}{\partial t} dt$ (equ. 3.10)

(transformation "plasticity ")

$d\varepsilon_{an} = k \frac{\partial n}{\partial t} dt$ (equ. 3.16)

("pure" transformation strain)

$\frac{\partial n}{\partial t} = \frac{\partial n}{\partial T} \cdot \dot{T}$ (equ. 3.11)

Delorme

$Q^{-1} = \frac{k}{J} \frac{\partial n}{\partial T} \frac{\dot{T}}{\omega}$ (equ. 3.12)

$\frac{\partial n}{\partial t} = \frac{\partial n}{\partial T} \cdot \dot{T} + \frac{\partial n}{\partial \sigma} \cdot \sigma$ (equ. 3.14)

Dejonghe

$Q^{-1} = \frac{k}{J} \left\{ \frac{\partial n}{\partial T} \frac{\dot{T}}{\omega} + \frac{2}{3\pi} \sigma_0 \frac{\partial n}{\partial \sigma} \left[1 - \left(\frac{\sigma_c}{\sigma_0} \right)^3 \right] \right\}$ (equ. 3.15)

$\frac{\partial n}{\partial t} = \frac{\partial n}{\partial T} \cdot \dot{T}$ (equ. 3.11)

Delorme

$Q^{-1} = \frac{4k}{\pi J} \frac{\partial n}{\partial T} \frac{\dot{T}}{\omega \sigma_0}$ (equ. 3.17)

$\frac{\partial n}{\partial t} = \frac{\partial n}{\partial T} \cdot (\dot{T} + \alpha \cdot \sigma)$ (equ. 3.19)

Gremaud-Bidaux

$$Q_i^{-1} = \frac{2k}{J} \frac{\partial n}{\partial T} \frac{1 - \frac{\pi}{2\alpha} \frac{\dot{T}}{\omega \sigma_0}}{1 + \frac{\pi}{2\alpha} \frac{\dot{T}}{\omega \sigma_0}} \frac{\dot{T}}{\omega \sigma_0}, \quad \frac{\dot{T}}{\omega \sigma_0} < \frac{2\alpha}{3\pi}$$

$$Q_{ii}^{-1} = \frac{k}{4J} \frac{\partial n}{\partial T} \left(\frac{\dot{T}}{\omega \sigma_0} + \frac{2\alpha}{\pi} \right), \quad \frac{2\alpha}{3\pi} < \frac{\dot{T}}{\omega \sigma_0} < \frac{2\alpha}{\pi}$$

$$Q_{iii}^{-1} = \frac{k}{2J} \frac{\partial n}{\partial T} \frac{\dot{T}}{\omega \sigma_0}, \quad \frac{\dot{T}}{\omega \sigma_0} > \frac{2\alpha}{\pi}$$

(equations 3.20)

The second interpretation of equation (3.10) is related to the shear-type deformation which occurs during martensitic transformations and which is proportional to the amount of transformed volume. In this interpretation the applied oscillating stress is believed to favor certain martensitic variants and to lead to a macroscopic deformation in the sense of the applied stress. The constant k of equation (3.12) in this case becomes:

$$k = \frac{\alpha}{4} \frac{(\varepsilon^t)^2}{\Delta G^t} \tag{3.13}$$

where α is the fraction of variants which are oriented by the applied stress and ΔG^t is the average driving force of the transformation.

As an extension of Delorme's model of transformation plasticity, Dejonghe et al. (1976) added a stress dependent term of the transformation rate to equation (3.11). When this is done, $\partial n/\partial t$ becomes:

$$\frac{\partial n}{\partial t} = \frac{\partial n}{\partial T} \dot{T} + \frac{\partial n}{\partial \sigma} \dot{\sigma} \tag{3.14}$$

and this equation accounts for the possibility that material transforms under the action of the applied oscillating stress. Furthermore, Dejonghe et al. considered dn to include the amount of martensite which retransforms during one oscillation. Assuming that there is a critical stress (σ_c) that is necessary in order to reorientate the already existing variants or to stress-induce new variants, Q^{-1}_{Tr} becomes:

$$Q^{-1}_{Tr} = \frac{k}{J} \left\{ \frac{\partial n}{\partial T} \frac{\dot{T}}{\omega} + \frac{2}{3\pi} \sigma_0 \frac{\partial n}{\partial \sigma} \left[1 - \left(\frac{\sigma_c}{\sigma_0} \right)^3 \right] \right\} \tag{3.15}$$

Incorporating the possibility of stress-induced transformation, this explains the experimental observation that a small IF peak exists for $\dot{T} = 0$ and that the height of this non-transient IF peak is dependent on σ_0 (figure 3.10).

Model of "Pure" Transformation Strain: $d\varepsilon_{an}$ ($\partial n/\partial t$)

In the work of Delorme, the $\dot{T}/\omega$-dependence of the IF according to equation (3.12) has been in good agreement with the experimental results, but the σ_0-independent transient part of the IF peak was not observed for smaller oscillation amplitudes ($\sigma_0 < 10^{-4}\ G$). Therefore, an alternative mechanism has been proposed by Delorme et al. (1973), which accounts for the situation where σ_0 is not high enough with respect to the internal stresses to orient the transforming variants. Then, σ_0 only contributes to the transformation when its sense coincides with the direction of

the transforming variants. This is equivalent to the absence of the transformation plasticity and it results in a "naturally" oriented martensitic structure, where $d\varepsilon_{an}$ is independent of σ_0 *("pure" transformation strain)*:

$$d\varepsilon_{an} = k\, dn \tag{3.16}$$

Taking equation (3.11) for $\partial n/\partial t$, it follows that $Q^{-1}{}_{Tr}$ is equal to:

$$Q^{-1}_{Tr} = \frac{4k}{\pi J}\frac{\partial n}{\partial T}\frac{\dot{T}}{\omega\,\sigma_0} \tag{3.17}$$

The established σ_0-dependence of $Q^{-1}{}_{Tr}$ has been confirmed later on by Morin et al. (1980) for the IF peak measured in Cu-Zn-Al alloys. They observed that $Q^{-1}{}_{Tr}$ decreases with increasing σ_0 for small oscillation amplitudes ($\sigma_0 < 10^{-4}\, G$).

The constant k in equation (3.17) is determined by the stress-free transformation strain that is produced in the habit plane system (ε^t). In the case of a polycrystal, ε^t is multiplied by an orientation factor of 0.4, and another factor μ ($\mu < 1$), which accounts for the absence of energy dissipation when those variants whose orientation is not in the sense of σ_0 transform:

$$k = 0.4 \cdot \mu\, \varepsilon^t \tag{3.18}$$

However, there is one discrepancy between the experimental results and the equations for $Q^{-1}{}_{Tr}$ as presented in the model of Delorme. Experimental results showed that $Q^{-1}{}_{Tr}$ does not increase linearly with $\dot{T}/\omega$. This effect has been reported for different materials: in Cu-Al-Ni by Postnikov and Sharshakov (1972), in Ni-Ti by Zhu et al. (1988) and in pure cobalt by Bidaux (1988). This problem led Gremaud and Bidaux (1987) to develop a new model, which defines the role of the oscillating measuring stress for the transformation according to the Clausius-Clapeyron equation (equation 3.3).

In the new approach of Gremaud and Bidaux the anelastic deformation ($d\varepsilon_{an}$) is related to a "pure" transformation strain, as has been proposed by Delorme in the second part of his model (equation 3.16). The important point of the new model is that it takes into account the influence of the applied stress amplitude (σ_0) on the transformation rate ($\partial n/\partial t$). This occurs in the sense that the thermodynamic equilibrium of the material changes and the variants which are favored by σ_0 are induced to transform. Following this idea $\partial n/\partial t$ becomes equal to:

$$\frac{\partial n}{\partial t} = \frac{\partial n}{\partial T} \cdot (\dot{T} + \alpha \cdot \dot{\sigma}) \tag{3.19}$$

where α is the Clausius-Clapeyron factor ($\alpha = v\varepsilon^t/\Delta S$), v is the molar volume and ΔS is the entropy change of both phases.

In this model, energy dissipation is only considered to occur during the time (Δt), in which the transformation is induced by the oscillating measuring stress (σ_0). Δt is determined by the condition that $\dot{\varepsilon}_{an} > 0$, which is equivalent with the assumption of a *complete hysteretic deformation* during IF measurement. The integration time for equation (3.8), Δt, is dependent on $\dot{T}$, ω and σ_0. The calculations of the deformation produced by a single variant give, depending on the value of $\frac{\dot{T}}{\omega\sigma_0}$, three different expressions for the IF (equations 3.20 in table 3.2). These expressions correspond to the three different regimes in the $Q^{-1}(\frac{\dot{T}}{\omega\sigma_0})$ plot (figure 3.13). The non-linear dependence in regime I arises from the fact that, at low $\dot{T}/\omega$-values, dissipation occurs when the stress is near to its maximum value (σ_0). As $\dot{T}/\omega$ increases, Δt increases but the IF does not increase correspondingly, because dissipation occurs in a stress range lower than σ_0.

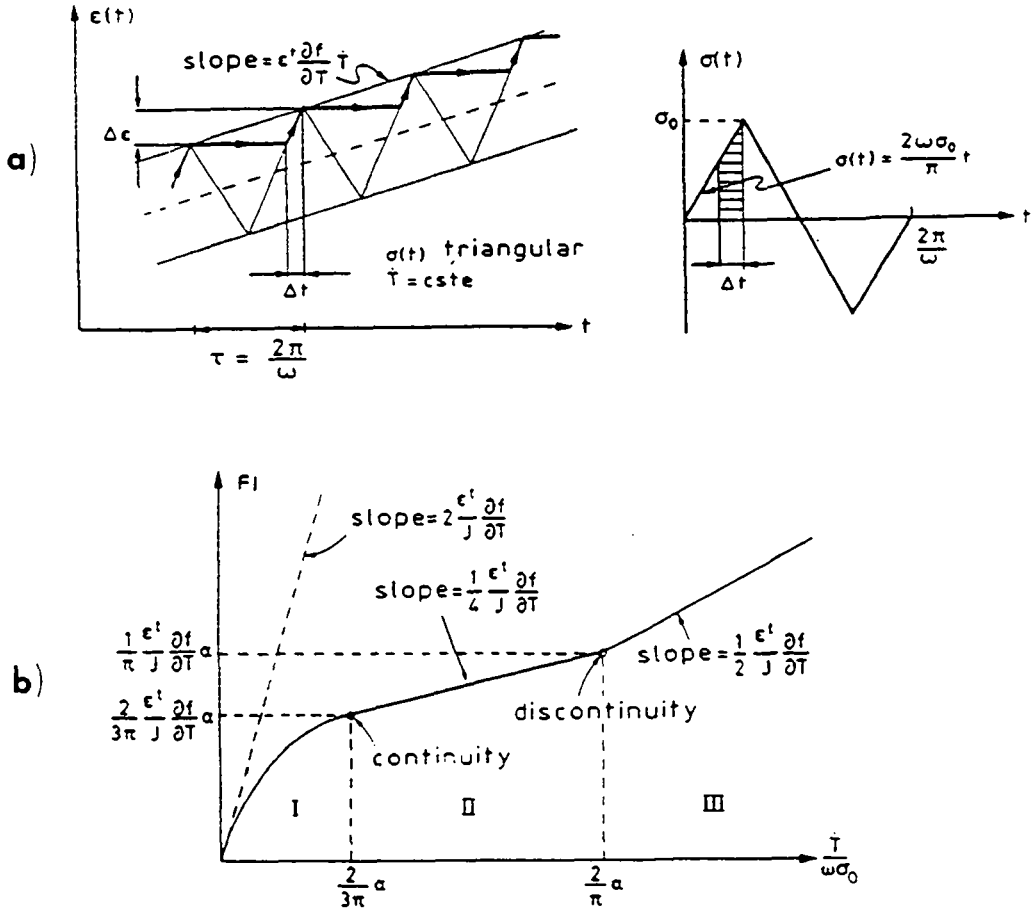

Figure 3.13: Model of Gremaud and Bidaux (1987):
a) Schematic evolution of the deformation ($\varepsilon(t)$) when both $\dot{T}$ and σ are changing simultaneously. b) Theoretical transient IF as a function of $\frac{\dot{T}}{\omega\sigma_0}$.

3.6 Analysis of the IF Behaviour during Complete Transformation Cycles

3.6.1 How to Proceed ?

In the preceding paragraphs we have seen that there are a number of IF models that have been proposed to explain the IF behaviour during martensitic transformations. These models have attempted to explain the physical origins of the different IF contributions. The experimental results of the present investigation show that the transient part of the IF (Q^{-1}_{Tr}) is by far the largest contribution to the IF peak. Q^{-1}_{Tr} arises from the transformation mechanisms which are active under the mutual influence of external and internal stresses and exhibits significant differences in the studied Cu-Zn-Al alloys. The static IF contributions ($Q^{-1}_{\dot{T}=0}$ and $Q^{-1}_{\dot{\sigma}=0}$) only allow for the characterization of microstructural properties after internal stresses have been relaxed. Therefore, the analysis of the IF peak during transformation will concentrate on the transient IF (Q^{-1}_{Tr}). This analysis is divided into two parts.

In the first part, the IF behaviour will be analyzed for the complete transformation cycles that were measured in different Cu-Zn-Al alloys, in order to examine the influence of the microstructural evolution on the transient IF. The existing IF models predict a linear relationship between Q^{-1}_{Tr} and $\partial n/\partial T$ (table 3.2). Since the external parameters ($\dot{T}(\dot{\sigma})$, f and ε_0) were kept constant in the different specimens, the microstructural parameter can also be expressed by the volume fraction which transforms during one oscillation cycle (Δn). The relationship between Q^{-1}_{Tr} and Δn becomes equal to:

$$Q^{-1}_{Tr} = k \cdot \Delta n \qquad (3.21)$$

where k is a constant.

Δn has been calculated for temperature-and stress-induced transformations as well as for $\dot{T}$-experiments by applying the following equations:

T-induced transformation:
$$\Delta n = \frac{\partial n}{\partial T} \cdot \frac{\dot{T}}{f} \qquad (3.22a)$$

σ-induced transformation:
$$\Delta n = \frac{\partial n}{\partial \sigma} \cdot \frac{\dot{\sigma}}{f} \qquad (3.22b)$$

$\dot{T}$-experiments ($\dot{T} = 0$):
$$\Delta n = \frac{\partial n}{\partial t} \cdot \frac{1}{f} \qquad (3.22c)$$

In the second part, the dependence of Q^{-1}_{Tr} on the external parameters will be examined. Considering the predictions of the existing models (table 3.2) and the present result that Q^{-1}_{Tr} decreases with increasing ε_0 ($\varepsilon_0 = \sigma_0/G$), the following equation for Q^{-1}_{Tr} will be assumed:

$$Q^{-1}_{Tr} = k \cdot \frac{\partial n}{\partial T} \cdot f\left(\frac{\dot{T} G}{\omega \sigma_0}\right) \tag{3.23}$$

The dependence of Q^{-1}_{Tr} on the external parameters is expressed by $f(\frac{\dot{T}G}{\omega\sigma_0})$, a not explicitly determined function that will be studied by examining the observed IF peaks in dependence of $\dot{T}$, ω and σ_0.

3.6.2 Q^{-1}_{Tr} as a Function of the Transformed Volume Fraction: $Q^{-1}_{Tr}(\Delta n)$

In this part of the IF analysis the validity of the assumption that Q^{-1}_{Tr} is linearly dependent on the transformed volume fraction per oscillation (Δn), will be examined. Equation (3.21) has been applied for the analysis of thermal transformation cycles that were measured in alloys 1 and 2, for the stress-induced transformations and for the $\dot{T}$-experiments performed on alloy 2A. Q^{-1}_{Tr} has been determined by subtracting $Q^{-1}(\dot{T}=0)$ or $Q^{-1}(\dot{\sigma}=0)$ from Q^{-1}_{tot} (equations 3.4) and Δn has been determined using the equations (3.22).

Temperature-Induced Transformations

Figure 3.14 shows the analysis of the complete thermal transformation cycles. Q^{-1}_{Tr} and Δn which have been derived from the cooling curves of figure 3.2, are plotted as a function of T and peaks are found in Q^{-1}_{Tr} and Δn for all specimens. Both peaks coincide well for the trained specimen of alloy 2B, but only one side of the peaks can be superimposed on the measurement of the untrained specimens (alloys 1 and 2A). In the latter case, two temperature regimes with different linear relationships between Q^{-1}_{Tr} and Δn have been distinguished:

T-regime I: $T_{Peak} < T < M_S$

T-regime II: $M_f < T < T_{Peak}$

According to T-regimes I and II, two different slopes (k_I and k_{II}) can be defined for the beginning and for the end of the transformation (figure 3.14). Because k_{II} is bigger than k_I, one can conclude that for a given Δn, the IF values are higher at the end of the transformation than in the beginning. This indicates that additional IF contributions arise in the course of martensitic transformations, which must be related to a microstructural parameter that is different from the transformed volume fraction per oscillation (Δn), see discussion in chapter 6.

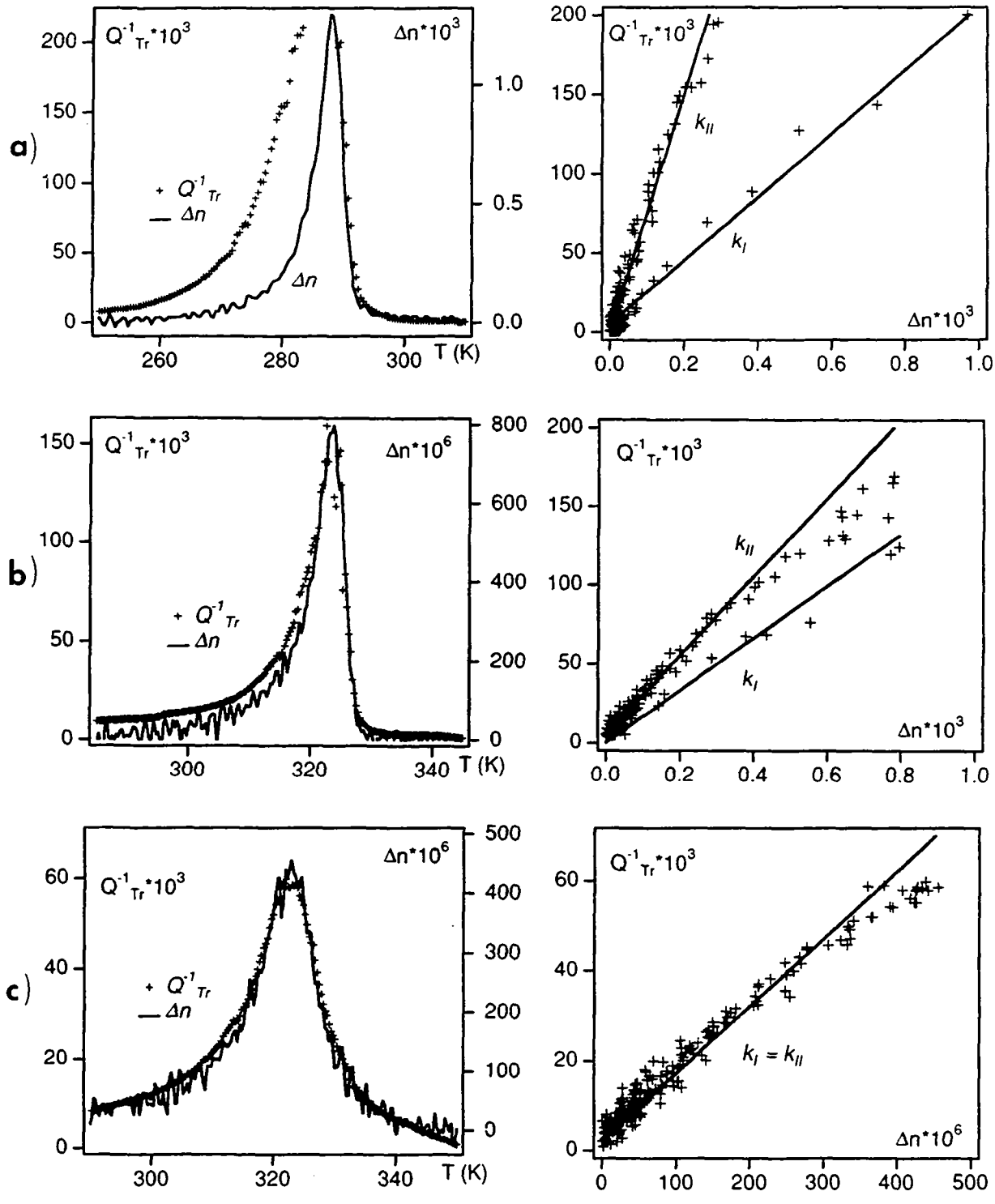

Figure 3.14: $\Delta n\ (T)$ and $Q^{-1}_{Tr}\ (T)$ during cooling and Q^{-1}_{Tr} as a function of Δn for a) alloy 1, b) alloy 2A and c) alloy 2B.

Further quantitative comparison of the IF peaks has been conducted by integrating equation (3.21) combined with equation (3.22a):

$$K = \frac{1}{\dot{T}} \int_{M_S}^{T} Q_{Tr}^{-1} f \, dT = k \cdot n \qquad (3.24a)$$

K is in analogy to the model of Delorme et al. (1973) the so-called "normalized" IF, since it only depends on the amount of transformed volume (n), and k is the same constant as in equation (3.21).

K is shown as a function of n during temperature-induced transformations in figure 3.15. This figure includes all of the studied alloys and one can see that the linear dependency of K on n is only valid for the trained specimen 2B. A single constant k is found for this specimen, but non-linear curves are obtained for specimens 1, 2A and 3. The different slopes (k_I and k_{II}) have been measured for alloys 1, 2A and 3 and the results are equivalent to those of figure 3.14. As can be seen from the $K(n)$ curve of alloy 3 (M_S = 200 K), the transformation temperature is not an important parameter for the observed transient IF behaviour.

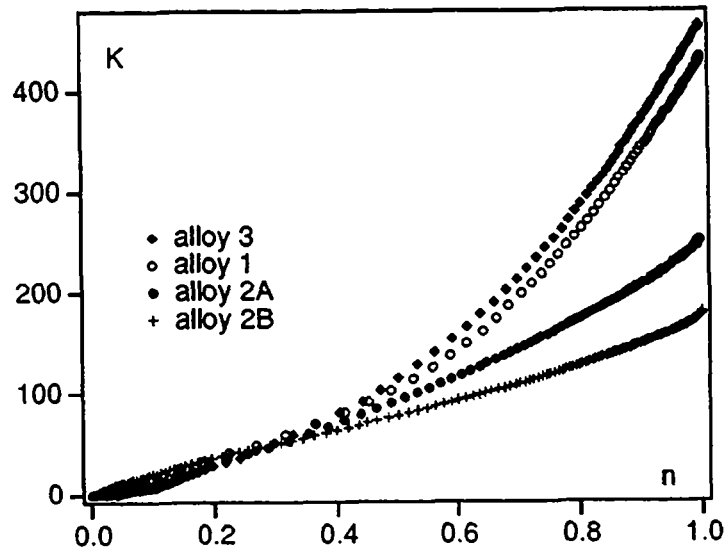

Figure 3.15: Normalized IF (K) as a function of n in Cu-Zn-Al alloys.

Stress-Induced Transformations

Figure 3.16a illustrates the evolutions of $Q^{-1}{}_{Tr}$ and Δn that have been calculated from the stress-induced transformation cycle of alloy 2A (figure 3.6). For the analysis of the $Q^{-1}{}_{Tr}$ peak, equation (3.21) has been combined with equation (3.22b) and integrated to give:

$$K = \frac{1}{\dot{\sigma}} \int_{\sigma_c}^{\sigma} Q_{Tr}^{-1} f \, d\sigma = k \cdot n \qquad (3.24b)$$

Figure 3.16b shows that a linear dependency between K and n is observed during stress-induced transformation in alloy 2A.

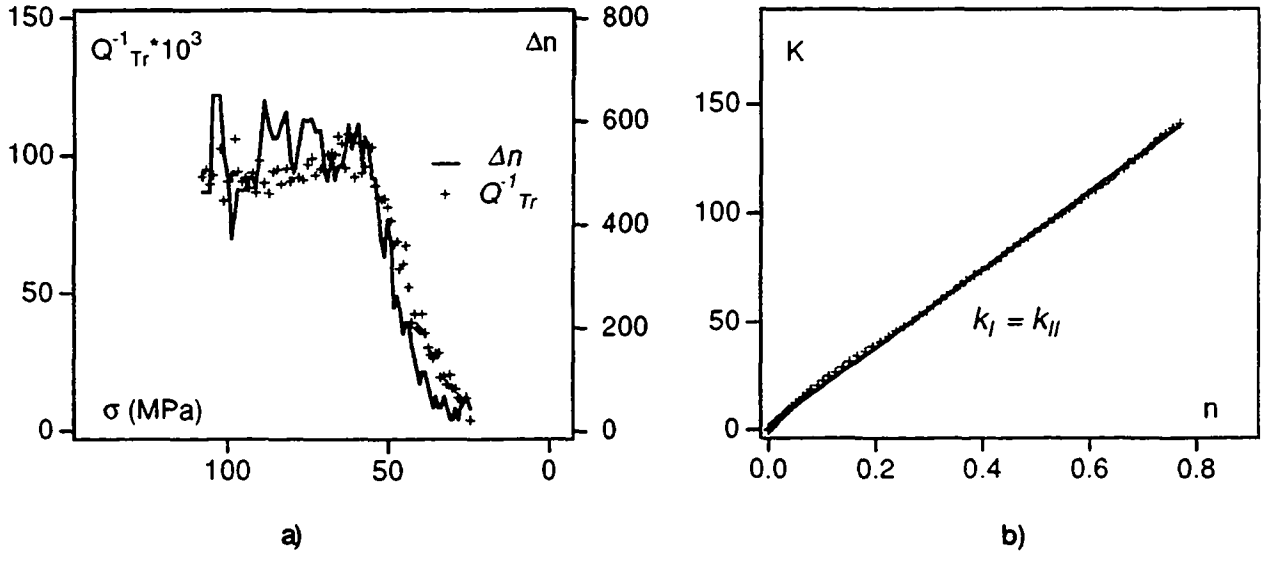

Figure 3.16: Analysis of Q^{-1}_{Tr} for stress-induced transformation in alloy 2: a) Q^{-1}_{Tr} and Δn as a function of σ, b) K as a function of n.

A quantitative comparison of the $K(n)$ diagrams obtained for temperature- and stress-induced transformations, is given in table 3.3. The two slopes that are listed have been evaluated from the $K(n)$ curves: The k_I-values were determined at the beginning ($0 < n < 0.25$) and the k_{II}-values at the end of the transformation ($0.75 < n < 1$). It is interesting to note that the k_I-values are approximately the same for all transformations, including the stress-induced transformation (alloy $2A_\sigma$). The biggest difference between k_I and k_{II} occurs in the coarse grain alloys 1 and 3.

Table 3.3: Values of k for the studied Cu-Zn-Al alloys.

k	alloy 1	alloy 2A	alloy 2B	alloy $2A_\sigma$	alloy 3
k_I	200	180	180	190	175
k_{II}	980	485	180	190	920

$\dot{T}$- Experiments

The amount of transformed volume *(n)* changed slightly and the IF decreased during the $\dot{T}$-experiments (figures 3.8a and 3.9). For an individual $\dot{T}$ - curve, the relationship between Q^{-1}_{Tr} and Δn can be analyzed by combining equations (3.21) and (3.22c) and integrating to get:

$$K = \int_{t_1}^{t_2} Q^{-1}_{Tr} f \, dt = k \cdot (n_2 - n_1) \qquad (3.24c)$$

In figure 3.17, the *k*-values that were obtained for different $\dot{T}$-curves are plotted versus the actual amount of transformed volume *(n)* that existed when the transformation was stopped. It can be seen that the *k*-values measured during $\dot{T}$-experiments increase as a function of *n*, especially at the end of the transformation ($n > 0.5$). A comparison of the k_I- and k_{II}-values obtained during constant $\dot{T}$ transformations shows that the amount of IF (given by *K*), related to the change in transformed volume fraction ($n_2 - n_1$), can be very high during $\dot{T}$-experiments. This result confirms the assumption that the transient part of the IF peak is not only due to the transformed volume fraction per oscillation (Δn). An additional damping mechanism that operates when the transformation is stopped inside the hysteresis could be the reorientation of martensitic variants in order to relax locally high internal stresses (see also discussion in chapter 6).

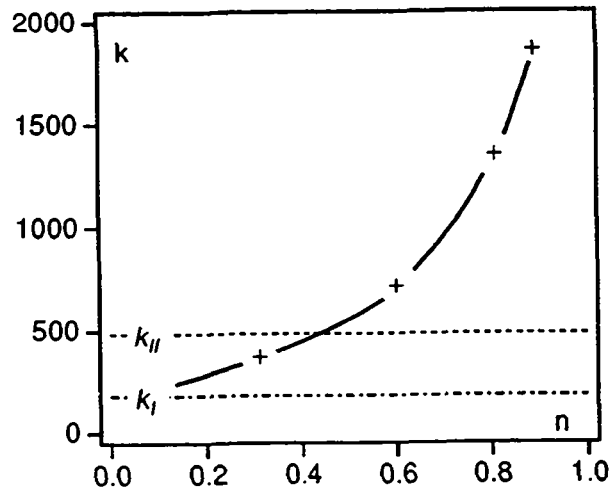

Figure 3.17: Analysis of Q^{-1}_{Tr} during $\dot{T}$- experiments: *k* as a function of *n*.

3.6.3 The Dependence of Q^{-1}_{Tr} on External Parameters: $Q^{-1}_{Tr}(\dot{T}, \omega, \sigma_0)$

The transient part of the IF peak cannot always be described by a single linear dependency of Q^{-1}_{Tr} on Δn. The difference in the measured values of k_I and k_{II} suggests that there is a change in the mechanism that controls the anelastic deformation in Cu-Zn-Al alloys. Since the biggest difference was found for the thermally-induced transformation in alloy 1, the quantitative analysis of k_I and k_{II} has been conducted with the obtained results of this alloy. The dependence of both parameters on the external parameters such as temperature rate $\dot{T}$, oscillation frequency ω and oscillation amplitude σ_0 has been determined by integrating equation 3.23:

$$\frac{\int_{T_1}^{T_2} Q_{Tr}^{-1}\, dT}{n_2 - n_1} = f\left(\frac{\dot{T}}{\omega\,\sigma_0}\right), \qquad \frac{\int_{T_1}^{T_2} Q_{Tr}^{-1}\, dT}{n_2 - n_1} = k' \qquad (3.25)$$

The parameter k' has been determined in temperature regime I for $0 < n < 0.25$ (k_I') and in temperature regime II for $0.75 < n < 1$ (k_{II}'). Figure 3.18 shows the dependence of k_I' and k_{II}' on $\frac{\dot{T}\,G}{\omega\,\sigma_0}$ ($G/\sigma_0 = \varepsilon_0$).

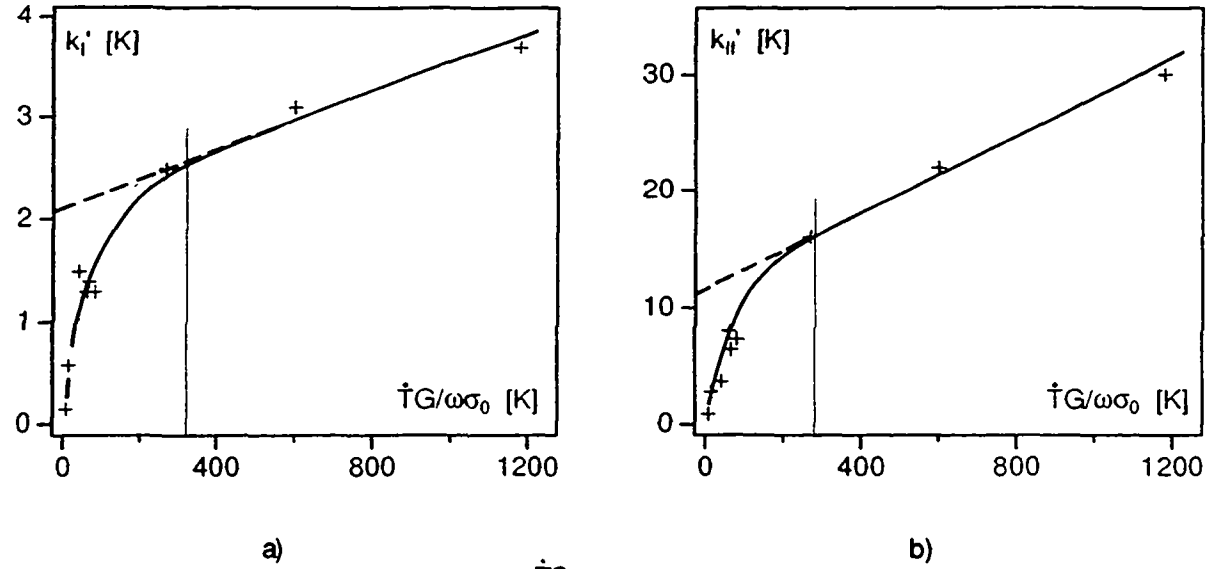

Figure 3.18: Constant k' as a function of $\frac{\dot{T}G}{\omega\sigma_0}$ for alloy 1, obtained from IF measurements, where $\dot{T}$ and ε_0 were changed independently. a) k_I', b) k_{II}'.

The graphs of figure 3.18 show that k_I' and k_{II}' are not proportional to $\frac{\dot{T}\,G}{\omega\,\sigma_0}$ and that a transition point between two different regimes exists at around 300 K. This transition point is of particular interest since it is predicted by the model of Gremaud et al. (1987), see figure 3.13. In this

model, the position of the transition point is related to the "Clausius-Clapeyron" factor α and therefore to the transformation strain ε^t (equations 3.20):

$$\frac{\dot{T}}{\omega \sigma_0} = \frac{2}{3\pi}\alpha, \quad \alpha = \frac{V}{\Delta S}\varepsilon^t \tag{3.26}$$

$$\varepsilon^t = \frac{3\pi}{2}\frac{\dot{T}}{\omega \sigma_0}\frac{\Delta S}{V} \tag{3.27}$$

For $\frac{\dot{T}}{\omega \sigma_0} = 300/G$, where $G = 50$ GPa (Van Humbeeck, 1983), it follows that:

$$\alpha = 2.8 \cdot 10^{-2}\ \text{K/MPa},$$

and taking $V = 7.6\ \text{cm}^3/\text{mole}$ and $\Delta S = 1.5$ J/moleK (Lovey et al., 1992) yields:

$$\varepsilon^t = 5.6 \cdot 10^{-3} \tag{3.28}$$

The obtained value for ε^t allows for the calculation of the theoretical k'-value at the transition point by using the equations for $Q^{-1}{}_{Tr}$ that are given in the Gremaud-Bidaux model (table 3.2):

$$k' \left(\frac{\dot{T}}{\omega \sigma_0} = \frac{2}{3\pi}\alpha\right) = \varepsilon^t \cdot \frac{\dot{T} G}{\omega \sigma_0} = 1.7\ \mathbf{K} \tag{3.29}$$

where $\frac{\dot{T} G}{\omega \sigma_0}$ has been supposed to be 300K. As can be derived from figure 3.30, a good correlation exists between this k'- value and the experimental k_I'- value, but the k_{II}'- value is very much higher than k':

$$k_I' = \mathbf{2.5\ K} \tag{3.30}$$

$$k_{II}' = \mathbf{16\ K}$$

One can conclude that only in the beginning of the transformation the measured IF (k_I') is sufficiently well explained by the employed models, which assume that the transformed volume fraction during oscillation dominates the IF mechanism. And, it has to be emphasized, that the ε^t-values derived from the $k'(\frac{\dot{T}}{\omega \sigma_0})$ curves (figure 3.18) are very much smaller than those values that are obtained during static deformation in Cu-Zn-Al alloys ($\alpha = 1$ MPa/K and $\varepsilon^t{}_{tot} = 0.19$, according to Lovey et al.,1992). This indicates that during IF measurements only "effective" values of the transformation strain ($\varepsilon^t{}_{eff}$) can be obtained ($\varepsilon^t{}_{eff} << \varepsilon^t{}_{tot}$). Considering all of the analyzed IF values that are listed in table 3.3, the following relationship between the macroscopic (total) transformation strain ($\varepsilon^t{}_{tot}$) and the "effective" transformation strain ($\varepsilon^t{}_{eff}$) has been obtained:

$$\varepsilon^t{}_{tot} = a \cdot \varepsilon^t{}_{eff}, \qquad a = 25 \pm 7 \tag{3.31}$$

The difference of static and dynamic transformation strains (ε^t_{tot} and ε^t_{eff}) suggests that two basic assumptions of existing IF models have to be examined more in detail. These are the crystallographic nature of the anelastic deformation as well as the hysteretic character of the deformation, both of which will be systematically investigated during single variant transformations. The results of this study are presented in chapter 4.

3.7 Hysteresis Effects during Incomplete Transformation Cycles

3.7.1 Definition of Partial Transformation Cycles and Transformation Sub-Loops

When a transformation cycle does not cover the temperature interval between M_f and A_f the transformation is not completed and the cycle is called an incomplete transformation cycle. There are several possibilities for describing transformation paths inside the overall hysteresis. The difference between partial transformation cycles and transformation sub-loops has to be defined for the understanding of the following study.

Figure 3.19 shows, schematically, the possible transformation paths which are described in the $n(T)$ plane during incomplete transformation cycling. During a *partial forward transformation cycle* the forward transformation is interrupted at a temperature between M_s and M_f and then followed by a complete reverse transformation (figure 3.19a). *Partial reverse transformation cycle* means that a fully martensitic specimen is heated to a temperature below A_f and then cooled to M_f (figure 3.19b).

In comparison to a partial forward transformation cycle, a *forward transformation sub-loop* is associated with a transformation path where the forward transformation is interrupted but the subsequent heating cycle is not completed and the specimen is cooled again from a temperature below A_f. A small closed loop or sub-loop is formed within the main hysteresis loop, and it closes precisely on the main cooling curve when the cooling portion of the sub-cycle is finished (figure 3.19c). In analogy to that, *a reverse transformation sub-loop* is associated to a transformation path, where the reverse transformation is interrupted but the subsequent cooling cycle is not completed and the specimen is heated again from a temperature above M_f. Again, a small closed loop is formed and it closes precisely on the main heating curve (figure 3.19d).

In addition to partial transformation cycles, the stability of transformation sub-loops has been studied in the present Cu-Zn-Al alloys (table 3.1) during both partial temperature and stress cycling. During *partial temperature cycling (PTC)* the temperature rate was reversed repetitively

in a fixed temperature interval ($T_1 < T < T_2$, figure 3.19c), while during *partial stress cycling (PSC)* the stress rate was reversed repetitively in a fixed stress interval.

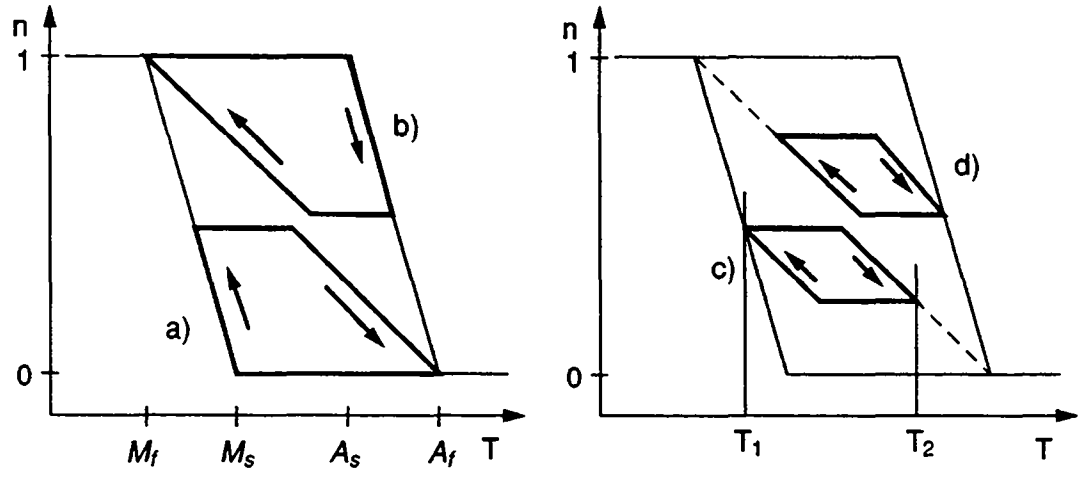

Figure 3.19: Transformation paths during partial forward (a) and partial reverse (b) transformations, as well as during forward and reverse transformation sub-loops (c and d).

3.7.2 Hysteresis Effects during Partial Transformation Cycles

Macroscopic Hysteresis Effects

The macroscopic hysteresis behaviour during partial forward and partial reverse transformation cycles has been characterized by electrical resistance measurements, from which the evolution of the transformed volume fraction has been established. Figure 3.20 shows examples of partial transformation cycles as measured in alloy 2A.

The results show that when a forward transformation was interrupted at various temperatures between M_s and M_f during cooling, the subsequent partial reverse transformation cycle was always completed precisely at A_f, irrespective of the amount of martensite formed during cooling (figure 3.20a). Correspondingly, when a fully martensitic specimen was heated to various temperatures below A_f and there cooled to M_f, the formation of martensite during the partial cooling cycle was always completed at M_f, irrespective of the amount of austenite formed at the reverse point (figure 3.20b). This behaviour has been found to be quite systematic, and is in accordance with results which have been reported in literature by Cornelis and Wayman (1976) as well as by Zhongguo and Dazhi (1988).

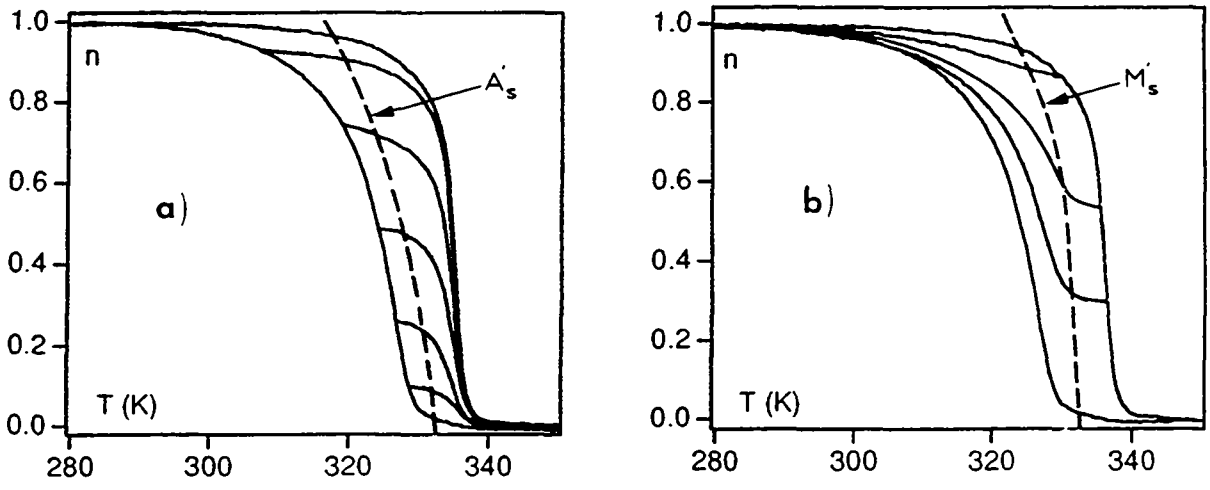

Figure 3.20: Partial reverse and forward transformation cycles (a and b, respectively) as observed in alloy 2A. A_S' and M_S' are the transformation start temperatures.

The transformation paths inside the overall hysteresis resulting from partial transformations are characterized by a transition from a small $n(T)$ slope to a drastic increase of this slope. In accordance with Cornelis and Wayman (1976), martensite start temperatures (M_S') for the partial forward as well as austenite start temperatures (A_S') for the partial reverse transformations have been defined. In figure 3.20 they are plotted by a dashed line, where each point corresponds to a 10% change in the transformed volume fraction, with respect to the volume fraction that was transformed at the beginning of a given partial cycle. One can see that the transformed volume changes already before the M_S' (A_S') temperature is reached. This observation does not agree with the results published by Cornelis et al. (1976), which indicated a temperature interval at the beginning of a partial cycle, where the transformed volume did not change; during a partial forward (reverse) transformation cycle no transformation was observed provided that the extend of cooling (heating) was limited to the M_S' (A_S') temperature.

The discrepancy of the present results and the results of Cornelis et al. (1976) might be related to the resolution of the transformed volume fraction that is associated with the accuracy of electrical resistance (R) measurements. The resolution of R is generally not better than1 $\mu\Omega$, even not in more sophisticated methods, as for example the method developed by Amengual et al. (1989). Since the electrical resistivity in Cu-Zn-Al alloys is relatively low ($\rho \approx 10\ \mu\Omega$ cm) the variations of R, especially in the beginning of partial cycles are small (2 $\mu\Omega$/K), as is shown by the experimental curves of figure 3.21a. This variation is smaller than the $R(T)$ slope that is measured when no transformation takes place ($dR/dT = 4\ \mu\Omega$/K). If the difference of both slopes is due to transformation, a transformation hysteresis should be measured when the temperature rate is reversed. However, as figure 3.21b shows, the measured curve can be the

same during forward and reverse transformation, but can at the same time represent two different *R(T)* curves, having a thermal hysteresis of at least 0.5 K. Since this hysteresis effect is larger than the temperature hysteresis that was measured for the motion of single martensite-austenite interfaces (Lovey et al., 1990), transformation processes with a very small thermal hysteresis are not detectable by means of conventional electrical resistance measurements. Therefore, small changes of the transformed volume fraction can be assumed in the beginning of partial transformation cycles. This result will be confirmed by the IF behaviour that has been measured simultaneously during partial transformation cycles.

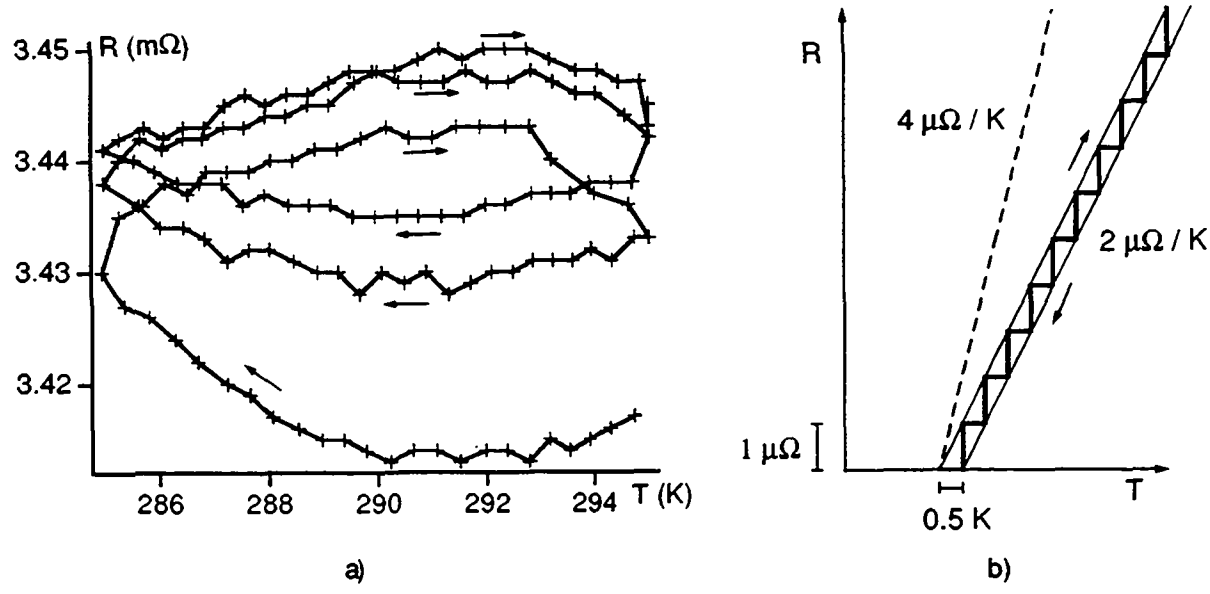

Figure 3.21: a) Typical variation of the electrical resistance (*R*) during transformation sub-loops. b) The limit of thermal hysteresis resolution is 0.5 K, if the *R*-variation is 2 μΩ/K and the resolution of *R* is not better than 1 μΩ.

The Internal Friction (IF) Behaviour during Partial Temperature Cycles

The IF behaviour that was measured during partial transformation cycles is illustrated in figure 3.22. It shows that Q^{-1} drops drastically at the reversion points but increases immediately after passing through the minimum. This indicates that a strictly hysteretic behaviour does not exist, at least not in a microscopic scale. In other words, after reversing the temperature rate there is not a fixed temperature interval in which the microstructure of the material does not change at all. Furthermore, as the analysis of the IF behaviour will show, the values of $Q^{-1}{}_{Tr}$ can be explained by the transformation rate and the constants k_I and k_{II} that were found during complete transformation cycles. Therefore, one must conclude that *partial temperature cycles are always accompanied by changes in the transformed volume fraction.*

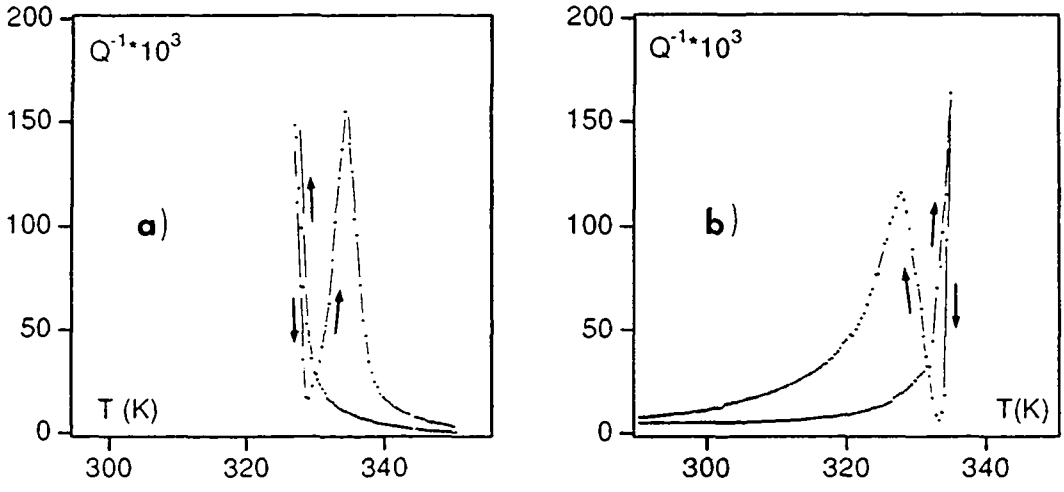

Figure 3.22: Evolution of the internal friction (Q^{-1}) during a partial forward (a) and a partial reverse transformation cycle (b), corresponding to the cycles of figure 3.20.

3.7.3 The Stability of Transformation Sub-Loops during Partial Temperature and Stress Cycling

Partial Temperature Cycling (PTC)

Figures 3.23 and 3.24 show examples of transformation sub-loops that were formed during *partial temperature cycling (PTC)* in alloy 1 (coarse grains) and alloy 2 (fine grains). The cycles were performed within a fixed temperature interval of 10 K and repeated 10 times. Figure 3.23a (alloy 1) shows the formation of forward transformation sub-loops. As can be seen, the volume fraction that is transformed during one sub-cycle depends on the site of the hysteresis where the transformation was stopped before cycling. At the end of the transformation ($n > 0.7$) small temperature cycles transformed less volume than when the transformation was stopped at $n = 0.5$. Subsequent transformation sub-loops are not well superimposed in both cycling programs but shift with increasing number of cycles. This observation indicates that *hysteresis instabilities occur during repetitive cycling* when starting from the main cooling curve. In comparison to this, reverse transformation sub-loops that were started from the main heating curve showed a smaller shift (figure 3.23b), indicating that less hysteresis instabilities occur in this case.

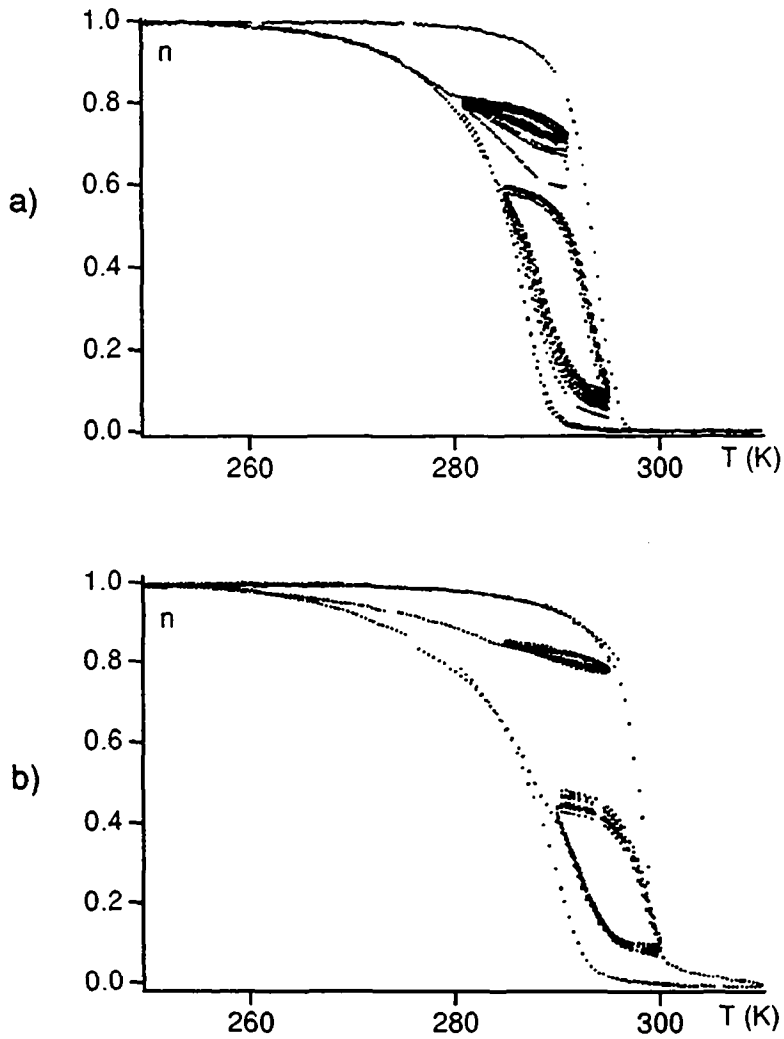

Figure 3.23: Formation of transformation sub-loops in alloy 1 during repetitive partial temperature cycling (PTC) starting from the main cooling (a) and the main heating branch (b).

Figure 3.24 illustrates, on an enlarged scale, the effect of hysteresis instabilities during repetitive partial temperature cycles in alloy 2. In this alloy, the shift of sub-loops to higher transformed volume fractions occurred during repetitive transformation cycles that started from both the cooling and heating branches of the main hysteresis curve.

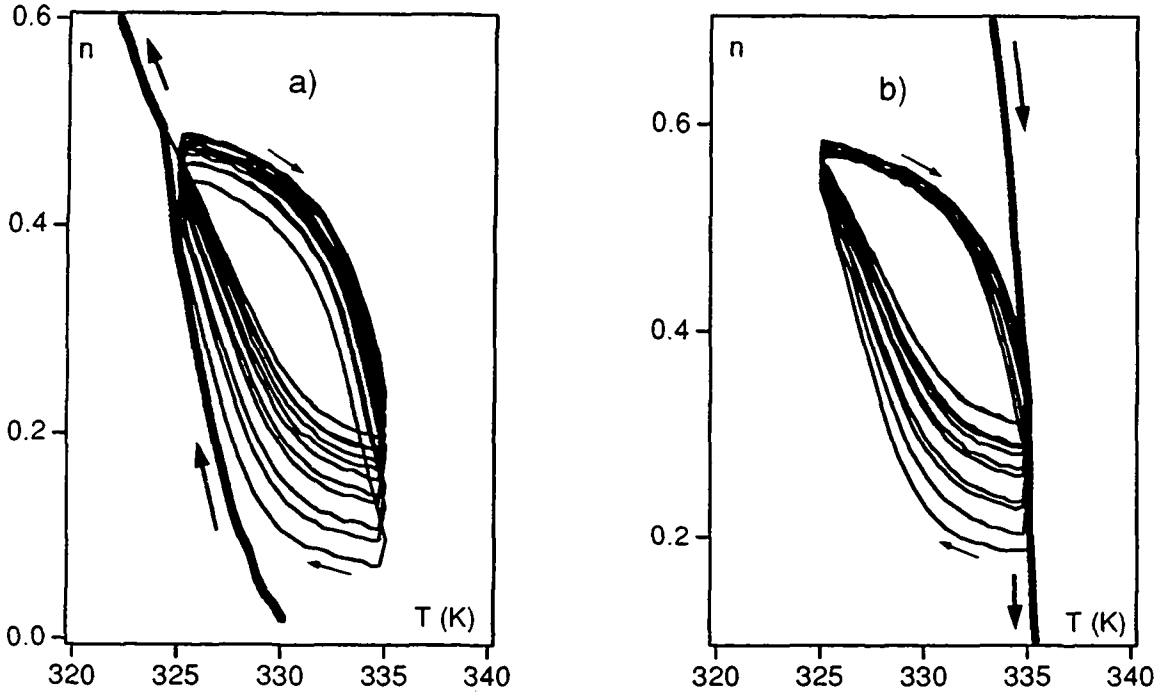

Figure 3.24: Formation of transformation sub-loops in alloy 2 during repetitive partial temperature cycling (PTC) starting (a) from the main cooling curve, and (b) from the main heating curve of the hysteresis.

Figure 3.25 shows the Q^{-1}- and f-behaviour during PTC programs in alloy 1, after the forward transformation was stopped at four different sites on the R-hysteresis curve. The Q^{-1}- and f-curves corresponding to the PTC programs b) - d) are displaced to the right hand side with respect to the cycling program in figure a). Strong variations of Q^{-1} and f can be observed during all cycling experiments and can be described by *"butterfly" shaped Q^{-1}- and f-curves.* As can be see from the R-curves, the increase (decrease) of the internal friction (frequency) is dependent on the volume fraction which is transformed during one small temperature cycle.

The influence of a two-way shape memory training on the stability of small transformation cycles could be studied in alloy 2. The cycling behaviour of both untrained and trained specimens (alloy 2A and 2B, respectively) has been compared by using PTC's around M_f, after the specimens were cooled from the austenitic state. Figure 3.26 shows the evolutions of R, f and Q^{-1} during this cycling program. The f-curves are shifted with respect to the Q^{-1}-curves, and one can see that the behaviour of f and Q^{-1} in alloys 2A and 2B is qualitatively the same as for alloy 1 (figure 3.25). However, the observed instabilities of the f- and Q^{-1}-evolutions are very much smaller in the trained than in the untrained specimen (figure 3.26b).

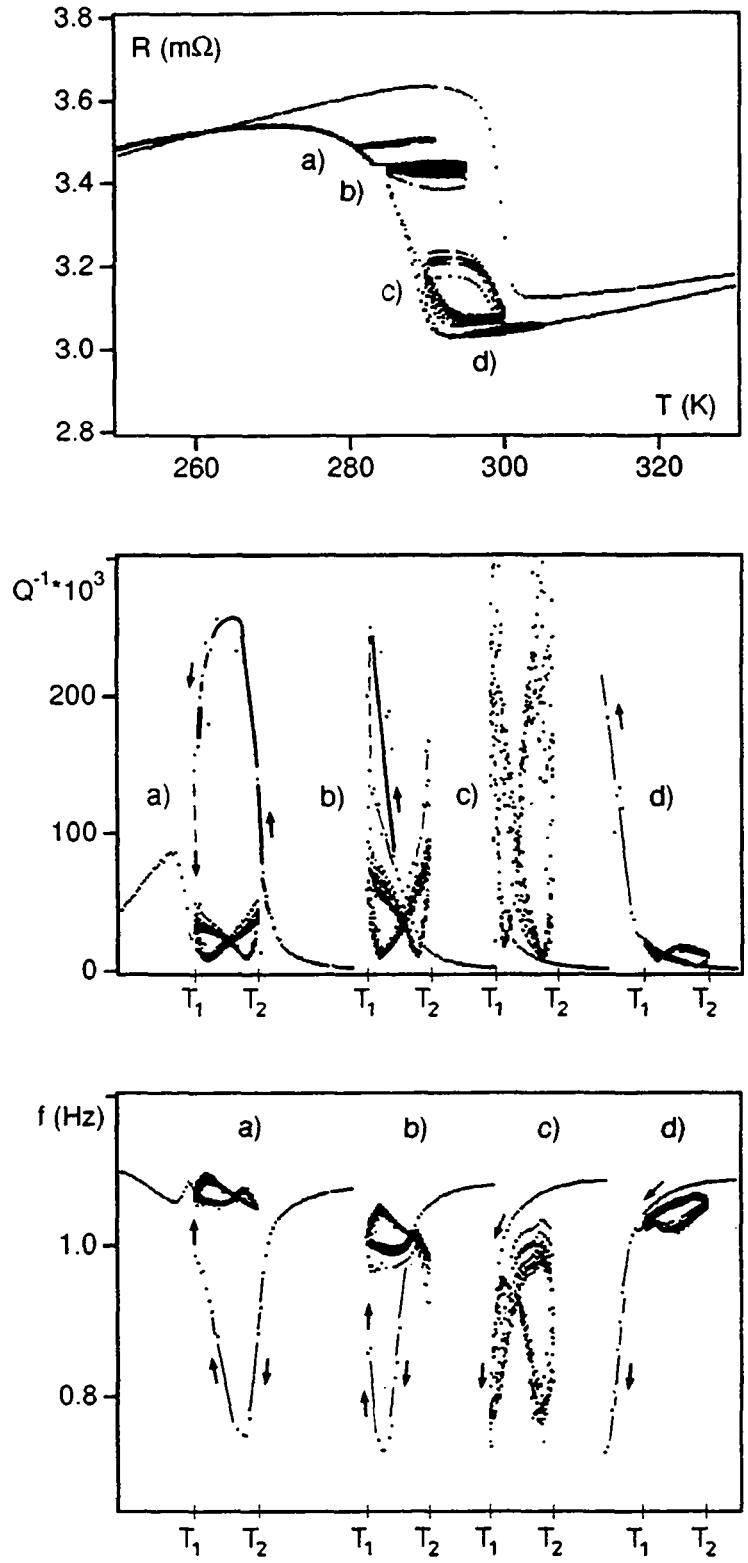

Figure 3.25: Internal friction (Q^{-1}) and resonance frequency (f) during partial temperature cycling in alloy 1.

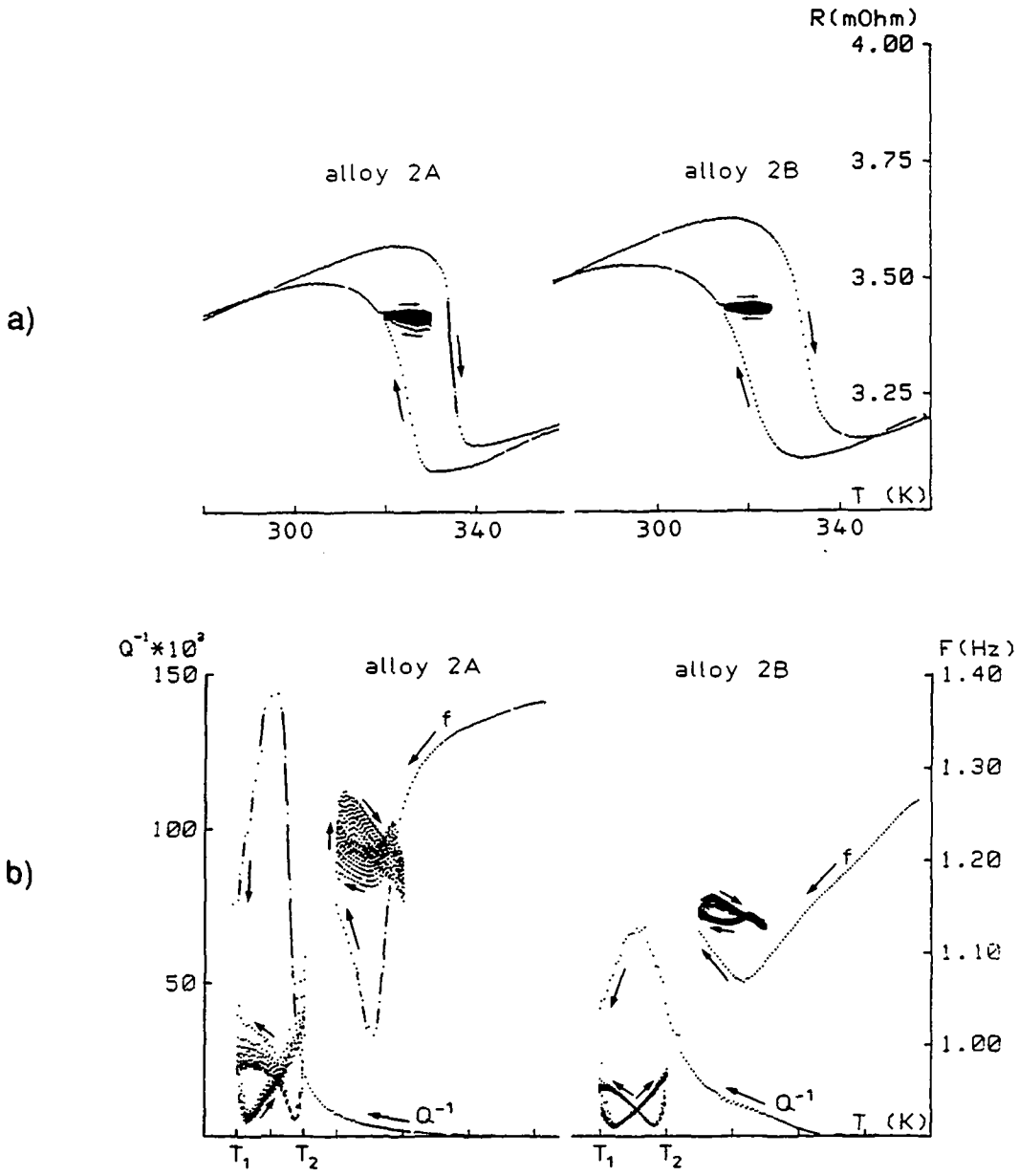

Figure 3.26: Electrical resistance (R), internal friction (Q^{-1}) and resonance frequency (f) during partial temperature cycling in alloys 2A (not trained) and 2B (trained).

The instability of transformation sub-cycles has been further investigated by the temporal evolution of n and Q^{-1} during the cycling programs. Figure 3.27 shows two examples of PTC behaviours observed in alloys 1 (M_s = 290 K) and alloy 3 (M_s = 200 K). It can be seen that in both alloys the upper value of n (corresponding to the end of the cooling part of the sub-loop) increases slightly while the lower n-value (corresponding to the end of the heating part of the sub-loop) increases significantly. The resulting amount of transformed volume per sub-loop

(Δn_{sub}) decreases progressively in the course of the PTC-programs. These results indicate that the transformation temperature (M_S) has no influence on the appearance of hysteresis instabilities. When the cycling program is left by further cooling, the *effect of a "micromemory"* has been observed, as is indicated by arrows in figure 3.27. The micromemory is characterized by a discontinuous change of the slope in the $n(t)$ curve as well as by a local Q^{-1}-minimum corresponding to a local f-maximum.

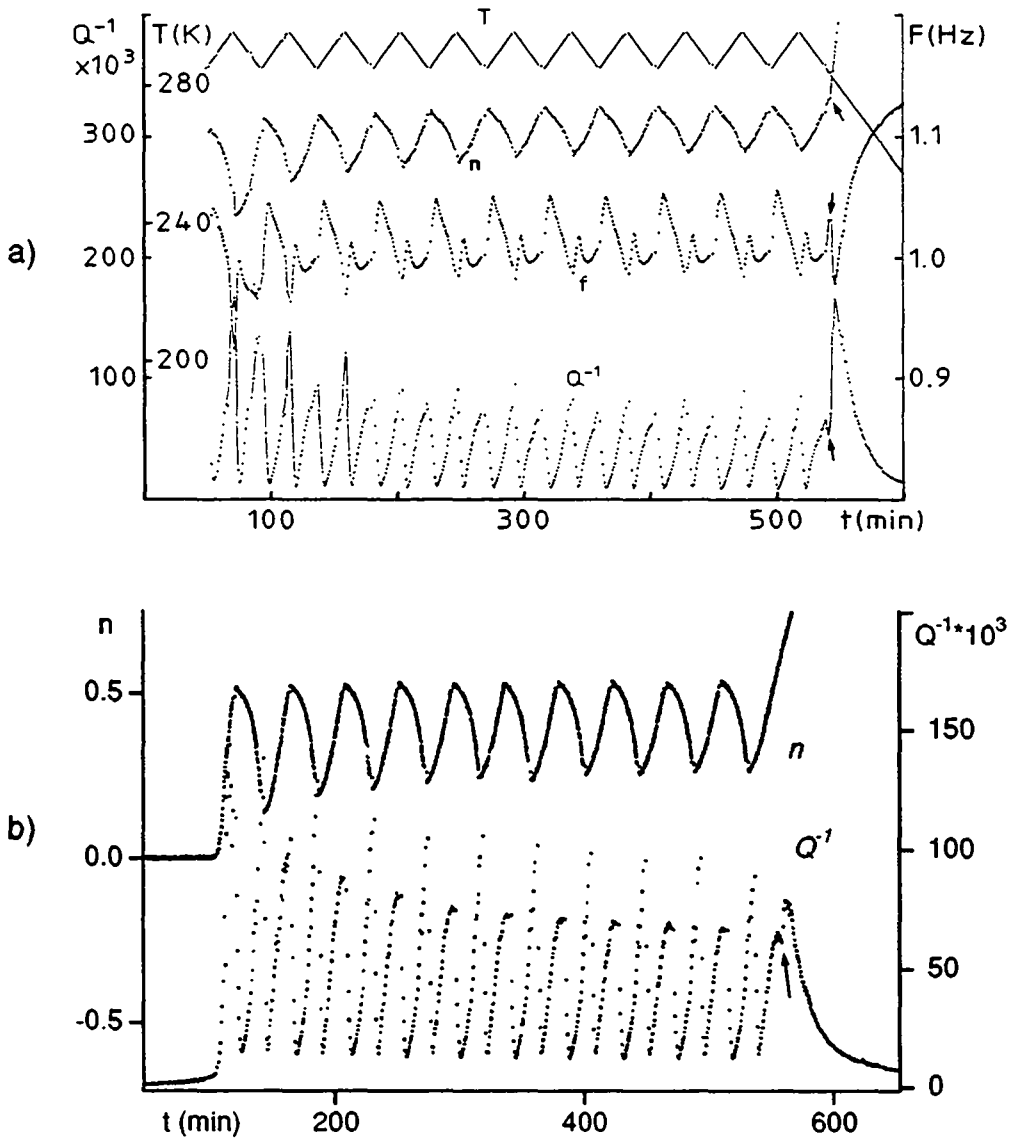

Figure 3.27: Temporal evolution of T, n, Q^{-1} and f during PTC:
a) alloy 1 (285 K < T < 295K), and b) alloy 3 (200 K < T < 210K).

The Micromemory Effect

The micromemory effect which arises at the moment when the cycling program is quit in order to proceed with the forward transformation (figure 3.27), has been found in all of the studied alloys. Further investigations showed that *the micromemory has not a permanent character.* That means if the micromemory temperature is passed by 2 K or 3 K on cooling, and the temperature rate is subsequently reversed, no irregularity is found in the heating curves of Q^{-1} and f. This indicates that the hysteresis instabilities are not associated with the production of defects (vacancies, dislocations) that could influence the further motion of transforming interfaces. This argument is supported by both observations that Q^{-1} and f join the main transformation curves if the micromemory is passed during further transformation (figure 3.28) and that the transformation temperatures of subsequent complete cycles do not change as compared to those cycles, which were conducted before PTC.

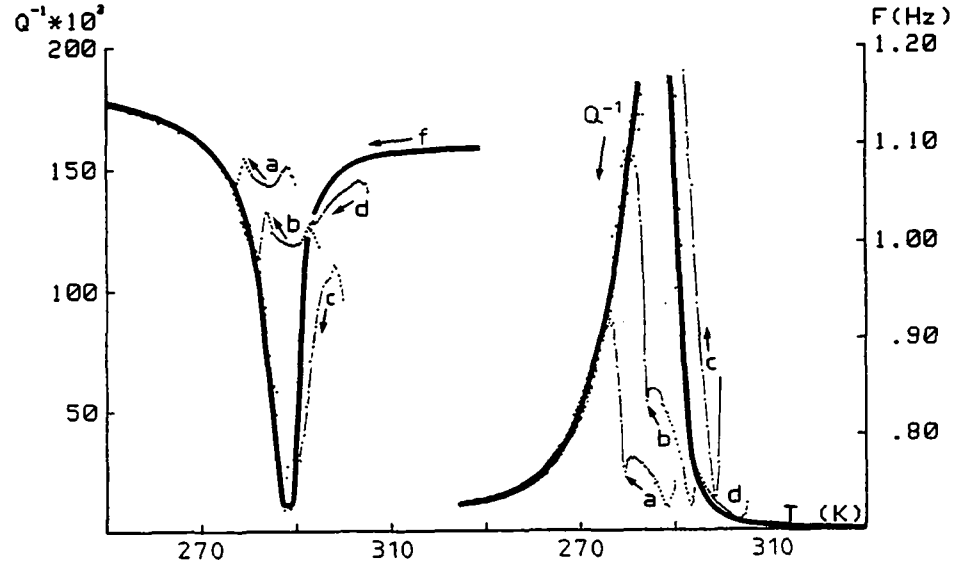

Figure 3.28: Q^{-1} and f during the cooling cycle after the PTC-programs a) - d) of figure 3.25. The main cooling curves are represented by thick lines.

PTC has also been performed in a differential scanning calorimeter (DSC). Figure 3.29 shows cooling curves of the measured differential heat after different numbers N_{cycle} of partial thermal cycles between T_1 and T_2. It can be seen that the amount of the released heat during one cycle is decreasing with increasing number of cycles and that a micromemory is also found in the differential heat when continuing the transformation after cycling. This is indicated by a local minimum at the lower cycling temperature T_2. It is important to note that after passing the

minimum at T_2 all curves attain exactly the cooling curve that was measured during a complete transformation ($N_{cycle} = 0$).

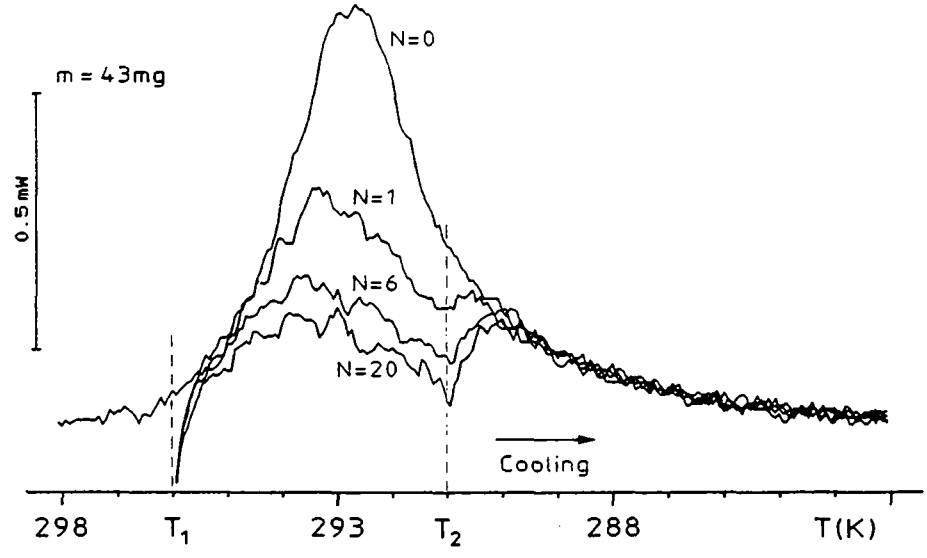

Figure 3.29: The differential heat during calorimetric runs after *N* partial cycles (alloy 1).

Partial Stress Cycling (PSC)

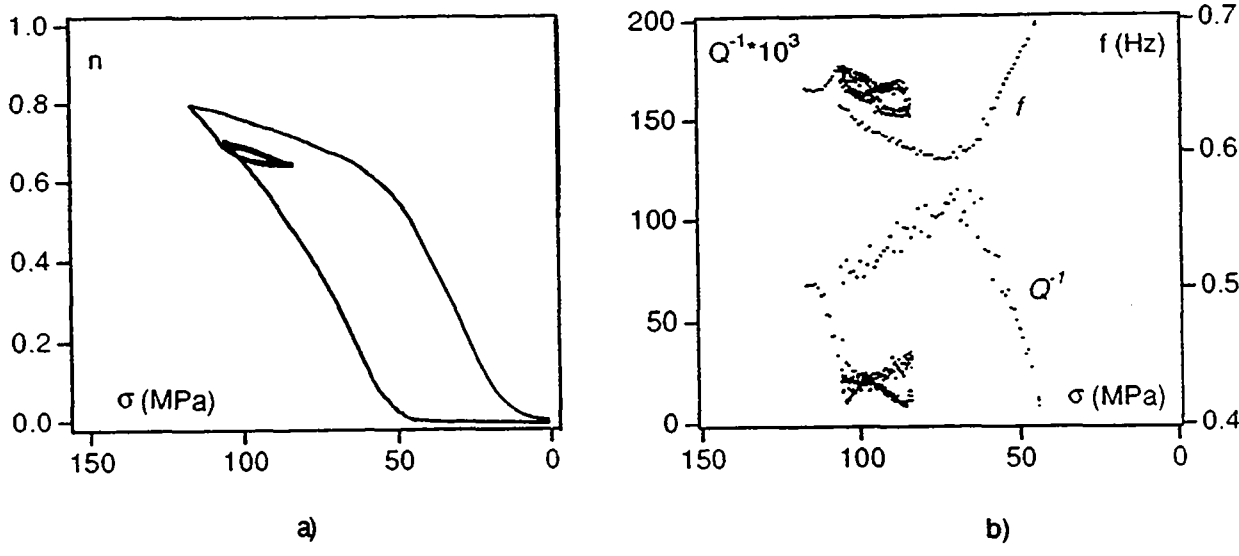

Figure 3.30: Formation of forward transformation sub-loops during repetitive partial stress cycling (PSC) in alloy 2A. a) Transformed volume fraction (n) as a function of stress (σ), b) Internal friction (Q^{-1}) and resonance frequency (f).

Sub-loop formation during stress-induced transformations has been studied by *partial stress cycling (PSC)* experiments performed with specimens of alloy 2A. As an example, figure 3.30 presents sub-loops obtained when the forward transformation was interrupted during loading. 10 small unloading/loading cycles have been conducted with a stress amplitude of 15 MPa. In comparison to partial temperature cycling, the hysteresis sub-loops formed during stress-induced transformation do not shift with increasing number of cycles and the internal friction behaviour is characterized by stable "butterfly" shaped curves of both the Q^{-1}- and f-curves (figure 3.30b).

3.7.4 Analysis of the Partial Transformation Cycling Behaviour

Macroscopic Hysteresis Effects

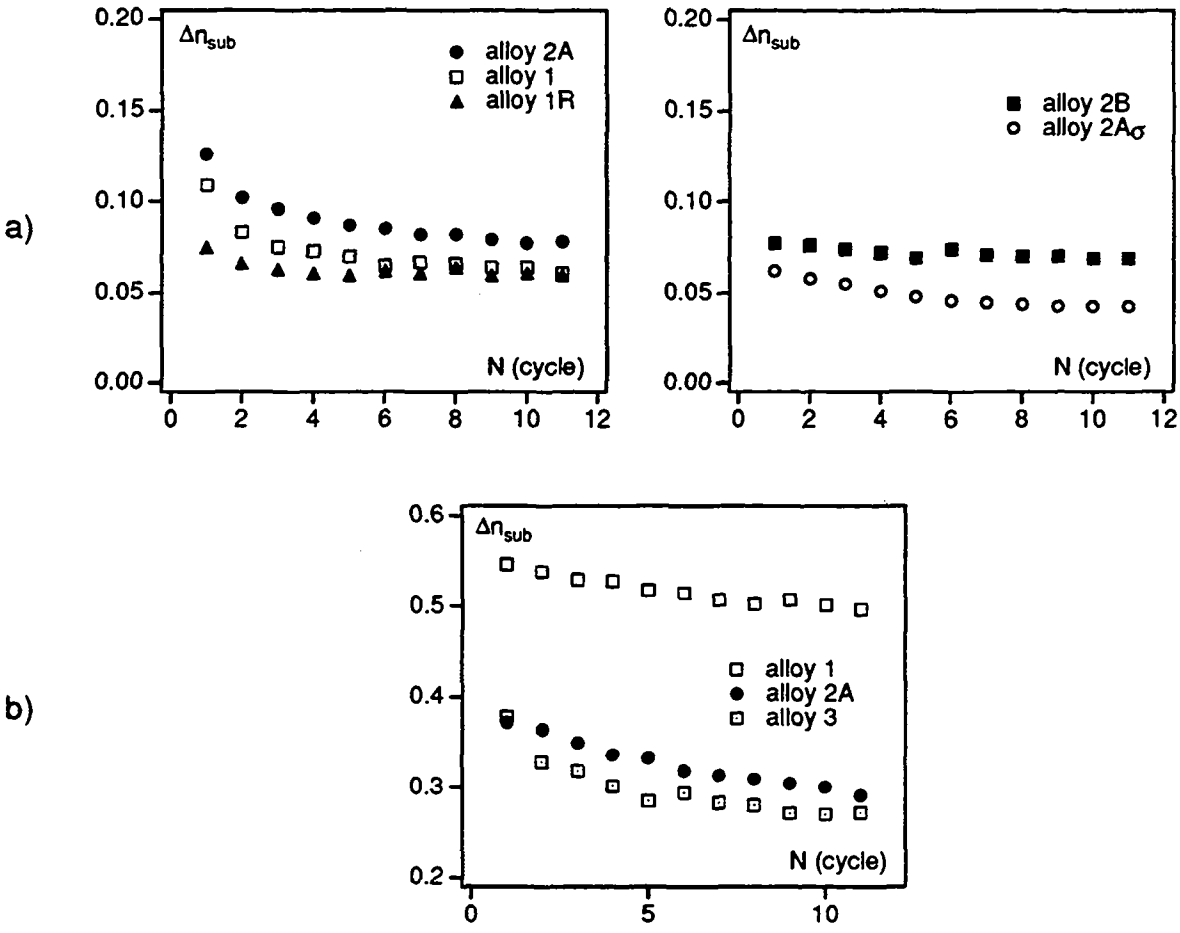

Figure 3.31: Transformed volume fraction per sub-cycle (Δn_{sub}) as a function of the cycle number (N_{cyle}). The cycles were started at $n \approx 0.75$ (a) and at $n \approx 0.50$ (b), in alloy 1 (coarse grains), alloy 2 (fine grains), alloy 2B (trained specimen) and alloy 3 (M_S = 200 K).

A comparison of the stability of transformation sub-loops studied in all the present alloys is shown in figure 3.31, where the amount of transformed volume fraction per sub-loop (Δn_{sub}) has been plotted as a function of the number of cycles (N_{cycle}). Figure 3.31a represents results of PTC and PSC programs that were started when the specimen was primarily in the martensitic state ($n \approx 0.75$) before cooling or heating was stopped. In figure 3.31b PTC programs have been conducted on specimens that contained equal portions of austenite and martensite ($n \approx 0.5$). The results show that the most intense hysteresis instabilities are observed for the *forward* transformation sub-loops in alloys 1 and 2A. On the other hand, PTC forming *reverse* transformation sub-loops appears to reduce the hysteresis instabilities, see Δn_{sub} (N_{cycle}) curve of alloy 1R. Alloys 2B and $2A_\sigma$, which form educated and stress-induced martensite show a relatively stable transformation sub-loop behaviour. Hysteresis instabilities are also observed during PTC at low temperatures in alloy 3 (M_S = 200 K). This suggests that the incomplete transformation behaviour in Cu-Zn-Al alloys is not significantly affected by the transformation temperature.

Internal Friction Behaviour

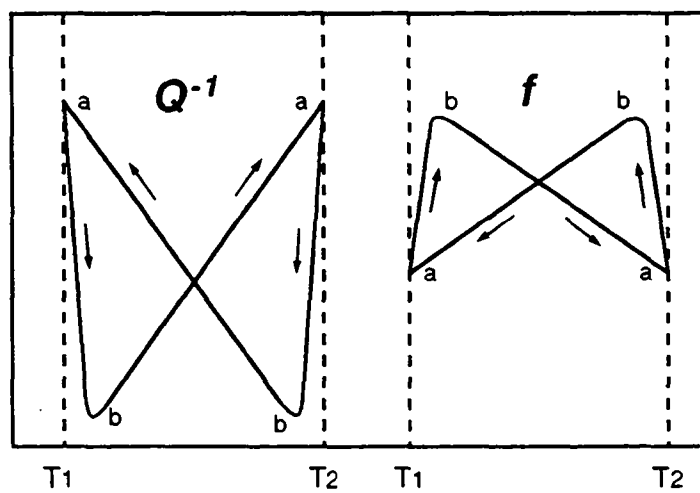

Figure 3.32: Schematic of the "butterfly" shaped curves of Q^{-1} and f obtained during the formation of a transformation sub-loop.

The results of the IF behaviour during incomplete transformation cycles have shown that PTC and PSC cause "butterfly" shaped curves of f and Q^{-1}. This behaviour is schematically represented in figure 3.32 for one partial cycle or transformation sub-loop. Qualitatively, the origin of the butterfly curves can be explained as follows: When the sign of $\dot{T}$ or $\dot{\sigma}$ is reversed at points "a", Q^{-1} decreases rapidly to a minimum while f increases to a maximum at the beginning

of the subsequent partial cycle (points "*b*"). Points "*b*" describe the situation, where the rate of the external driving force goes to zero in the specimen ($\dot{T} = 0$ or $\dot{\sigma} = 0$). The drastic decrease of Q^{-1} is therefore due to the $\dot{T}$- or $\dot{\sigma}$-effect. This indicates that during a partial transformation cycle the most important IF contribution stems from the transient part (Q^{-1}_{Tr}), since the "static" contribution is very low for the case when the transformation rate is zero. When transformation restarts, Q^{-1} increases (f decreases) until the sign of $\dot{T}$ or $\dot{\sigma}$ is again reversed (points "a").

To a first approximation, Q^{-1}(point b) can be seen as the isothermal contribution ($Q^{-1}(\dot{T} = 0)$) or constant-stress contribution ($Q^{-1}(\dot{\sigma} = 0)$) to Q^{-1}(point a). Q^{-1}_{Tr} (point a) corresponds to the difference between Q^{-1}(point a) and Q^{-1}(point b). The quantitative analysis of Q^{-1}_{Tr}(a) as a function of the number of partial cycles (N_{cycle}) should give information about possible microstructural changes which occur in the course of a particular cycling program.

This analysis will be conducted in terms of the established equations (3.24), which correlate the transient part of IF (Q^{-1}_{Tr}) with the volume fraction that is transformed during one oscillation (Δn):

$$K = \frac{1}{\dot{T}} \int_{T_1}^{T_2} Q_{Tr}^{-1} f \, dT = k \int_{n_1}^{n_2} dn \qquad (3.32)$$

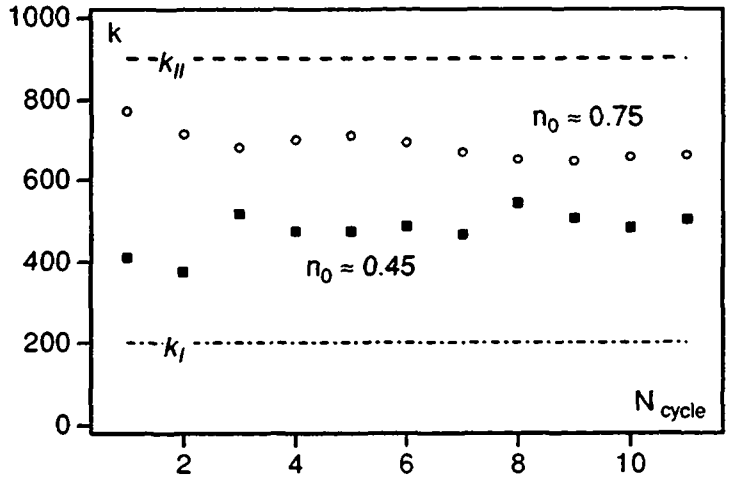

Figure 3.33: Evolution of the internal friction represented by the constant k as a function of the cycle number (N_{cycle}).

In alloy 1, K has been determined for the forward transformation sub-cycles of the PTC programs b) and c) of figure 3.25. The value of the proportionality constant of equation (3.32), k, has been calculated for each sub-cycle and is plotted in figure 3.33 as a function of the

number of sub-cycles (N_{cycle}). It can be compared to the k-values that were observed during a complete transformation (k_I and k_{II}). As it can be seen the k-values of partial transformation cycles are contained in the borders given by the k-values of a complete transformation cycle. Therefore, the contribution to the IF in a given transformation interval ($n_1 < n < n_2$) does not change significantly compared to complete transformations. During small transformation cycles the measured IF values are also higher at the end of the transformation than in the beginning.

The Micromemory Effect

Figure 3.34 shows the temperature region of the micromemory that arises at the moment when the cycling program is quit in order to proceed with the transformation and which is characterized by a local minimum of the IF (Q^{-1}) and a change of the transformation slope ($n(T)$). The measured IF has been analyzed in the temperature region of the micromemory. Special emphasis has been given to the transition point where the overall hysteresis loop is joined after the cycling program is quit (see arrows in figure 3.34).

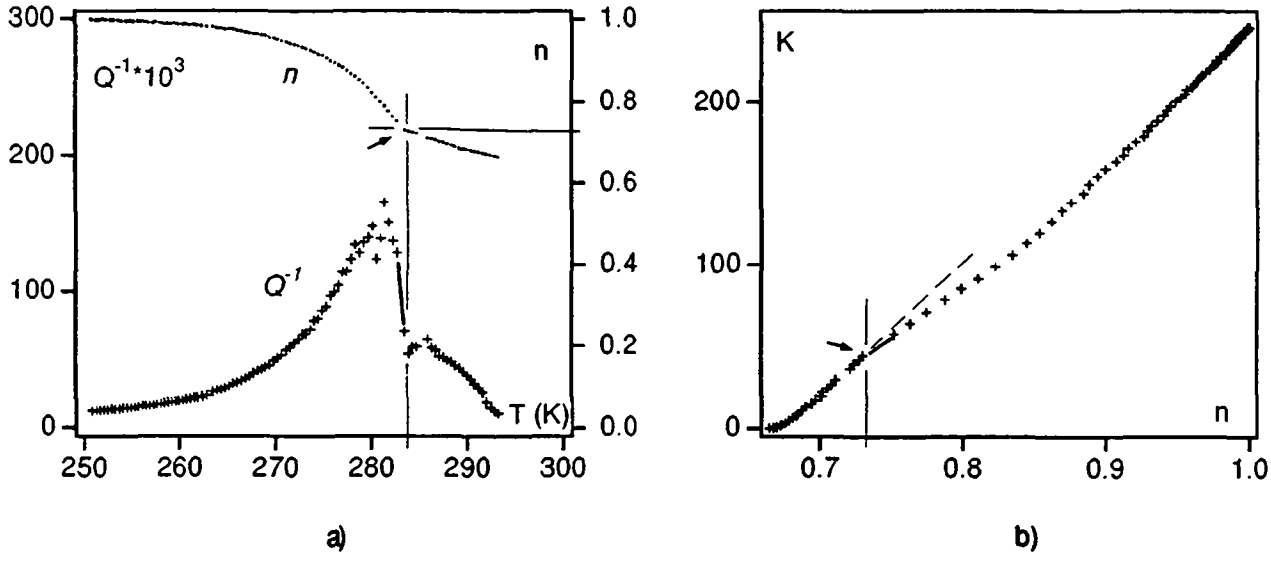

Figure 3.34: Analysis of the IF behaviour when the micromemory appears:
a) Q^{-1} and n as a function of T. b) The normalized IF (K) as a function of n.

The evaluation of K shows that a small change of the $K(n)$ slope exists at the micromemory point (figure 3.34b); the amount of IF per transformed volume fraction (equivalent with $K(n)$) decreases during the very next transformation after PTC, before it increases again at the end of the transformation. It can be concluded that during repetitive cycling the energy dissipation measured by IF decreases. This indicates that the additional contributions to the IF which arise

especially at the end of the transformation and which could be related to relaxation processes, decrease during repetitive local transformation cycling. The importance of relaxation processes for both the internal friction behaviour and the reported hysteresis instabilities will be subject for the discussion in chapter 6.

3.8 Conclusions

i) The goal of this chapter has been to study the transformation mechanisms in different Cu-Zn-Al polycrystalline alloys. The alloys, which are characterized by different grain sizes and thermomechanical histories, exhibit differences in the macroscopic hysteresis effects, the martensitic microstructures and the internal friction behaviour. The observed internal friction (IF) peaks are all characterized by a dominant transient part (Q^{-1}_{Tr}).

ii) The analysis of the IF peak has demonstrated that depending on the studied alloy, the transient IF (Q^{-1}_{Tr}) can not be completely explained by the transformed volume fraction per oscillation (Δn). The proportionality between Q^{-1}_{Tr} and Δn has only been observed during the formation of stress-induced martensite (specimen $2A_\sigma$) and educated martensite (specimen 2B). During thermally-induced transformations in non-educated specimens (alloys 1, 3 and 2A), different linear slopes in the Q^{-1}_{Tr} (Δn) have been found (k_I in the beginning and k_{II} at the end of the transformation). Since the k_{II}-values were always higher than the k_I-values it must be concluded that additional damping mechanisms operate at the end of martensitic transformations. In chapter 5, possible mechanisms like the reorientation between different martensitic variants and changes in the stacking sequence of individual variants, are studied by transmission electron microscopy.

iii) The "effective" transformation strain (ε^t_{eff}) that was deduced from the measured IF values, is significantly smaller than the macroscopic shear strain determined by static deformation experiments. This result implies that more information is needed about the nature of anelastic deformation during martensitic transformation. The IF study of single variant transformations which is presented in chapter 4, attempts to supply this information.

iv) During partial transformation cycles it was observed that the transformed volume fraction changes as soon as the reversion point is passed, without a significant temperature hysteresis. These observations are related to butterfly-like Q^{-1} and f curves which confirm the permanent changes in the transformed volume. Transformation sub-loops shift during partial temperature cycling, especially during spontaneous transformations. It was found that the transformed volume fraction per sub-loop decreases, while the volume fraction of martensite slightly increases. The IF analysis suggests that the dissipated energy per cycle decreases with increasing number of cycles. These hysteresis effects will be discussed in detail in chapter 6.

CHAPTER 4

The Hysteresis Effect during Single Variant Transformations in Cu-Zn-Al Single Crystals : Results and Discussion

This chapter is addressed to the investigation of the hysteresis effect that is associated with martensitic transformations where only one variant converts the parent phase into the product phase. The single variant system allows to characterize the energy dissipation which stems from the interaction of transforming interfaces with crystal defects, in the absence of interactions between differently oriented martensitic variants. Optical microscopy observations have shown that the macroscopic hysteresis effect that is involved in the movement of a single interface is very small (Lovey et al., 1990).

In this work, single variant transformations have been studied by means of internal friction (IF) measurements. The quantitative relationship between the macroscopic hysteresis effect (enclosed surface of the σ-ε curve) and the microscopic hysteresis effect (IF behaviour) has been established and the deformation system that is operating during the IF measurement has been identified by knowing the crystallographic relationships of the single variant system. The information of the exact nature of anelastic deformation and its hysteretic character is essential for developing a complete understanding of the IF behaviour that has been reported for Cu-Zn-Al alloys in chapter 3.

4.1 Theoretical Considerations

Since the preferential growth of only one single variant requires the application of an external stress, the conducted IF experiments consist of the simultaneous application of both an external tensile stress (σ_t) and an oscillating measuring stress (σ_m). The variations of σ_t govern the transformation of the martensitic variant and σ_m modifies, slightly, the resolved shear stress on the transforming interfaces. The resulting IF is a measure of the anelastic deformation that is produced when the interface moves in the direction of σ_m.

For quantitative interpretations of the IF, the component of σ_m which acts on the transforming interfaces, has to be calculated for the imposed torsion deformation. Therefore, this chapter starts with a theoretical analysis of the shear stress distribution which results from torsion deformation in different specimen geometries. Shear stress components have been calculated for those crystallographic systems where transformation deformation is presumed. This analysis is needed to define the crystallographic nature of anelastic deformation and to quantify the microscopic hysteresis effect that accompanies single variant transformations.

4.1.1 Deformation in Torsion Mode: Calculation of the Shear Stress Distribution

Standard Specimen Geometry

When a standard parallelepiped specimen (geometry A in figure 4.1) is subjected to a torsion moment (M_t), opposite shear stresses are created on all cutting planes in the specimen. Numerical calculations which have been done with the finite element program IDEAS, show that a symmetrical distribution of positive and negative shear stress components of τ_{xy} and τ_{yz} are obtained in the (xz) cutting plane (figure 4.2). In this case, an interface which traverses the specimen can not be displaced by the applied torsion moment without distorting the habit plane (figure 4.1b). The stresses acting on the interface rather would produce a wavy habit plane and, because this is not a very probable situation, only *"local" distortions of the interfaces are expected for the standard specimen geometry A.*

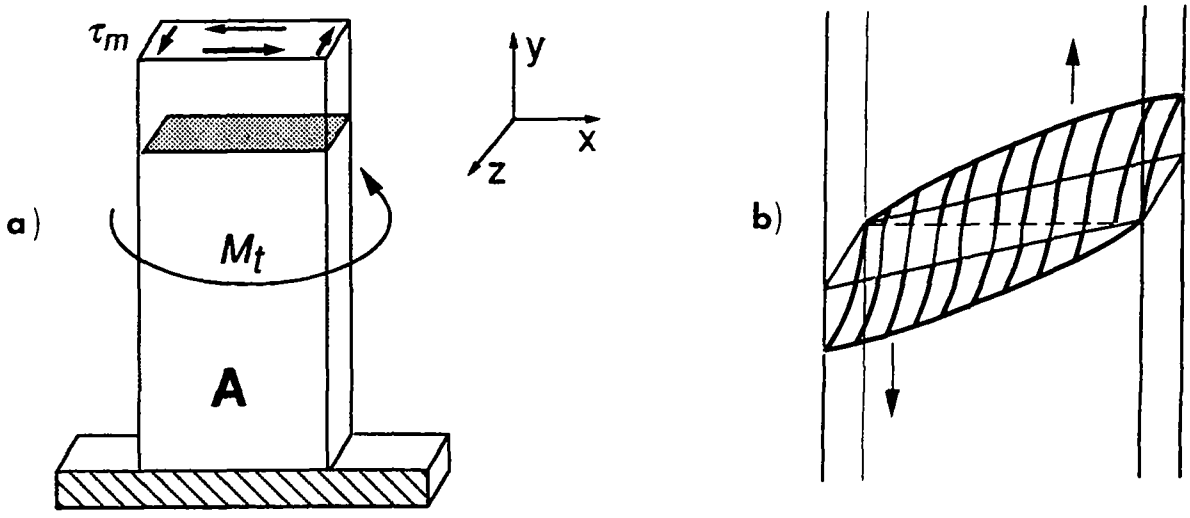

Figure 4.1: a) Distribution of τ_m during torsion in a parallelepiped specimen (geometry A).
b) "Theoretical" distortion of a transforming interface when the torsion moment (M_t) is applied to the standard specimen (geometry A).

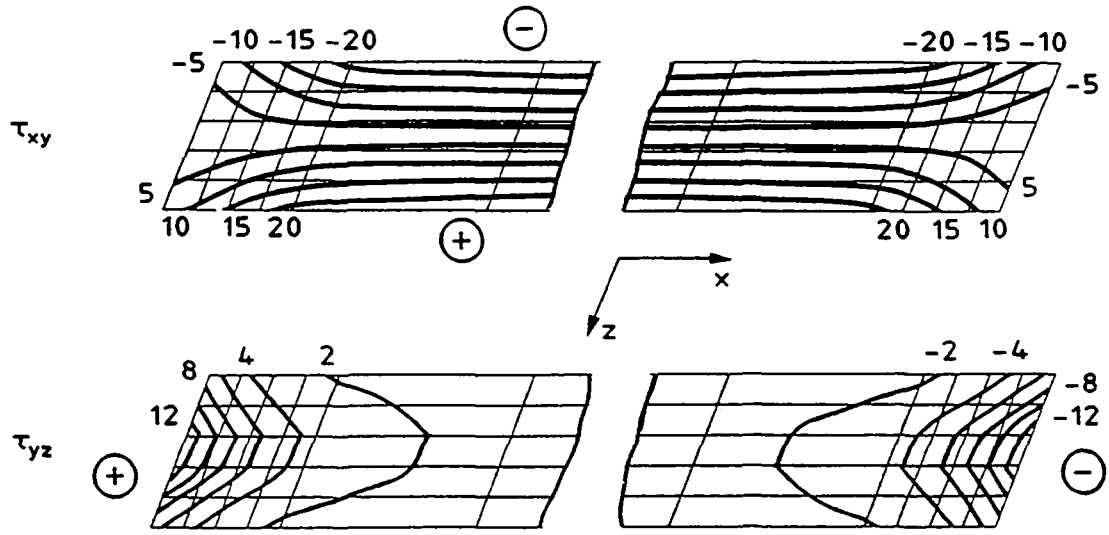

Figure 4.2: Symmetrical distribution of τ_{xy} and τ_{yz} (in MPa) during torsion in the hatched (*xz*) cutting plane of geometry A (figure 4.1a). Note that $\tau_{xy} = \tau_{yx}$.

The "Window" Specimen

An alternative specimen geometry has been proposed by Ahlers (1990). In this new specimen, a prepared "window" separates two small parallelepipeds (geometry B in figure 4.3). The stress analysis conducted for this specimen geometry shows a significant asymmetry for the shear stress component τ_{yz} in both parallelepipeds (figure 4.4). Since the stress component τ_{xy} is also symmetrically distributed, a net shear deformation in the *z*-direction results. In this case, the interfaces can be displaced while the habit plane remains undistorted (figure 4.3b). Therefore, *"global" interface displacements should be possible during IF measurement for specimen geometry B.*

However, there is one drawback to the specimen geometry B. The obtained shear effect with respect to the torsion effect is rather small, considering the absolute displacement of a small parallelepiped, which occurs during the imposed deformation. This is illustrated in figure 4.5, where the movement of a cross section in the *(xz)* plane is shown. The boundary conditions have been chosen in such a way that the lower part of the window specimen was blocked and the upper *(xz)* plane was rotated by the torsion angle that is imposed during IF measurements. Since the displacement of the parallelepiped in the *z*-direction is about 10 times larger than it is in the *x*-direction (figure 4.5), the pure shear deformation (γ_{yz}^{shear}) is expected to be 10 times larger than the pure torsion deformation ($\gamma_{yz}^{torsion}$). But, the finite element calculations show that the pure shear effect ($\gamma_{yz}^{shear} = 0.8 \cdot 10^{-4}$) is actually slightly smaller than the torsion effect ($\gamma_{yz}^{torsion} = \pm 1.2 \cdot 10^{-4}$), see also table 4.1.

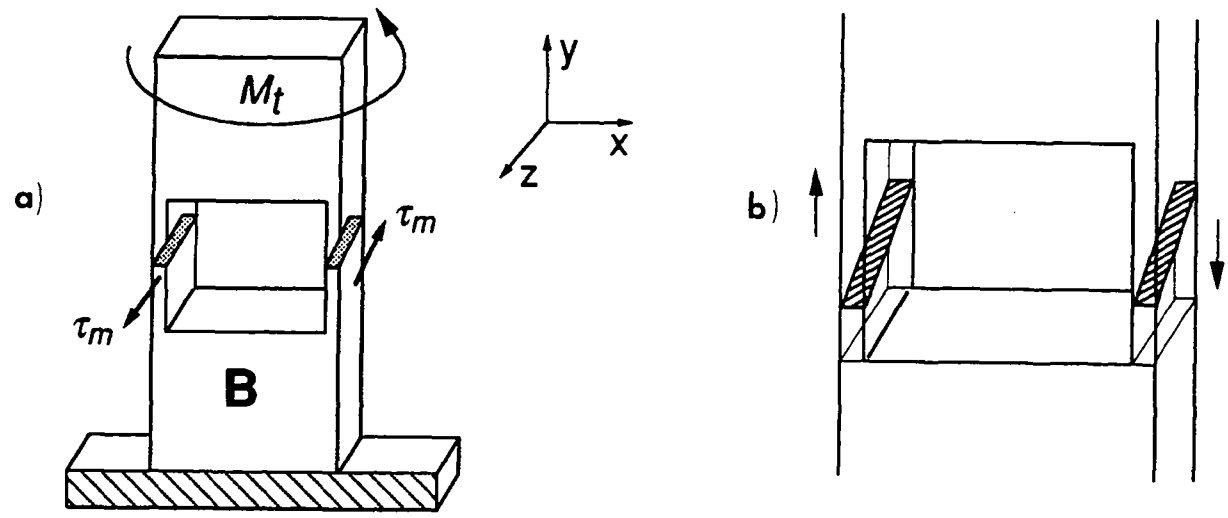

Figure 4.3: a) Distribution of τ_m during torsion in a "window" specimen (geometry B).
b) "Global" displacement of transforming interfaces in both parallelepipeds.

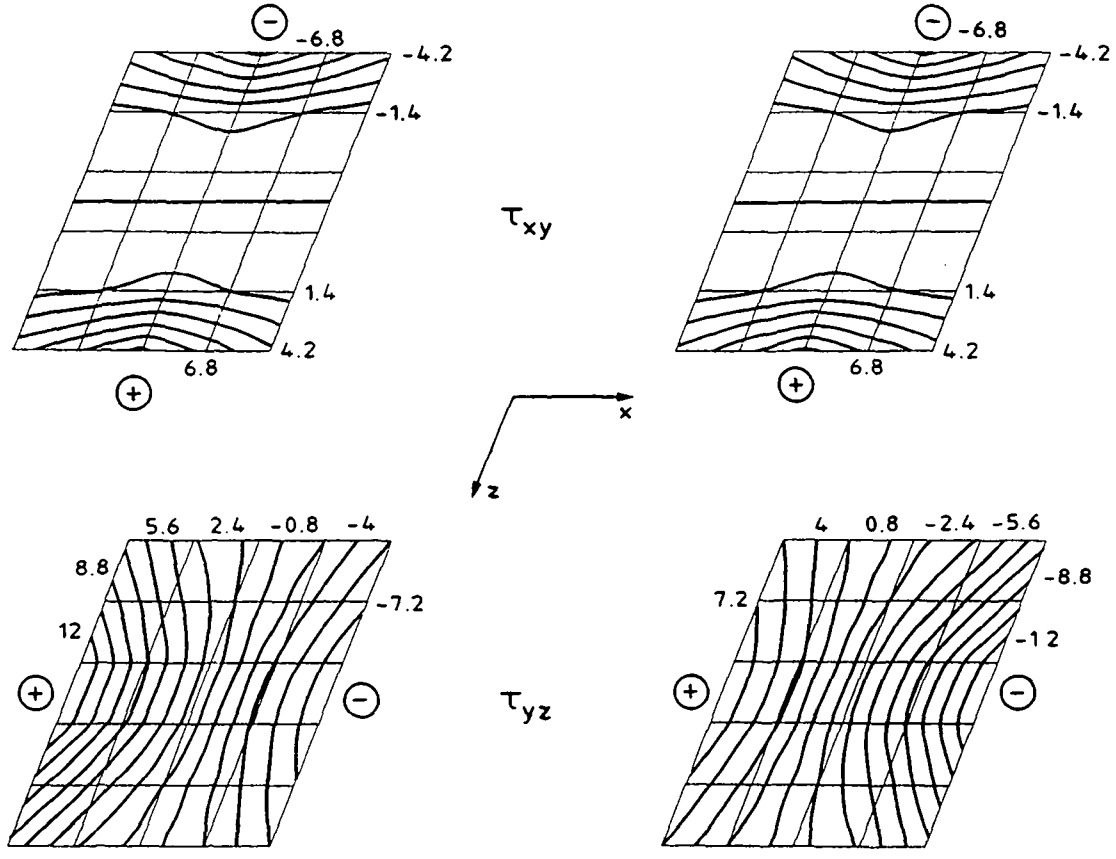

Figure 4.4: τ_{xy} and τ_{yz} (in MPa) during torsion in the hatched (xz) cutting plane of geometry B. Note that τ_{yz} is not symmetrically distributed and a net shear strain in the z-direction results.

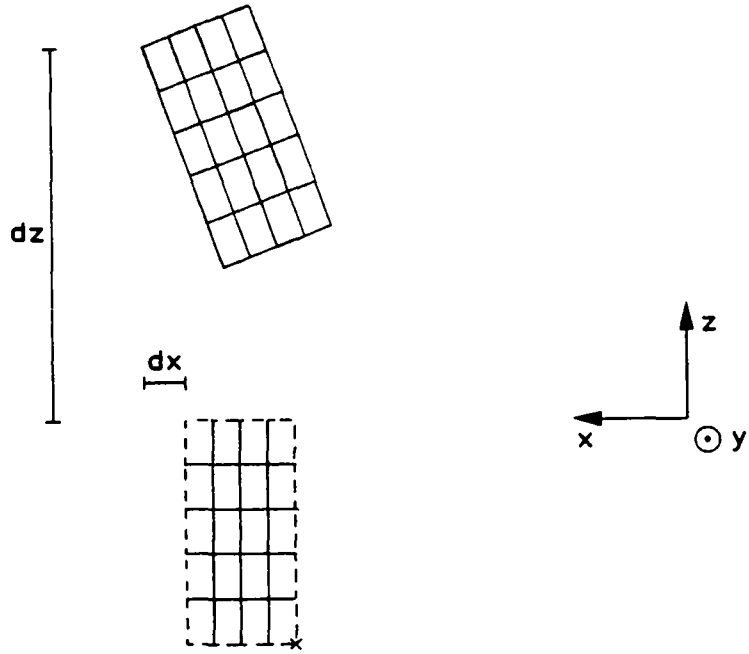

Figure 4.5: The movement of a (*xz*) cutting plane of the small parallelepiped during the imposed deformation.

Table 4.1: Results of the finite element calculations for the employed "window" specimen.

geometry	b = 0.4mm, c = 0.2mm, L = 3.5mm
nodal displacements	$dx = 8.5 \cdot 10^{-4}$mm, $dz = 8.7 \cdot 10^{-3}$mm
theoretical deformations	$\gamma_{yz}^{shear} = dz / L = 2.5 \cdot 10^{-3}$ $\gamma_{yz}^{torsion} = c / L \cdot \tan(2dx/b) = 2.4 \cdot 10^{-4}$
calculated deformations (IDEAS)	$\gamma_{yz} = 2.0 \cdot 10^{-4} / -1.2 \cdot 10^{-4}$ (max / min) $\rightarrow \gamma_{yz}^{shear} = 0.8 \cdot 10^{-4}$ $\rightarrow \gamma_{yz}^{torsion} = \pm 1.2 \cdot 10^{-4}$

The relatively small shear effect has to be associated with the bending deformation that is created in the parallelepipeds under the given boundary conditions. Because the lower part of the parallelepipeds is fixed by the massive part of the window specimen, the movement of the upper part of the parallelepiped is partially subjected to the case of a beam bending. This can be

followed in figure 4.6, where the deformed geometry of the parallelepiped is shown. The distribution of the bending stress (σ_y) and the shear stress component (τ_{yz}) in the (yz) plane demonstrates the importance of both the bending and shear effect for the displacement of the parallelepiped in the z-direction. From the theory of elasticity one knows that the portion of dz which is caused by the bending effect increases drastically with the length of the specimen (L), while the shear deformation is constant and independent of L (Timoshenko, 1963). In the present case, the bending deformation is 10 times larger than the shear deformation. This result explains why the pure shear deformation is small as compared to the torsion effect.

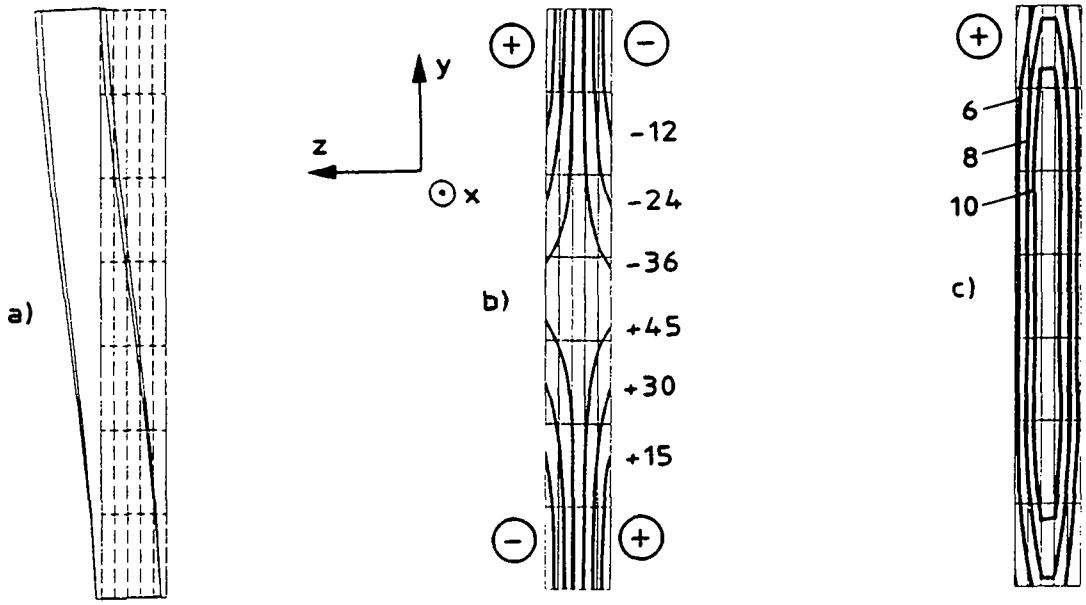

Figure 4.6: The deformation of the parallelepiped in the z-direction is mainly due to the bending stress (σ_y) and only partially due to the shear stress (τ_{yz}).

In spite of the relatively small shear effect that results during the imposed torsion deformation in the parallelepipeds, it is important to note that a net shear stress acts on the transforming interfaces and, in contrast to geometry A, this "window" specimen allows to measure the microscopic hysteresis that is involved in single variant transformations.

4.1.2 Orientation Dependence of the Resolved Shear Stresses in the Habit and Basal Plane Systems

The shear stress components that act in the principle deformation systems during the transformation have been calculated for both the habit plane and basal plane systems. As has been

shown in chapter 1, these systems are the crystallographic shear systems where the lattice distortion and the lattice invariant deformation occur during transformation.

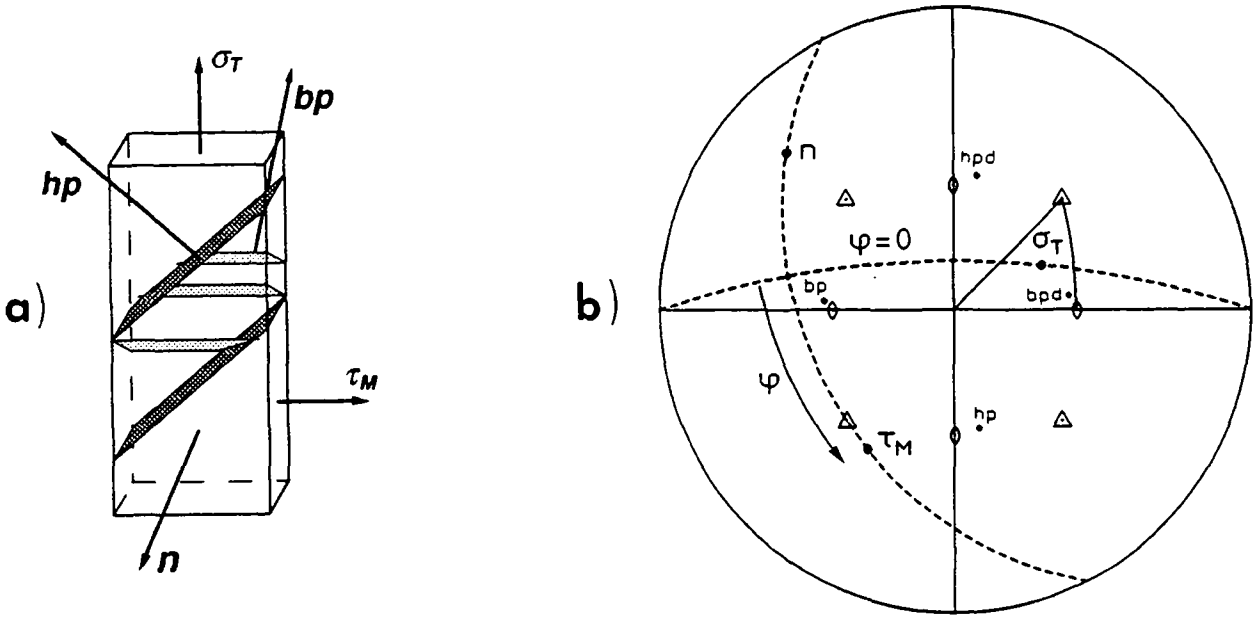

Figure 4.7: The orientation relationship between the specimen orientation (σ_T, τ_M and n) and the habit and basal plane normals of the transforming variant (*hp* and bp):
a) Schematic representation, b) Stereographic standard projection.

Figure 4.7a shows, schematically, the orientation relationship between the specimen geometry (given by tensile stress σ_t, measuring stress τ_m and surface normal n) and the habit and basal plane systems. The orientations of the habit plane normal *hp*, the basal plane normal *bp* and the shear directions in these planes, *hpd* and *bpd*, have been calculated using the phenomenological crystallographic theory that is described in chapter 1. Table 4.2 shows the results obtained when values of tetragonal distortion (ψ) and volume change (r) are used as input parameters for the present Cu-Zn-Al alloy. Apart from the habit plane normal and the shear vector in the habit plane the orientations of the three axes of the martensitic unit cell are expressed in terms of the cubic lattice vectors. The b-axis corresponds to the basal plane normal (*bp*) while the c-axis represents the shear direction in the basal plane (*bpd*). The orientations of the specimen geometry, as well as the habit and basal plane systems, have been transferred onto a standard stereographic projection, which is illustrated in figure 4.7b.

Table 4.2: Orientations of the habit and basal planes and their deformation directions calculated by using the phenomenological theory (as formulated in chapter 1). The volume change parameter (r, see definition in §1.2.3) corresponds to a zero volume change.

```
***** INPUT *****
Tetragonal distortion:   0.94
Volume change parameter: 1.259921
***** OUTPUT ****
Habit plane:   {0.672824, 0.144013, 0.72565}
Shear vecteur: {-0.739802, 0.130975, 0.659953}
Shear:  0.190084
a:  {0.995514, 0.0184183, 0.0928056}
b:  {-0.0808362, 0.6753, 0.7331}
c:  {-0.0491691, -0.737313, 0.673759}
```

The resolved shear stresses in the habit plane (τ_{hp}) and in the basal plane (τ_{bp}) have been determined for $\tau_m = \tau_{yz} = \tau_{zy}$ in the small parallelepipeds of geometry B. The results show that τ_{hp} and τ_{bp} are strongly dependent on the orientation of the lateral specimen surface (n) as is shown in figure 4.8. The angle φ represents the rotation of n, see the stereographic projection (figure 4.7b). The maximum values of τ_{hp} and τ_{bp} depend on the orientation of σ_t. The results of these calculations are needed for a systematic study of the orientation dependence of the IF, from which the importance of the respective deformation systems for the anelastic deformation can be determined.

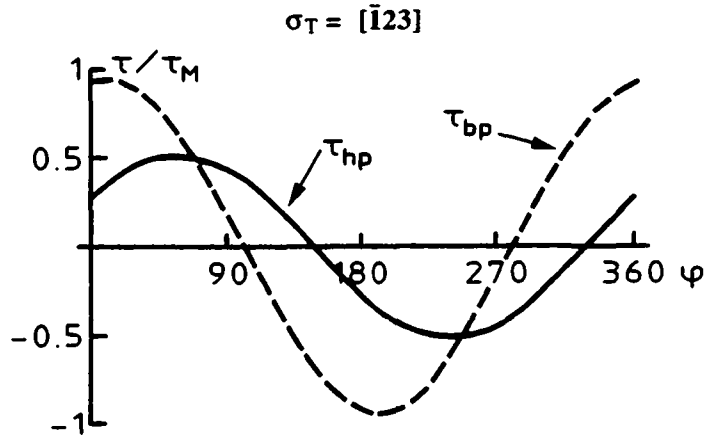

Figure 4.8: Variation of the habit and basal plane shear stress component (τ_{hp} and τ_{bp}) as a function of the rotation angle (φ) of n for a given σ_t orientation.

4.2 Specimens

Specimens with the designed geometries (A and B) and orientations have been cut by electro-erosion from a Cu -13.5 Zn -17.3 Al single crystal (M_S = 285 K). The surface of the specimens have been mechanically polished to a 1µm diamond paste and finally electrochemically polished in a 20% H_2SO_4 / Methanol solution at 290 K and 5 V. Figure 4.9 shows a specimen of geometry B that was used for IF measurements.

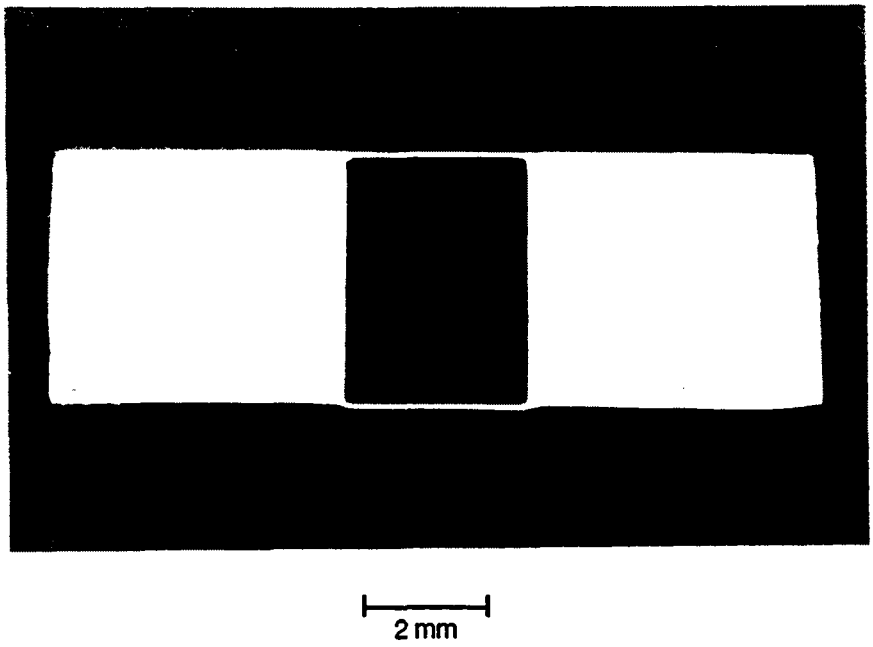

Figure 4.9: Optical micrograph showing a prepared IF specimen with geometry B.

4.3 Interface Displacement and Stress Distribution

4.3.1 IF and Specimen Geometry

Figure 4.10 shows a σ_t-ε curve that is typical for both types of specimen geometry. The influence of the specimen geometry on the displacement mode of the transforming interfaces ("global" and "local"), and therefore on the IF, is demonstrated in figure 4.11. The Q^{-1}-values of the standard geometry A (figure 4.11a) are very low compared to the Q^{-1}-values of the "window" specimen B (figure 4.11b). The registrated IF curve only shows a maximum during loading and unloading in the latter case. This IF maximum is associated with a minimum of the resonance frequency (f), as it is generally observed during martensitic phase transformation,

and the Q^{-1}-values of the martensitic single variant are significantly higher than those of the parent phase.

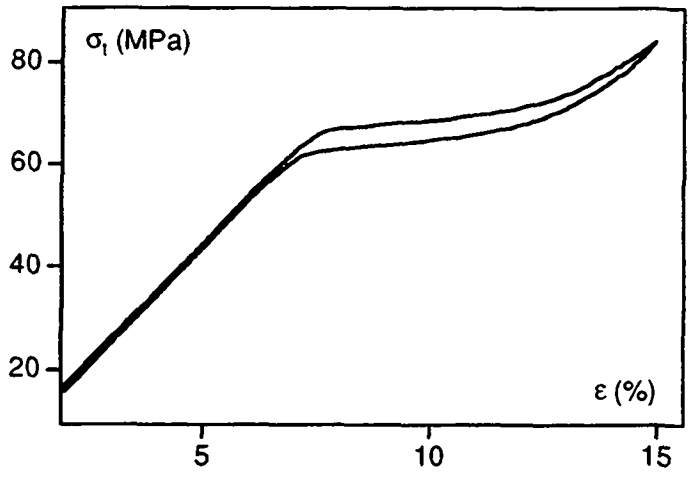

Figure 4.10: σ_t - ε curve measured at T = 317 K, $\dot{\sigma}_t$ = 0.6 MPa/min.

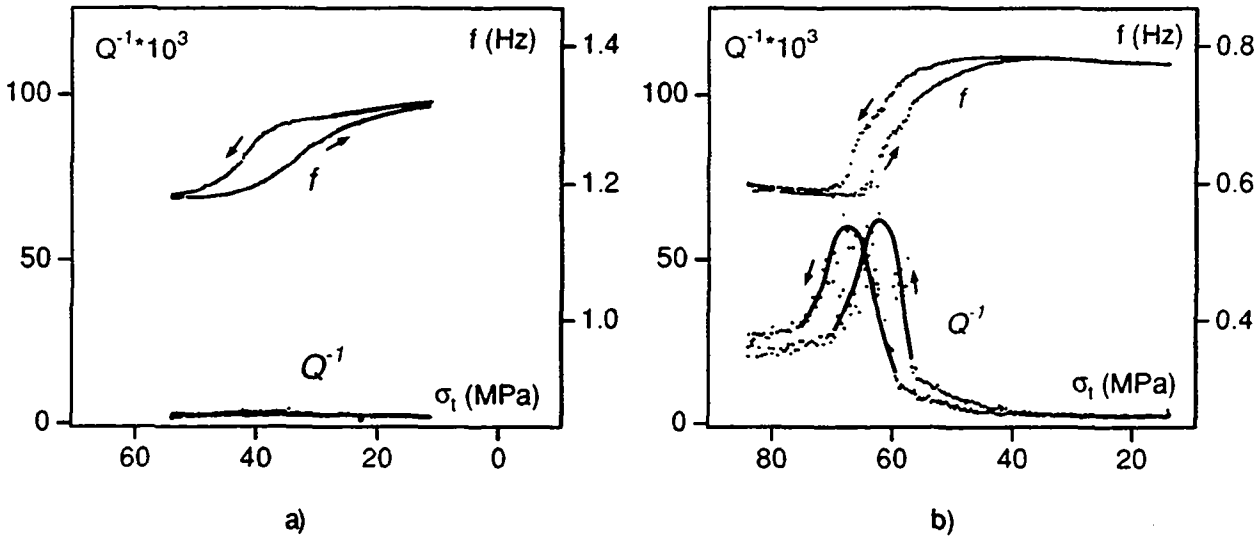

Figure 4.11: Internal friction (Q^{-1}) and resonance frequency (f) as a function of σ_t (oscillation amplitude $\varepsilon_0 = 2 \cdot 10^{-4}$) : a) geometry A and b) geometry B.

These results indicate that the orientation distribution of shear stresses in the habit plane has a significant effect on the measured IF that is associated with moving interfaces. Important anelastic deformation and energy dissipation only occurs, when shear deformation along the entire interface is possible (specimen geometry B). Local interface displacements (i.e. the

movement of interface dislocations) do not contribute significantly to the internal friction that is associated with single variant transformations (specimen geometry A).

4.3.2 Comparison to Other IF Measurements of Single Variant Transformations

The observations of this study have been compared with other results of IF measurements during single variant transformations (Dejonghe et al., 1975 and Morin et al., 1982). Morin measured the IF in a standard specimen and observed an IF peak with a height that is at least 10 times greater than for the standard geometry of this work (figure 4.11a). This discrepancy may be due to a difference in the experimental conditions. Morin et al. induced the martensitic single variant by cooling under an applied tensile load to temperatures below the M_f temperature. Subsequently, the applied stress was removed and the IF was measured during the retransformation of the single variant upon heating. The problem of this method is that when the specimen is cooled below M_S the growth of the induced single variant will stop in the vicinity of the specimen grips and in most cases, as it has been directly observed in the present study, other variants can nucleate at the grips. Since no direct observation of the specimen surface was done during the measurement of Morin et al. (1982), the occurrence of the relatively high damping peak during heating could be due to the retransformation of differently oriented martensitic variants.

In the work of Dejonghe et al. (1975), another experimental technique was used for the IF measurement. A martensitic single variant was induced in tension and then the specimen was mounted into a resonant bar apparatus, where flexural vibrations were used for the determination of the IF. In this case, the direction of the measuring stress coincides with the tensile stress that is used for inducing the martensitic variant, but the transforming interfaces are subjected to tensile and compressive stresses at the same time during the IF measurement. The relatively high damping peak that was observed by Dejonghe et al., is therefore surprising. On the other hand, the resonance frequency used in this method was very high (in the kHz regime) so that this effect could be associated with other damping mechanisms than interface motion, as for example the vibration of interface dislocations.

It must be concluded that none of these IF measurement techniques was the ideal experiment for obtaining very accurate results, from which quantitative values of the microscopic hysteresis effect could be established. In both cases, the transforming interfaces were not perfectly activated by the applied measuring stress. As we will see in the following paragraphs, the preparation of window specimens that was developed in this study presents an advance for the investigation of the microscopic hysteresis effect that is involved in single variant transformations. The very best technique for this purpose, however, should be an alternating shear

deformation without simultaneous bending or torsion deformation, that could be realized with a special fatigue machine.

4.4 The Nature of Anelastic Deformation during IF Measurements : The Orientation Dependence of the IF

The effect of orientation has been studied for both the transitory part of the IF peak (Q^{-1}_{Tr}) and for the non-transient part ($Q^{-1}_{\dot{\sigma}=0}$) that was measured at constant stress levels. As has been established in chapter 3, Q^{-1}_{Tr} is the difference between the total amount of damping (Q^{-1}_{tot}) and $Q^{-1}_{\dot{\sigma}=0}$:

$$Q^{-1}_{Tr} = Q^{-1}_{tot} - Q^{-1}_{\dot{\sigma}=0} \qquad (4.1)$$

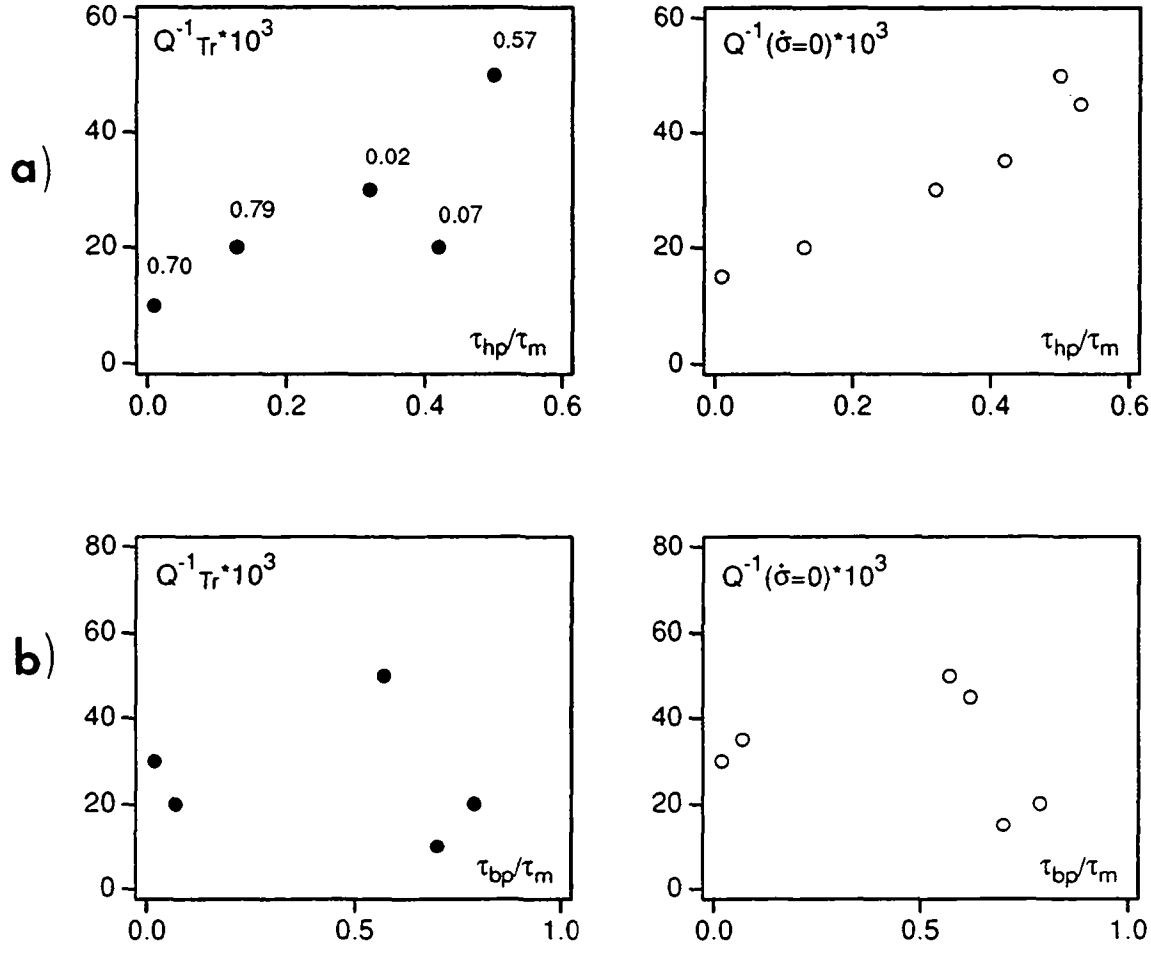

Figure 4.12: The transient part (Q^{-1}_{Tr}) and the non-transient part ($Q^{-1}_{\dot{\sigma}=0}$) of IF as a function of:
a) The shear stress component in the habit plane (τ_{hp}/τ_m), where the numbers above the data points (left diagram) represent the shear stress component in the basal plane (τ_{bp}/τ_m).
b) The shear stress component in the basal plane (τ_{bp}/τ_m).

Figure 4.12a illustrates that both IF contributions increase almost linearly with the shear stress component of the habit plane system (τ_{hp}/τ_m) while their dependence on the shear stress component of the basal plane system (τ_{bp}/τ_m) is not well determined. Some additional IF contributions appear to come from the deformation in the basal planes. This can be seen by the fact that the $Q^{-1}{}_{Tr}$ - and $Q^{-1}{}_{\dot{\sigma}=0}$ - values do not go to zero for $\tau_{hp} = 0$ and $\tau_{bp} = 0.7$ (figure 4.12a). The results of figure 4.12 confirm the general assumption that the transformation deformation along the habit plane governs the anelastic deformation during IF measurements and that the deformation along the basal planes does not contribute systematically to the IF. This can be understood by considering the possible mechanisms by which anelastic deformation could occur on the basal plane. The influence of the elastic stress on single variant transformations is small, when the interface can move to the specimen surface and the elastic stress is relaxed by a macroscopic shear deformation. Therefore, the stacking fault sequence on the basal planes once formed during the growth of a single variant, can be preserved. In the absence of changing elastic or internal stresses there is no driving force for the movement of partial dislocations on the basal planes (see TEM observations in chapter 5) and therefore the anelastic deformation on that system is not very important.

4.5 The Hysteretic Character of the Interface Motion during IF Measurements

4.5.1 IF and Transformation Kinetics

The transient part of the IF peak ($Q^{-1}{}_{Tr}$) is associated with the transformation kinetics (chapter 3). $Q^{-1}{}_{Tr}$ is therefore dependent on the volume fraction which is transformed during one oscillation. According to Gremaud and Bidaux (1987), the oscillating measuring stress ($\sigma_m = \sigma_0 \sin\omega t$) contributes to the transformation by modifying the thermodynamic equilibrium of the specimen. The additional displacement of transforming interfaces creates anelastic deformation during σ_t - induced transformation. This anelastic deformation can be expressed as follows:

$$d\varepsilon_{an} = \varepsilon^t \frac{\partial n}{\partial \sigma} (\dot{\sigma}_t + \dot{\sigma}_m)\, dt \qquad (4.2)$$

where ε^t is the transformation strain in direction of σ_m and $\partial n/\partial\sigma$ is the transformed volume per stress unit.

Starting from the basic equation for Q^{-1} (equation 3.8), $Q^{-1}{}_{Tr}$ has been derived with equation (4.2), under the condition that $\dot{\sigma}_t << \dot{\sigma}_m$:

$$Q^{-1}_{Tr} = \frac{1}{\pi \sigma_0 \varepsilon_0} \int_{cycle} \sigma_m \, d\varepsilon_{an} = \frac{\varepsilon^t}{\pi} \frac{\partial n}{\partial \sigma_t} \frac{\dot{\sigma}_t}{f \varepsilon_0} \qquad (4.3)$$

where f is the oscillation frequency and ε_0 is the oscillation strain amplitude.

Integrating equation (4.3), the relation between Q^{-1}_{Tr} and n becomes:

$$\frac{1}{\dot{\sigma}_t} \int_{\sigma_c}^{\sigma} Q^{-1}_{Tr} \, f \, d\sigma_t = \frac{1}{\pi} \frac{\varepsilon^t}{\varepsilon_0} n \qquad (4.4)$$

According to Delorme and Gobin (1973), the left part of equation (4.4) is defined by K, the "normalized" IF:

$$K = \frac{1}{\dot{\sigma}_t} \int_{\sigma_c}^{\sigma} Q^{-1}_{Tr} \, f \, d\sigma_t \qquad (4.5)$$

n has been calculated from the σ_t-ε curve by assuming that the pseudoelastic strain ($\varepsilon_{psel} = \varepsilon_{tot} - \varepsilon_{el}$, where ε_{tot} and ε_{el} are the total and the elastic strains) is dominated by the macroscopic shear deformation in the habit plane system. The maximum transformation strain (ε^t_{max}) in the habit plane of the studied Cu-Zn-Al alloy is equal to : $\varepsilon^t_{max} = 0.19$, see table 4.2. Considering the Schmid factor (S) of the stress-induced variant with respect to σ_t, n is calculated to be:

$$n = \frac{\varepsilon_{tot} - \varepsilon_{el}}{\varepsilon^t_{max} \cdot S} \qquad (4.6)$$

The relationship between K and n has been investigated for the IF peak of figure 4.11b. A linear relationship between the normalized IF and the transformed volume has been found for $0 < n < 0.75$, as is shown in figure 4.13. This comparison has not been conducted for n-values greater than 0.75, because the completion of the transformation ($n > 0.75$) is restricted by the drastic increase of the cross section when the transforming interface moves into the window-"corner" of the small parallelepipeds (figure 4.3). Therefore, only the $K(n)$ slope for the free interface motion has been considered in figure 4.13.

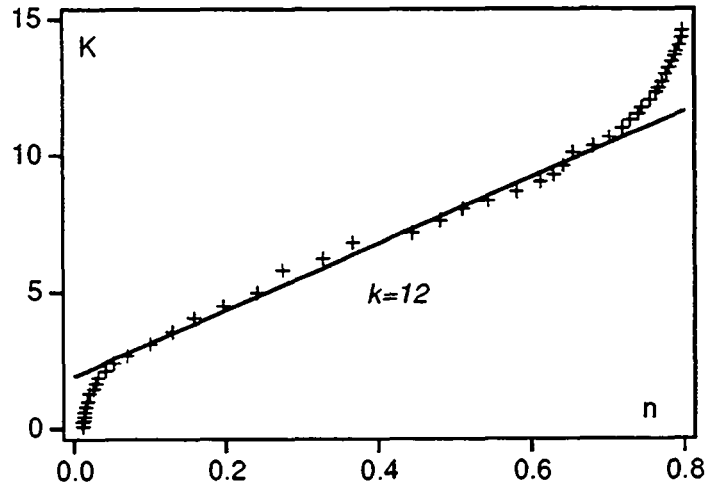

Figure 4.13: The normalized IF (K) as a function of the transformed volume fraction (n).

The measured value ($k_{exp.}$ =12) can be compared to the theoretical slope (k_{theor}) which is given by equation 4.4 :

$$k_{theor.} = \frac{\varepsilon^t}{\pi \varepsilon_0} \quad , \quad \varepsilon^t = \varepsilon^t_{max} \frac{\tau_{hp}}{\tau_m} \tag{4.7}$$

where for ε^t the habit plane deformation has been assumed. For the studied specimen orientation ($\tau_{hp}/\tau_m = 0.31$) and the applied strain amplitude ($\varepsilon_0 = 2 \cdot 10^{-4}$) it follows that $k_{theor.} = 94$ and thus:

$$k_{theor.} = 94 \neq 12 = k_{exp.} \tag{4.8}$$

The discrepancy between the theoretical and experimental IF values ($k_{theor.} / k_{exp.} = 8$) suggests that at least one of the basic assumptions for the IF modeling is not correct, namely the assumption that complete hysteretic interface motion occurs during one oscillation cycle. The result that the experimental IF values are significantly lower than the theoretical ones indicates that the interface motion during IF measurement is less hysteretic and partially reversible. The following paragraph is addressed to demonstrate the relationship between the partial reversibility of interface motions and the macroscopic transformation hysteresis. For that IF measurements have been conducted in Cu-Zn-Al specimens that contain γ precipitates and show a larger transformation hysteresis than the specimens which have been studied in the last paragraphs.

4.5.2 The Effect of γ Precipitates on the IF

The effect of γ precipitates on the martensitic transformation in Cu-Zn-Al has been the subject of studies by Rapacioli and Chandrasekaran (1979), as well as Auguet et al. (1989). The presence of γ precipitates have been reported to shift the transformation temperatures and to increase the slope and the width of the hysteresis.

γ precipitates are formed when the stable β phase is quenched from intermediate temperatures ($T \approx 500°C$). They form during the non-equilibrium quenching procedure and grow when further aged for short times at temperatures around 400°C. The TEM micrograph of figure 4.14a characterizes the size and distribution of γ precipitates that have been obtained in this study. The Cu-Zn-Al single crystalline specimens were quenched from $T = 500°C$ and aged for 5 seconds in a salt bath that had a temperature of 400°C. The γ precipitates have a cuboidal shape and an average size of $r = 0.1$ µm. In order to verify that single variant transformations are still possible for the given size of precipitates, TEM thin foil specimens have been deformed *in situ*. In fact, the observations showed that one single variant transforms the specimens and that the precipitates are incorporated in the stress-induced variant (figure 4.14b).

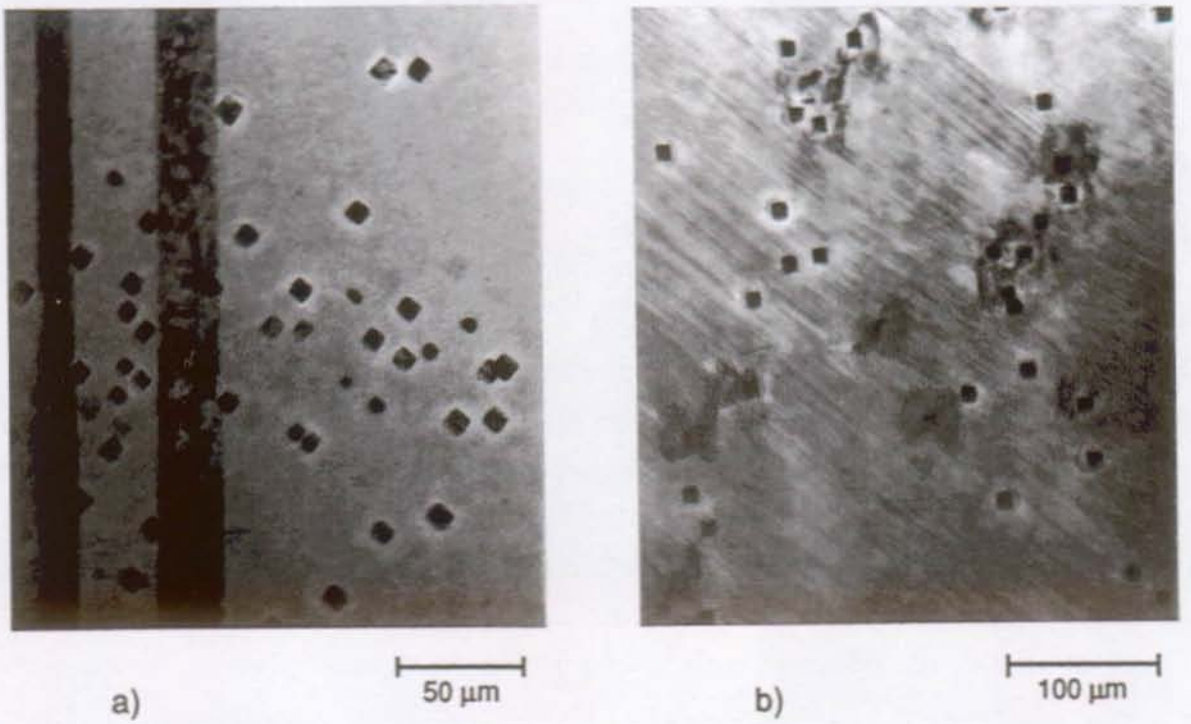

Figure 4.14: TEM micrographs showing:
a) The formation of γ precipitates after the heat treatment described in the text and
b) the γ precipitates embedded in the martensitic single variant after *in situ* stress-induced transformation.

Figure 4.15 shows the influence of these γ precipitates on both the macroscopic hysteresis and the internal friction (IF) behaviour. The macroscopic hysteresis is significantly larger in the specimen containing γ precipitates as compared to the hysteresis of specimens without precipitates (figure 4.10). This observation is in agreement with the study of Auguet et al. (1989), who reported a significant increase of the transformation hysteresis width when the precipitate size (r) becomes larger than 0.06 µm. The influence of a larger hysteresis on the evolution of the transitory IF that is measured during single variant transformations, is represented by the $K(n)$ curve of figure 4.15b. It can be seen that K is proportional to n during the main part of the transformation, as it was also found in figure 4.13. However, the $K(n)$ slope $k_{exp.\gamma}$ (matrix with γ precipitates, figure 4.15), is higher than $k_{exp.}$ (matrix without γ precipitates, figure 4.13):

$$k_{exp.\gamma} = 27 > 12 = k_{exp.} \qquad (4.9)$$

This result shows that the measured values of internal friction (IF) during single variant transformations increase when the macroscopic hysteresis effect is larger due to the presence of γ precipitates. On the other hand, even $k_{exp.\gamma}$ is too small in order to explain the theoretical values for the transient IF ($k_{theor.}$). The following paragraph demonstrates that the observed IF values can be explained by the stress hysteresis that is involved in the motion of a single martensite-austenite interface, indicating that the internal friction values are a direct measure of the *microscopic hysteresis effect* that is involved in martensitic phase transformations.

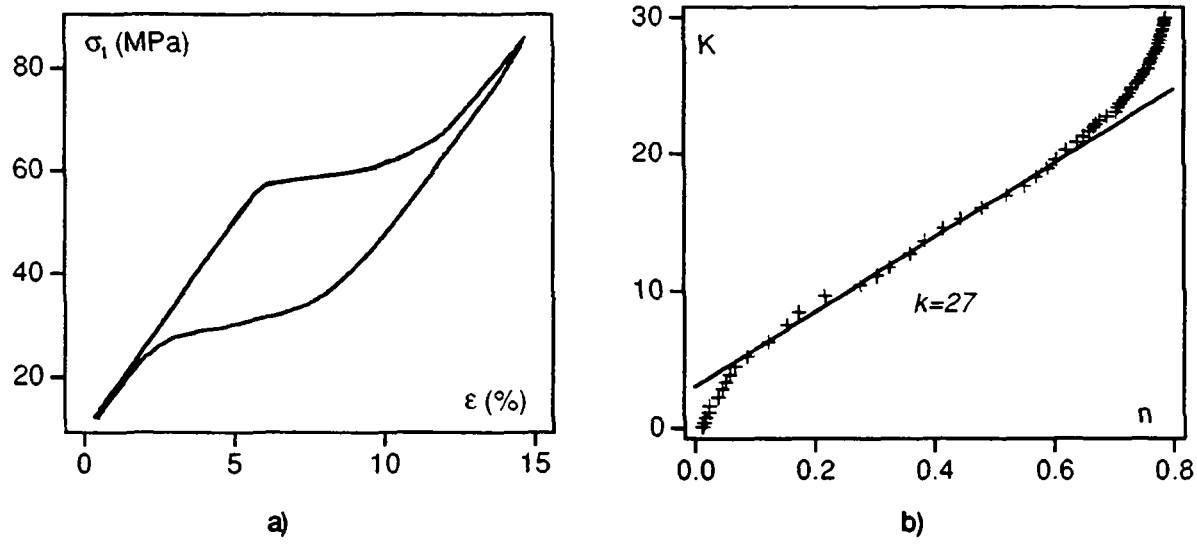

Figure 4.15: Macroscopic hysteresis effect and IF behaviour of a Cu-Zn-Al specimen that contains γ precipitates:
a) Transformation hysteresis (σ_t - ε curve) and b) normalized IF (K) as a function of n.

4.5.3 Quantitative Comparison of the Macroscopic Hysteresis Effect and Internal Friction Values : The Microscopic Hysteresis Effect

The macroscopic hysteresis effect and the measured IF behaviour can be compared by establishing the values of the stress hysteresis ($\Delta\sigma$) which is involved in both effects. $\Delta\sigma$ defines the stress interval that separates the stress-strain curves measured during loading (forward transformation) and unloading (reverse transformation).

During stress-induced martensitic transformations of precipitate-free specimens the macroscopic hysteresis (σ_t -ε curve) shows an average width of $\Delta\sigma_{tot}$ = 1.5 MPa (resolved stress, figure 4.10). The contribution of the interface motion itself should be smaller because the value above includes also the hysteresis effect that is due to nucleation. The macroscopic stress hysteresis that is involved in single interface motions has been measured to be 0.2 ± 0.1 MPa in precipitate-free Cu-Zn-Al single crystals (Lovey et al., 1992).

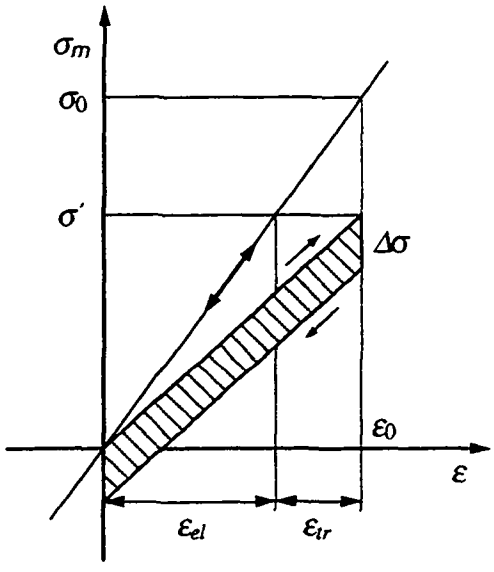

Figure 4.16: Determination of the stress hysteresis ($\Delta\sigma$) during IF measurements. The stored elastic energy ($W = 0.5\ \sigma' \cdot \varepsilon_0$) is a function of the transformation strain (ε_{tr}).

During IF measurements, $\Delta\sigma$ can be established from the elastic and dissipated energies (ΔW and W, respectively) according to the definition of Q^{-1} ($Q^{-1} = \Delta W / 2\pi W$, equation 2.1). Figure 4.16 shows how both energy contributions can be calculated for the present type of IF measurement where the oscillation amplitude (ε_0) is imposed to the specimen before free vibrations take place. If no transformation occurs during one oscillation cycle, the evolution of

the oscillating measuring stress (σ_m) follows the elastic slope determined by the shear modulus (G). When the oscillation amplitude is maximum, it follows that:

$$\sigma_m = \sigma_0 = G \cdot \varepsilon_0 \qquad (4.10)$$

In the case where transformation strain (ε_{tr}) is produced in the direction of σ_m, the stress-value at ε_0 (σ') will be lower than σ_m. The dependence of σ' on ε_{tr} can be expressed as follows:

$$\sigma' = \sigma_0 \cdot (1 - \varepsilon_{tr}/\varepsilon_0) = G \cdot (\varepsilon_0 - \varepsilon_{tr}) \qquad (4.11)$$

The stored elastic energy (W) decreases with increasing ε_{tr} because:

$$W = 0.5\, \sigma' \cdot \varepsilon_0 = 0.5\, G \cdot \varepsilon_0 \cdot (\varepsilon_0 - \varepsilon_{tr}) \qquad (4.12)$$

Considering that the stress hysteresis ($\Delta\sigma$) is independent of ε_{tr}, the dissipated energy (ΔW) is equal to:

$$\Delta W = \Delta\sigma\, \varepsilon_0 \qquad (4.13)$$

The combinations of equations (4.12) and (4.13) with the definition of Q^{-1} (equation 2.1) allows for the determination of $\Delta\sigma$ from the measured IF:

$$\Delta\sigma = \pi\, G\, (\varepsilon_0 - \varepsilon_{tr})\, Q^{-1} \qquad (4.14)$$

ε_{tr} can be determined for a given value of Q^{-1}, if the transformed volume fraction per oscillation (Δn), the maximum transformation strain (ε^t_{max}), and the Schmid factor (S) are all knowns:

$$\varepsilon_{tr} = \Delta n\, \varepsilon^t_{max}\, S \qquad (4.15)$$

where Δn can be derived from the corresponding Q^{-1}-value and the constant k : $\Delta n = Q^{-1}/k$.

The final equation for $\Delta\sigma$ becomes:

$$\Delta\sigma = \pi\, G \left(\varepsilon_0 - \varepsilon^t_{max}\, S\, \frac{Q^{-1}}{k}\right) Q^{-1} \qquad (4.16)$$

Referring to the example of figure 4.13 (k = 12), it follows for Q^{-1} = 0.03:

$$\Delta\sigma = 0.20 \pm 0.05 \text{ MPa} \qquad (4.17)$$

where the value of the elastic shear modulus (G = 45 MPa) for the given specimen orientation was deduced from the equations that have been given by Van Humbeeck (1983) for the elastic constants of Cu-Zn-Al alloys .

The obtained value for $\Delta\sigma$ is in very good agreement with the results published by Lovey et al. (1992) for a single martensite-austenite interface moving in a precipitate-free matrix. The stress hysteresis for single variant transformations in specimens containing γ precipitates (k = 27) becomes:

$$\Delta\sigma = 0.60 \pm 0.05 \text{ MPa}, \qquad (4.18)$$

and this result confirms that not only the macroscopic hysteresis effect becomes larger, but also the microscopic stress hysteresis responsible for the measured internal friction increases, when the transforming variants have to incorporate γ precipitates. Therefore, one can suggest that *the internal friction values obtained during single variant transformations give a direct measure of the microscopic hysteresis effect that is involved in the motion of single martensite-austenite interfaces.*

Furthermore, the results of this investigation indicate that the microscopic hysteresis effect has to be considered for the interpretation of the anelastic effect (internal friction) that occurs during martensitic phase transformations. It can be concluded that *the motion of martensite-austenite interfaces during single variant transformations is partially reversible and not completely hysteretic.* Figure 4.17 illustrates the influence that complete hysteretic and partially reversible interface motion have on the anelastic deformation ($d\varepsilon_{an}$) during IF measurements. When the interface motion is partially reversible, the anelastic deformation that is produced during the increase of σ_m, can be partially removed when σ_m is reversed. In this case, the measured amount of dissipated energy or damping is substantially smaller than what is predicted by the theoretical assumption of a complete hysteretic interface motion (see IF models in chapter 3).

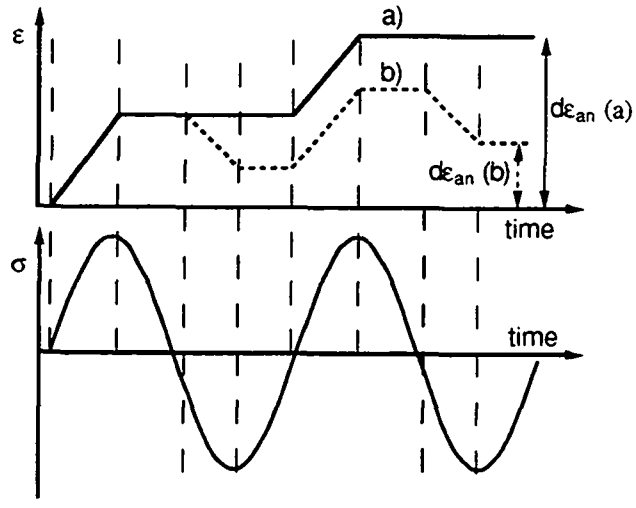

Figure 4.17: Anelastic deformation created during IF measurement when complete hysteretic or partial reversible interface motion is assumed ($d\varepsilon_{an}(a)$ and $d\varepsilon_{an}(b)$, respectively).

4.6 Conclusions

- A special specimen geometry has been developed for the study of martensitic single variant transformations by means of IF measurements. With this geometry, a net shear stress acts on the transforming interfaces during oscillations.

- The results of the IF measurements show that local interface displacements do not contribute significantly to the energy that is dissipated during martensitic transformations in Cu-Zn-Al alloys. Global interface displacements are responsible for the observed high damping (IF) peak. From the measured orientation dependence of the IF, it has been concluded that the dominant deformation mechanism for the IF is the transformation strain, which is produced in the habit plane system rather than in the basal plane system.

- A quantitative analysis of the observed IF values has demonstrated that the interface motion during IF measurement is not completely hysteretic as it is assumed in all of the existing IF models. The calculated stress hysteresis that resulted from the measured IF values of this study are in very good agreement with the macroscopic hysteresis effects that have been observed during single interface displacements. In Cu-Zn-Al alloys, the interface movement during IF measurements is a partially reversible process and the IF values give a direct measure for the microscopic hysteresis effect that is involved in the transformation process.

CHAPTER 5

Microstructural Evolution in Cu-Zn-Al Martensite Observed during TEM *in situ* Transformations : Results and Discussion

This chapter is addressed to the investigation of the microstructural evolution that occurs during martensitic phase transformations in shape memory alloys. The transformation behaviour has been observed by transmission electron microscopy (TEM) during *in situ* deformation and transformation of Cu-Zn-Al martensite.

The observations presented in this chapter include the motion of martensitic interfaces and partial dislocations that occurred during both stress and temperature variations. The interface migration mechanisms of internally faulted martensite and the partial dislocation motion are discussed in connection with existing models. The interface migration mechanism is revised with respect to the experimental observations that were obtained from the motion of a particular twin boundary, joining the A- and D-type variants (figure 1.17). The existence of glissile partial dislocations and the related changes in the stacking sequence are explained. The relationship between the observed microstructural development and the macroscopic hysteresis and internal friction behaviours, will be the subject of chapter 6.

5.1 Migration of Twin Boundaries in M18R Martensite

5.1.1 Introduction

The migration of intervariant boundaries as well as the atomic structure of martensitic interfaces have received a significant amount of attention in the last years. The reason for this interest is that the mobility of martensitic interfaces is essential for the existence of a recoverable deformation in shape memory alloys. During shape memory deformation, coalescence and rearrangement of martensite variants favors a single crystal that corresponds to the variant which gives the maximum strain in the direction of the applied stress. If all of the martensite-martensite interfaces are mobile under relatively low stresses, as compared to those stresses which are

required for the dislocation motion in shape memory alloys, the deformation can be completely recovered during the reverse transformation.

The interest of this investigation has been to study the microstructural mechanisms which are responsible for the macroscopic and microscopic hysteresis effects that have been reported in chapter 3. The motion of martensitic interfaces that occurs in order to relax the elastic strain energy is a dissipative mechanism which could explain the hysteresis instabilities observed during repetitive partial temperature cycling and the unusual increase of the internal friction (IF) at the end of thermally-induced transformations (see discussion of chapter 6).

Figure 5.1 presents an optical micrograph which shows the characteristic surface relief of shape memory martensite that results from the differently oriented variants, called A, B, C and D (chapter 1). The variants are joined by three different crystallographic interfaces, the A/B, A/C and A/D interfaces. The A/B and A/C type couplings appear because they are highly favorable in terms of the self-accomodation of the martensitic shear deformation. On the other hand, the non-self-accommodating A/D pairs are thought to appear in order to adjust the local stress field, or to accommodate changes in growth directions (Adachi and Perkins, 1985).

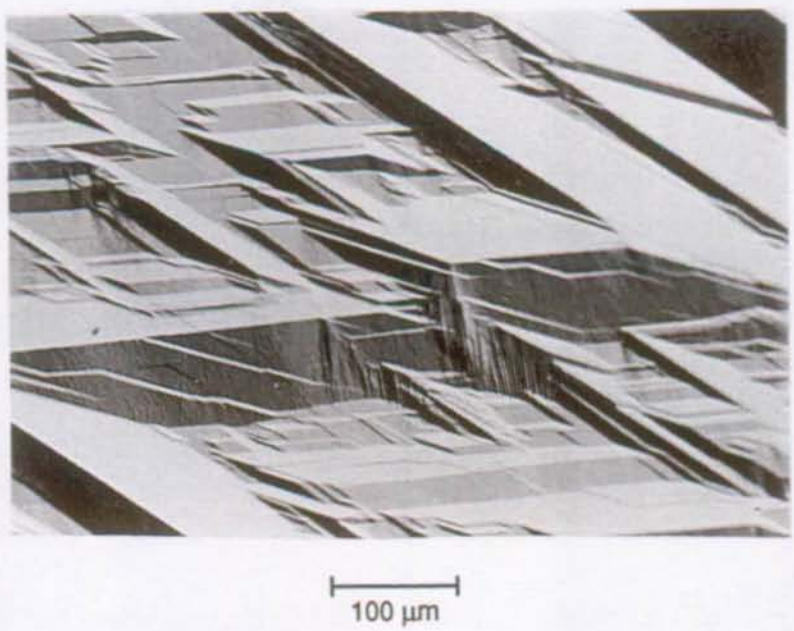

Figure 5.1: An optical micrograph (taken under polarized light condition) that shows the typical morphology of thermoelastic martensite in Cu-Zn-Al alloys. Three different crystallographic interfaces have to be considered (see text).

The TEM observations of this study are concerned with the motion of the A/D type boundary because of the particular interest on the modifications that occur in the martensitic structure during internal stress variations. The motion of the A/D type interface has been studied for different specimen orientations. The influence of internal and external stress fields on the displacement mechanism has been investigated, and special emphasis has been placed on determining the conditions that lead to changes of stacking sequences in the converting variants.

5.1.2 Specimen Orientations

Two different specimen orientations have been chosen for the *in situ* deformation experiments, and they are listed in table 5.1. Orientation 1 is characterized by a very low Schmid factor in the A/D-twinning plane (S_{tp}) and a high Schmid factor in the basal planes (S_{bp}) of both variants. Orientation 2 exhibits the opposite stress conditions, namely a high value for S_{tp} and a relatively low value for S_{bp}.

Table 5.1: Specimen orientations and Schmid factors for the A/D type twinning plane (S_{tp}) and the basal planes (S_{bp}) of the A- and D-variants.

Orientation	Tensile axis T	Foil normal N	S_{tp}	S_{bp}
1	$[001]\beta_1$	$[100]\beta_1$	0.05	0.50
2	$[\bar{1}34]\beta_1$	$[1\bar{1}1]\beta_1$	0.48	0.12

The specimen geometry is shown in figure 5.2. During *in situ* deformation, the observations have been restricted to those transparent regions, where the edges of the hole are parallel to the applied tensile stress (T), because only in these regions the stress components are parallel to T (chapter 2).

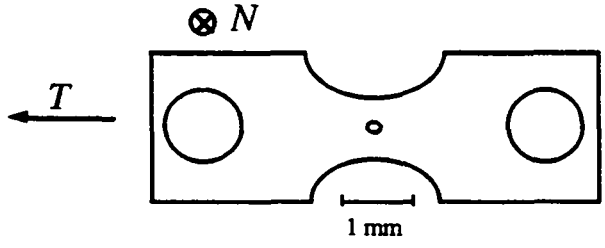

Figure 5.2: Schematic of a thin foil specimen. T is the tensile axis and N is the surface normal.

5.1.3 Crystallographic Relationships of the A/D Type Interface

The martensitic variants A and D are twin related and have a common interface that is also the twinning plane. The orientation relations between A- and D-type variants of a self-accomodating group were first established by Tas et al. (1973). These relationships, which are illustrated in the stereographic projection of figure 5.3, have also been confirmed in the present study. The twinning plane between variants A and D is parallel to the $(1\ 0\ 0)_{\beta_1}$ plane. The martensite plane parallel to this plane is approximately 2° from the $(2\ 0\ 20)_{\beta_1}'$ plane. The interface between variants A and D is typically not straight, but it has been observed to be roughly parallel either to the $(2\ 0\ 20)_{\beta_1}'$ or to the $(2\ 0\ \overline{16})_{\beta_1}'$ plane.

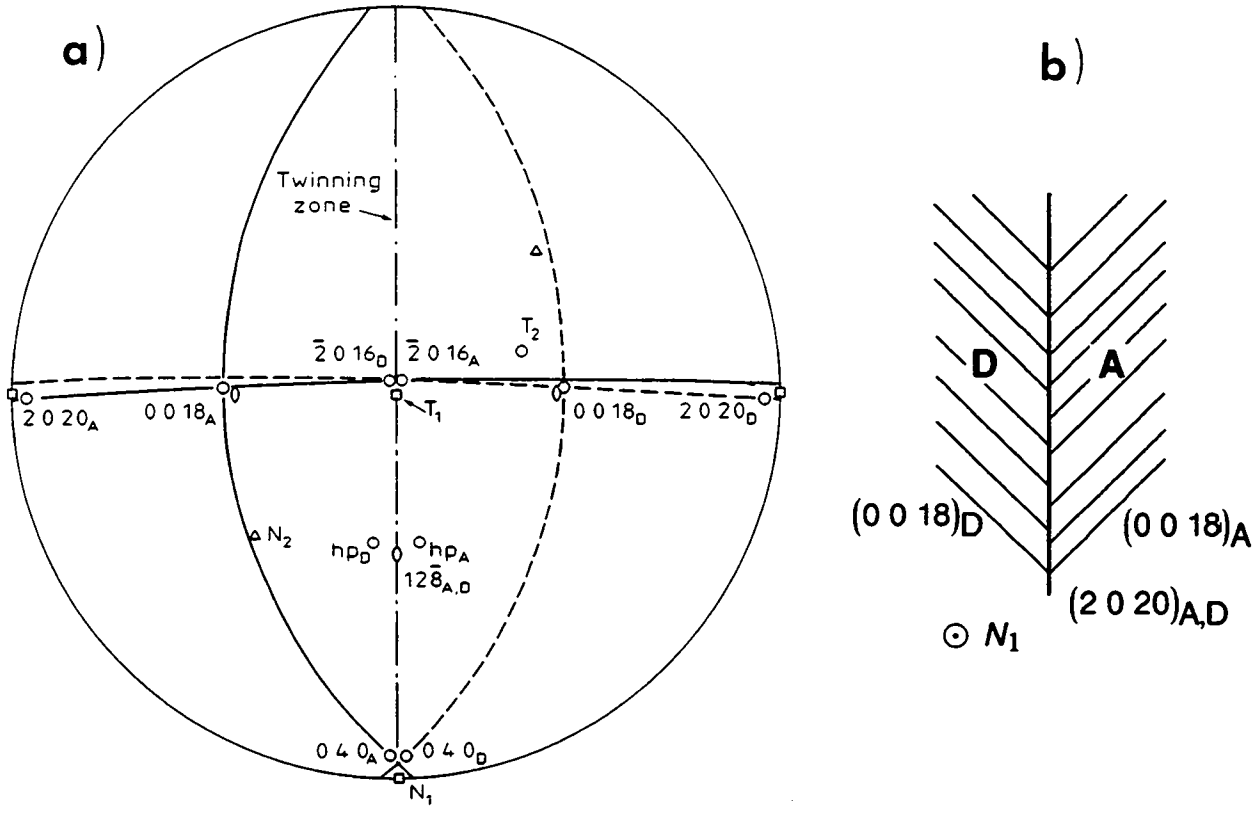

Figure 5.3: a) Stereographic standard projection showing the crystallographic relationship between variants A and D. T_1 and T_2 are the tensile axis directions and N_1 and N_2 are the surface normals of the two orientations. b) Schematic of the A/D interface presenting the situation where both basal planes $(0\ 0\ 18)_{A,D}$ and the common interface $(2\ 0\ 20)_{A,D}$ are edge on (foil normal N_1).

Figures 5.4 and 5.5 show typical examples of A/D variant combinations that were observed in the martensitic microstructure of the studied specimens. In figure 5.4a, a D-type variant is embedded in an A-type variant and two A/D interfaces are visible. The contrast of parallel lines

in both variants is due to the random stacking faults which are edge on in the specimen. The specimen normal is parallel to the common $[0\ \bar{1}\ 0]_{\beta_1'}$ direction in this case (orientation 1). The diffraction pattern taken at the interface (figure 5.4b) shows that the basal planes of variants A and D and the c^*-axis are almost perpendicular to each other.

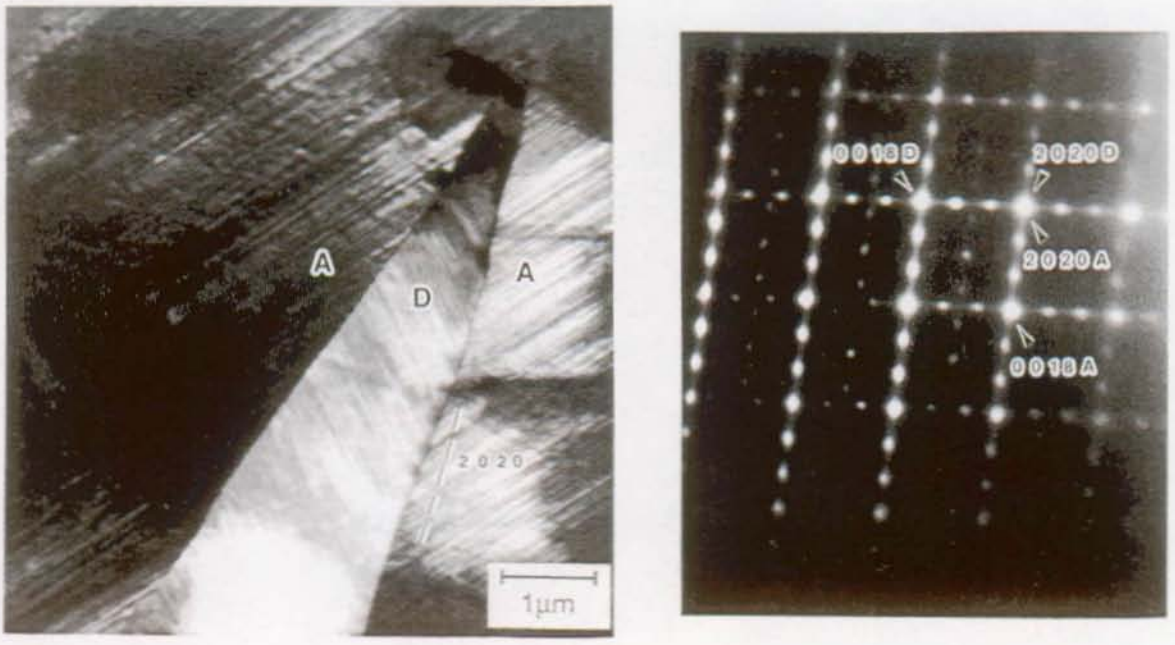

a) b)

Figure 5.4: Coupling of an A-type and a D-type variant:
a) Bright field image. b) Diffraction pattern taken at the interface. The foil normal is the common $[0\bar{1}0]_{\beta_1'}$-direction (orientation 1).

When the basal planes are inclined with respect to the electron beam, the random stacking faults on the basal planes give rise to the fringe contrasts in figure 5.5a. This photograph also shows stacking faults that end inside the variant and are limited by partial dislocations. Careful examination of the diffraction patterns of the joined variants (figure 5.5b) and a comparison with the stereographic projection of figure 5.3 proves that the observed variants are of the A- and D-type.

a)

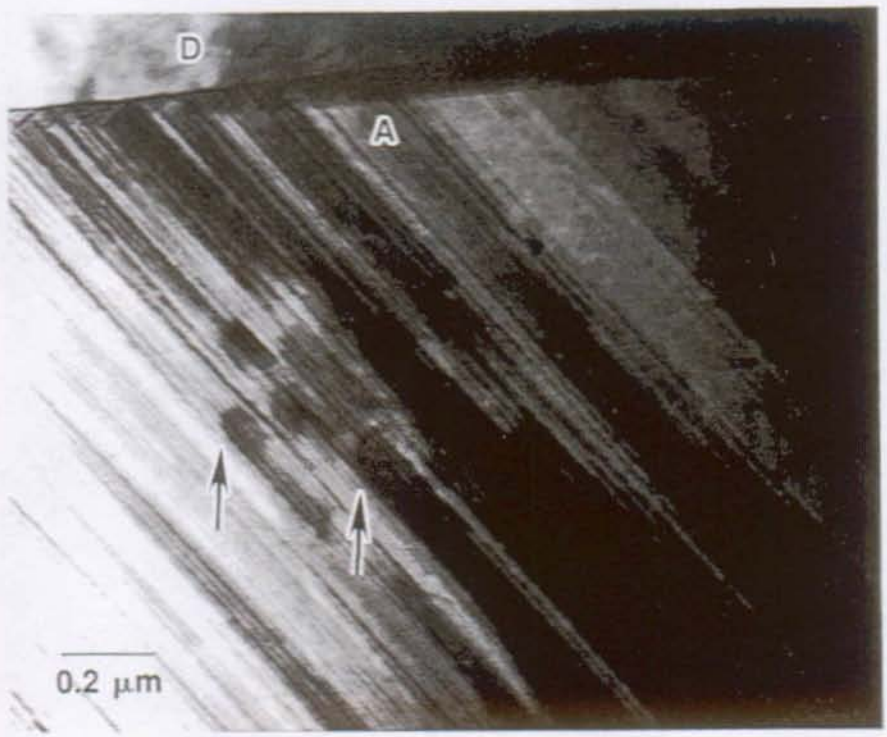

b)

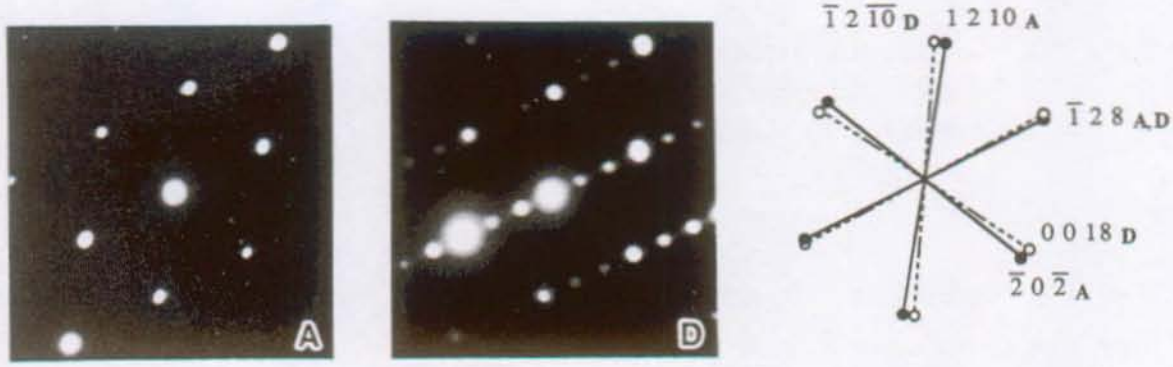

Figure 5.5: a) Bright field image showing the fringe contrast of random stacking faults in variant A. The stacking faults that end inside the variant are marked with arrows.
b) Diffraction patterns taken in variants A and D. The schematic shows the superposition of both diffraction patterns. $Z = [29\bar{2}]_A \| [210]_D$ (orientation 2).

5.1.4 Migration of the A/D Type Interface

In specimens with the tensile axis T_1, the A/D interface is not strongly activated by the external tensile stress because the Schmid factor (S_{tp}) is very small. Therefore, the displacement of this interface can only be observed when the internal stress changes along the interface, e.g. during reorientation between other variant combinations in the surrounding material. An example of the A/D interface motion is illustrated in figure 5.6. The sequence of photographs in this figure was copied from the recorded video tape, and it shows a total interface displacement of 0.23 μm in 5 seconds. The interface displacement is illustrated by the schematical drawing in figure 5.6e. This schematic represents the interface positions as copied from the photographs together with reference lines of typical stacking faults in each variant. The photos show that the stacking sequence in the upper variant changes when the interface is displaced. This can be observed qualitatively by comparing the stacking fault contrasts with respect to the reference fault, which does not change its contrast during the recorded sequence (5.6a - d).

In contrast to orientation 1, the displacement of the A/D interface in specimens with tensile axis T_2 was directly controlled by the external tensile stress. The movement was observed to be very smooth and in general the stacking sequence was preserved, as the photos in figure 5.7 show. The movement and the stacking fault contrasts have been analyzed with the help of the reference line and the marked reference stacking fault. The stacking fault contrast did not change in this sequence of photographs, where the interface is displaced to the left hand side of the pictures by a total displacement of 0.1 μm in 8 seconds.

When the applied stress was released, the A/D interface movement was partially reversed for orientation 2, while in specimens with orientation 1 no reverse interface motion was observed. The reverse interface motion could be promoted by the elastic energy that was stored in the bulk material while the thinned regions of the TEM specimen were deformed. This observation is interesting because different hysteresis behaviours can be deduced for interface motions that occur with and without stacking fault changes. Apparently, interface motions accompanied by stacking fault changes are more hysteretic than interface motions where the stacking sequence is preserved.

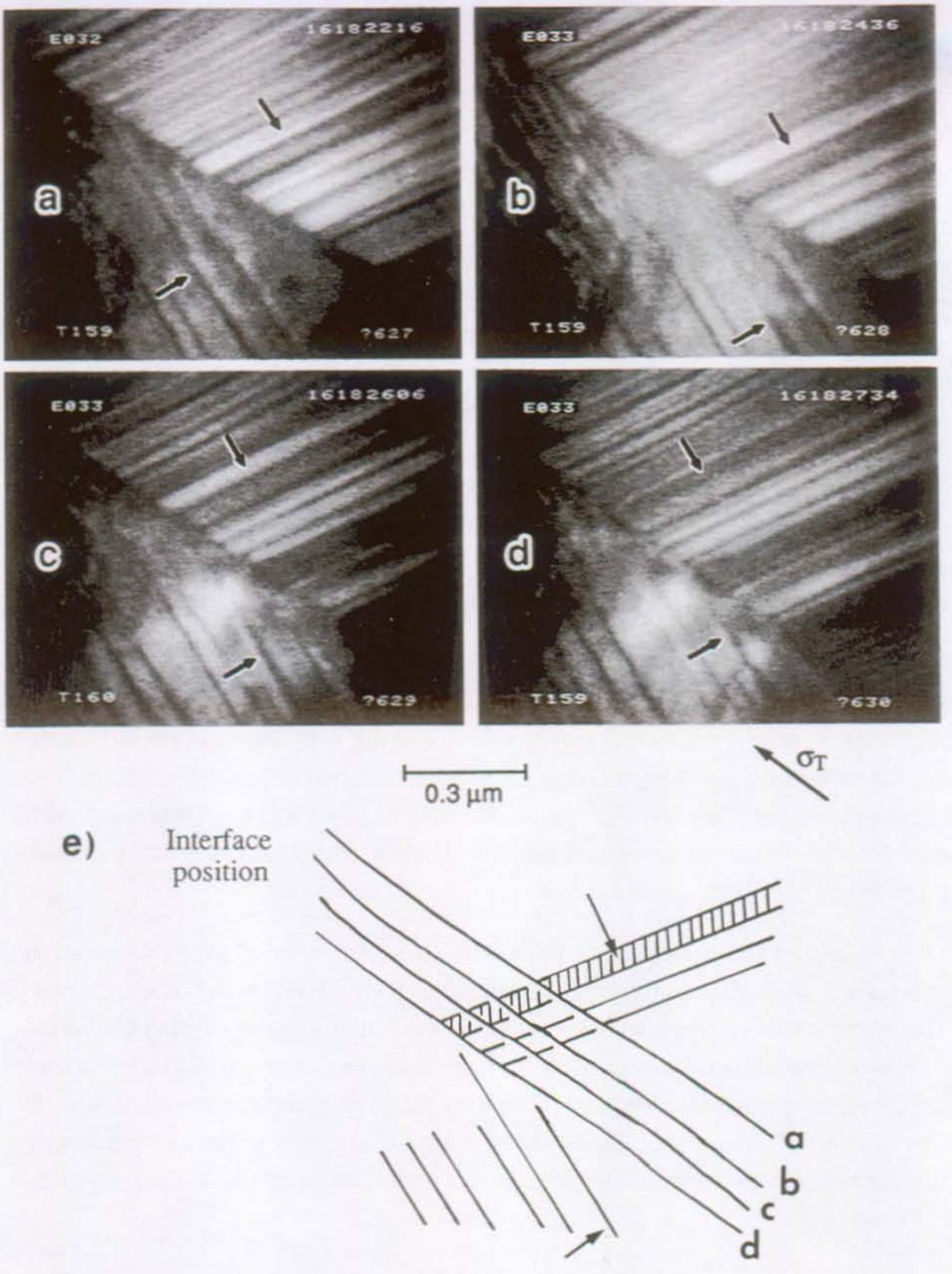

Figure 5.6: Movement of an A/D interface during deformation, specimen orientation 1. The series of photographs a) - d) were taken with a total time difference of 1 sec. The arrows mark reference contrasts on one stacking fault in each variant. The schematic at the bottom (e) shows the advance of the interface from picture a) to picture d).

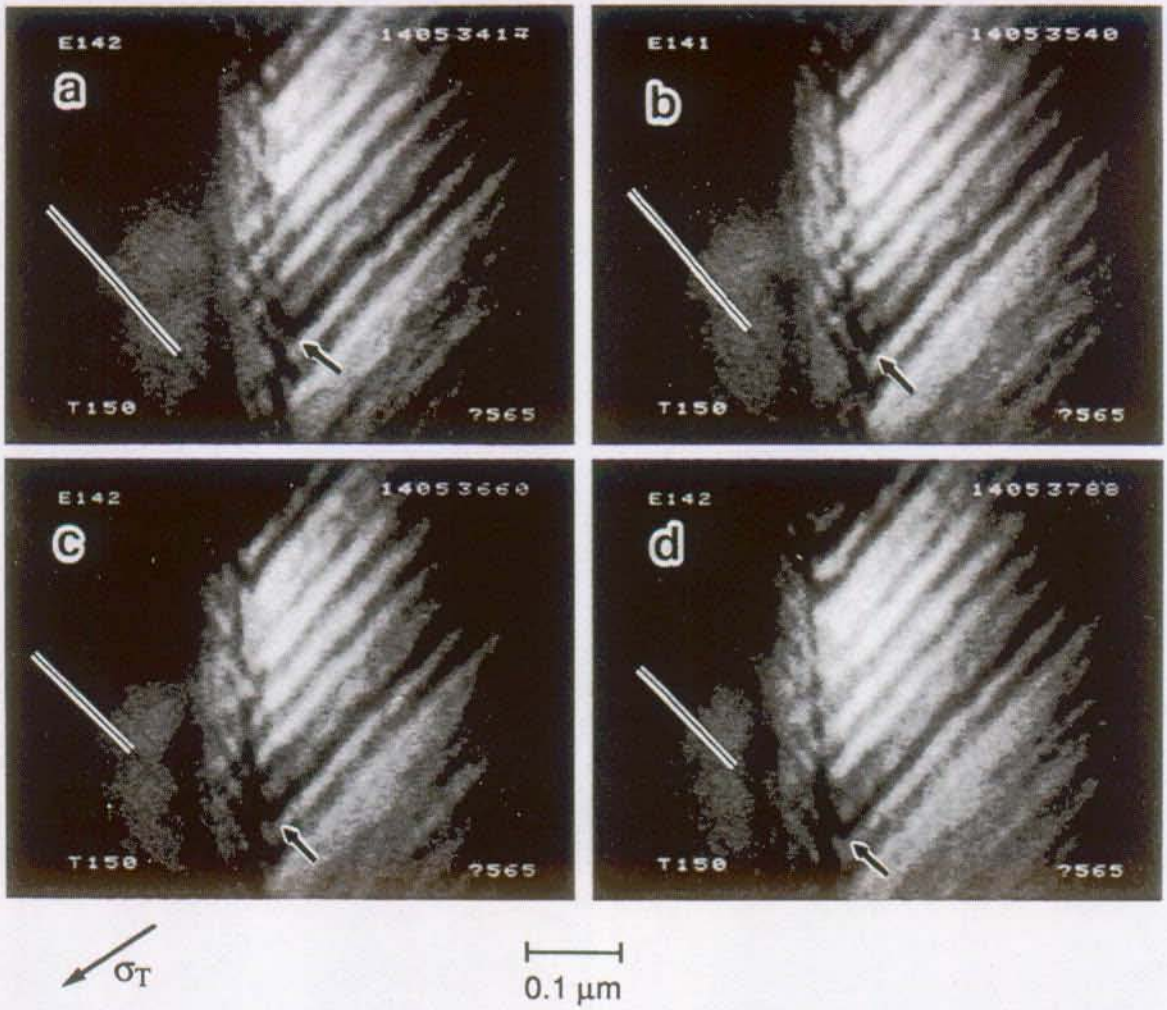

Figure 5.7: Movement of an A/D interface during deformation, specimen orientation 2. The series of photographs a) - d) are taken with a time difference of 2 sec. The reference line and the pointed reference contrast illustrate the interface displacement towards the left hand side of the pictures. In this case, the stacking fault contrasts do not change.

5.1.5 Faults Created during Reorientation between Variants A and D

The creation of faults has been observed during the disappearance of the common interface between the converting A- and D-variants. Figure 5.8a shows the situation where a small D-type variant is embedded in an enlarged A-variant. When the growth of the A-variant occurs the tip of the shrinking D-variant retracts and different contrasts of the joined regions in the A-variant appear, see sequence of photographs in figures 5.8b -d. Other examples of defects introduced during reorientation are shown in figure 5.9. Most line directions of these fault contrasts are perpendicular to the stacking fault contrasts and therefore also perpendicular to the basal planes.

Electron diffraction across these "interfaces" did not reveal any misorientation between the joined regions of martensite, within the experimental accuracy of the diffraction method. This observation suggests that these "interfaces" exist inside one single variant orientation. Further crystallographic analysis, however, was not possible during the *in situ* experiments because only one tilt axis was available and did not allow for the realization of the necessary contrast conditions. The described faults could not be reexamined because they disappeared completely when the specimens were heated to room temperature.

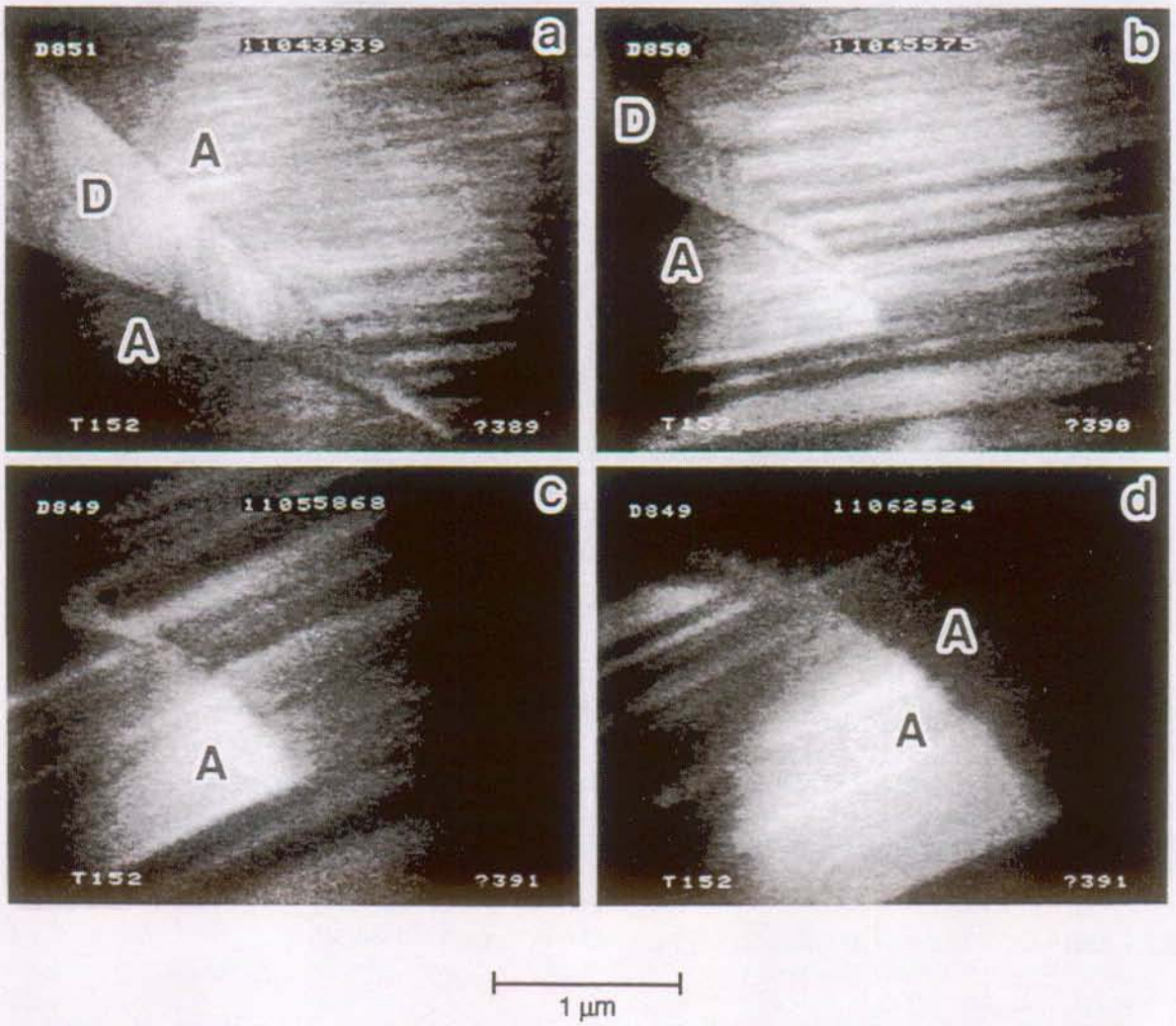

Figure 5.8: The creation of a fault (an apparent "interface") during reorientation between A- and D-type variants.

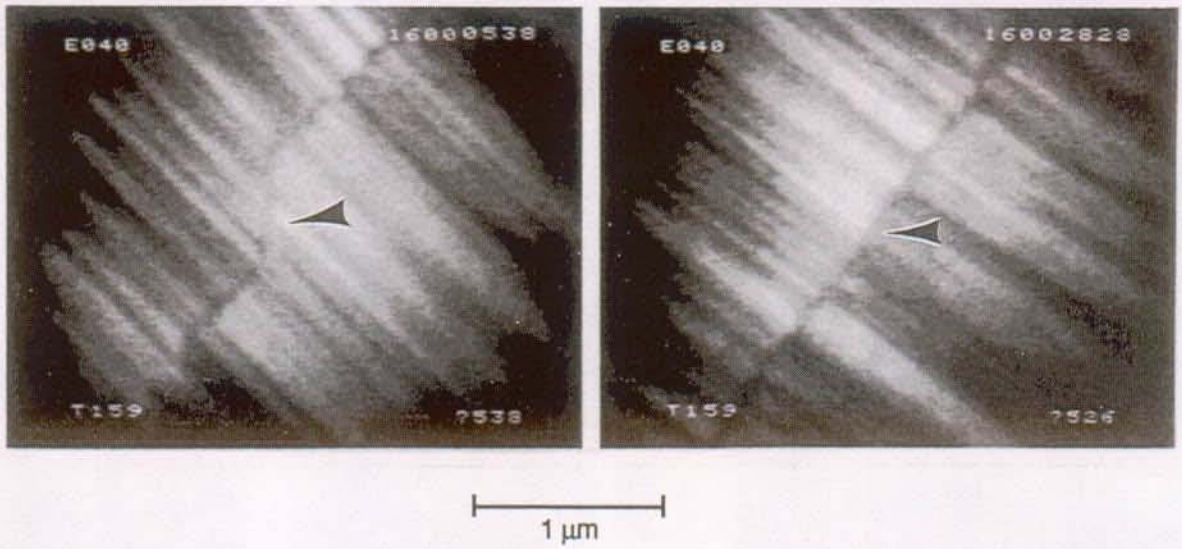

Figure 5.9: Defects in the A-variant that were observed after reorientation.

5.2 Migration of Partial Dislocations

The movement of partial dislocations on the basal planes of martensitic variants has been reported in the literature, for the case where the electron beam is focused to a small part of the specimen, see for example an early publication of Nishiyama and Kajiwara (1962). In such a case, the sudden heating caused by the electron beam concentration creates a local internal stress field in which partial dislocations can be created or displaced. The observations presented in this section show that the movement of partial dislocations also occurs when a martensitic specimen is heated to temperatures slightly above the retransformation temperature (A_S) with a small heating rate (1 K/min).

The initiation of partial dislocation movement has been observed to occur under two different conditions. The dissolution of internal "interfaces", as they have been described in the previous paragraph, is accomplished by partial dislocation motion and the presence of internal stress fields in the vicinity of immobile intervariant boundaries also initiates the motion of partial dislocations. Figure 5.10 shows the disappearance of an internal "interface" that occurred when retransformation started in the neighboring regions during heating. As can be seen by the interrupted band contrast on the basal planes in the upper region, the disappearance of such a defect is accompanied by frequent motion of stacking faults that end inside this variant. In figure 5.11, the moving stacking fault contrasts are clearly visible. An exact crystallographic

analysis could not be done because of the single tilt limitation during *in situ* observations, but it is reasonable to assume that the observed stacking fault motion is a result of partial dislocations that glide across such a defect. The driving force for such a process is an internal stress field which is built up during the retransformation of martensite.

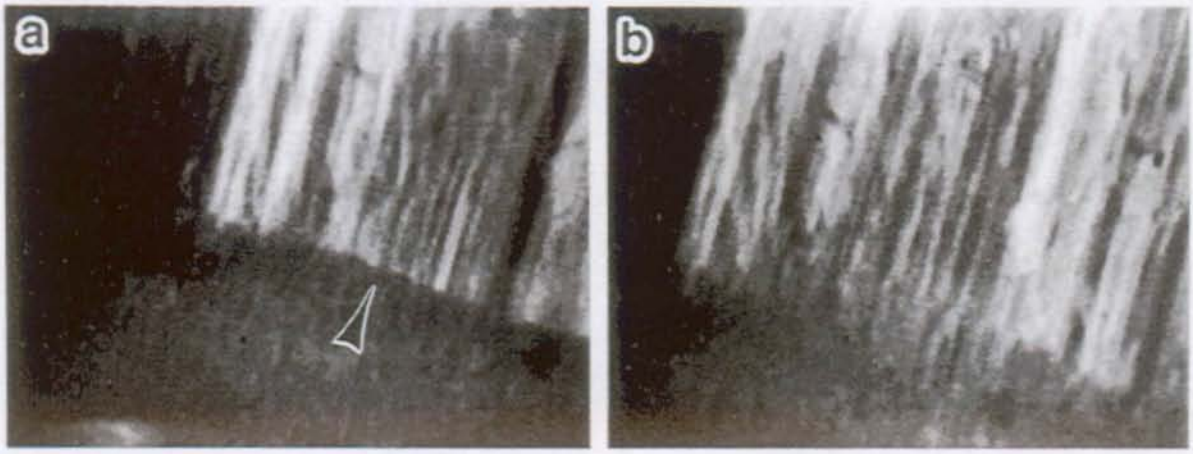

Figure 5.10: Movement of partial dislocations during heating. The photographs a) - b) were taken with a time difference of 1 second and they show the disappearance of a defect inside of an A-type variant during heating.

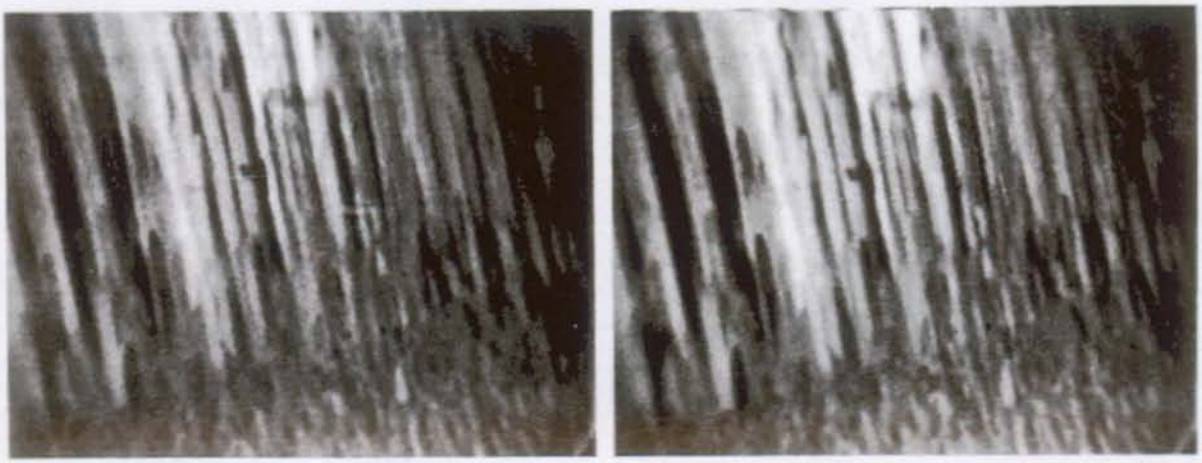

Figure 5.11: Mobile stacking faults in the vicinity of an internal fault of the type that was observed in figure 5.10.

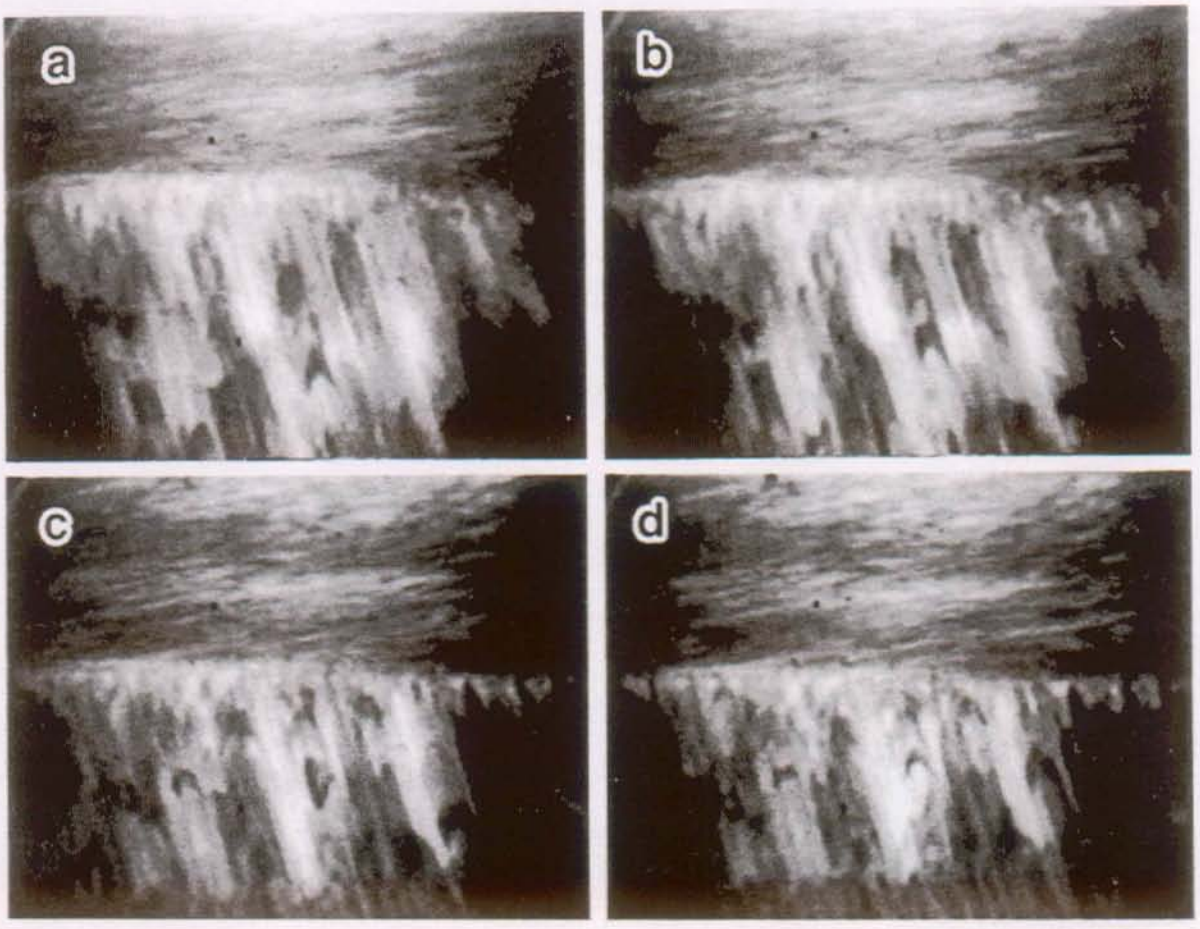

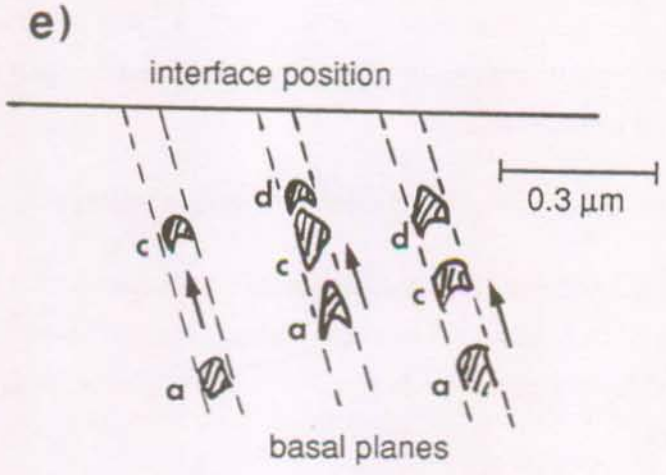

Figure 5.12: Movement of partial dislocations during heating. The photographs a) - d) are taken with a time difference of 1 second showing two variants which are separated by a horizontal interface. The schematic drawing (e) represents moving stacking faults in the lower variant which propagate towards the interface.

The motion of partial dislocations in the field of an internal stress was also observed for the situation that an interface of two variants is not mobile. Immobile interfaces are formed between variants which have a non-convertible orientation relation. According to Saburi and Nenno (1982) those variants belong to different self-accomodating groups and can only be converted by reorienting into a third variant.

Figure 5.12 shows a martensitic region where a horizontal interface separates two non-convertible variants. The sequence of photographs (5.12a-d) that was recorded during heating, shows the movement of partial dislocations on the basal planes of the lower variant. Note that the interface position did not change, but the displacement of individual stacking faults can be followed using the schematic drawing of figure 5.12e. In this case, the internal stresses that originated from the retransformation process could not be reduced by interface motion, but they have been compensated by shear processes along the basal planes of each variant.

5.3 Summary of the Results

i) The migration mechanism of the A/D type twin boundary in M18R martensite is dependent on the orientation of the external stress which is applied during deformation. When the resolved shear stress in the twinning plane (τ_{tp}) is high (orientation 2), the interface motion can be controlled by external stress variations. In this case, a very smooth motion occurred and the stacking fault sequences was preserved. However, if τ_{tp} is low (orientation 1), internal stress variations cause a jerky, inhomogeneous interface motion which is frequently accompanied by changes in the stacking disorders of the converting variants. In contrary to orientation 1, a partial reversible interface motion was observed for orientation 2.

ii) The mechanism of stacking fault changes during interface motion is not clearly visible.

iii) Slowly moving stacking faults have been observed in the vicinity of defects perpendicular to the basal planes and immobile interfaces when internal stresses are built up in the martensitic phase during heating. In this case, stacking fault changes can be explained by the glide of partial dislocations on the martensitic basal planes.

The goal of the following discussion is to explain the motion of A/D type interfaces and the mechanism by which the stacking faults change. Existing models, which describe the movement of twin boundaries as well as the formation of stacking faults in β_1' martensite, will be considered.

5.4 Discussion

5.4.1 Existing Models of Interface Displacement

Deformation Twinning

The interfaces in Cu-Zn-Al martensite are twin related and have well defined twin boundaries that can be displaced. The mobility or the conversion mode of martensitic interfaces has been generally explained by deformation twinning. The theory of deformation twinning, as has been published by Bilby and Crocker in 1965, attempts to predict the operative twinning elements of crystalline materials from a knowledge of their crystal structures. Bilby and Crocker defined a deformation twin as follows: "A deformation twin is a region of a crystalline body which has undergone a homogeneous shape deformation in such a way that the resulting product structure is identical with that of the parent, but oriented differently". By this definition, the deformation must be an invariant plane strain and since the two structures are identical, the deformation must be a simple shear.

The formal description of a transformation twin contains four elements (K_1, K_2, η_1, and η_2) which are illustrated in figure 5.13. K_1 is called the twin plane or composition plane, which is the invariant (undistorted) plane containing the direction of shear (η_1). K_2 is the second undistorted (but rotated) plane of the shear and it intersects K_1 in a line perpendicular to η_1. The shear plane S is, by definition, that plane which is normal to K_1 and contains η_1. The direction η_2 lies along the line of intersection of the shear plane and K_2. Depending on the orientation relations between the twinned crystals, two different types of deformation twins can be distinguished: The type I twin (reflexion in K_1 or rotation of π about the normal to K_1) and the type II twin (rotation of π about the normal to η_1 or reflection in the plane normal to η_1).

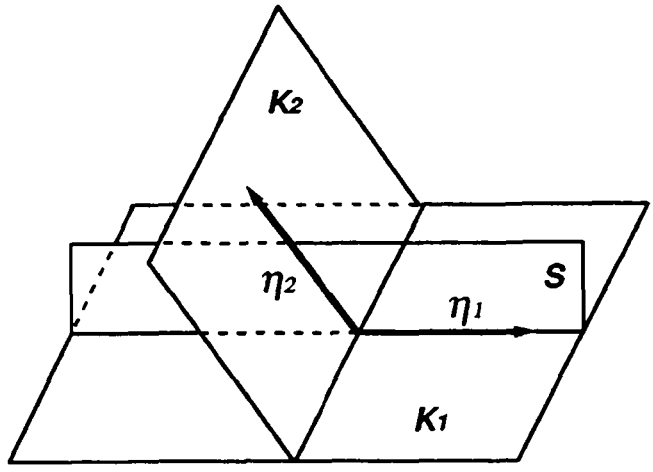

Figure 5.13: Twinning elements for a deformation twin.

Dislocation models of twinning have to account for the macroscopic deformation which accompanies twinning. In the case of a simple shear on the twinning plane, as is observed in *bcc* metals, the deformation can result from the movement of partial dislocations. Figure 5.14 shows how the displacement of a/6[111] partial dislocations on every successive {112} plane produces a deformation twin. The production of these dislocations on the right sequence of atomic planes is explained by the "pole mechanism", which was developed for *bcc* metals by Cottrell and Bilby (1951). Analogous mechanisms have been proposed for twinning in *hcp* and *fcc* metals (Thompson and Millard, 1952, and Hirth et al., 1964). However, in spite of extensive search, thin film microscopy has failed to reveal evidence which would support the existence of pole mechanisms.

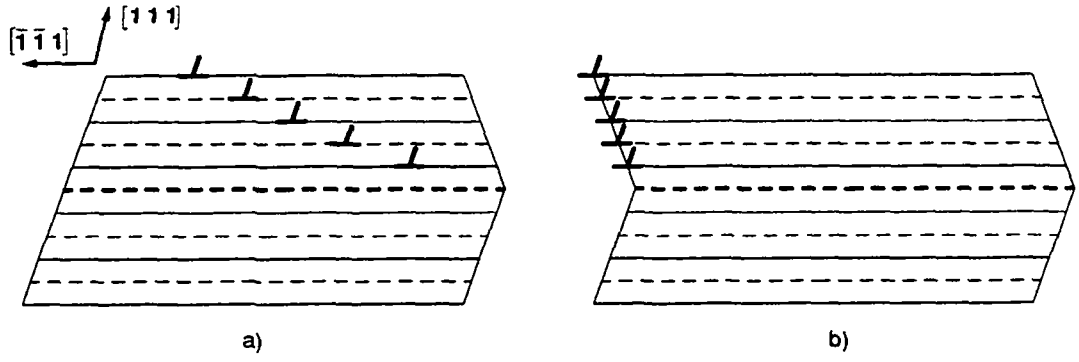

Figure 5.14: Illustration of twinning in a body-centered cubic lattice. a) Section parallel to (110) showing the stacking sequence of (112) planes with one (a/6)[111] twinning dislocation on each plane in the upper part. b) The twinned crystal after the dislocations have moved across the crystal.

Otsuka and Shimizu (1974) analyzed deformation twinning modes in Cu-base martensites in terms of the model of Bilby and Crocker (1965). They obtained operative twinning elements for γ' martensite in Cu-Al-Ni, which are in good agreement with those resulting from the phenomenological theory of martensitic transformations. Saburi and Nenno (1982), as well as Adachi et al. (1986), calculated the twinning elements for the fundamental variant-accomodation twins of β_1' martensite (table 5.2). However, difficulties do arise when a discrete dislocation mechanism has to be defined for the formation of a deformation twin in M18R martensite. None of the twin planes in M18R martensite is a close-packed plane and the only close packed planes are the basal planes. Therefore, it is very unlikely that dislocations move in the non-close-packed martensitic interfaces in order to accomplish the twinning shear. Considering the almost perfect atomic matching across the twin interfaces in M18R martensite (section 5.4.2), it is reasonable to assume that small atomic shuffles can bring the converting variants into coincidence. Another important aspect that characterizes the interface migration of internally

faulted martensites, is the role of stacking disorders which will be emphasized in the following microscopical description of the interface motion.

Table 5.2: Twinning elements (K_1, K_2, η_1 and η_2) and shear deformation (g) for the fundamental variant-accomodation twins in β_1' martensite, taken from Adachi et al. (1986).

Interface	K_1	K_2	η_1	η_2	g
A/C type	$\bar{1}\,\bar{2}\,8$	$1, \overline{1.538}, \overline{3.842}$	$1, \overline{0.753}, \overline{0.063}$	$\bar{1}\bar{0}\,\bar{9}\,1$	0.363
A/B type	$1, 1.538, \overline{3.842}$	$\bar{1}\,2\,8$	$\bar{1}\bar{0}\,9\,1$	$1, 0.753, \overline{0.063}$	0.363
A/D type	$1\,0\,10$	$\bar{1}\,0\,8$	$\bar{1}\bar{0}\,0\,1$	$8\,0\,1$	0.097

Influence of Stacking Disorders on the Interface Motion

The motion of twin boundaries between internally faulted martensitic variants is expected to be affected by the randomly distributed stacking disorders that are present in the converting variants. The schematic of figure 5.15 illustrates this problem. When the lower variant grows and the boundary moves upward (from position 1 to position 2), the planes B and C (indicated by arrows in the upper variant) must change into the planes A and B (underlined in the lower variant).

Two different mechanisms have been proposed for this case: First, Fukamachi and Kajiwara (1980) assumed that interfaces which contain stacking disorders keep their character while moving (figure 5.15b). This means that the boundary atoms of the upper variant have to move steadily from the indicated B and C positions into the A and B positions of the lower variant. Furthermore, Fukamachi and Kajiwara (1980) assumed that the motion of the interfaces is retarded by the stacking disorders. On the other hand, Katata and Saka (1989), who studied the motion of interfaces by transmission electron microscopy (TEM) during *in situ* deformation, claim that the interface motion is not affected by the presence of stacking disorders. Moreover, they found that the A/D type interface is only retarded, if equal and not different stacking faults of both variants meet each other at the common interface.

The alternative mechanism is to assume that the interfaces change their character during motion. Lovey et al. (1985) suggested that the imperfect twin interface changes into a perfect configuration and defects parallel to the interface are left behind (figure 5.15c). Another

possibility, the emission of a new stacking disorder, has been proposed by Adachi and Perkins (1985).

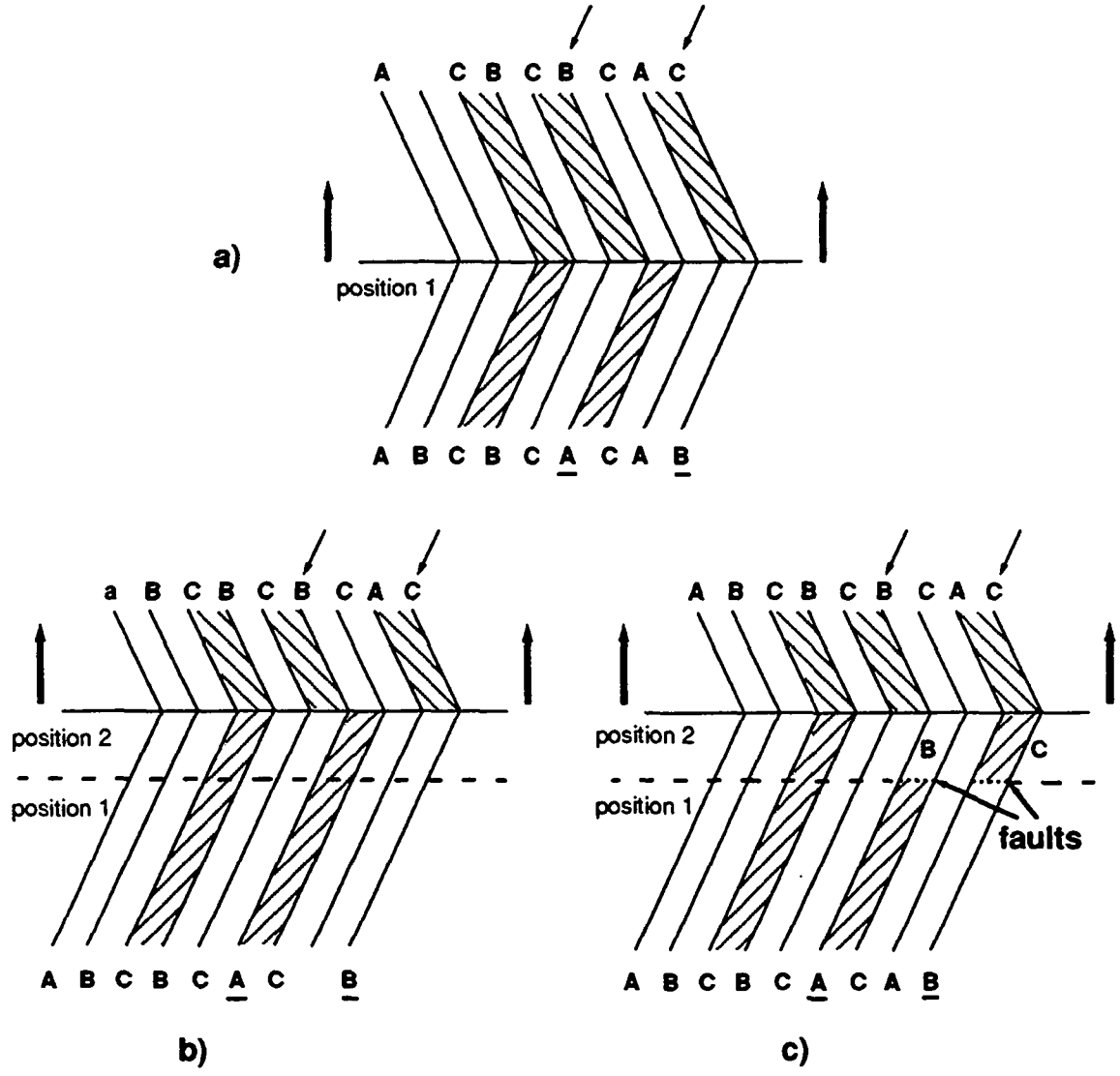

Figure 5.15: a) An interface containing stacking disorders moves upwards.
b) The stacking sequence (indicated by A, B and C) is preserved in both variants.
c) The stacking sequence is changed in the lower variant.

Crystallographic Nature of Stacking Faults in M18R Martensite

The crystallographic nature of random stacking faults on the basal planes of internally faulted martensite was initially attributed to a shear type fault. Chakravorty and Wayman (1977) assumed that random stacking faults are introduced into the perfect M18R structure by means of the slip of partial dislocations having a Burgers vector of $\vec{b} = \pm\frac{1}{3}[100]_{\beta_1}$. The reversible

motion of these dislocations has been explained in terms of the model of Otsuka and Wayman (1975), who decomposed the austenite-martensite interface into an array of ordered dislocations on every third $(0\ 0\ 1)_{\beta_1'}$ plane (figure 5.16).

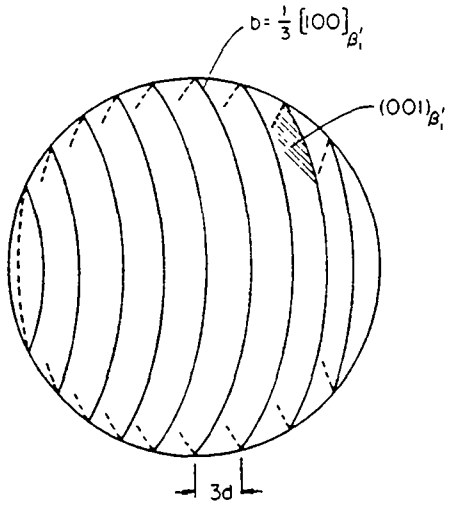

Figure 5.16: Dislocation model of the martensite-austenite interface as proposed by Otsuka and Wayman (1975).

The detailed TEM analysis of Andrade et al. (1984) and the high resolution electron microscopy (HREM) studies of Cook et al. (1983) and Lovey (1987) all indicated that the observed random stacking faults in M18R martensite are of the sequence or structural type. The fault vectors have been found to be $\pm\frac{1}{18}[691]_{\beta_1'}$ or $\pm\frac{1}{18}[\bar{6}91]_{\beta_1'}$. These fault vectors describe a single violation of the perfect M18R stacking sequence in form of one removed or inserted close packed plane. Depending on the character of the local environment which is created in the M18R structure, three different types of stacking faults can be distinguished: the hexagonal-type, the cubic type, and the twin-type fault (figures 5.17d - f). It is important to emphasize that none of these faults can be derived from the M18R sequence by a simple shear operation. Stacking faults that result from simple shears on the basal planes (displacement vector $\vec{b} = \pm\frac{1}{3}[100]_{\beta_1'}$, see figures 5.17b and c) have never been observed.

The formation of the sequence stacking faults is believed to take place during the transformation process. Andrade et al. (1984) have used the transformation mechanism of Ahlers (chapter 1) to explain how these sequence faults are formed by "wrong" shuffles during the second shear of the Ahler's model. Wrong shuffles allow for the accomodation of strain, which is induced during the transformation, and account for the simultaneous occurrence of the lattice invariant deformation and the homogenous lattice deformation. On the other hand, Andrade et al. (1984) showed that after transformation the sequence fault formation during a complex deformation of

the fully formed martensite by a sequence of $\pm\frac{1}{3}[100]\beta_1'$ dipoles may only be considered as a less realistic mechanism. In the following section it will be proposed that a simple $\pm\frac{1}{3}[100]\beta_1'$ partial dislocation motion occurs in the plane of an already existing sequence stacking fault so that this fault transforms into another type of sequence fault, without introducing a pure shear type stacking fault in the M18R structure.

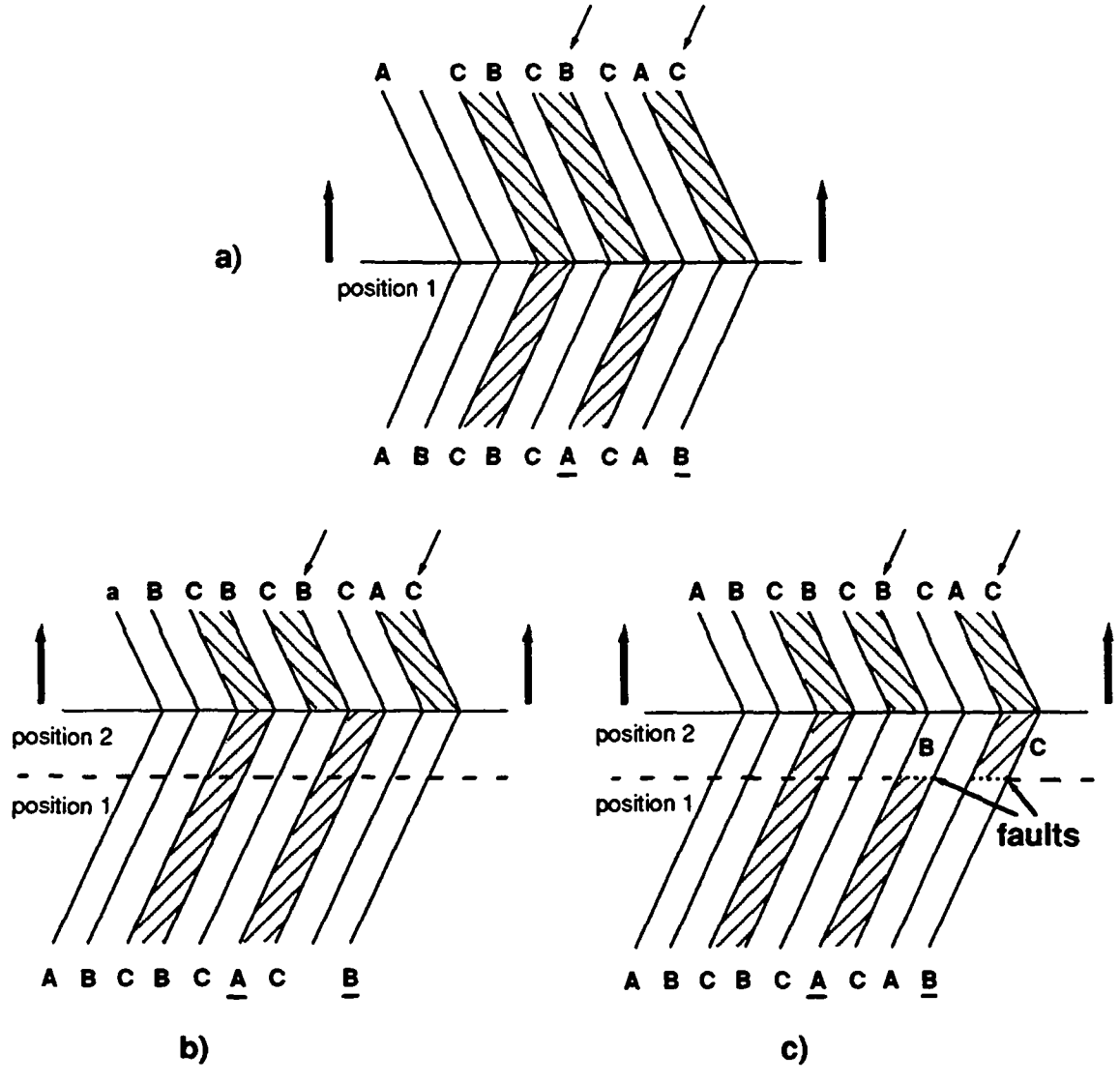

Figure 5.17: Random stacking faults in the M18R structure: a): perfect M18R structure, b) and c): shear type stacking faults (after shear in the pointed directions), d) - f): sequence type stacking faults (d) hexagonal type, e) cubic type, f) twin type).

5.4.2 Mechanism of the A/D Type Interface Motion

The mechanism of the A/D type interface motion as will be proposed in the following, attempts to explain the following points:

i) The origin of stacking fault changes during interface motion.

ii) The change of the stacking sequence by partial dislocation glide without introducing a pure shear type stacking fault.

iii) The stress conditions which lead to different modes of the A/D type interface displacement.

Stacking Fault Changes during A/D Interface Motion

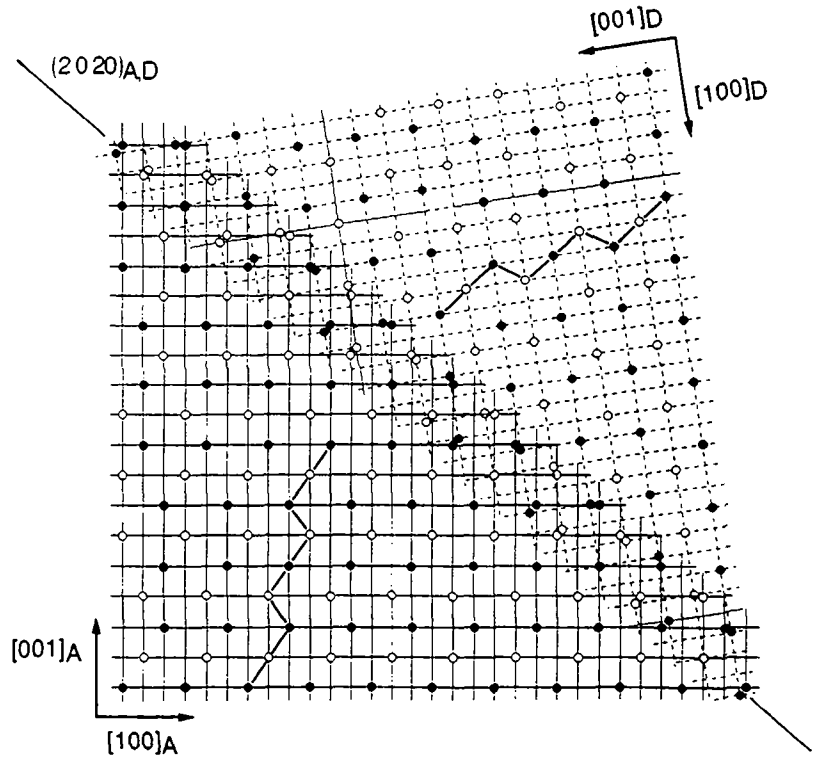

Figure 5.18: Atomic matching across a perfect A/D type interface, viewed along the common $[0\ 1\ 0]_{\beta'_1}$-direction (A-lattice full lines, D-lattice dashed lines). The close packed planes are stacked along the $[0\ 0\ 1]_{\beta'_1}$-direction. Note the regular stacking faults after every third $(0\ 0\ 18)_{\beta'_1}$ plane.

Changes of stacking disorders take place in order to improve the interfacial atomic configuration. This can be seen by viewing the atomic arrangement across a perfect A/D type interface, as is shown in figure 5.18. In the perfect M18R structure, where no random stacking faults are considered, the atomic matching is very good when the variants combine on the mutual $(2\,0\,20)_{\beta_1}'$ planes. The relative correspondence of atoms on both sides of the A/D interface is very close and small shufflings can bring both variants into coincidence. This observation confirms theoretical calculations of twinning shears and shuffles published by Saburi and Nenno (1982). However, the atomic arrangement across the A/D interface becomes energetically less favorable when random stacking faults, which are necessarily present in the faulted M18R structure, are introduced. Figure 5.19a shows the case where a cubic type stacking fault of the A-variant encounters a hexagonal type fault of the D-variant at the common interface. The resulting boundary energy of the $(2\,0\,20)_{\beta_1}'$ plane is visibly higher because of the atomic misfit along the interface.

This relatively poor matching can be improved, by the glide of one partial dislocation of the $(0\,0\,18)[100]_{\beta_1}'$ basal plane system. This dislocation will either introduce a new random stacking fault or change the character of an already existing stacking fault. In the first case a pure shear type stacking fault is created, while the latter case allows for the preformed sequence type stacking fault to keep its character after transformation. In order to account for the absence of pure shear type stacking fault, a criterion that has been concluded from "static" TEM analysis, only the latter mechanism will be considered in the following. The conversion between different types of sequence stacking faults has been suggested by Rios-Jara and Guénin (1987). This mechanism explains the Burgers vector of perfect dislocations, which remain in the austenitic phase after one transformation cycle.

Figure 5.19 shows how a cubic stacking fault can be transformed into a hexagonal fault by a $\frac{1}{3}[100]_{\beta_1}'$ shear on the indicated $(0\,0\,18)_{\beta_1}'$ plane. As can be seen in figure 5.19b the matching of atoms across the A/D interface is improved significantly after this shear. Fairly good matching between hexagonal faulted regions in M18R martensite has also been proposed by Katata and Saka (1989). It follows that due to the readjustment by changes of the stacking sequences, the A/D interface is very often not strictly determined and curved segments are observed. High resolution electron microscopy (HREM) observations prove that deviations of the theoretical $(2\,0\,20)_{\beta_1}'$ interface can be observed at the atomic scale (figure 5.20). The lattice image of figure 5.20a shows the fine structure of the A and D variants, viewed along the $[010]_{\beta_1}'$ direction. The fringe contrast is due to both the regular and random stacking faults. At higher magnification (figure 5.20b), the observations showed that the A/D interface is even irregular in depth so that atomic resolution of the interface structure could not be obtained.

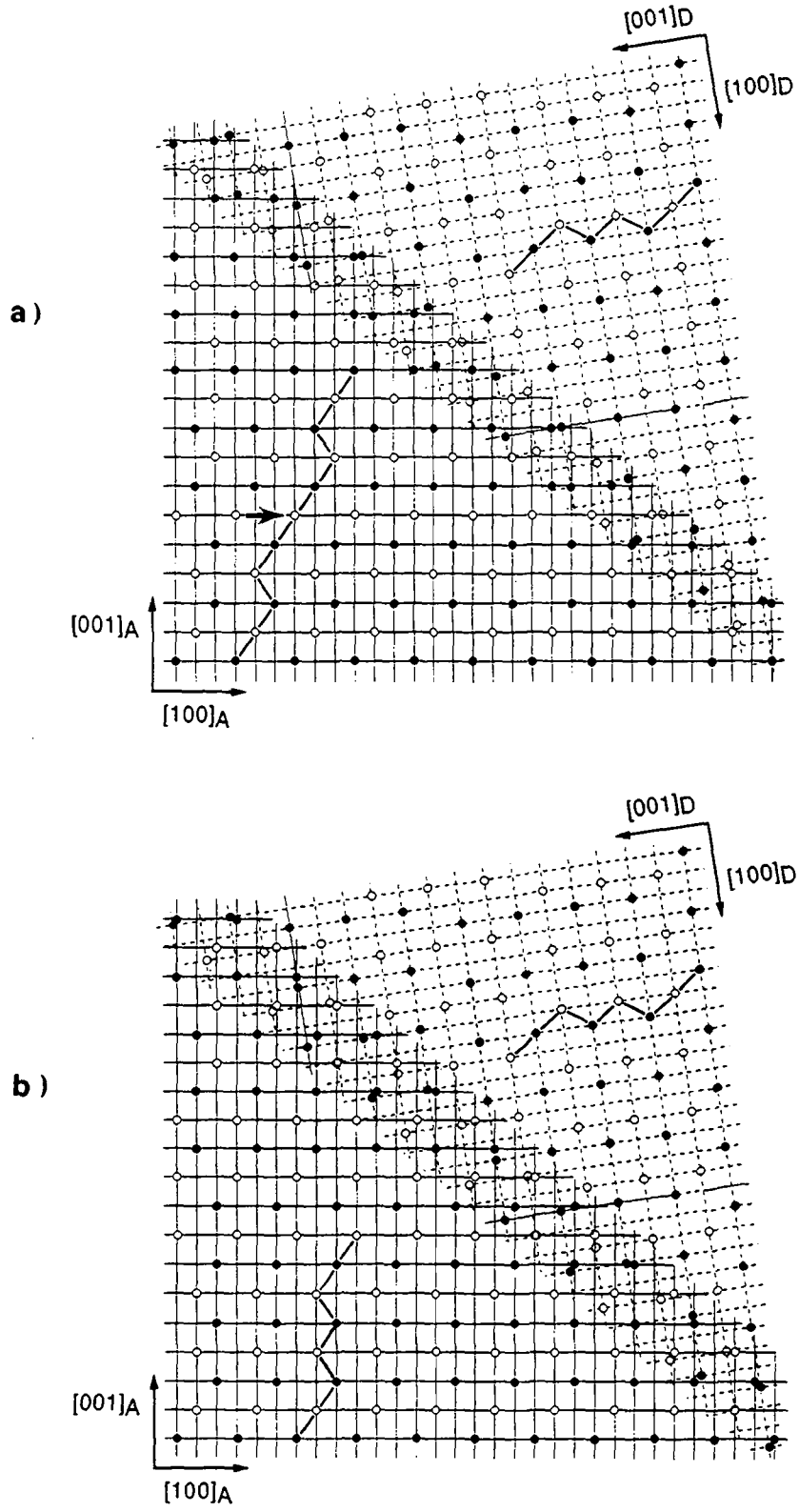

Figure 5.19: Atomic matching across an A/D type interface containing stacking disorders:
a) cubic fault in variant A and hexagonal fault in variant D.
b) M18R with a hexagonal stacking fault in both variants.

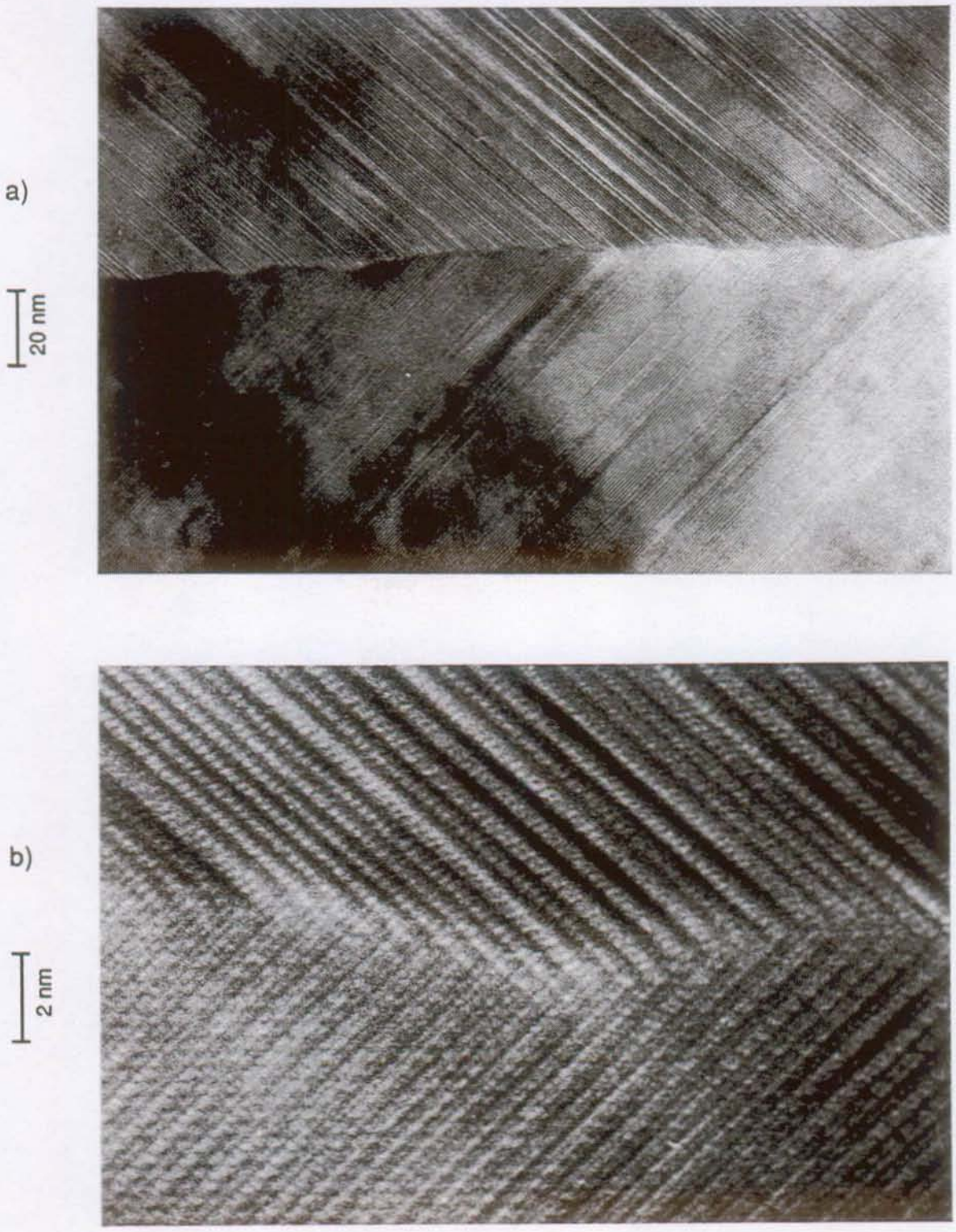

Figure 5.20: High resolution electron micrographs (taken by K.Hemker) showing an A/D type interface, viewed along the $[010]_{\beta_1'}$ direction:
a) The fringe contrast is due to both the periodic and random stacking faults. b) Photo taken at higher magnification shows that the A/D interface is irregular in depth.

The $\frac{1}{3}[100]_{\beta_1'}$ shear is assumed to occur by the motion of partial dislocations, even though their motion has not been directly observed during the A/D interface migration. However, this investigation has shown that glissile partial dislocations exist in M18R martensite. Otsuka and Wayman (1975) have suggested that the creation of $\frac{1}{3}[100]_{\beta_1'}$ partial dislocations comes from the formation of partial dislocation loops on the basal planes and not from the dissociation of perfect dislocations. Experimental evidence for partial dislocation loops has been given by the fact that most of the partial dislocations show identical contrast behaviour. This actually indicates that they have the same Burgers vector and do not result from the dissociation of a perfect dislocation.

Influence of Internal and External Stresses

The second important point in the description of the A/D type interface motion is to define the influence that the concurrent driving forces (external and internal stresses) have on the migration characteristics. It is assumed that :

- The external stress field (σ_{ext}) represents the driving force for a global interface displacement when the martensitic structure is deformed. The dominant parameter for σ_{ext} is the homogeneous shear stress component of the applied tensile stress in the deformation twinning system (τ_{tp}).

- The internal stress field (σ_{int}) drives the interface into the most favorable configuration in order to relax the internal stress. σ_{int} is dominated by a relatively inhomogeneous distribution of shear stress components that act in the basal planes of the converting variants (τ_{bp}). σ_{int} can arise from modifications of the neighboring martensite structure in the course of reorientation or from the τ_{bp} - component of the applied tensile stress during deformation.

Considering the observed dependence on the specimen orientation, the mechanism of the A/D interface movement can be described according to the extreme conditions of σ_{int} and σ_{ext}:

I) $\sigma_{ext} >> \sigma_{int}$

If $\sigma_{ext} >> \sigma_{int}$, the external driving force for the interface displacement is much larger than the internal force that drives the interface into the best relaxed interface configuration. In this situation, the interface moves in order to produce a macroscopical deformation in the direction of the applied stress. This fact implies that the interface energy is rather high and that the

A/D-interface always stays in a straight position during motion (figure 5.21a). The interface movement occurs without changes in the stacking disorder.

II) $\sigma_{ext} << \sigma_{int}$

This case accounts for the situation where the driving force for internal stress relaxation exceeds the driving force for a global interface displacement. Therefore, the interface energy is lowered to a minimum and curved segments of the A/D boundary are formed (figure 5.21b). The interface motion only occurs if σ_{int} can not be compensated by local changes of the stacking sequence. In this case, a jerky interface movement occurs over small distances and an inhomogeneous distribution of τ_{bp} leads to stacking fault changes which may occur frequently in order to adjust local differences in the stackings at the interface.

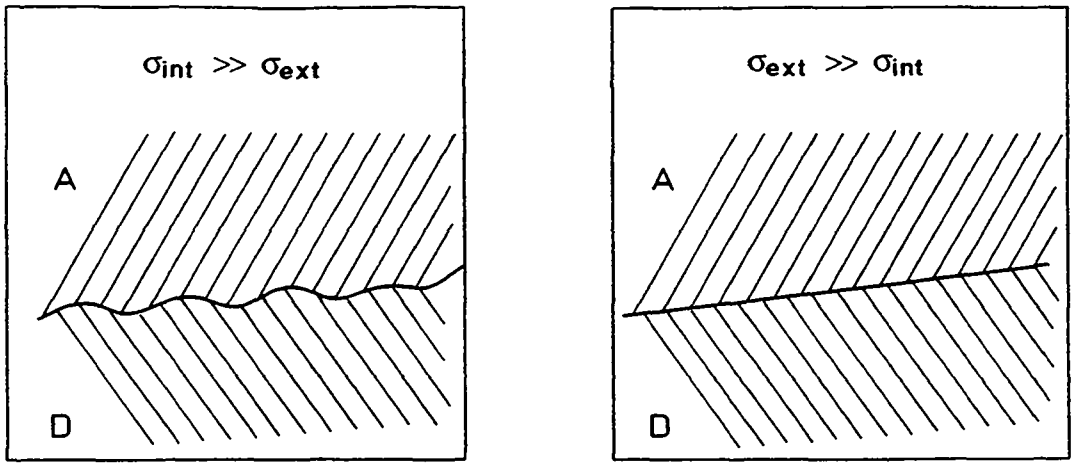

Figure 5.21: A/D type interface motion for different stress conditions. For explanations see text.

When comparing the presented model of the A/D type interface motion with those models that have been described in this chapter, the following aspects are worth mentioning:

- Stacking fault changes are possible. The observations of Katata and Saka (1989) indicating that the stacking disorders are preserved must be related to the very small distance of interface motion (10 nm) that they observed. In contrast, the distances observed in the present work are significantly larger (100 - 200 nm, figures 5.6 and 5.7) and therefore the probability of stacking changes increases.

- Stacking fault changes are possible without the formation of defects (figure 5.15b) in contrast to the mechanism that was proposed by Lovey (1987). The fast moving partial dislocations

which are emitted at the interfaces cover the whole basal plane with a new stacking faults, as it was also suggested by Adachi and Perkins (1985). This indicates that the stress necessary for the creation of partial dislocations is also sufficient for their displacement and no faults are created inside the martensitic variant.

5.5 Conclusions

- The displacement mechanism of the A/D type intervariant twin boundary in M18R martensite depends on the relative combination of the internal and external stresses acting in both the twinning and basal planes of the converting variants. When the resolved stress on the basal planes is high enough, the stacking sequences inside the variants change frequently. But, when the interface motion is controlled by an elevated shear stress in the twinning plane, the stacking disorders are preserved.

- Stacking fault changes occur during A/D interface motion in order to improve the atomic matching across the interface. Randomly distributed sequence type stacking faults can be converted from one type to another by the motion of partial dislocations on the basal planes. This mechanism is consistent with both the existence of glissile partial dislocations and the displacement vectors that have been published for the stacking faults in M18R martensite.

CHAPTER 6

General Discussion: Hysteresis Effect, Microstructure and Internal Friction in Cu-Zn-Al Shape Memory Alloys

The aim of this work has been to develop a more complete understanding of the macroscopic hysteresis effect and to identify its relationship to the microstructural mechanisms that are responsible for energy dissipation during martensitic phase transformations. As has been outlined in chapter 1, the measurement of internal friction (IF) has been used to relate both the microstructural evolution and the associated energy dissipation (figure 1.27).

This discussion starts with a summary of the results that characterize the relationship between the macroscopic hysteresis effects, the IF behaviour and the microstructural aspect. The results include single and polyvariant martensitic transformations as well as different incomplete transformation cycling programs all of which were performed in Cu-Zn-Al alloys. A description of the damping mechanism that is believed to be responsible for the anelastic deformation during martensitic transformation in shape memory alloys, will be presented. Special emphasis will be put on the influence that microstructural parameters have on the IF behaviour.

The second part of the discussion is addressed to the interpretation of the macroscopic hysteresis effects. These effects are discussed in the light of microstructural mechanisms which have been identified with the combined methods of IF measurements and TEM *in situ* observations. The phenomenological hysteresis model of the thermoelastic balance equation will be formulated and used for the prediction of hysteresis loops during both complete and incomplete transformation cycles. A microscopical interpretation of the functional forms of the non-chemical energy contributions that enter into the thermoelastic balance equation, will also be given. Typical hysteresis effects such as asymmetric hysteresis behaviour, the shape of internal transformation paths and shift of transformation sub-loops will be explained by integrating both phenomenological and microstructural informations.

6.1 The Relationship between Microscopic and Macroscopic Hysteresis Effects

6.1.1 Single Variant and Polyvariant Transformations

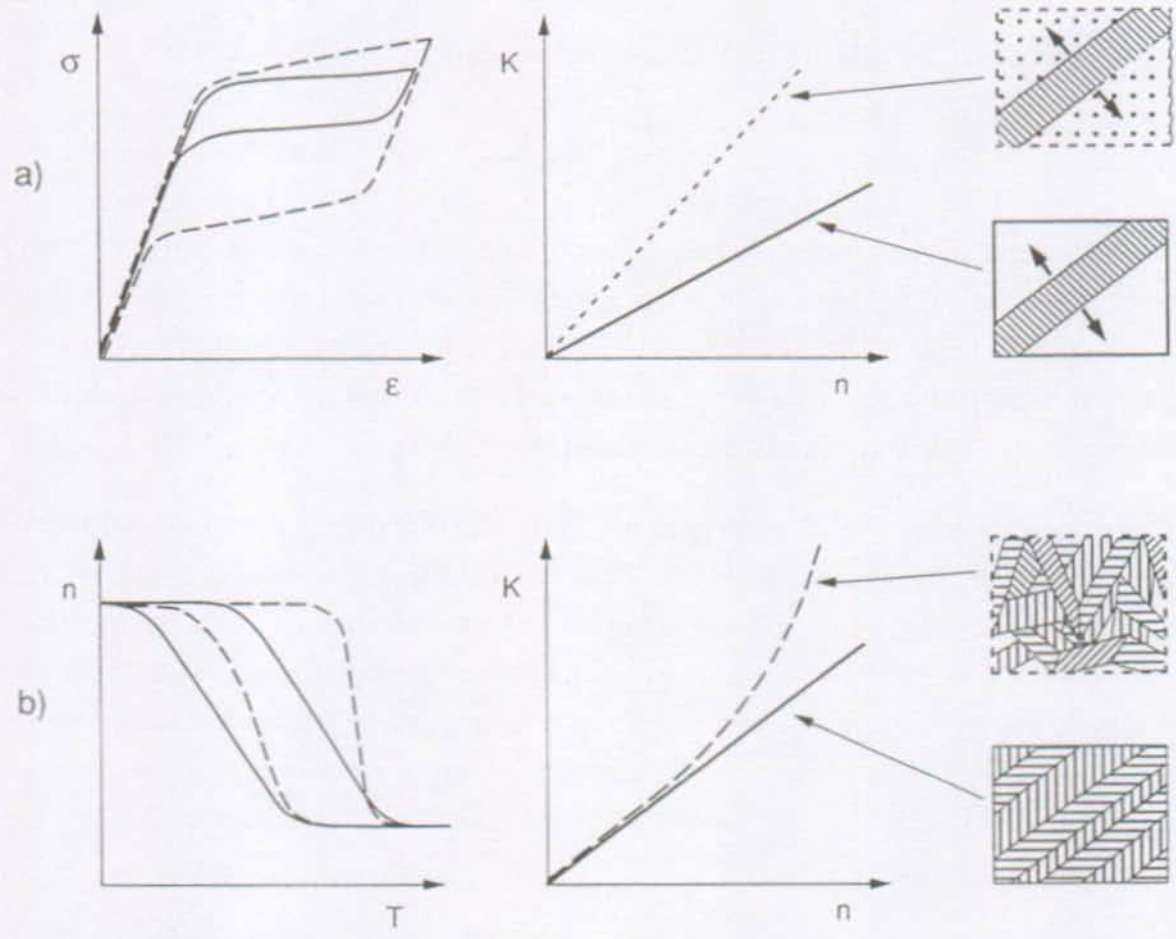

Figure 6.1: Relationships between macroscopic hysteresis, internal friction and microstructure:
a) Single variant transformations with and without precipitates (dashed and full lines, respectively),
b) Polyvariant transformations that form few and many different variants (dashed and full lines, resp.).

The relationship between the microscopic (IF) and macroscopic hysteresis effects is most evident during single variant transformations and it has been quantitatively established in chapter 4. The small stress hysteresis that has been derived from the IF values ($\Delta\sigma = 0.2$ MPa) corresponds to the stress hysteresis which has been measured for the motion of a single martensite-austenite interface by Lovey et al. (1992). Figure 6.1a shows that in a defect-free austenitic single crystal, the transforming interfaces dissipate only a small amount of energy on macroscopic (enclosed surface of the σ - ε curve) and microscopic scales ("normalized" IF (K) as a function of the transformed volume fraction, n); in the presence of γprecipitates both hysteresis effects increase equivalently.

During martensitic polyvariant transformations the macroscopic hysteresis effect and the IF behaviour are both dependent on the martensite morphology, which develops during transformation (figure 6.1b). When only a few different variants are formed (educated martensite and stress-induced martensite), the transformation hysteresis has a symmetric shape and the "normalized" IF (K) increases linearly with the transformed volume fraction (n). The formation of many different martensitic variants or self-accomodating groups is accompanied by an increasing hysteresis width ("asymmetric hysteresis") and a non-linear increase of K as a function of n.

6.1.2 Incomplete Transformation Cycles

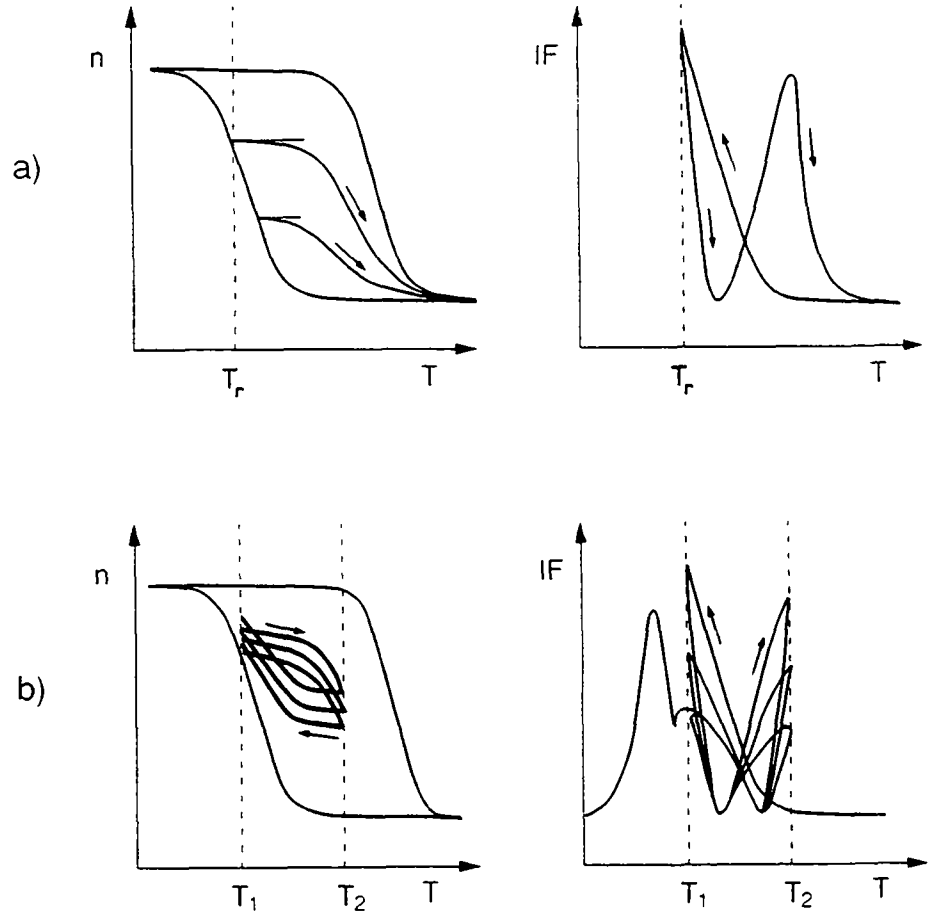

Figure 6.2: Relationships between macroscopic hysteresis and internal friction behaviour: a) Partial transformation cycles, and b) the shift of transformation sub-loops. Note the "butterfly" shaped Q^{-1}-curves during incomplete transformations.

Incomplete transformation cycles in Cu-Zn-Al shape memory alloys are characterized by distinct internal transformation trajectories. The transformed volume changes slightly during the partial heating and cooling cycles as soon as the temperature of the reversion point (T_r) is passed (figure 6.2a). The simultaneously observed IF behaviour demonstrates that Q^{-1} changes continuously, following a "butterfly" shaped curve.

Hysteresis instabilities have been observed during repetitive temperature cycling (PTC). The transformation sub-loops shift as a function of the number of cycles towards higher transformed volume fractions and the transformed volume per cycle decreases (figure 6.2b). The associated IF evolution is characterized by decreasing values of the transient IF ($Q^{-1}{}_{Tr}$), but the results of the IF analysis indicate that the damping mechanism is the same during incomplete cycles as it is during complete transformation cycles (chapter 3).

6.2 The Damping Mechanism of Cu-Zn-Al Shape Memory Alloys

6.2.1 General Aspects of Anelasticity during Martensitic Phase Transformations

The principle origin of damping or energy dissipation during dynamic deformation tests is the anelastic deformation that is produced by the applied measuring stress. The effect of anelasticity is, in many cases, associated with thermally activated relaxation mechanisms, but during martensitic phase transformations the "anelastic" deformation is due to the hysteretic movement of crystal defects which are involved in the transformation process. The observed IF peak does not represent a relaxation peak but is instead purely hysteretic (athermal) in character. In spite of the inconsistency in terminology, the damping phenomena of shape memory alloys will nevertheless be referred to as the effect of *anelastic* deformation.

The quantitative interpretation of damping mechanisms requires the definition of the crystallographic nature of the defects and the associated systems, where the anelastic deformation takes place. For the case of non-thermally activated anelasticity an additional statement about the hysteretic character of deformation during the IF measurement is required. Furthermore, the relationship between the deformation and the applied measuring stress has to be defined. The current understanding of anelasticity during martensitic phase transformations are summarized in the following with respect to the IF models that are presented in chapter 3.

The crystallographic nature of anelastic deformation has been related to the shear deformation, which is created in the habit plane when a transforming interface between martensite and austenite moves. It has been assumed that the deformation is completely

hysteretic. According to this mechanism, the anelastic deformation ($d\varepsilon_{an}$) is proportional to the transformation strain (ε^t) and the transformed volume per oscillation (Δn). The influence of the applied measuring stress ($\sigma_m = \sigma_0 \sin\omega t$) is reflected on $d\varepsilon_{an}$ either directly ("transformation plasticity") or indirectly through a modification of Δn ("pure transformation strain").

The results of this study have shown that both the hysteretic character and the nature of anelastic deformation during martensitic transformation are more complex than is mentioned above. The macroscopic hysteresis effect and the microstructural properties of an investigated shape memory alloy have to be considered for the explanation of the anelastic effect. It has been demonstrated that the motion of martensite-austenite interfaces during single variant transformations is not completely hysteretic. Instead, the interface motion during IF measurement is partially reversible and dominated by the small macroscopic hysteresis effect, which is involved in the displacement of single martensite-austenite interfaces. The anelastic deformation during martensitic polyvariant transformations is, similar to that during single variant transformations, not completely hysteretic, but depends in addition on the evolution of the martensitic microstructure.

The following discussion of anelasticity in Cu-Zn-Al shape memory alloys concentrates on the explanation of the transient IF (Q^{-1}_{Tr}) which has been expressed for the IF analysis in chapter 3 by equation (3.23):

$$Q^{-1}_{Tr} = k \cdot \frac{\partial n}{\partial T} \cdot f\left(\frac{\dot{T}}{\omega \sigma_0}\right) \qquad (6.1)$$

This equation will be used to discuss two different aspects. The dependence of Q^{-1}_{Tr} on the external parameters, $f\left(\frac{\dot{T}}{\omega \sigma_0}\right)$, will be used to define the influence of the applied measuring stress (σ_0) on the anelastic deformation. The influence of microstructural properties will be explained by both the transformed volume fraction per cycle (Δn, $\Delta n = \frac{\partial n}{\partial T} \cdot \frac{\dot{T}}{f}$, for $\dot{T}$, f and σ_0= const.) and the "*fragmentation*" parameter ($x = x\,(n)$) that accounts for the additional IF contributions at the end of martensitic transformations.

6.2.2 The Relationship between Anelastic Deformation and Applied Measuring Stress

The results of this work have shown that the transient part of the IF peak decreases as a function of σ_0 and increases non-linearly as a function of $\frac{\dot{T}}{\omega \sigma_0}$, see the schematics of figure 6.3. The decrease of Q^{-1}_{Tr} with increasing σ_0 (figure 6.3a) is correctly predicted by both the second part of Delorme's model (equation 3.17) and the model of Gremaud-Bidaux

(figure 3.25), but the non-linear dependency of $Q^{-1}{}_{Tr}$ on $\frac{\dot{T}}{\omega \sigma_0}$ is only predicted by the latter model. Figure 6.3b shows that the transient IF that was observed at the beginning of the transformation (k_I') differs only slightly from the calculated k' curves of the Gremaud-Bidaux model, but differ drastically from the linear slope of k' versus $\frac{\dot{T}}{\omega \sigma_0}$ as proposed in the Delorme's model. Therefore, it has been concluded that the role of the external parameters on the transient IF peak is sufficiently explained by the model of Gremaud-Bidaux. The mechanism of anelastic deformation in this model is based on the Clausius-Clapeyron equation, which defines the relationship between T and σ_0 for the transformation strain.

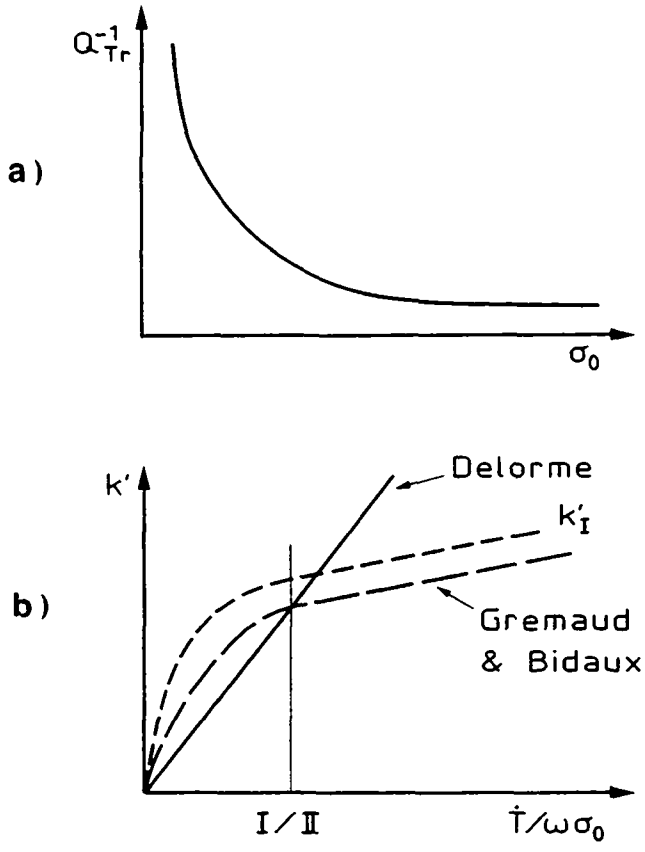

Figure 6.3: Schematic representations of a) $Q^{-1}{}_{Tr}$ as a function of σ_0 and b) Experimental (k_I') and theoretical curves for k' as a function of $\frac{\dot{T}}{\omega\sigma_0}$.

With this result, it can be concluded that the anelastic deformation ($d\varepsilon_{an}$) in Cu-Zn-Al alloys does not result from the effect of *transformation plasticity*, according to the first model of Delorme (equation 3.10), because a σ_0 independent transient IF (equation 3.12) has not been observed. The absence of transformation plasticity is equivalent to the assumption that the oscillating measuring stress is low with respect to other stresses. This is the case during stress-induced transformations, where the external tensile stress (σ_{ext}) controls the growth of those variants which give the maximum deformation, and during temperature-induced

transformations, where internal stresses (σ_{int}) determine the orientation of the transforming variants. Both situations are schematically presented in figures 6.4a and 6.4b. Transformation plasticity only occurs, if σ_0 is comparable to σ_{int} (figure 6.4c). In the present study, however, the oscillation amplitudes were lower than the critical value necessary to obtain a σ_0 independent transient IF.

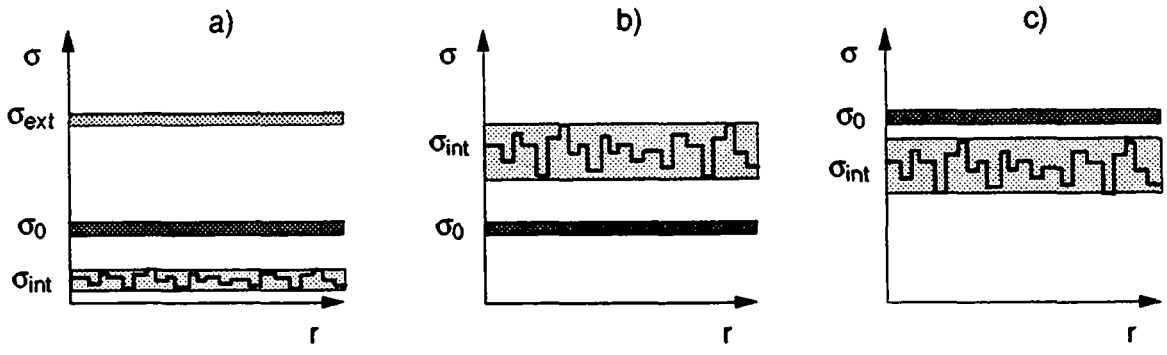

Figure 6.4: The applied oscillation stress in comparison with the external stress (σ_{ext}) and internal stress (σ_{int}) levels during stress-induced transformations (a) and temperature-induced transformations with a small and a high oscillation amplitude (b) and c), respectively).

We therefore consider the case of a *"pure" transformation strain*, which is independent of σ_0, according to equation (3.16). The role of σ_0 is restricted to the influence on the microstructural parameter. In the case where the microstructural parameter is the transformed volume fraction (Δn), σ_0 and T are assumed to be equivalent parameters, which determine the transformation rate that is given in equation (3.19).

In conclusion, σ_0 participates in the growth of transforming interfaces but does not determine the direction of their movement.

This conclusion is also valid for the transient IF at the end of the transformation (k_{II}') because it shows qualitatively the same dependence on $\frac{\dot{T}}{\omega\,\sigma_0}$, as it was observed for k_I' (figure 3.18). The quantitative difference between both contributions ($k_{II}' > k_I'$) will be explained by introducing an additional microstructural parameter (the "fragmentation" parameter) that has to be considered for k_{II}'.

6.2.3 The Damping Mechanism and the Role of Microstructural Parameters

In most anelastic phenomena it is appropriate to assume that the internal or microstructural parameters are constant during one oscillation cycle. When this is true, the stress-strain dependence can be analyzed as a function of time and temperature. However, the transient anelastic deformation associated with phase transitions is due to the transformation kinetics and is therefore dependent on structural changes that occur during one oscillation period. To a first approximation, the structural changes have been described by the volume fraction that is transformed during one oscillation, Δn (Delorme, 1973). A linear relation between the transient IF (Q^{-1}_{Tr}) and Δn, or equivalently, between the "normalized" IF (K) and the amount of transformed volume (n) would result, if the microstructural mechanisms that give rise to energy dissipation were independent of the transformation stage (actual amount of transformed volume).

The results of the present study show that a linear dependency between K and n is only observed when the number of transforming variants is very small (figure 6.1). This is true for single variant transformations and polyvariant transformations where a macroscopic shape change occurs during transformation (in trained materials and during stress-induced transformations). On the other hand, a non-linear relationship between K and n is observed during thermally-induced transformation of non-educated specimens (figure 6.1b), where the transformation strain can not be released in terms of macroscopic deformation, but has to be accommodated by different arrangements of martensitic variants. During accomodation, already existing martensitic structures can be rearranged by the displacement of mobile martensitic interfaces. The first behaviour (K proportional to n) will be attributed to the case of *IF without variant interaction* and the second behaviour (non-linear dependency of K and n) will be defined as *IF with variant interactions*.

IF during Transformation without Variant Interactions

When the anelastic deformation is only influenced by the formation and growth of martensitic variants and the interfaces between different variants are not displaced (no variant interaction), the principle damping mechanism is the hysteretic movement of the transforming martensite-austenite interfaces in the direction of the oscillating measuring stress. This situation is best represented by single variant transformations, where no martensite-martensite interfaces exist. The results of this study have shown that, in this case, *the anelastic deformation occurs in the habit plane system and its hysteretic character is associated to the macroscopic hysteresis effect.*

It was shown that the transient IF (Q^{-1}_{Tr}) depends linearly on the stress component of the habit plane system (τ_{hp}/τ_m), while the shear stress component of the basal plane system (τ_{bp}/τ_m) does not influence the Q^{-1}_{Tr} values (figure 4.12) and that the normalized IF is proportional to the amount of transformed volume (figure 4.13).

The interface migration during IF measurement is not completely hysteretic as it has been assumed in the IF models, but it has been found to be partially reversible (figure 4.17). The stress hysteresis which is involved during IF measurements of single variant transformations, was quantitatively evaluated in chapter 4. The results showed that the microscopic stress hysteresis that was obtained from the measured IF values is in good agreement with the small macroscopic hysteresis ($\Delta\sigma = 0.2$ MPa) that was determined for single interface transformations (Lovey et al., 1992). In the presence of γ precipitates the microscopic stress hysteresis increases ($\Delta\sigma = 0.6$ MPa), according to the increasing macroscopic hysteresis.

In polyvariant Cu-Zn-Al alloys the values of the effective anelastic deformation (ε^t_{eff}) that result from the measured IF, are much smaller (factor 25) than the theoretical ε^t - values which would result from IF models that are based on a complete hysteretic interface motion. Therefore, the effective transformation strain during IF measurement of Cu-Zn-Al polycrystals must also be explained by a partially reversible interface motion. This behaviour can be explained by the thermoelastic character of martensite and the small transformation hysteresis in shape memory alloys. The IF models that assume a complete hysteretic interface motion have been developed for non-thermoelastic martensitic transformations (in Fe-Cr-Ni and Co-Ni by Delorme and in pure Co by Bidaux), which show a very large transformation hysteresis. Consequently, the possibility that the interface motion can be reversible during IF measurements must not be considered and the assumption of complete hysteretic interface motions is correct for the case of non-thermoelastic martensitic transformations.

IF during Transformation with Variant Interaction : Model of Fragmentation

When differently oriented martensitic variants interact during the transformation and intervariant boundaries (martensite-martensite interfaces) are displaced, the transient IF (K) is no longer a linear function of n, indicating that the amount of anelastic deformation increases with higher transformed volume fractions. In this case, the influence of the microstructural evolution on the measured IF is not sufficiently described by the volume fraction that is transformed during one oscillation (Δn). Therefore, a second microstructural parameter will be introduced, which explains the additional anelastic deformation that comes from the displacement of martensite-martensite interfaces during the interaction between different martensitic variants. The quantitative description of variant interactions is conducted in terms

of the model of fractal geometry, which has been applied to the characterization of martensitic microstructures by Hornbogen (1987).

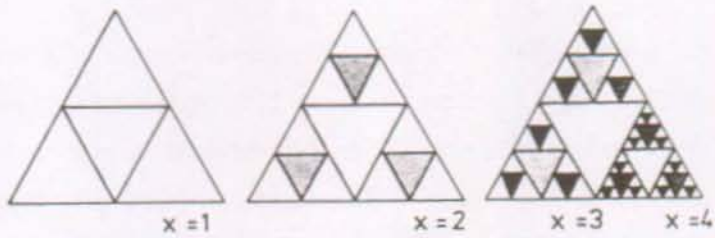

Figure 6.5: Geometrical model of subsequent fragmentations of a triangle (Hornbogen, 1987), showing the degree of fragmentation (x).

a)

b)

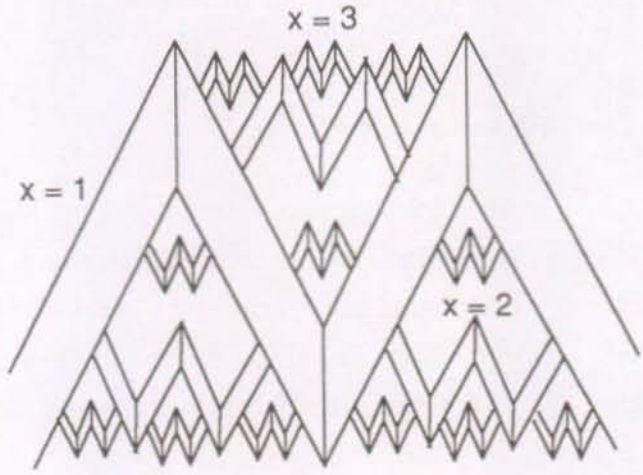

Figure 6.6: a) Fragmentation effect observed by optical microscopy in the martensitic microstructure of alloy 1, close to a grain boundary, b) Schematic drawing.

The model of fractal geometry has been used to characterize the microstructure of several types of martensite, including the morphology of martensite in shape memory alloys. Fractal martensite is built up of successive fragmentation of previously formed variants. Fragmentation or the appearance of smaller variants occurs, if the lateral growth of the transforming variants is restricted by the increasing elastic stress at the martensite-austenite interfaces. The formation of new orientations is prompt and it has the most probable nucleation site at the β/β' interface. Figure 6.5 presents the principle features of fractal geometry with a simplified model which shows the fragmentation of a triangle and defines the degree of fragmentation (x).

Evidence for the fractal nature of martensite in the studied Cu-Zn-Al alloys has been found especially in the microstructure of the coarse grain alloys. As an example, figure 6.6 demonstrates the fragmentation of a V-shaped self-accomodating group; the experimental observation (figure 6.6a) can be compared to a schematic model (figure 6.6b). In this case, the degree of fragmentation or the number of variant generations varies between three and four ($3 < x < 4$). Each fragmentation results in an increase of the martensite interface density. Interactions between the new formed martensitic variants and the already existing structure must occur in order to adjust the new situation of elastic stresses. The martensitic phase modifies the arrangements of its microstructure and reorients the martensitic variants by the migration of mobile intervariant boundaries. The displacement of martensite-martensite interfaces in the field of a locally high elastic stress field, including partial dislocation and stacking fault motions, has been observed by transmission electron microscopy (chapter 5).

The non-linear increase of the transient IF as a function of n can be explained in terms of the "fragmentation" parameter, $x(n)$, if it is assumed that the additional anelastic deformation which is due to the migration of intervariant boundaries (martensite-martensite interfaces), increases with each fragmentation. In this case, the transient part of the IF peak (Q^{-1}_{Tr}) can be expressed as:

$$Q^{-1}_{Tr}(n) = k \cdot x(n) \cdot \Delta n \qquad (6.2)$$

In this equation, Q^{-1}_{Tr} is not only dependent on the amount of transformed volume per cycle (Δn), but also depends on the fragmentation parameter ($x(n)$). The dependence of the "fragmentation" parameter on n could in principle be established experimentally by measuring the fragmentation sequence during transformation in each grain and evaluating the average value of $x(n)$. However, this is a very extensive investigation and was beyond the scope of the present study. But, the $x(n)$ dependence has been calculated from the $Q^{-1}_{Tr}(n)$ curve and the k-value at the beginning of the transformation ($k = k_I$).

$x(n)$ is equal to:

$$x(n) = \frac{Q^{-1}_{Tr}(n)}{k_I \Delta n} \qquad (6.3)$$

The evolution of $x(n)$ as described by this equation is shown in figure 6.7 for the studied alloys. The obtained $x(n)$ curves are in good agreement with the predictions of the fractal theory (Hornbogen, 1987). This model suggests that the degree of fragmentation increases non-linearly at the end of the transformation and that the number of fragmentations should decrease with smaller grain sizes. In fact, figure 6.7 shows that a smaller degree of fragmentation is observed in the grain refined alloy 2 than in the coarse grain alloys 1 and 3. These results are further confirmed by the degrees of fragmentations that can be derived from the martensitic microstructures of both alloys (figures 3.1). The x - values of alloy 1 ($x \geq 4$) and alloy 2A ($2 \leq x \leq 3$) are comparable with the obtained values in figure 6.7. The martensite structures of both educated martensite (alloy 2B) and stress-induced martensite (alloy $2A_\sigma$) do not have fractal character and this explains the horizontal line in figure 6.7 ($x = 1$).

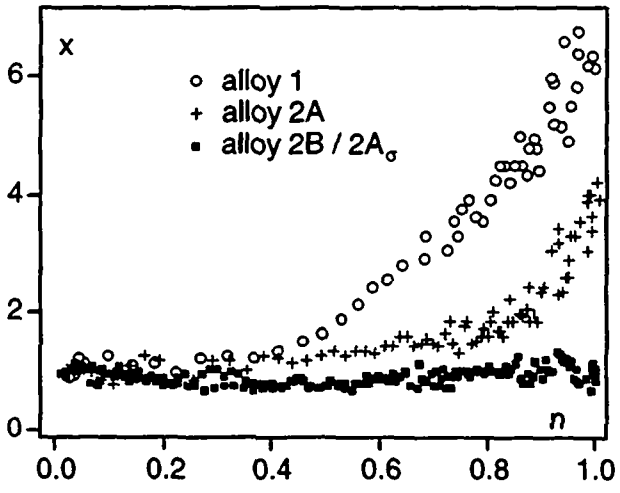

Figure 6.7: Degree of fragmentation (x) as a function of n in the studied Cu-Zn-Al alloys.

6.2.4 The Modified Equation for the Transient Part of IF, Q^{-1}_{Tr}

The equation for the transient part of the IF peak (Q^{-1}_{Tr}) that is observed during martensitic phase transformations in shape memory alloys, can be formulated as follows:

$$Q^{-1}_{Tr} = k \cdot x(n) \cdot \frac{\partial n}{\partial T} \cdot f\left(\frac{\dot{T}}{\omega \sigma_0}\right) \qquad (6.4)$$

The new Q^{-1}_{Tr} equation accounts for the dependence of the transient IF peak on both the transformation volume fraction per cycle (Δn) and the intensity of martensite variant

interactions *(x(n))*, which depends on microstructural properties of the parent phase (e.g. grain size) or the transformation conditions (educated and stress-induced martensite). Δn is associated with the anelastic deformation due to the movement of martensite-austenite interfaces and the fragmentation parameter *x(n)* includes the anelastic deformation due to the movement of martensite-martensite interfaces in the course of accomodation (fragmentation) processes. On the other hand, $x(n)$ can also be interpreted with the relationship between the transformation hysteresis effect and the internal friction. The motion of martensitic interfaces relaxes locally the elastic strain energy and this leads to an increase in stress hysteresis of the martensite-austenite interface motion. Both effects, the additional martensite-martensite interface motions and the more hysteretic martensite-austenite interface motion increase the dissipated energy and explain the simultaneous increase of the macroscopic and microscopic hysteresis effects at the end of martensitic transformations.

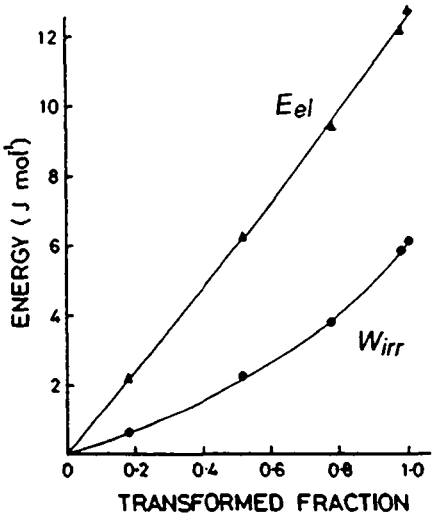

Figure 6.8: Elastic energy (E_{el}) and dissipated energy (W_{irr}) as a function of n as measured by calorimetry during partial temperature cycles (Planes et al.,1988).

A recent study of Planes et al. (1988) has employed calorimetric measurements of partial transformation cycles in order to determine the dissipated energy in dependence of the transformed volume fraction. The obtained results, see figure 6.8, demonstrate a non-linear dependence of dissipated energy (W_{irr}) on the transformed volume fraction. This behaviour is very similar to the dependence of the "normalized" IF on the transformed volume (figure 6.1b). The dissipated energy of a calorimetric run stems from a thermal analysis where chemical and non-chemical energy contributions have to be separated (chapter 1). On the other hand, the internal friction is a direct measure of local energy dissipation, where chemical energy contributions are not involved. The equivalent results of both methods prove that microscopic and macroscopic hysteresis contributions are closely related to each other.

6.3 The Macroscopic Hysteresis Effect and Responsible Transformation Mechanisms

This discussion of macroscopic hysteresis effects starts with the formulation of the phenomenological model that is based on the thermoelastic balance equation (equation 1.9). The functional forms of the non-chemical balance forces which are necessary for the prediction of the experimentally observed hysteresis curves, will be established and correlated with the necessary microstructural conditions. The characteristic features of the macroscopic hysteresis that have been observed in this investigation (i.e. the asymmetric hysteresis shape, the internal transformation paths and the shift of transformation sub-loops) will be explained with the microstructural changes that occur in shape memory martensites during the relaxation of the elastically stored energy.

6.3.1 The Phenomenological Model of the Thermoelastic Balance Equation

As already established by Salzbrenner and Cohen (1979), the main characteristics of the hysteresis loop (i.e. temperature-stress location, slope and width) are intimately related to the energy terms, which contribute to the thermoelastic balance. The thermoelastic balance is an equilibrium condition, where it is assumed that the total Gibbs free energy difference per unit volume between martensite and parent phase (Δg) is zero:

$$\Delta g^{P\rightarrow M}(n,T) = 0 \quad \text{and} \quad \Delta g^{M\rightarrow P}(n,T) = 0 \tag{6.5}$$

$\Delta g^{P->M}$ and $\Delta g^{M->P}$ are the total Gibbs free energy differences per unit volume between martensite and parent phase during forward and reverse transformations, respectively. n stands for the fraction of transformed volume and T is the temperature.

The total Gibbs free energy per unit volume consists of a chemical (g_{ch}) and a non-chemical energy contribution (g_{nch}), where the latter is usually separated into the reversible elastic energy (g_{el}) and the irreversible, dissipated energy (g_{dis}). The balance equations for both the forward (P->M) and reverse (M->P) transformations are given by:

$$\text{P -> M:} \qquad g_{ch}^{P\rightarrow M} + g_{el}^{P\rightarrow M} + g_{dis}^{P\rightarrow M} = 0 \tag{6.6}$$

$$\text{M -> P:} \qquad g_{ch}^{M\rightarrow P} + g_{el}^{M\rightarrow P} + g_{dis}^{M\rightarrow P} = 0 \tag{6.7}$$

According to Olson and Cohen (1975) these thermoelastic balance equations represent a local equilibrium at individual interfaces. In a partially transformed specimen, g_{ch} is constant through a chemically homogeneous material but g_{el} and g_{dis} are inhomogeneous. If this were not true, the thermoelastic equilibrium would be reached at the same point for every portion of the material and it would transform homogeneously.

The concept of thermoelastic balance has been applied by Li Lü et al. (1990) for the development of a mechanical hysteresis model and has been revised into a very illustrative and useful form by Cesari et al. (1992). The thermoelastic balance equation will therefore be formulated as it was presented by Cesari.

Formulation of the Thermoelastic Balance Equation (Cesari et al., 1992)

In the description of Cesari et al. (1992) the thermoelastic balance equation is also written as the balance of competing forces: the chemical driving force (g_{ch}), the reversible elastic force (g_{el}) and the dissipative frictional force (g_{dis}). The knowledge of the functional forms of the competing forces would allow for the calculation of the $n(T)$ path and therefore for the determination of the hysteresis loop. The chemical driving force is usually assumed to vary linearly with temperature:

$$g_{ch}^{P\rightarrow M}(T) = -\Delta s(T_0-T) \qquad (6.8a)$$

$$g_{ch}^{M\rightarrow P}(T) = \Delta s(T_0-T) \qquad (6.8b)$$

where Δs is the transformation entropy change per volume unit and is considered to be the same for both forward and reverse transformations. T_0 is the equilibrium temperature where the parent and martensite phases have the same chemical free energy.

The functional forms of the non-chemical forces are not straightforward. Although possible microscopical interpretations for these contributions are given in section 6.3.2., direct information is neither available from the theoretical point of view nor from the experimental results.

The elastic force can be considered to simply increase linearly with the amount of transformed volume (n).

P -> M: $$g_{el}^{P\rightarrow M}(n) = b \cdot n \qquad (6.9a)$$

M -> P: $$g_{el}^{M\rightarrow P}(n) = -b \cdot n \qquad (6.9b)$$

where b is a constant. b is the same for both transformations, if g_{el} is completely reversible in such a way that the elastic energy stored during forward transformation is completely released during the reverse transformation.

The frictional force, which opposes both transformations, is supposed to consist of both a constant friction force that is independent of n, and a friction term that is proportional to n:

P -> M: $$g_{dis}^{P\rightarrow M}(n) = a^{P\rightarrow M} + c^{P\rightarrow M} \cdot n \qquad (6.10a)$$

M -> P: $$g_{dis}^{M\rightarrow P}(n) = a^{M\rightarrow P} + c^{M\rightarrow P} \cdot (1-n) \qquad (6.10b)$$

where *a* and *c* are constants that can be different during forward and reverse transformation.

By inducing equations (6.8) - (6.10) into equations (6.6) and (6.7) the *thermoelastic balance for a complete forward and reverse transformation cycle* can be expressed by:

P -> M: $$-\Delta s\,(T_0-T) + b \cdot n + a^{P\rightarrow M} + c^{P\rightarrow M} \cdot n = 0 \qquad (6.11a)$$

M -> P: $$\Delta s\,(T_0-T) - b \cdot n + a^{M\rightarrow P} + c^{M\rightarrow P}\,(1-n) = 0 \qquad (6.11b)$$

With equations (6.11), the transformation path, *n(T)*, that describes a complete hysteresis loop is equal to:

P -> M: $$T = T_0 - \frac{a^{P\rightarrow M}}{\Delta s} - \frac{b + c^{P\rightarrow M}}{\Delta s} \cdot n \qquad (6.12a)$$

M -> P: $$T = T_0 + \frac{a^{M\rightarrow P} + c^{M\rightarrow P}}{\Delta s} - \frac{b + c^{M\rightarrow P}}{\Delta s} \cdot n \qquad (6.12b)$$

From equations (6.12) the M_S and M_f temperatures as well as the A_S and A_f temperatures can be derived and a complete hysteresis cycle can be established.

The thermoelastic balance equations (6.11) and (6.12) can also be employed to describe the hysteresis behaviour of transformation sub-loops. For that, a partial forward transformation cycle is considered to start at a given point (n_f,T) on the main heating curve and a partial reverse transformation cycle to start at (n_r,T) on the main cooling curve.

The balance equations for incomplete transformation cycles are equal to:

P -> M (n_f,T): $$-\Delta s\,(T_0-T) + b \cdot n + a^{P\rightarrow M} + c^{P\rightarrow M} \cdot (n-n_f) = 0 \qquad (6.13a)$$

M -> P (n_r,T): $$\Delta s\,(T_0-T) - b \cdot n + a^{M\rightarrow P} + c^{M\rightarrow P} \cdot (n_r-n) = 0 \qquad (6.13b)$$

The martensite start temperature M_S' during the partial cooling cycle and the austenite start temperature A_S' during the partial heating cycle can be calculated to be:

$$M_S' = T_0 - \frac{a^{P\rightarrow M} + b \cdot n_f}{\Delta s} \qquad (6.14a)$$

$$A_S' = T_0 + \frac{a^{M\rightarrow P} - b \cdot n_r}{\Delta s} \qquad (6.14b)$$

By considering the experimental observations that a partial cooling cycle precisely closes at M_f while a partial heating cycle does the same at A_f (figure 3.20), the slope of the frictional force (c) has been defined for a transformation sub-loop (c_{sub}) to be:

$$c_{sub} = \frac{c + a - a_{sub}}{1 - n_{sub}} \qquad (6.15)$$

where a_{sub} is the constant friction force during the sub-loop and n_{sub} is the starting n-value of the sub-loop (n_r or n_f).

Simulation of Different Transformation Cycles

A *complete transformation cycle* as described in equations (6.11) is illustrated in figure 6.9. It can be seen that $a^{P->M}/\Delta s$ gives the undercooling below T_0 that is required to start the forward transformation and that the hysteresis width is equal to $(a^{P->M} + a^{M->P} + c^{M->P})/\Delta s$. Even if $a^{P->M}$ is equal to $a^{M->P}$, T_0 is not located halfway between M_s and A_f nor is T_0' located halfway between A_s and M_f. This result disagrees with the model as proposed by Tong and Wayman (1975), but it can be explained by the fact that the temperature spans $M_f - M_s$ and $A_f - A_s$ are not only determined by the elastic force $(b/\Delta s)$, but also by the friction force that opposes forward and reverse transformation ($c^{P->M}/\Delta s$ and $c^{M->P}/\Delta s$, respectively).

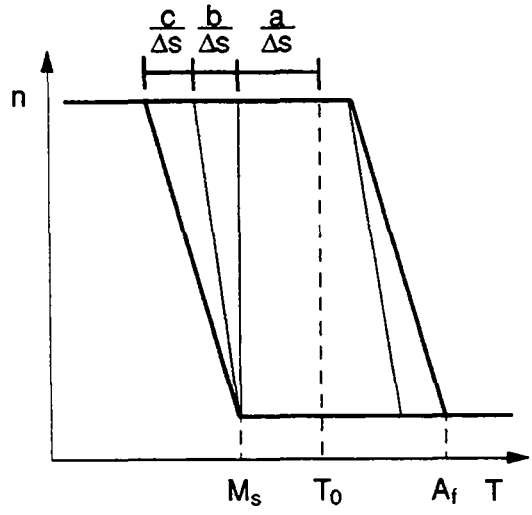

Figure 6.9: Simulated hysteresis loop showing a complete transformation cycle, calculated with the thermoelastic balance equations (3.11).

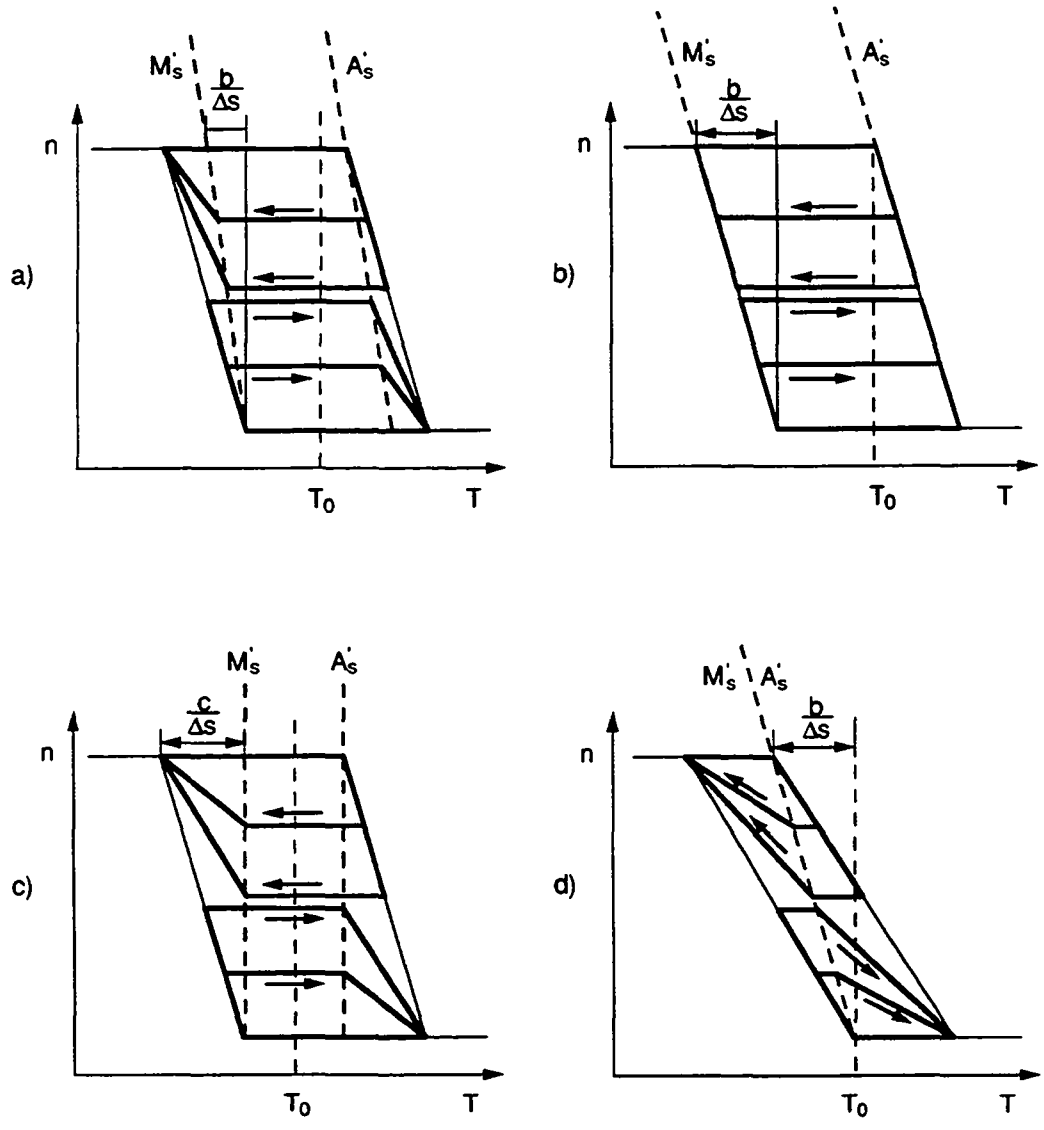

Figure 6.10: Simulated hysteresis loop with incomplete transformation cycles, applying the thermoelastic balance equations (6.13) : a) General case, b) complete elastic slope ($c = 0$), c) complete "dissipative" slope ($b = 0$), and d) the constant friction force is zero ($a = 0$).

The transformation paths during *incomplete transformation cycles* are illustrated in figure 6.10. Four different situations are shown, which are characterized by particular choices of the a, b and c parameters of the balance equations (6.13):

i) Figure 6.10a represents the general case, where all parameters are unequal to zero. The starting temperatures for forward and reverse transformation (M_S' and A_S') lie exactly on the purely elastic slope ($b/\Delta s$) inside the main hysteresis loop. The dependence of the M_S' and A_S' temperatures on the transformed volume fraction, where a particular partial

cycle begins, is determined by the constant friction force (parameter a) and the elastically stored energy (parameter b), according to equations (6.14).

ii) If the slope of the main hysteresis curve is only determined by the stored elastic force and the dissipative force only consists of a constant friction term ($c = 0$), it follows that the M_S' and A_S' temperatures lie exactly on the cooling and heating branches of the main hysteresis curve (figure 6.10b).

iii) If the entire thermoelastic slope arises from the increasing friction force during transformation and no reversible elastic contribution is considered ($b = 0$) the M_S' and A_S' curves are vertical lines displaced by $+a$ and $-a$ with respect to the T_0 temperature and coincide with the M_S and A_S temperatures of the main hysteresis (figure 6.10c).

iv) Figure 6.10d shows the case, where both reversible and irreversible contributions are important for the slope of the transformation hysteresis, but where the value of the constant frictional force (a) is set zero. In this case, the forward transformation starts at T_0.

The simulation of hysteresis curves in terms of the thermoelastic balance equation shows that many different hysteresis features that are experimentally observed, can be reproduced with appropriate choices of the parameters a, b and c. From the mathematical formulation of this phenomenological model it can be concluded that:

i) The existence of different hysteresis slopes during the forward and reverse transformation as well as the existence of internal transformation trajectories requires that the friction force depends on the transformed volume fraction ($c \neq 0$).

ii) In particular, the asymmetric shape of the transformation hysteresis has to be described with different friction forces that oppose the forward and reverse transformations ($c^{P->M} \neq c^{M->P}$) and the existence of M_S' and A_S' temperatures inside the main hysteresis has to be associated with different friction forces that are involved in partial and complete transformation cycles ($c_{partial\ cycle} \neq c_{complete\ cycle}$).

However, there is no evidence that this mathematical description can be related to the microstructural properties of shape memory alloys. Therefore, the goal of the following section is to find out whether microstructural features can be defined, which are in agreement with the particular phenomenological formulations. The microscopical description starts with the definition of the basic conditions that possible obstacles have to fulfill in order to cause the elastic and friction forces as they have been assumed in this paragraph. It will be demonstrated that the resistance forces or the energy barriers that have to be overcome during

the successive fragmentation of martensitic variants, is an appropriate parameter in order to explain the necessary terms of both the elastic and dissipative energies.

6.3.2 Microscopical Description of the Non-Chemical Energy Contributions

The Distribution of Obstacles

The slope of the transformation hysteresis is due to a combination of reversible elastic forces and irreversible friction forces, both of which increase as a function of the transformed volume ($b \neq 0$, $c \neq 0$). Figure 6.11 demonstrates that a finite hysteresis slope only results, if the obstacles which resist the transformation, are inhomogeneously distributed. The schematic of figure 6.11a describes, in a two-dimensional situation, a transforming interface that has a constant length (L_0) and moves upwards from the lower position (in direction of the coordinate r). In this presentation, r is equivalent with the amount of transformed volume. The moving interface has to transform regions that contain obstacles whose density increases successively. For the sake of this generalized situation, the exact nature of these obstacles is not determined, but they can be associated with precipitates that are contained in an austenitic matrix. The more complicated obstacle type that is needed for the explanation of the observed hysteresis effects in Cu-Zn-Al alloys, is defined in section 6.3.3.

The situation where the chemical driving force is entirely balanced by an increasing elastic force and the frictional forces do not contribute to the hysteresis slope ($b \neq 0$, $c=0$) can be associated with coherent precipitates which are *elastically deformed* by the transforming interface. If the obstacles are homogeneously distributed in the matrix, the stored elastic energy is proportional to r ($\Delta G_{el} = \text{const} \cdot r$). Consequently, the repulsive elastic force is independent of r ($g_{el} = d\Delta G_{el}/dr = \text{const}$) and a transforming interface would overcome all of the obstacles at the critical value of the external driving force. If the obstacles are inhomogeneously distributed, the stored elastic energy is no longer proportional to r. Then, the repulsive elastic force depends on r and a continuous increase of the external driving force is required to transform the regions where the density of obstacles increases (figure 6.11b). The elastically deformed obstacles assist the reverse interface motion which is then completed below T_0.

The situation, where the slope of the transformation is completely determined by an increasing friction force ($c \neq 0$, $b=0$) can be associated to the case, where incoherent particles are *plastically deformed* by the transforming interface. When the interface passes a region of homogeneously distributed obstacles, the dissipated energy increases linearly with r ($W_{irr} = \text{const} \cdot r$), the friction force is constant during transformation ($g_{dis} = dW_{irr}/dr = \text{const}$)

and the transforming interface would overcome all of the obstacles at the critical driving force. Therefore, the existence of a friction force which depends on the transformed volume fraction can be taken as a strong indication of inhomogeneously distributed obstacles. In this case, an increasing driving force for the forward transformation is required (figure 6.11c) and the start of the reverse transformation is shifted to higher temperatures as compared to figure 6.11b, because no elastic energy has been stored during the forward transformation. Figure 6.11d gives the example of a hysteresis curve where both increasing elastic and friction forces are created when the obstacles are deformed during transformation.

In conclusion, *the existence of both an increasing elastic force ($b \neq 0$) and an increasing friction force ($c \neq 0$) requires that obstacles which store elastic energy and dissipate energy during transformation, are inhomogeneously distributed in the material.*

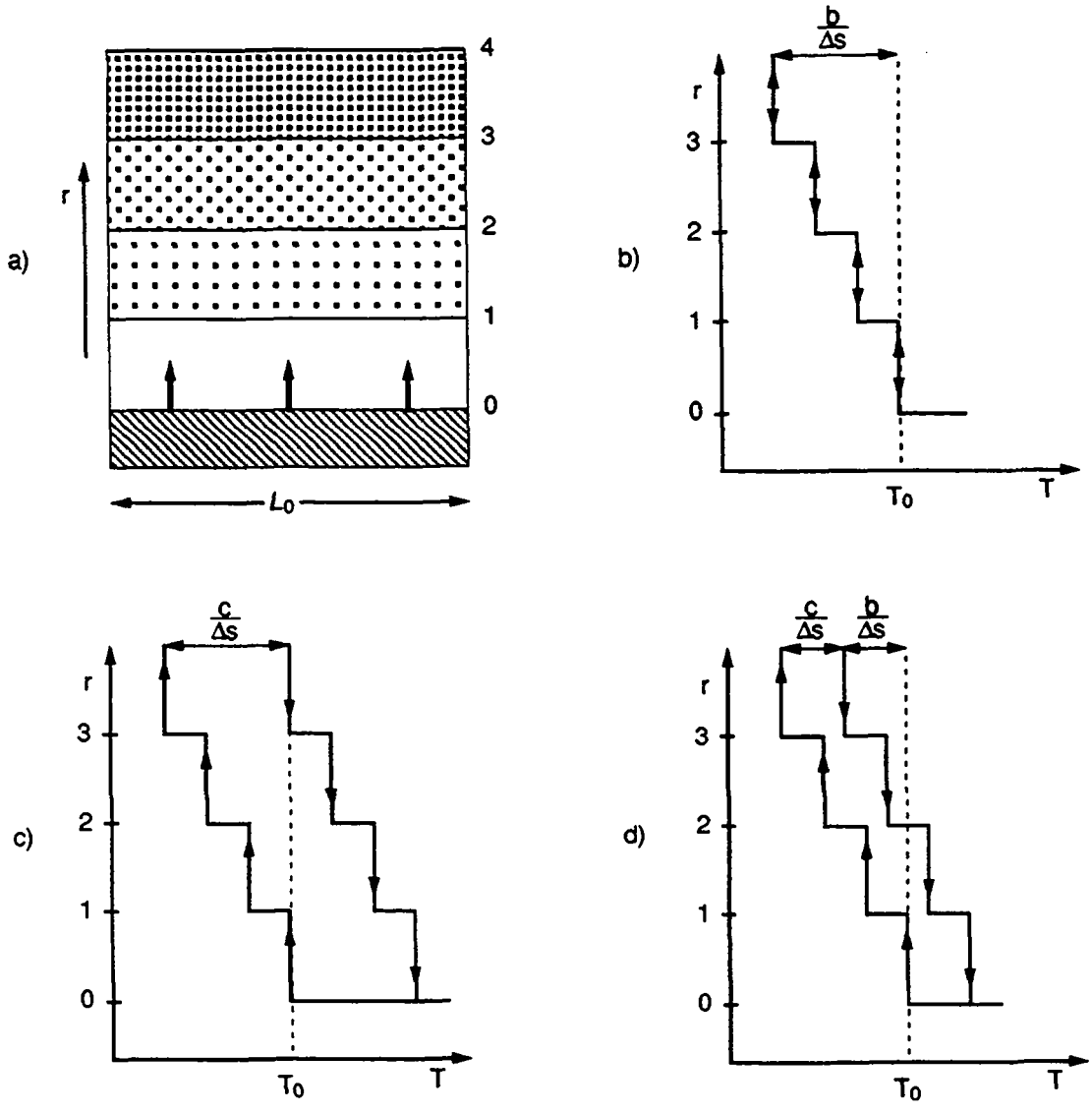

Figure 6.11: Schematic of a transforming interface in a matrix containing obstacles (a) and the associated transformation paths for $c = 0$ (b), $b = 0$ (c) and the general case (d).

The Stability of the Obstacle's Distribution

The obstacles in the microscopical situation of figure 6.11a can be described by a profile of the resisting elastic and friction forces ($g_{nch}(r) = g_{el}(r) + g_{dis}(r)$). Figure 6.12a shows the obstacle profile which results if it is assumed that equal portions of energy are dissipated during the forward and the reverse transformation. If the obstacle profile does not change during forward transformation, the trajectories of partial forward transformation cycles would follow straight lines and join the main hysteresis curve without any change in the transformed volume fraction (figure 6.12b). The same argument is valid for partial reverse transformation cycles and it follows that both M_S' and A_S' temperatures would not exist, if the resistance force of obstacles at a given transformed volume fraction were constant and independent of the transformation history.

It follows that *the existence of internal transformation paths (including M_S' and A_S' temperatures) is associated with modifications in the obstacle profile (size and distribution) that occur by microstructural changes during the particular transformation trajectories.* In other words, the distribution of obstacles which give rise to both the storage of elastic energy and the dissipation of energy, changes depending on the history of the transformation path which is followed to reach a given transformed volume fraction.

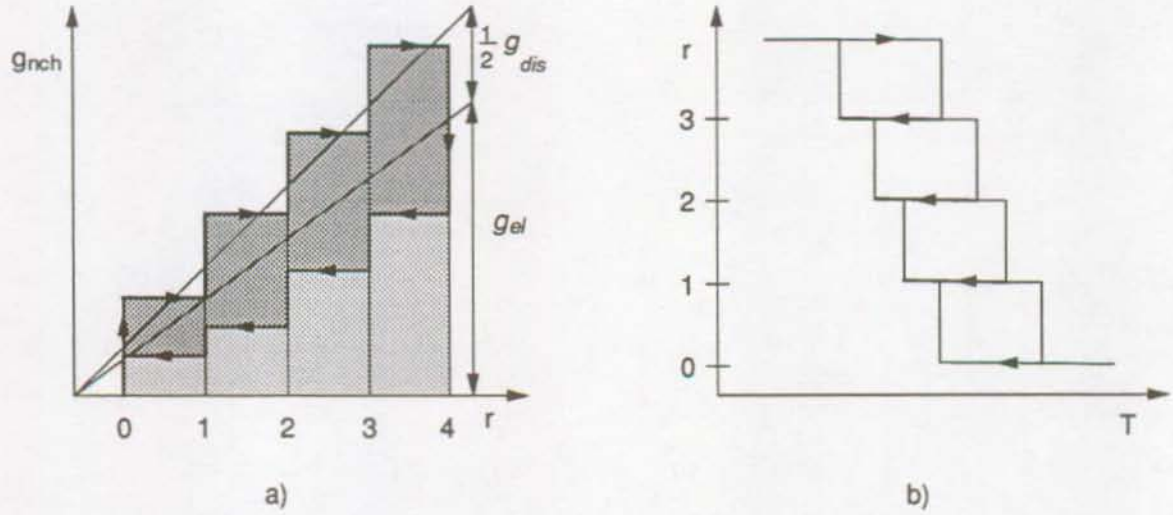

Figure 6.12: a) The profile of obstacles that oppose the transformation as shown in figure 6.11a.
b) The associated transformation paths having straight line internal trajectories.

The phenomenological model of the thermoelastic balance equation, as formulated for partial transformation cycles, indirectly accounts for microstructural changes that modify the resistive forces. In this model, the friction force that depends on the transformed volume

fraction, is "reset to zero" when a transformation path is stopped before reversion takes place ($n = n_r$ in equations 6.13), and it is assumed that the friction forces change during a partial cycle in order to "memorize" the reversion points ($c_{sub} \neq c$ in equation 6.15). Both assumptions have strictly "technical" or mathematical signification and therefore demand a microscopical explication that is in agreement with the particular properties of thermoelastic martensites. This explication will be given by the microstructural changes that occur when the elastically stored energy is relaxed.

6.3.3 The Mechanism of Elastic Energy Relaxation and Associated Hysteresis Effects

General Description

Relaxation of elastically stored energy is known to be an important contribution to the amount of dissipated energy during martensitic transformations (Delaey et al., 1986). In general, relaxation of elastic energy occurs in order to decrease a local (internal) elastic stress field. In this study, relaxation processes were directly observed during TEM *in situ* transformations which are covered in chapter 5. The results show that an internal stress field can drive the motion of martensitic interfaces which is, in this case, accompanied by changes in the stacking fault sequences and the motion of partial dislocations. IF measurements showed that at the end of the transformation additional energy dissipation arises and it was concluded that the hysteretic motion of martensitic interfaces and partial dislocations is responsible for this dissipation effect.

"Obstacles" that oppose the martensitic transformation and give rise to the relaxation of elastic energy can be associated with energy barriers that have to be overcome, during stress-free transformations, by the successive fragmentation of martensitic variants and groups (figure 6.6). An energy barrier arises when the growth of one system of martensitic variants is limited by the increasing elastic force and the formation of another variant system that would accommodate the elastic stresses, requires nucleation. At the moment where nucleation takes place it can be assumed that the new system of martensitic variants grows very fast and the elastically stored energy is reduced in an out-of-equilibrium process so that energy is dissipated. In the further course of the transformation more and more elastic energy has to be accommodated and the successive fragmentation of martensitic variants is accompanied with increasing amounts of energy relaxation. Then, the dissipative energy contribution (friction force) that is associated with the relaxation of elastic energy increases with the transformed volume fraction ($c \neq 0$).

The Asymmetric Hysteresis Shape

Since the stored elastic energy opposes the forward and promotes the reverse transformation it is possible to claim that the energy barriers or the "obstacles" that are associated with the successive fragmentation and the amount of relaxed elastic energy, are higher during forward transformation than they are during the reverse transformation. It follows that the friction force that arises from this process, is significantly higher during the forward than during the reverse transformations ($g_{dis}^{P->M} >> g_{dis}^{M->P}$) and a transformation hysteresis with different slopes (*asymmetric hysteresis shape*) results. This is shown in figure 6.13.

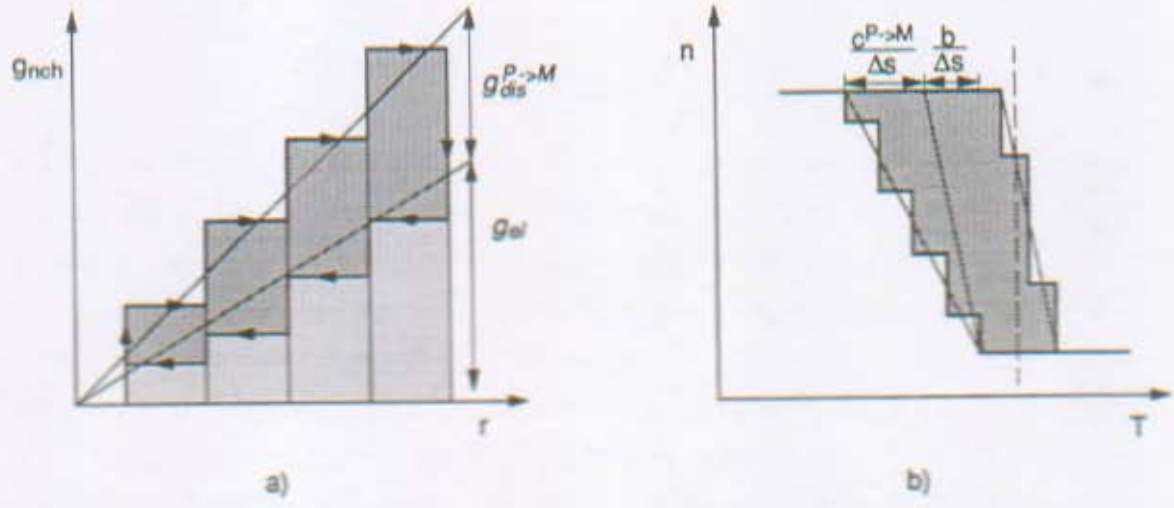

Figure 6.13: a) The profile of "obstacles" that is associated with the successive fragmentation of martensitic variants. The dissipated energy due to the relaxation of elastic energy is higher during the forward than during the reverse transformation ($g_{dis}^{P->M} >> g_{dis}^{M->P}$) and an asymmetric hysteresis curves results (b).

A *symmetric hysteresis* is formed when the amount of relaxed elastic energy during the successive formation of martensitic variants is negligible and only a constant friction force must be considered for the shape of the transformation hysteresis. This is the case for stress-induced transformations and the formation of educated martensite where the elastically stored energy is reduced by the macroscopic shape change.

Internal Hysteresis Curves during Partial Transformation Cycles

During partial transformation cycling, M_S' and A_S' temperatures exist inside the macroscopic hysteresis and, in a microscopic scale, the transformed volume changes slightly as soon as the reversion temperature is passed (figure 6.2a). The analysis of the "butterfly" curves of Q^{-1} and f has confirmed that partial transformation cycling is always accompanied by changes in the transformed volume. In the following, these observations are explained by the variation of the elastic strain energy inside the material and the local character of relaxation processes both of which change the "obstacle" profile during transformation.

The stored elastic energy that is built up during the forward transformation and released during the reverse transformation, is not homogeneously distributed in the transforming material. A high elastic strain field acts on individually transforming martensitic variants (figure 6.14a) because they can only minimize their strain energy by an appropriate sequence of the basal plane stacking faults. On the other hand, combinations of several martensitic variants or self-accomodating groups (figure 6.14b) compensate the elastic strain fields very effectively by the formation of common interfaces. Due to the variety of defects and variant combinations that are created during martensitic transformations, a given transforming material is certainly composed of a whole spectrum of elastic energy distributions.

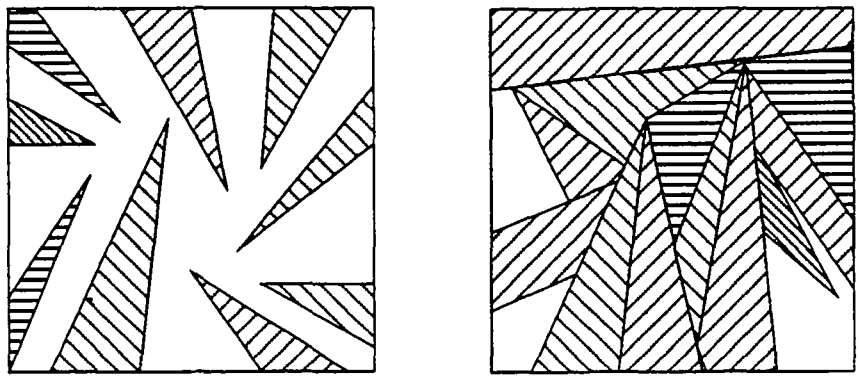

Figure 6.14: Schematic of martensitic microstructures with different amounts of stored elastic energy: a) Individual martensitic variants inside the austenite, ΔG_{el} is high. b) Combinations of different martensitic variants, ΔG_{el} is low.

This idea will be applied to explain the "obstacle" profile that represents the elastic and friction forces during complete and partial transformation cycles (figure 6.15a). During

complete transformations a given transformed volume fraction (n_f) is associated with a typical arrangement of martensitic variants and a particular distribution of the elastic and dissipative energy terms ($g_{nch}^{complete}$). If one considers that during further martensitic transformation relaxation occurs in both the new formed martensite and the structure that already existed at n_f, the subsequent retransformation leads to a martensitic microstructure at n_f that has a different distribution of the elastic and friction forces. By starting a partial forward transformation cycle at n_f, the distribution as well as the absolute values of the resistive forces ($g_{nch}^{partial}$) are different. In the schematic of figure 6.15b, four different obstacles are assumed for the partial forward cycle at n_f, instead of the two larger obstacles that were present at n_f during the complete forward transformation cycle. Consequently, the forward transformation during the partial cycle starts at a higher temperature than during the complete cycle ($M_s^{partial} > M_s^{complete}$).

On the other hand, partial reverse transformation cycles will start at lower temperatures when the specimen was cooled from the austenitic state, because the elastic energy that promotes the reverse transformation is higher on the cooling branch than it is on the heating branch of the hysteresis ($A_s^{partial} < A_s^{complete}$).

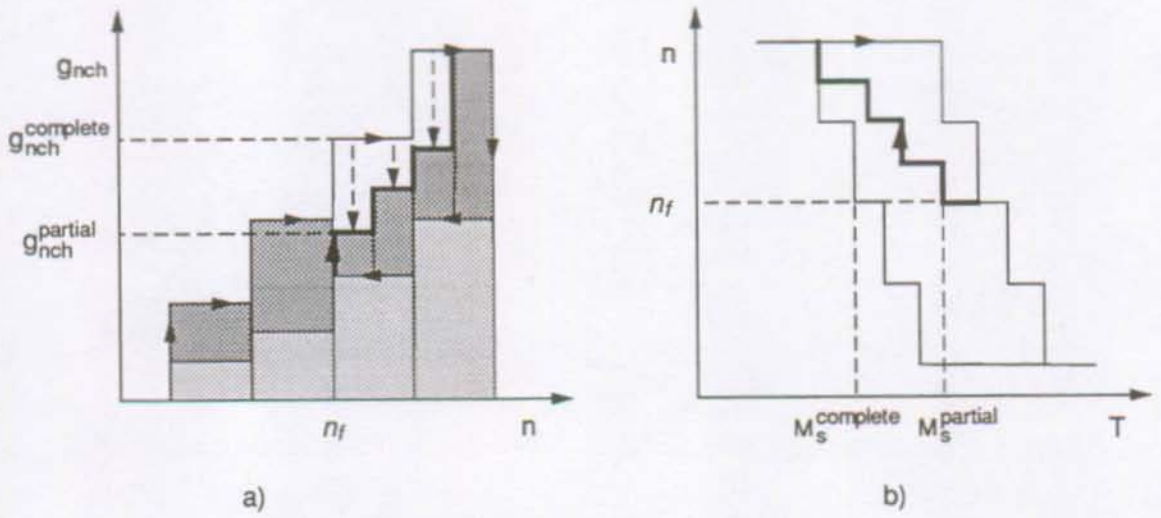

Figure 6.15: The profile of obstacles and the associated transformation paths during partial temperature cycles.

The Shift of Transformation Sub-Loops during Repetitive Temperature Cycling

During repetitive temperature cycling (PTC) the transformation sub-loops have been observed to shift to higher values of the transformed volume fraction. This shift can be understood by considering the importance of the elastic strain energy and its relaxation processes for "obstacle" forces that resist the martensitic transformation.

When repetitive transformation sub-loops are performed in a fixed temperature interval ($T_1 < T < T_2$) it can be assumed that successive stress relaxation occurs in the martensitic structure. Then, the energy barriers or the resistive forces ($g_{nch}^{partial}$) that oppose the martensitic transformation during the partial cooling cycles (C_1, C_2 and C_3) decrease progressively (figure 6.16a), and this increases the martensite start temperature (M_s') of subsequent cycles (figure 6.16b). Therefore, the volume fraction of martensite increases ($n_3 > n_2 > n_1$). The start temperature of the reverse transformation (A_s') of subsequent heating cycles increases, because the elastic energy that promotes the reverse transformation decreases in the course of the relaxation processes. Due to the decreasing temperature span (T_2 - A_s') in which reverse transformation takes place, the volume fraction that is retransformed during one transformation sub-loop decreases with increasing number of cycles. Since the elastic energy can only be relaxed on a local scale during small transformation cycles, the elastic energy will smoothly decrease to a final value so that the transformation sub-loops stabilize after a certain number of cycles (typically 10 cycles).

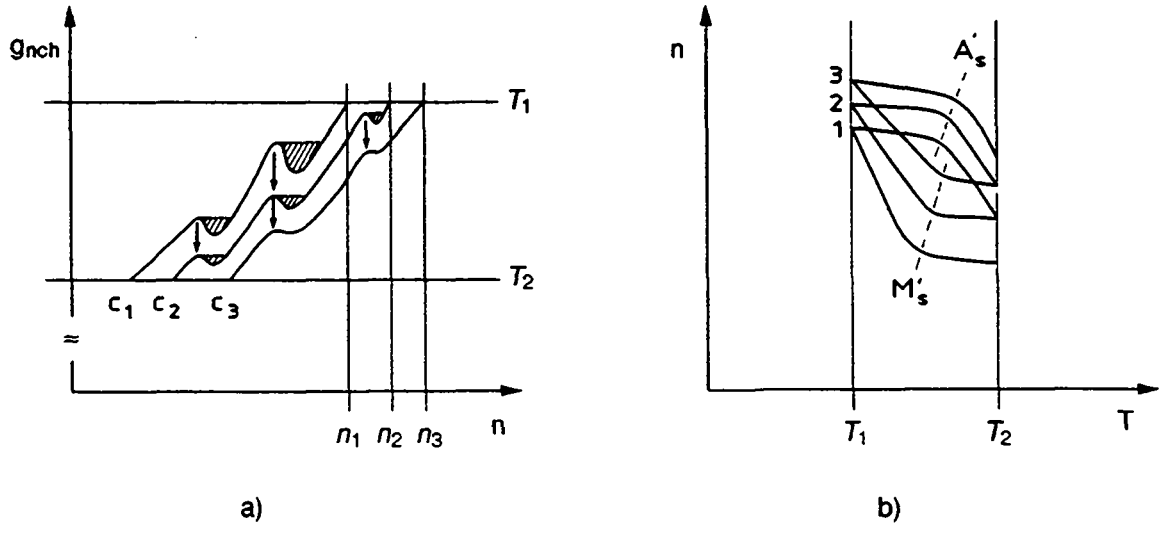

Figure 6.16: a) The change of the obstacle profile during repetitive partial temperature cycling.
b) The shift of transformation sub-loops due to the changing M_s' and A_s' temperatures.

The relaxation of elastic energy is most important for spontaneous (stress-free) thermally-induced transformations, since the elastically stored energy has to be accommodated without a shape change of the material. During stress-induced transformations the elastic energy is compensated by the applied stress and a resulting macroscopic transformation strain. The transformation hysteresis of trained specimens showed a small $n(T)$ slope (figure 3.2c), indicating that the elastically stored energy is high at the end of the forward transformation and relaxation processes are less frequent than during spontaneous transformations. This can be understood by considering that the dislocation structure (introduced in the parent phase during training) favors particular variants and opposes the reorientation into other variant orientations, even if this would reduce the elastically stored energy. In the absence of relaxation processes, the energy barriers that oppose the martensitic transformation (obstacle profile) do not change and as a consequence, the transformation hysteresis has a more symmetrical shape and the sub-cycles do not shift in the course of repetitive transformation cycling.

6.4 Suggestions for Future Work on Hysteresis Effects

This investigation has shown that the elastic and dissipative energy terms are not independent contributions of the transformation hysteresis in shape memory alloys, but have to be seen as hysteresis parameters which are strongly correlated; the more energy is dissipated the less is the amount of elastically stored energy. An interesting subject for future work for studying the interaction between elastic and frictional forces during transformation, could be the investigation of the hysteresis behaviour in Cu-Zn-Al alloys that contain γ precipitates. Since the size and distribution of the γ precipitates and therefore the relative portions of energy storage and dissipation can be controlled by appropriate heat treatments, the hysteresis effects could be studied systematically. The experiments should contain both complete and incomplete transformations and could be conducted on a single alloy or even on a single specimen.

CONCLUSIONS

The hysteresis effect that is associated with martensitic transformations in Cu-Zn-Al shape memory alloys is strongly influenced by the microstructural properties of the transforming material. In this investigation, internal friction (IF) measurements and *in situ* transmission electron microscopy (TEM) observations have been combined in an attempt to relate the microscopic hysteresis effects that are associated with microstructural transformation mechanisms to the macroscopic hysteresis effect.

The IF experiments have supplied quantitative information about the microscopic hysteresis effects that accompany the transformation process. In *single variant transformations*, the microscopic hysteresis (IF) results from a small stress hysteresis ($\Delta\sigma = 0.2$ MPa) which is equal to the macroscopic stress hysteresis that is involved in the motion of a single martensite-austenite interface. It was shown that the interface motion during IF measurement is not completely hysteretic, as is assumed in existing models, but it is a partially reversible process. Furthermore, it was found that the majority of energy dissipation comes from anelastic deformation on the habit planes, while only small contributions arise from the anelastic deformation on the basal planes (lattice invariant deformation). During martensitic *polyvariant transformations*, it was observed that the transient internal friction peak not only depends on the transformation rate, but also on the interactions (reorientations) between different martensitic variants. It was proposed that the motion of martensite-martensite interfaces occurs during the formation of new variant groups in order to reduce the elastic strain energy. This effect has been phenomenologically described by the fragmentation parameter which accounts for the increase of mobile martensitic interfaces that move in the direction of the oscillation stress and contribute to the microscopic hysteresis effect.

The TEM observations of *in situ* transformation and deformation experiments showed that internal and external stress variations change the martensitic microstructure. The motion of partial dislocations on the martensitic basal planes was observed to accommodate local internal stress fields and the motion of martensite-martensite interfaces occurred when an external stress was applied. The motion of an A/D type twin boundary of the M18R martensite was accompanied by stacking fault changes inside the converting variants, in contrast to the migration mechanism that is assumed in literature. It was proposed that stacking fault changes improve the atomic matching across the interface and that they can be accomplished by the motion of partial dislocations, which convert existing sequence stacking faults from one type

into another. This mechanism is consistent with both the existence of partial dislocations and the displacement vectors that have been published for the stacking faults in Cu-Zn-Al martensite.

The most important macroscopic hysteresis effects that were observed in this study, are the symmetric/asymmetric shape of different transformation hysteresis, the formation of internal hysteresis trajectories during partial transformation cycles, and the shift of transformation sub-loops in the course of repetitive small temperature cycles (hysteresis instabilities). These effects have been phenomenologically explained by applying the thermoelastic balance equation, which presents the transformation process as a balance between the chemical driving force and the non-chemical (elastic and frictional) forces. Along with the mathematical formulation of the balance equation, microscopic interpretations (based on the results of the IF and TEM studies) have been outlined for the non-chemical forces. It was proposed that frictional forces which give rise to energy dissipation, can be associated with the relaxation of elastically stored energy. Following this idea, the investigated transformation systems can be characterized as follows:

During *stress-free (spontaneous) transformations*, the elastic strain energy is reduced by the formation of different martensitic variants which have compensating shear deformations. The amount of elastically stored energy that is irreversibly relaxed, increases in the course of the transformation and as a result, the macroscopic hysteresis width increases as a function of the transformed volume (asymmetrical hysteresis shape). The transformation trajectories of partial transformation cycles are influenced by the inhomogeneous distribution of the non-chemical forces inside the material, which depends on the transformation history. In particular, during repetitive transformation cycling the elastically stored energy can be progressively relaxed such that the volume fraction of martensite increases with increasing number of cycles.

During *stress-induced transformations* in polycrystals and temperature-induced *transformations in educated materials*, the formation of selected martensitic variants produces a macroscopic shape change and the amount of relaxed elastic energy is significantly lower. As a consequence, the hysteresis effect is less dependent on relaxation processes. This explains the symmetrical hysteresis shape and the relative stability of transformation sub-loops during repetitive cycling.

REFERENCES

Abu Arab A., Ahlers M., *Acta metall.*, **36** (1988) 2627.

Adachi K., Perkins J., *Met. Trans. A*, **16** (1985) 1551.

Adachi K., Perkins J., Wayman C.M., *Acta metall.*, **34** (1986) 2471.

Ahlers M., *Z. Metallkde.*, **65** (1974) 636.

Ahlers M., *Scripta metall.*, **8** (1974) 213.

Ahlers M., *Progress in Material Science*, **30** (1986) 135.

Ahlers M., private communication (1990).

Amengual A., Torra V., Isalgue A., Marco F., *Thermochimica Acta*, **155** (1989) 115.

Andrade M., Ph. D. Thesis, Katholieke Universiteit Leuven, Belgium, 1983.

Andrade M., Chandrasekaran M., Delaey L., *Acta metall.*, **32** (1984) 1809.

Auguet C., Cesari E., Rapacioli R., Manosa L., *Scripta metall.*, **23** (1989) 579.

Baur J., Kulik A., *J. Physique*, **44** (1983) C9-357.

Belko V.N., Darinsky B.M., Postnikov V.S., Sharshakov I.M., *Phys. of Met. and Metallogr.*, **27** (1969) 140.

Bidaux J.-E., Ph.D. Thesis Lausanne EPFL, Thèse No 761, 1988.

Bidaux J.-E., Gremaud G., Benoit W., *Proc. ECIFUAS*, Cracow, Poland, 1991, to be published.

Bilby B.A., Crocker A.G., *Proc. Roy. Soc. (London) A*, **288** (1965) 240.

Boresi A.P., Sidebottom O.M., "*Advanced Mechanics of Materials*", New York, John Wiley & Sons, 1985.

Bowles J.S., Mackenzie J.K., *Acta metall.*, **2** (1954) 129, 138 and 224.

Carrard M., Guisolan B., Martin J.-L., *J. Phys. E : Sci. Instrum.*, **16** (1983) 480.

Cesari E., Pons J., Segui C., *J. Physique*, **IV(1)** (1991) C4-41.

Chakravorty S., Wayman C.M., *Acta metall.*, **25** (1977) 989.

Christian J.W., *"The Theory of Transformations in Metals and Alloys"*, Oxford, Pergamon Press, 1965.

Cohen M., Olson G.B., Clapp P.C., 1979, *Proc. ICOMAT 1979*, Cambridge (MA), MIT, p.1-11.

Cook J.M., O'Keefe M.A., Smith D.J., Stobbs W.M., *J. Microscopy*, **129** (1983) 295.

Cornelis I., Wayman C.M., *Scripta metall.*, **10** (1976) 359.

Cory J.S., McNichols J.L., *J. Appl. Phys.*, **59** (1985) 3282.

Cottrell A.H., Bilby B.A., *Phil. Mag.*, **42** (1951) 573.

Coujou A., Lours P., Roy N.A., Caillard D., Clement N., *Acta metall. mater.*, **38** (1990) 825.

Dejonghe W., De Batist R., Delaey L., De Bonte M., *Shape Memory Effect in Alloys*, Plenum Press, New York, 1975, p. 451.

Dejonghe W., De Batist R., Delaey L., *Scripta metall.*, **10** (1976) 1125.

Dejonghe W., Delaey L., De Batist R., Van Humbeeck J., *Metal Science*, **11** (1977) 523.

Delaey L., *Proc. First JIM Int. Symp. New Aspects of Mart. Transf.*, Kobe, 1976, p.135.

Delaey L., in *"Phase Transformations in Materials"*, ed.: Haasen P., VCH, Weinheim, 1991.

Delaey L., Deruyttere A., Aernoudt E., Roos J.R., *INCRA Research Report* (Project No. 238), 1978.

Delaey L., Aernoudt E., *Proc. ICOMAT 1986*, The Japan Institute of Metals, p.926-933.

Delaey L., Ortin J., Van Humbeeck J., *Proc. Phase Transformations 1987*, p.60-66.

Delorme J.F., Gobin P.F., *Métaux*, **573** (1973) 185 and **574** (1973) 209.

De Vos J., Aernoudt E., Delaey L., *Z. Metallkde.*, **69** (1978) 438.

Falk F., *Acta metall.*, **28** (1980) 1773.

Fukamachi M., Kajiwara S., *Jap. J. appl. Phys.*, **19** (1980) 479.

Gotthardt R., Guisolan B., Buffat P., *J. Microsc. Spectrosc. Electron.*, **4** (1979) 587.

Granato A., Lücke K., *J. of Appl. Phys.*, **27** (1956) 583 and 789.

Gremaud G., Bidaux J.-E., Benoit W., *Helv. physica acta*, **60** (1987) 947.

Guénin G., Gobin P.F., *Met. Trans. A*, **13** (1982) 1127.

Guénin G., Clapp P.C., *Proc. ICOMAT 1986*, The Japan Institute of Metals, p.171.

Hirth J.P., in *"Deformation Twinning"*, Eds.: Reed-Hill R.E., Hirth J.P., and Rogers H.C., Gordon and Breach, New York, 1964, p.112.

Hornbogen E., *Z. Metallkde.*, **10** (1987) 352.

Kaufmann L., Cohen M., *Progress in Metal Phys.*, **7** (1958) 165.

Katata K., Saka H., *Phil. Mag. A*, **59** (1989) 677.

Koshimizu S., Ph.D. Thesis Lausanne EPFL, Thèse No 416, 1981.

Kurdjumov G.V., Khandros L.C., *Dokl. Akad. Nauk. SSSR*, **66** (1949) 211.

Li Lü, Aernoudt E., Wollants P., Van Humbeeck J., Delaey L., *Z. Metallkde.*, **81** (1990) 613.

Lovey F.C., *Acta metall.*, **35** (1987) 1103.

Lovey F.C., Van Tendeloo G., Van Landuyt J., Delaey L., Amelinckx S., *phys. stat. sol. (a)*, **86** (1984) 553.

Lovey F.C., Van Tendeloo G., Van Landuyt J., Amelinckx S., *Scripta metall.*, **19** (1985) 1223.

Lovey F.C., Amengual A., Torra V., Ahlers M., *Phil. Mag. A*, **61** (1990) 159.

Lovey F.C., Isalgue A., Torra V., *Acta metall. mater.*, **40** (1992) 3389.

Mayergoyz I.D., *J. Appl. Physics*, **57** (1985) 3803.

Mercier O., Melton K.N., *Scripta metall.*, **10** (1976) 1075.

Morin M., Guénin G., Gobin P.F., *Proceedings ECIFUAS*, Manchester, England, 1980, p.275.

Morin M., Guénin G., Gobin P.F., *J. de Physique*, **43** (1982) 685.

Müller I., Xu H., *Acta metall.*, **39** (1991) 263.

Nakanishi N., in *"Shape Memory Effects in Alloys"*, Ed.: J.Perkins, Plenum Press, New York, 1975, 147.

Nishiyama Z., *"Martensitic Transformations"*, New York, Academic Press, 1978.

Nishiyama Z., Kajiwara S., *Trans. JIM*, **3** (1962) 127.

Nowick A.S., Berry B.S., *"Anelastic Relaxation in Crystalline Solids"*, Academic Press, New York, 1972.

Olson G.B., Cohen M., *Scripta metall.*, **9** (1975) 1247.

Olson G.B., Cohen M., *Scripta metall.*, **11** (1977) 345.

Olson G.B., Cohen M., *Met. Trans. A*, **6** (1982) 791.

Ortin J., *J. Appl. Phys.*, **71** (1992) 1454.

Ortin J., Planes A., *Acta metall.*, **36** (1988) 1873.

Ortin J., Planes A., *Acta metall.*, **37** (1989) 1433.

Ortin J., Planes A., *J. Physique*, **IV(1)** (1991) C4-13.

Otsuka K., Shimizu K., *Trans. JIM*, **15** (1974) 109.

Otsuka K., Wayman C.M., *Scripta metall.*, **9** (1975) 1017.

Otsuka K., Shimizu K., *Intern. Metals Review*, **31** (1986) 93.

Paskal Y.I., Monasevich L.A., *Phys. Met. Metall.*, **52** (1981) 95.

Pelegrina J.L., Ahlers M., *Acta metall. mater.*, **40** (1992), 3221.

Planes A., MacQueron J.L., Ortin J., *Phil. Mag. Letters*, **57** (1988) 291.

Planes A., Romero R., Ahlers M., *Acta metall. mater.*, **38** (1990) 757.

Postnikov V.S., Sharshakov I.M., *Fiz. Met. Metallov.*, **33** (1972) 222.

Rapacioli R., Ahlers M., *Scripta metall.*, **11** (1977) 1147.

Rapacioli R., Chandrasekaran M., *Proc. ICOMAT 1979*, p.596.

Rios-Jara D., Guénin G., *Proc. ICOMAT 1986*, The Jap. Inst. of Met., 1987, p.757.

Saburi T., Nenno S., *Proc. Int. Conf. on Solid to Solid Phase Transf.*, Eds.: Aaronson et al., The Metall. Soc. of AIME, New York, 1982, p.1455.

Salzbrenner R.J., Cohen M., *Acta metall.*, **27** (1979) 739.

Schaller R., Van Humbeeck J., *Intern. Summer School on Mech. Spectroscopy*, Cracow, 1992.

Scheil E., Müller J., *Archiv. Eisenhütten*, **27** (1956) 801.

Schroeder T.A., Wayman C.M., *Acta metall.*, **25** (1977) 1375.

Secrétan B., Martinet B., Vittoz B., *J. mathém. et phys. appl.*, **XIII** (1962) 96.

Segers D., Van Humbeeck J., Dorikens-Vanpraet L., Lemahieu I., Dorikens M., *Scripta metall.*, **22** (1988) 521.

Shimizu K., *Mem. Inst. Sci. Ind. Res. Osaka Univ.*, **34** (1977) 9.

Stalmans R., Van Humbeeck J., Delaey L., *Acta metall. mater.*, **40** (1992) 2921.

Steiner A., Ph.D. Thesis Université de Genève, Thèse No 2180, 1986.

Suzuki H., *Proc. ICOMAT 1986*, The Japan Institute of Metals, p.43-48.

Tas H., Delaey L., Deruyttere A., *Met. Trans. A*, **4** (1973) 2833.

Thompson N., Millard D.J., *Phil. Mag. A*, **43** (1952) 422.

Timoshenko S., *"Résistance des Matériaux"*, Librairie polytechnique Béranger, 1963.

Tong H.C., Wayman C.M., *Acta metall.*, **23** (1975) 209.

Torra V., Tachoire H., *Thermochim. Acta*, **203** (1992) 419.

Van Humbeeck J., Ph. D. Thesis, Katholieke Universiteit Leuven, Belgium 1983.

Van Humbeeck J., in *"Internal friction in solids"*, Proc. of the Summer School on IF in Solids, Krakow, Poland, 1984, p.131-149.

Van Humbeeck J., Delaey L., *Z. Metallkde.*, **75** (1984) 760.

Van Humbeeck J., Stoiber J., Gotthardt R., *Proc. ICIFUAS 1989*, p.321.

Van Humbeeck J., Stalmans R., *Materials Science Forum*, **56-58** (1990) 405.

Wechsler M.S., Liebermann D.S., Read T.A., *Trans AIME*, **197** (1953) 1503.

Yoshida I., Sugai T., Tani S., Motegi M., Minamida K., Hayakawa H., *J. Phys. E : Sci. Instrum.*, **14** (1981) 1201.

Zhongguo W., Dazhi Y., *Scripta metall.*, **22** (1988) 1245.

Zhu J.S., Schaller R., Benoit W., *phys. stat. sol. (a)*, **108** (1988) 613.

ACKNOWLEDGMENTS

During the course of this work I have received the invaluable help of many people from the Institut de génie atomique. I would like to thank all of them for their support and encouragement.

In particular, I wish to acknowledge my adviser Dr. Rolf Gotthardt for his guidance, encouragement and enthusiasm during all phases of this investigation. I am also indebted to Dr. Jaques-Eric Bidaux and Dr. Jan Van Humbeeck for their valuable advice and fruitful discussions. To Prof. M. Ahlers I express my gratitude for his comments and suggestions.

Bernard Guisolan and Michel Longchamp are thanked for their excellent work in both the development and construction of the *in situ* straining stage as well as the modifications of the torsion pendulum. Alfred Neuenschwander for his various glass works, Alessandro Ichino for his help with the electronics and Andrzej Kulik for advice about computing are all gratefully acknowledged. I thank Jean Hägi and Gérald Beney for the preparation of the Cu-Zn-Al single crystals, Philippe Bugnon for his valuable help in preparing specimens, Nathalie Guisolan for the many photographs she produced and Claude Jaquat for the great number of figures he drew for this manuscript.

Special thanks go to Dr. Kevin Hemker for both his friendship and correcting the English of this thesis. Along with him I would like to thank all of my friends at "Boys Night", who gave me indispensable mental refreshment every week. Thanks are also addressed to the members of the "apéro" on Fridays at 11.30 a.m.

Last but not least, I wish to acknowledge the love and encouragement of my family and especially my wife Doris, for her help, support and understanding.

This work was financially supported by the "Commission pour l'Encouragement de la Recherche Scientifique (CERS)".

CURRICULUM VITAE

Johannes STOIBER

né le 07 octobre 1961, originaire de Erlangen (Allemagne)

marié, un enfant

1972 - 1981	Ohm - Gymnasium (Erlangen) Obtention de la maturité
1982 - 1988	Friedrich-Alexander Universität Erlangen-Nürnberg Obtention de diplôme d'ingénieur en science de matériaux
1988 - 1992	Assistant à l'Institut de Génie Atomique, EPF Lausanne Enseignement des travaux pratiques avancés, section physique, et des exercises de mécanique générale